INTERFACES IN MODIFIED CELLULOSE NANOCRYSTALS REINFORCED POLYETHYLENE

Doctoral thesis submitted to the University of Exeter in fulfilment of the requirements
of the degree of Doctor of Philosophy in Engineering

Nor Hanifawati Binti Inai

April 2019

Declaration

INTERFACES IN MODIFIED CELLULOSE NANOCRYSTALS REINFORCED POLYETHYLENE COMPOSITES

Submitted by Nor Hanifawati Binti Inai to the University of Exeter
in fulfilment of the requirements of the degree of
Doctor in Philosophy in Engineering in April 2019

I certify that all of the material in this thesis which is not my own work has been identifies and that no material has previously been submitted and approved for the award of a degree by this or any other university.

Signature ……

Abstract

Composites, comprising high density polyethylene (HDPE) reinforced with cellulose nanocrystals (CNCs), with difference sources of CNCs (cotton and tunicate) and different types of compatibilisers, have been prepared by melt compounding. The weight fraction of CNCs was varied from 0.5 to 5 wt.%. CNCs are rod shaped nano-sized crystalline fractions of cellulose fibres, with high aspect ratios, that can be obtained via acid hydrolysis of cellulosic material. The Young's modulus of CNCs around 57-143 GPa depending on the origin of CNCs and this value is comparable to man-made glass fibres (~70 GPa), considering that CNCs has a lower density (1.3-1.6 g cm^{-3}) than glass fibres (2.5 g cm^{-3}). All these properties are highly favourable for using CNCs as a nanofiller/reinforcements in polymer matrix composite materials. Better understanding of cellulose nanocomposites motivate the study to look deeply on interaction between polymer matrix and filler (nanocellulose) hence lead to the advancement of nanocellulose values so that it could be used universally into various biomaterials. In this study, a comparison between two different sources of CNCs demonstrated that the origin of the starting raw cellulosic governs the resulting reinforcing effect *via* aspect ratio, surface charge and crystallinity index. Unfortunately, the tendency of CNCs to form agglomerates led to difficulties in achieving effective reinforcement especially when simply mixing into a matrix material in the solid state. As a result, it has become clear that new approaches to composite construction will be required if effective composite reinforcement using CNCs is to be achieved.

Enhanced mechanical properties of CNCs reinforced HDPE composites with the addition of low loadings of CNCs were reported, compared to neat HDPE samples. Tunicate CNCs reinforced HDPE composites led to higher strength and modulus than cotton CNCs reinforced HDPE composites at the same CNCs concentration. This is thought to be due to the enhanced reinforcing effect of tunicate, due to their much larger aspect ratio (60.7 ± 30.7) compared to cotton (16.3 ± 5.7). The use of maleic anhydride polyethylene and polyethylene oxide as a compatibiliser was found to increase the tensile strength and Young`s modulus of the CNCs reinforced HDPE

composites. The mechanical properties of these composites were found to mainly depend on the aspect ratio of CNCs and the interaction of the HDPE matrix and the reinforcement phase. Further studies are conducted to investigate the stress transfer mechanism in CNCs reinforced with HDPE composites using Raman spectroscopy. The peak position of a Raman band located initially at the ~1095 cm^{-1} position is reported to shift towards a lower wavenumber under the application of tensile deformation. These shifts correspond to the direct deformation of the molecular backbone of cellulose, which is dominated by a C-O stretching mode. Higher Raman band shift rates with respect to tensile strain of this band are observed for the nanocomposites produced using the MAPE and PEO as compatibilisers. This demonstrates that stress is transferred from the matrix to the fillers more effectively with the presence of the compatibiliser, supporting the enhancement of the mechanical properties of the composite. Nanocomposites made from tunicate CNCs shows higher gradient of shift compares to nanocomposites made from cotton CNCs due to higher aspect ratio of tunicate CNCs. Finally, the combination of Raman mapping with chemical images and image analysis has been used to study the morphology of the CNCs in the nanocomposites. The cross-sectional areas of nanocomposite samples were investigated using confocal Raman microscopy. Raman spectroscopy is shown to provide and collect an accurate `fingerprint` of the composition of the cross-sections of the nanocomposites. The conversion of these set of Raman spectra to chemical images provides high contrast and reliability for the image analysis. The image analysis approach allows a quantitative assessment of the degree of mixing and degree of aggregation of CNCs in the HDPE matrix. This analysis showed that CNCs were mixed to varying degrees in the HDPE matrix. These results provide a further step in understanding and inspecting the mechanism of CNCs enhanced polymer matrices.

Acknowledgements

During the work that has resulted in this thesis, many people have contributed and been involved in different ways. I am very grateful to all of you and would like to thank everybody for your time and support. There are some in particular that I would like to take the opportunity to express my gratitude to.

First of all, I would like to express my deep and sincere gratitude to my supervisor, Professor Stephen Eichhorn, for his continuous encouragement, supervision and support. My co-supervisor, Professor Oana Ghita deserves all considerable credit for always being around to help me and for sharing your knowledge. This thesis would not have been possible without their help and guidance. I am grateful for the knowledge and skills I have learned by discussing problems and ideas with them.

I would like to convey thanks to the Lab Manager in the X-AT; Tommy (Dr. Yat-Tarng Shyng) for providing training, and for being always open to discuss; technical and non-technical, have always been helpful and a great pleasure. I am most grateful to Dr. Ellen Green for support with Raman spectroscopy, Dr. Hong Chang for use in Imaging Suite and Dr. Christian Hacker for use of TEM. I would also like to thank to Prof. Christoph Weder, Dr. Jens Natterodt and Dr. Nicharat Apiradee from Adolphe Merkle Institute, University of Fribourg for hosting me while I was in Switzerland for tunicate nanocrystals preparation.

I owe my deep gratitude to the most professional mentor Dr. Anna Lewandowska for invaluable help and advice with Raman spectroscopy; Dr Nandula Wanasekara, Dr Daniel Hewson and Dr James Beard for their time and valuable discussions that enabled me to improve my thesis beyond what I could have achieved independently.

Thanks to my friends for being so helpful, and providing relief from my studies. Thanks to (in no particular order): Masitah, Victor, Fatimah, Moon, Mary, Caterina, Rachel, Sya, Fariha, Kak Sheryn, Kak Razimah and Jue to name but a few. My loving thanks to my parents and my siblings for their unconditional love and support. FINALLY, I am greatly indebted to my husband Mohammad Fadhli bin Hj. Jaberi for his love, encouragement and sacrifices throughout the study. May we all reunite in Jannah. Amin.

Dissemination

Journal Papers

- **N.H. Inai**, A.E. Lewandowska, O.R. Ghita, S.J. Eichhorn. Interfaces in polyethylene oxide modified cellulose nanocrystal - polyethylene matrix composites. *Composites Science and Technology,* 2018, 154,128-135.
- A.E. Lewandowska, **N.H. Inai**, O.R. Ghita, S.J. Eichhorn. Quantitative analysis of the distribution and mixing of cellulose nanocrystals in thermoplastic composites using Raman chemical imaging. *Royal Society of Chemistry*, 2018, 8, 35831- 35839.

International Conference and Training Schools

- 4th Annual Action Conference Optical Nanospectroscopy IV, March 2017, Lisbon, Portugal. Poster Presentation: Interfacial Assessment of Cellulose Nanocrystal Reinforced Thermoplastic Composites using Raman Spectroscopy.
- COST FP1205: Cellulosic Material Properties and Industrial Potential (Final meeting), March 2017, Stockholm, Sweden. Poster Presentation: Melt Extrusion of Cellulose Nanocrystals Reinforced Polymer.
- COST Training School FP1205: International Training School on Nanocellulose Characterization, Potsdam, Germany. January, 2017. Poster Presentation: Effect of Compatibilizer on the Mechanical Properties of Cellulose Nanocrystal Reinforced Thermoplastic Composites.

Table of Contents

List of Tables

List of Figures

CHAPTER 1

INTRODUCTION

This chapter gives the background for this research. The introduction, problem statement and objectives of this research are also provided.

1.1 Introduction

Interest in biobased nanofillers for the development of polymer-based nanocomposites has increased markedly in recent years because of their great potential for producing a variety of high-value products with low impact on the environment. The ability to generate products that promotes biodegradability such as biomedical and pharmaceutical application, smart coatings, electronic materials is clearly evident. Nanocomposites are defined as composites with reinforcements in the nanometer range (<100 nm) in at least one dimension (Siqueira *et al.*, 2010). The potentially superior mechanical properties of cellulose nanocrystals (CNCs) compared to micron-sized fibres, make them ideal candidates as reinforcing fillers for polymeric matrices (Kalia *et al.*, 2011). CNCs are needle-like cellulose nanocrystals of 10-20 nm width and in between several hundred nanometers to micrometers in length (Klemm *et al.*, 2011). They are produced from various plant sources (*e.g.*, wood, pulp, cotton, hemp, ramie, kenaf) and animal sources (*e.g.*, tunicate, silk, wool) (Jonoobi, Harun, Mathew, & Oksman, 2010; Khandelwal & Windle, 2013; Klemm *et al.*, 2011; Sapkota, Kumar, Weder, & Foster, 2015). CNCs can be isolated through an acid hydrolysis procedure (Bondeson, Mathew, &

Oksman, 2006; Dong, Revol, & Gray, 1998; Elazzouzi-Hafraoui *et al.*, 2008; Nicharat, Sapkota, Weder, & Johan Foster, 2015). During this process, the amorphous regions are removed producing high purity cellulose crystals. There are a wide variety of possible applications for cellulose nanocomposites, varying from the replacement of synthetic reinforcements with more environmentally friendly materials to creating completely new types of biomaterials. Currently, cellulose nanocomposites are being considered for use in packaging, medical, automotive, electronics, construction and water treatment applications (Müller *et al.*, 2017). For this reason, this work seeks to investigate the potential of using low and high aspect ratio CNCs to reinforce a polymer matrix.

Nanocomposites have been processed by evaporation (Bulota, Jääskeläinen, Paltakari, & Hughes, 2011; Espino-Pérez *et al.*, 2013; Morán, Vázquez, & Cyras, 2013), impregnation (Ifuku, Nogi, Abe, Handa, & Nakatsubo, 2007), extrusion (Alloin, D'Aprea, Dufresne, Kissi, & Bossard, 2011; Goffin *et al.*, 2011) and hot pressing (Suryanegara, Nakagaito, & Yano, 2009). Wet processing methods such as evaporation/casting have been widely applied in most studies for the fabrication of CNCs reinforced composites (Capadona *et al.*, 2008; Fortunati *et al.*, 2012). The main advantage of these approaches is the preservation of the dispersed state of nanoparticles in the liquid medium and later in the polymeric matrix. This approach to disperse nanoparticles in thermoplastic matrices is however, to the most part, both non-economic and non-scalable on an industrial level. Melt compounding techniques such as extrusion or injection moulding are the industrial approaches of choice, and could allow the manufacture of a large range of products due to the fact that they have potential to be produced rapidly, cheaply and in a range of different shapes. It

is noted that some success has been had in combining thermally stable CNCs in melt processing, even reporting comparable results with solution casting approaches (Nicharat *et al.*, 2015).

There are however several major challenges to overcome before CNCs can be effectively incorporated into a thermoplastic polymer matrix during melt processing. One challenge is related to the highly hydrophilic character of CNCs, which inhibits their mixing and dispersion with hydrophobic thermoplastic matrices. Introducing hydrophilic fibres into hydrophobic material such as a thermoplastic will cause non-uniform fibre dispersion in the matrix and inferior fibre matrix bonding, which consequently results in poor mechanical properties of the polymeric composite. If blended mechanically, these two components may result in poor mechanical properties owing to their incompatibility.

Hydrophobic thermoplastic polymers, such as polypropylene (PP), polyethylene (PE), polylactic acid (PLA), cellulose acetate butyrate (CAB) and polycaprolactone (PCL), have been used as matrices in cellulose nanocomposites using solvent exchange or chemical modification to ensure better dispersion of the hydrophilic nanocellulose in the hydrophobic matrix. The addition of compatibilisers such as maleic anhydride, polyoxyethylene and polyethylene glycol have been shown to improve the compatibility between these two phases (Azouz *et al.*, 2012; Kosaka *et al.*, 2007; Pereda *et al.*, 2014). These approaches led to the direct melt mixing of filler, matrix and compatibiliser being applied in production of CNCs reinforced polymeric matrices.

In term of the characterization of nanocellulose-thermoplastic, most researchers have focused on understanding their mechanical properties, crystallinity, and thermal properties, thereby inferring the nature of the interactions between the filler and the matrix (Azouz *et al.*, 2012; de Menezes, Siqueira, Curvelo, & Dufresne, 2009; Sapkota, Jorfi, Weder, & Foster, 2014; Xu *et al.*, 2013)The morphologies of nanocellulose-thermoplastic composites have also been evaluated using scanning electron microscopy (SEM) (Alloin *et al.*, 2011; Espino-Pérez *et al.*, 2013; Nagalakshmaiah, Pignon, El Kissi, & Dufresne, 2016) and atomic force microscopy (AFM) (Ingvild Kvien, Tanem, & Oksman, 2005; Sapkota *et al.*, 2014). SEM permits the analysis of a large area. Limitation of the size of the fillers that can be resolved (submicron scale) and the resolution between components in composites make it often difficult to quantify the degree of mixing and aggregation of fillers using this technique. AFM has been found to be useful for morphological studies of cellulose-thermoplastic composites at spatial resolutions on the nanometer scale. Although AFM images can give nanoscale resolution, the evaluated area of the materials is limited to a few microns. Neither of these approaches enables a chemically sensitive quantitative estimation of the degree of mixing and aggregation between cellulose, compatibiliser and a thermoplastic matrix. So far, confocal Raman microscopy has been found to be useful to quantify the dispersion index of thermoplastic nanocomposites.

Raman spectroscopy has also been proven to be a powerful, sophisticated and non-destructive tool to monitor the deformation of nanocrystals in composites. However, very limited studies have been reported on quantifying the interfacial micromechanics of melt compounded thermoplastic-cellulose nanocrystals

composites. Most studies have reported thermoset or solution cast matrix systems (Pullawan *et al.*, 2014; Rusli *et al.*, 2011; Šturcová *et al.*, 2005). Therefore, it is necessary to analyse the interfacial properties of melt compounded thermoplastic-cellulose nanocrystals composites.

The main purpose of this project was to produce nanocellulose reinforced thermoplastic composites and investigate their mechanical and interfacial performance. The present work also reports on an attempt to investigate the feasibility of using Raman spectroscopy to determine the stress-transfer mechanism in a melt compounded thermoplastic cellulose nanocrystals composite. Another challenge was to evaluate the potential of Raman spectroscopy to quantify the degree of mixing and aggregation of CNCs in melt compounded HDPE. The combination of Raman spectroscopy with confocal microscopy generates chemical images and these images allow a direct visualisation of the mixing and aggregation of CNCs in the polymer matrix.

All basic materials used in this study will be characterized. Two types of CNCs that is produced from plants and marine animals based cellulose have been examined using transmission electron microscopy and x-ray diffraction, in order to observe their dimensions and crystal structure. Thermal stability of modified and unmodified CNCs have also been determined using thermogravimetric analysis. Raman spectra of CNCs and HDPE have been recorded and all band positions characterised. Tensile testing of both types of nanocomposites has also been carried out to determine their modulus, breaking strain and strength. Monitoring and analysis of crystallisation has also been carried out for various CNCs reinforced HDPE

composite formulations. Micromechanical tests were then carried out to compare the unmodified and modified CNCs reinforced HDPE composites and the Raman band shift rates with respect to fibre strain were determined. Finally, Raman imaging has been used to study the mixing and aggregation of CNCs in a polyethylene matrix composite.

1.2 Problem Statement

1. What are the characteristics of CNCs in order for them to be good reinforcements in a polymer matrix?
2. What effect do CNCs have on the crystal structure, mechanical and thermal properties of unmodified and modified CNCs reinforced HDPE composites?
3. How does the amount of CNCs present in the nanocomposites influence the properties of CNCs reinforced HDPE composites?
4. Does the addition of the compatibiliser influence the performance of the CNCs reinforced HDPE composites?
5. Is a Raman spectroscopic technique able to monitor the stress transfer process within melt compounded CNCs reinforced HDPE composites as a function of tensile deformation?
6. Is confocal Raman spectroscopy able to study the morphology and to quantify the degree of mixing and aggregation of CNCs in melt compounded polyethylene?

1.3 Objectives of the Study

1. To produce CNCs with different types of cellulose source by an acid hydrolysis process.
2. To produce nanocomposites using two different types of CNCs; cotton nanocrystals (cCNCs) and tunicate nanocrystals (tCNCs) and two different type of compatibiliser; maleic anhydride polyethylene (MAPE) and poly(ethylene oxide))(PEO).
3. To study the influence of aspect ratio of the reinforcing CNCs on properties of CNCs reinforced polyethylene composites.
4. To investigate the influence of different types of CNCs as well as compatibilisers on crystallisation, mechanical and thermal properties of nanocomposites.
5. To determine the effect of different loadings of CNCs on the crystallisation, mechanical and thermal properties of nanocomposites.
6. To study the micromechanical properties of nanocomposites samples upon the application of external tensile deformation using Raman spectroscopy.
7. To evaluate and quantify the degree of mixing and aggregation between components (CNCs, compatibilisers and HDPE) using Raman spectroscopy.

1.4 Structure of Thesis

This chapter has provided an introduction to the thesis including problem statements, objectives and the structure of the thesis. The subsequent chapters are as follows:

- ✓ Chapter 2 reviews the literature on cellulose, CNCs, nanocomposites and the use of Raman spectroscopy to study the stress transfer process in cellulose materials and cellulose reinforced composite materials. The application of confocal Raman spectroscopy to provides imaging with chemical `fingerprint` in nanocomposites is also discussed.
- ✓ Chapter 3 describes the experimental methodology used in this study including the preparation of CNCs and nanocomposites and technique used to characterise the properties of the nanocomposites.
- ✓ Chapter 4 describes the aspect ratio, crystallinity index, surface charge and Raman spectroscopy of the CNCs derived from cotton and tunicates. The physical and thermal properties of modified CNCs are also reported.
- ✓ Chapter 5 reports the study on the influences of different sources and loadings of CNCs and the effect of the addition of compatibilisers on the crystallinity, mechanical and thermal properties of the nanocomposites.
- ✓ Chapter 6 details the micromechanical properties characterisation of the nanocomposites using Raman spectroscopy.
- ✓ Chapter 7 is an evaluation of spatial distribution of CNCs in HDPE using confocal Raman spectroscopy.
- ✓ Chapter 8 gives concluding remarks and future perspectives.

CHAPTER 2

LITERATURE REVIEW

2.1 Cellulose

Cellulose is a renewable, biodegradable and the most abundant organic biopolymer, existing and produced by a wide range of living species such as plants, some animals, bacteria and some amoebas (Kalia *et al.*, 2011; Siqueira *et al.*, 2010). It is the primary structural component of the cell wall of higher plants and it can be obtained from various sources like wood, some bacteria, fungi and some algae. According to Reddy & Yang (2005), there are three main constituents of any natural fibres which are cellulose, hemicellulose and lignin. Different proportion of these components occur in a fibre depending on the age, source and the extraction conditions used to obtain the materials. Hemicelluloses and lignin act like a matrix whereas, cellulose acts like reinforcement to the matrix. This is one of the fundamental reasons why cellulose was chosen to be the reinforcing agent in the composites.

Cotton has the highest content of cellulose (80~95%) amongst plant fibres (Keshk & Omar, 2014; Khalil, Bhat, & Ireana Yusra, 2012; Siqueira *et al.*, 2010). The relative amount of the various compounds found in plant fibres cannot be equal from plant to plant. The different parts of the same plant also have different chemical compositions (Lee & Rowell, 1991). Different species of plant fibres have differences in their chemical composition, their ratio between cellulose, hemicellulose and lignin

and the orientation of the cellulose microfibrils within the cell wall (Brett & Waldron, 1996). The chemical composition and microfibril angle of several plant fibres are found to significantly vary, as shown in Table 2.1.

Table 2.1 Chemical composition and microfibrillar spiral angle of some plant fibres (Ashori, Harun, Raverty, & Yusoff, 2006; Bledzki & Gassan, 1999; Gassan, Chate, & Bledzki, 2001; Mwaikambo & Ansell, 2002; Smeder & Liljedahl, 1996)

Fibre	Latin name	Cellulose (wt.%)	Hemi cellulose (wt.%)	Lignin (wt.%)	Pectin (wt.%)	Micro-fibril angle(°)
Kenaf (Bast)	*Hibiscus cannabinus*	56.4	26.2	14.7	-	
Kenaf (Core)	*Hibiscus cannabinus*	46.1	29.7	22.1	-	
Ramie	*Boehmeria nivea*	68.6-76	13.1-15.0	0.6-1	1.9-2	
Hemp	*Cannabis sativa* L.	70-78	17.9-22	3.7-5	0.9	2-6.2
Flax	*Linum usitatissimum*	60-81	14-18.6	2-3	1.8-2.3	5-10
Jute	*Corchorus capsularis, Corchorus olitorius*	51-72	12-20.4	5-13	0.2	8
Cotton	*Gossypium hirsutum*	82.7-92	2-5.7	0.5-1	5.7	
Banana	*Musa acuminata L.*	60-65	6-19	5-10	3-5	
Coir	*Cocos nucifera L.*	43	0.3	45	4.0	
Henequen	*Agava fourcroydes Lemaire*	60-78	4-28	8-13	3-4	
Bagasse	*Sacchararum officinarum L.*	40	30	20	10	
Pineapple Leaf	*Acanas comosus*	80-81	16-19	12	2-2.5	14
Abaca	*Musa textilis*	60.8-64	21	12	0.8	

Sisal	*Agave sisalana Perrine*	43-88	10-13	4-12	0.8-2	10-22
Wood	-	45-50	23	27	-	

Mechanical properties of plant fibres are largely determined by the percentage of cellulose content, the degree of polymerization and the microfibril angle. A high cellulose content and low microfibril angle are desirable properties of a fibre to be used as a reinforcement in polymer composites. Figure 2.1 and Figure 2.2 indicates the increase of fibre strength and modulus related to the high percentage of cellulose and low microfibril angle respectively (Gherardi Hein & Tarcísio Lima, 2012; Lee & Rowell, 1991).

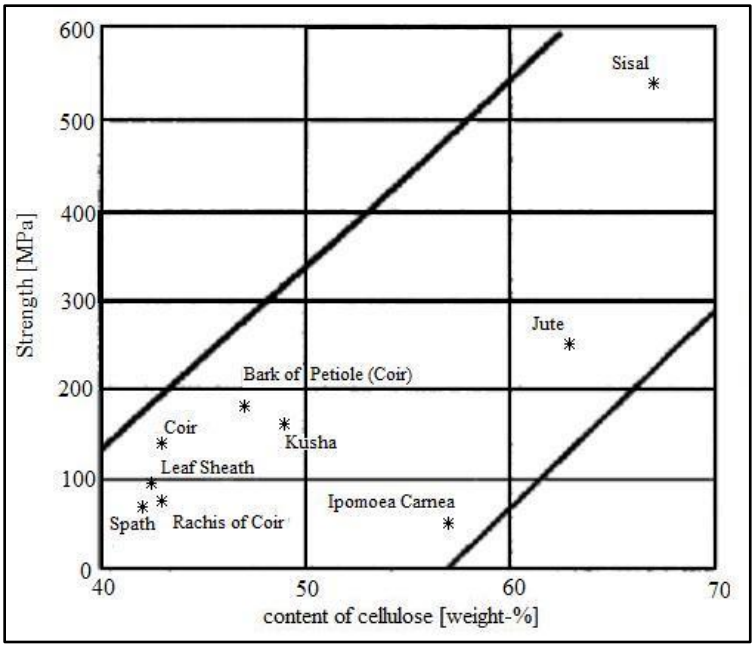

Figure 2.1 The relationship between fibre strength and cellulose content of various plant fibres (Lee & Rowell, 1991).

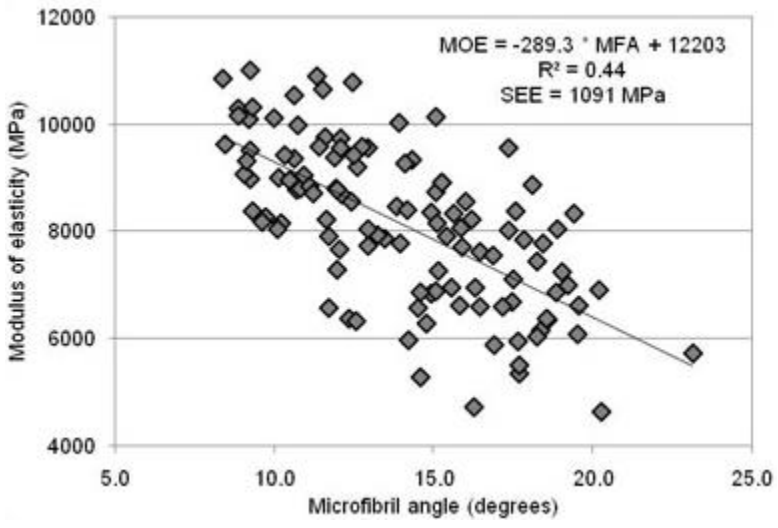

Figure 2.2 The relationship between elastic modulus of wood and microfibril angle (Gherardi Hein & Tarcísio Lima, 2012).

2.1.1 Properties and Chemical Structure of Celllulose

Cellulose is hydrophilic (having a strong affinity for water), has no taste and it is odourless. Due to its hydrogen-bonded supramolecular structures, cellulose is insoluble in water and most common organic liquids (Swatloski, Spear, Holbrey, & Rogers, 2002). Celluloses are built through the effect of hydrogen bonds. Cellulose molecules or chains interact with each other by hydrogen bonding and form microfibrils. While at the same time, the arrangement of microfibrils creates a single plant fibre. Cellulose fibres usually contain over 500,000 cellulose molecules and have thereby developed 2.5 billion hydrogen bonds. Even if the hydrogen bond is about 1/10 the strength of a covalent bond, the cumulative bonding energy provides the high tensile strength of cellulose (Puglia & Kenny, 2004). Figure 2.3 shows hydrogen bonds holding together cellulose chains to form a single microfibril.

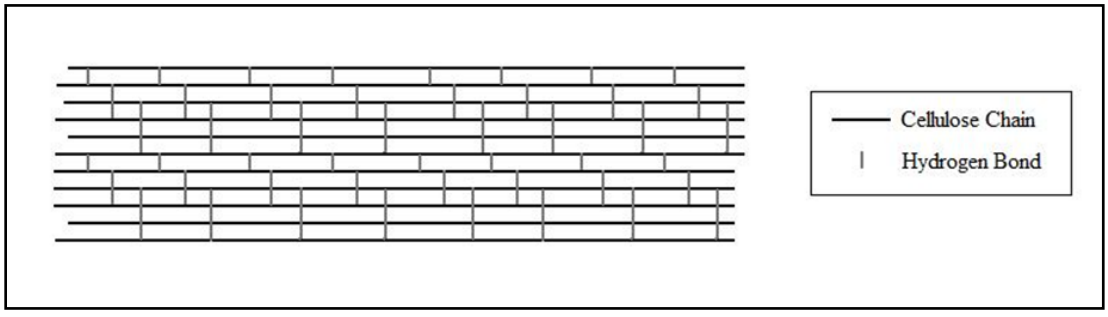

Figure 2.3 Concept of hydrogen bond joining together the cellulose chains.

According to Reddy & Yang, (2005), the word fibre refers to a bundle of individual cells with adequate strength, length, and fineness. Each individual cell or elementary fibre, normally has a length from 1 to 50 mm and a diameter of around 10 – 50 µm. Within the elementary fibre there are microfibrils which have a diameter of around 10-30 nm and are made up from a collection of 30-100 cellulose chain molecules (Thomas, Paul, Pothan, & Deepa, 2011). Figure 2.4 shows a flax bast fibre anatomy dissected into the smallest unit; the cellulose chain.

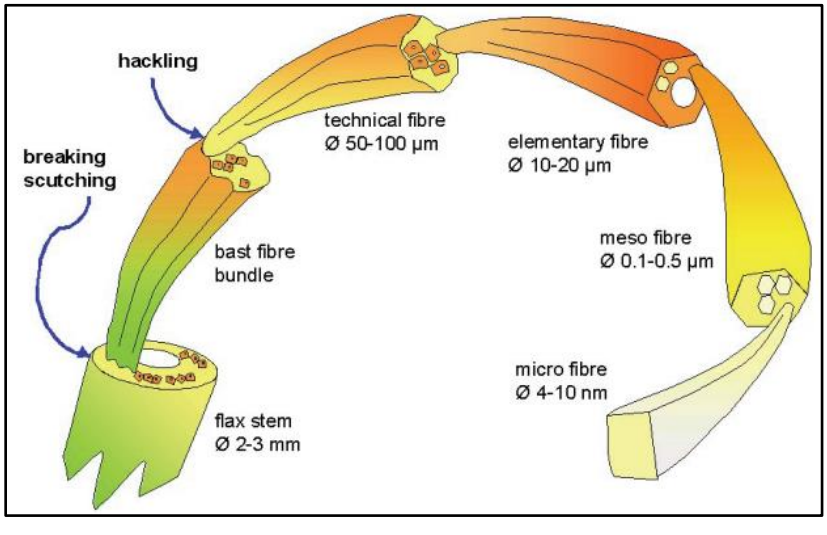

Figure 2.4 Cellulose is the main building blocks of plant fibre (Christer Wretfors, 2006).

Solid cellulose forms a microcrystalline structure with regions of high order, called crystalline regions and regions of low order, named amorphous regions. Amorphous

regions connect the crystalline parts as shown in Figure 2.5. The proportion of these two phases depends on the origin of the cellulose and defines the degree of crystallinity of the structure. The crystalline regions are stronger and makes it highly resistant to strong alkali and oxidising agents. The amorphous regions have lower density compared to crystalline regions due to random arrangement of cellulose chains (Kaplan, 1998). Hence, the presence of these amorphous regions makes the structure susceptible to acid hydrolysis and breakdown into individual crystallities.

.

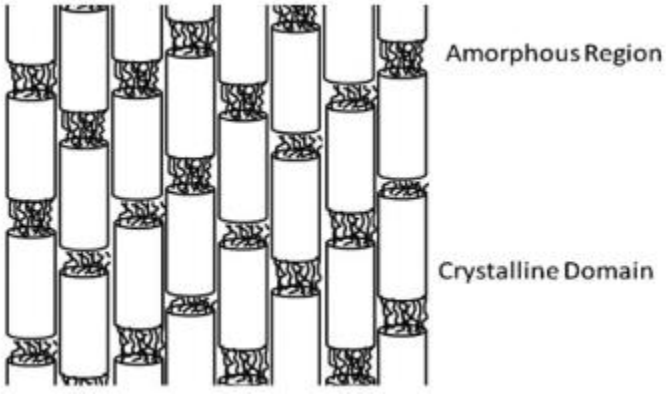

Figure 2.5 Schematic presentation of microcrystalline structure (Mariano, El Kissi, & Dufresne, 2014)

Cellulose is a natural polymer with the repeating formula of $(C_6H_{10}O_5)_n$. The chemical structure of cellulose is shown in Figure 2.6. It is a linear homopolymer of β–D-glucopyranose units which are connected by β-1,4-glycosidic linkage (Klemm, Philipp, & Mischnick, 1998). Cellulose has a linear chain conformation and is formed by the elimination of water between two hydroxyl groups, resulting in the formation of a glycosidic bond or oxygen bridge (Klemm et al., 1998). As shown in Figure 2.6, cellulose has a hydroxyl group rich structure which allows it to be chemically modified by various reactions such as acetylation, esterification and etherification. The number of repeating units per molecule is known as the degree of polymerisation

(DP). DP affect the properties of cellulose. DP varies between 300–1,700 for wood fibers and 800–10,000 for cotton and other plants, depending on origin and treatment of the cellulose raw material (Klemm, Heublein, Fink, & Bohn, 2005). The valuable and interesting properties of cellulose can be obtained from high DP or MW (molecular weight) materials (Dumitriu, 1996). Table 2.2 reports the DP of various sources of cellulose.

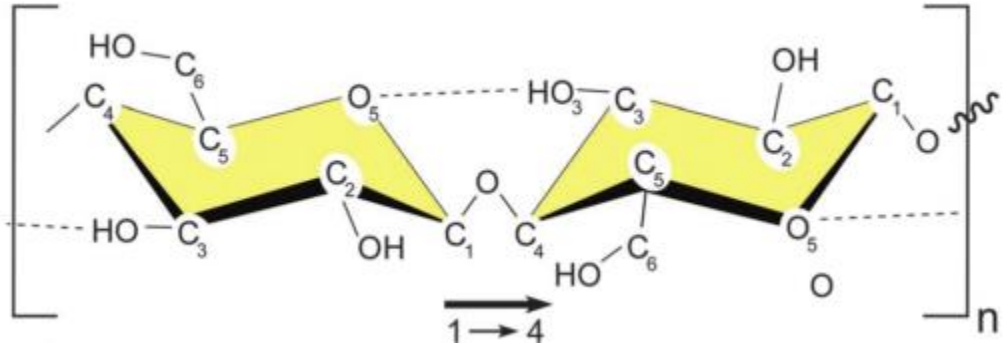

Figure 2.6 Polymeric chain structure of cellulose showing the β -1,4 – glycosidic linkage and intrachain hydrogen bonding (dotted line) (Moon, Martini, Nairn, Simonsen, & Youngblood, 2011)

Table 2.2 Degree of polymerisation of celluloses from various sources (Dumitriu, 1996).

Cellulose	Degree of polymerisation
Flax fibres	7,000-8,000
Cotton fibres	8,000-14,000
Wood fibres	8,000-9,000
Pulp cellulose (bleached)	500-2,100
Cotton linters	1,000-6,500
Valonia	25,000-27,000
Ramie fibres	9,000-11,000

Table 2.3 shows the comparison of selected mechanical and physical properties between natural fibres and synthetic fibres. Mechanical properties of natural fibres are much lower than those of conventional synthetic fibres such as glass or carbon fibres. However, hemp, flax and jute fibres have higher tensile moduli than E-glass fibres on a “per weight” basis due to the low density of natural fibres (~1.4 g cm^{-3}) compared to E-glass (~2.5 g cm^{-3}) (Fortea-Verdejo, Bumbaris, Burgstaller, Bismarck, & Lee, 2017).

Table 2.3 A comparison between the physical properties of selected natural fibres and synthetic fibres (Faruk, Bledzki, Fink, & Sain, 2012; Fortea-Verdejo et al., 2017)

Fibre	Density (g cm^{-3})	Young`s Modulus (GPa)	Tensile Strength (MPa)
Hemp	1.47	70	690
Flax	1.5	27.6	345-1500
Jute	1.3-1.49	13-26.5	393-800
Sisal	1.45	9.4-22	468-700
Ramie	1.55	61.4-128	400-938
E-glass	2.55	73	3400
Kevlar	1.44	60	3000

2.1.2 Utilization of Cellulose: Opportunities and Limitations

Natural fibres present many advantages compared to synthetic fibres which make them attractive as reinforcements in composite materials. Cellulose fibers present many advantages compared to synthetic fibers which make them attractive as reinforcements in composite materials. They come from an abundant and renewable resources (Habibi, Lucia, & Rojas, 2010; Islam, Alam, & Zoccola, 2013) at low cost

(Habibi *et al.*, 2010; Kalia *et al.*, 2011). Unlike brittle fibers, such as glass and carbon fibers, cellulose fibers are flexible and will not fracture when processed over sharp curvatures. This enables the fibers to maintain the desired aspect ratio for good performance. Their non-abrasive nature permits a high-volume fraction of filling during processing, and this results in high mechanical properties without the usual machine wear problems associated with synthetic fibers *e.g.* glass and ceramic. Cellulose fibres are non-toxic, easy to handle and present no health problems like glass fibers that can cause skin irritations and respiratory diseases when the fibrous dust is inhaled. They offer a high ability for surface modification (Kalia *et al.*, 2011; Lin & Dufresne, 2014), are economical, require low amounts of energy for processing, and are biodegradable. In terms of socio-economic issues, the use of cellulose fibers as source of raw materials is beneficial because it generates an economic development opportunity for non-food farm products in rural areas. These mentioned advantages are benefits and are not likely to be ignored by the plastics industry for use in the automotive, building, appliance, and packaging products (Islam *et al.*, 2013).

Although celluloses and their composites are potentially environmentally friendly and renewable, they have several bottlenecks to their use. This leads to unsatisfactory final of properties of the composites and limitated use as reinforcing agents in biocomposites. The primary drawback of using cellulose fibres is their limited thermal stability with noticeable degradation occurring as the melt processing temperature approaches 200 – 220 ºC (Manikandan Nair, Thomas, & Groeninckx, 2001; Siqueira *et al.*, 2010). This limits the type of thermoplastic that can be used with cellulose

fibres to low melting temperature thermoplastics such as polyethylene, polypropylene, polyvinyl chloride and polylactic acid.

Another drawback of using celluloses as reinforcing material is their limited compatibility with many thermoplastic matrices (Ashori, Babaee, Jonoobi, & Hamzeh, 2014; Eyley & Thielemans, 2014; Missoum, Belgacem, & Bras, 2013) due to their highly hydrophilic character (Dufresne & Belgacem, 2013). Generally, natural fibres are rich in cellulose and therefore contains large amount of hydroxyl groups which make it polar and hydrophilic in nature while most plastics are hydrophobic. Cellulose are not compatible, i.e., do not wet, with many thermoplastic matrices and this is also due to differences in polarity (Bahar *et al.*, 2012). Introducing hydrophilic fibres into hydrophobic materials such as thermoplastics will cause non-uniform fibre dispersion in the matrix and inferior fibre matrix bonding which consequently results in poor mechanical properties of the composite. This leads to the presence of voids or porosity and weak fibre-matrix interfaces which leads to poor overall mechanical properties (Akil *et al.*, 2011).

Cellulose fibre that produced from natural fibres are also suffer from high moisture absorption due to hydrogen bonding of water molecules to the hydroxyl groups within the cell wall. This leads to a moisture build-up in the fibre cell wall (fibre swelling) and also within the fibre-matrix interface. This is responsible for changes in the dimensions of cellulose-based composites, particularly in thickness and the linear expansion due to reversible and irreversible swelling of the composites. As a consequence, fibre-matrix adhesion is weak and the dimensional stability of cellulose-based composites particularly for outdoor applications will be greatly affected.

One of the major limitations of cellulose is their high biodegradability when exposed to the environment. This limits the service life of biocomposites particularly in outdoor applications. Natural fibres do not have the same consistency in quality as compared to synthetic fibres. Natural fibres also have non-uniformity and variation of dimensions, even between individual plants within the same cultivation. This inconsistency is due to a variety of reasons such as climate, crop variety, retting process, and processing equipment used for fibres (Kalia *et al.*, 2011; Thomsen *et al.*, 2006). The properties of natural fibres also varies greatly depending on the processing method used to break down to the fibre level. Natural fibres are also susceptible to rotting and possess low resistance to microbial attack. These limitations generate problems of stocking raw material for extended periods. There are many reports on the potential use and limitation of cellulose fibers as reinforcement in thermoplastics available in the literature (Mariano *et al.*, 2014; Moon *et al*., 2011; Siqueira *et al*., 2010). These studies show that the problems mentioned above are common, independent of the type and origin of the fiber employed.

2.1.3 Cellulose Nanocrystals

The study of cellulose nanofibres as a reinforcing phase in nanocomposites started two decades ago (Eichhorn, 2011; Khalil *et al.*, 2012). Since then a huge amount of literature has been devoted to cellulose nanofibres, and it is becoming an increasingly topical subject. Different descriptors of these nanofibres are often referred to in the literature. These include “nanowhiskers” (or just simply “whiskers”), “nanocrystals” or even “monocrystals”. These crystallites have also often been

referred to in literature as “microfibrils”, “microcrystals” or “microcrystallites”, despite their nanoscale dimensions. Based on the appearance and preparation methods, cellulose nanofibres can be classified into two main subcategories, namely cellulose nanocrystals (CNCs) and cellulose nanofibrils (CNFs). CNCs are short and needle-shaped, with diameters on the nanoscale and lengths generally in the range 100–500 nm. On the other hand, CNFs are flexible long nanofibers with diameters on the nanoscale and lengths on the micron scale. Technical Association of the Pulp and Paper Industry (TAPPI) proposed standard terms and their definition for cellulose nanomaterial (TAPPI WI3021), based on the nanocellulose size (Agarwal, 2017). The nomenclature, abbreviation and dimensions applicable to each subgroup are shown in Figure 2.7 and Table 2.3.

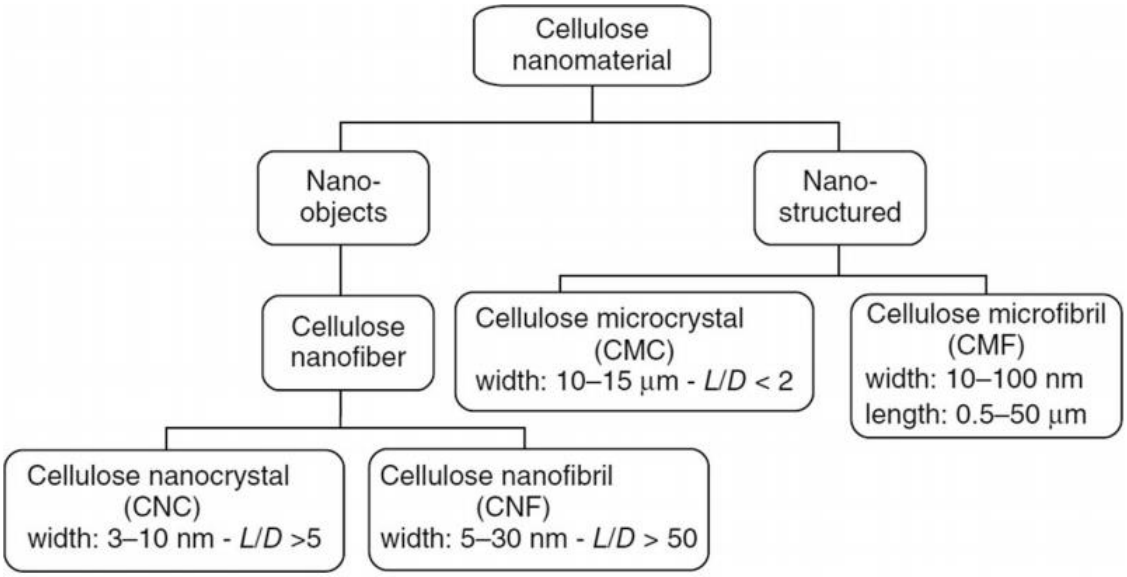

Figure 2.7 Standard terms for cellulose nanomaterials (TAPPI WI3021).

Table 2.4 Cellulosic nanomaterial dimensions (TAPPI WI3021).

Terminology of cellulose nanomaterials	Width (nm)	Length (nm)	Aspect ratio (length/width)
Cellulose nanofibril (CNF) Nanofibrillar cellulose (NFC)	2-10	>10,000	>1000
Cellulose nanocrystals (CNCs) Nanocrystalline cellulose (NCC) Cellulose nanowhiskers	2-20	100-600	10-100
Cellulose microcrystals (CMCs) Microcrystalline cellulose (MCC)	>1000	>1000	~1
Cellulose microfibril (CMF) Micrifibrillar cellulose (MFC)	10-100	500-10,000	50-100
Bacterial cellulose	10-40	>1000	100-150

2.1.4 Isolation of Cellulose Nanocrystals

In order for cellulose to be used as nano-reinforcement, the crystalline regions must be separated from the amorphous areas. The most common method for separation of cellulose crystals from amorphous region is acid hydrolysis. This includes a chemical treatment for the separation of nanocrystals and the use of mechanical energy to disperse them in an aqueous suspension. Under suitable conditions, acid hydrolysis breaks down the structure of cellulose into individual needle like crystalline rods by disrupting the amorphous regions (Moon *et al.*, 2011). This separation happens due to the faster hydrolysis kinematics of amorphous regions than the crystalline parts. The reaction continues until all the amorphous regions are hydrolyzed to glucose, and then slows down significantly as the remaining acid attacks the surface of the residual crystalline regions as well as the reducing end groups of cellulose.

CNCs have been produced from a variety of sources using acid hydrolysis such as tunicate (Elazzouzi-Hafraoui *et al.*, 2008; Favier, Chanzy, & Cavaille, 1995), cotton (Dong *et al.*, 1998; Pereda *et al.*, 2014), bamboo (Zhang *et al.*, 2014) and microcrystalline cellulose (Espino-Pérez *et al.*, 2013). The overall efficiency of the hydrolysis process is affected by several factors such as acid type, hydrolysis parameters (temperature and time) and acid concentration. For example, Fan & Li (2012) observed that too high (above 64%) sulfuric acid concentration of hydrolysis of cotton pulp would degrade the cellulose completely to yield sugar molecules and too low (below 60%) sulfuric acid concentration would yield only large poorly dispersed fibers and aggregates. Similarly, Beck *et al.,* (2005) demonstrated that

high acid concentrations (>65 wt %) were found to produce CNCs with a sulfate half ester content upwards of 391 mmol/kg CNCs but at a significantly reduced yield (<20%). Dong *et al.* (1998) observed that higher temperatures and longer reaction times of hydrolysis of microcrystalline cellulose produced shorter CNCs with low aspect ratios. This is in excellent agreement with Beck *et al.,* (2005), who obtained similar results upon extracting CNCs from softwood pulps. Beck *et al.,* (2005) demonstrated that shorter and less polydisperse CNCs were produced using longer hydrolysis times and increased acid- to-pulp ratios. Recently, Elazzouzi-Hafraoui *et al.,* (2007) studied the size distribution of CNs resulting from sulfuric acid hydrolysis of cotton treated with 65% sulfuric acid over 30 min at different temperatures, ranging from 45 to 72 °C. By increasing the temperature, they demonstrated that shorter crystals were obtained; however, no clear influence on the width of the crystal was revealed. Bondeson *et al.,* (2006) investigated the optimisation of the production of CNCs from microcrystalline cellulose derived from Norway spruce. The processing parameters, which varied during hydrolysis, were acid and microcrystalline cellulose concentrations, hydrolysis time and temperature. They reported that CNCs with length of 200-400 nm and width of less than 10 nm were produced using a sulphuric acid concentration of 63.5% (w/w) in 2 h with a yield of 30% (of initial weight).

The most common use for acid hydrolysis is sulfuric, followed by hydrochloric and phosphoric acid. Sulfuric acid (H_2SO_4) introduces the sulfate ester groups to the surface of CNCs, which promote dispersion of nanocrystals in aqueous solvents, resulting in highly stable suspensions (Beck-Candanedo, Roman, & Gray, 2005). However, the sulfate ester groups, introduced during sulfuric acid hydrolysis, have

been found to catalyse the degradation of cellulose, especially at higher temperatures (Roman & Winter, 2004). Espinosa *et al.*, (2013) reported the effect of different types of acid on nanocrystals for hydrolysed cotton cellulose. The other processing parameters were kept constant. Surprisingly it was found that CNCs hydrolysed by phosphoric acid exhibit much higher mechanical properties and thermal stability than commonly used sulfuric acid. Suflet, Chitanu, & Popa, (2006) phosphorylated microcrystalline cellulose and obtained monobasic cellulose phosphate with a degree of substitution of ≈ 1. The thermogravimetric analysis evidenced the stability of samples up to 200 °C allowing the application of monobasic cellulose phosphate in processes being used at higher temperatures.

2.1.5 Morphological Analysis of Cellulose Nanocrystals

The morphological characteristics of CNCs are usually carried out using several techniques such as transmission electron microscopy (TEM), field emission scanning electron microscopy (FESEM), atomic force microscopy (AFM), small angle neutron scattering (SANS) and polarised and depolarised dynamic light scattering (DLS, DDLS). The physical dimensions of CNCs are dependent on the preparation conditions during the isolation process, like hydrolysis time, hydrolysis reagent and temperature. Meanwhile, properties such as their aspect ratio, diameter, and tendency to aggregate are important parameters for CNCs. Hence, it is important to determine the physical properties of CNCs before they are dispersed in a polymer matrix.

Among all the techniques, TEM and AFM are most capable of providing detailed information on the dimensions and distribution of CNCs. TEM has been used to observe the features of individual CNCs due to its superior resolution. The principle of TEM is that when a high energy beam of electrons is shone through a very thin sample, the interactions between the electrons and the atoms can be used to observe features such as the crystal structure and features in the structure. Cellulose-based materials produce weakly scattered electrons due to the low atomic number element composition of the material, resulting in poor contrast in the images (Kvien and Niska, 2009). Usually, metal shadowing or negative staining using uranyl acetate is needed to improve the contrast and enhance the density. Figure 2.8 shows the TEM images of CNCs from different cellulose sources: (a) tunicin, (b) ramie, (c) cotton, (d) sugar beet, (e) MCC, and (f) bacterial cellulose (Siqueira *et al.*, 2010).

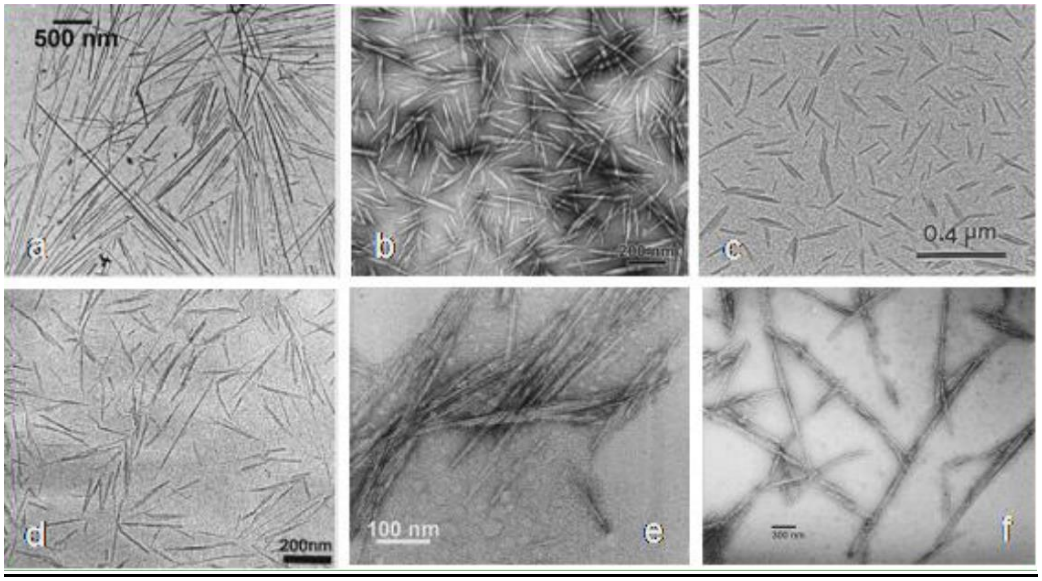

Figure 2.8 TEM images of diluted nanocrystal suspensions hydrolysed from various cellulose sources (Siqueira et al., 2010).

On the other hand, AFM is another widely used method to examine CNCs and bulk structures of nanocomposites (Hanley, Giasson, Revol, & Gray, 1992; Iwamoto, Kai, Isogai, & Iwata, 2009; Kvien *et al.*, 2005). AFM works by using a sharp tip to probe the surface feature by raster scanning. There are several studies on dimension of nanocelluloses which yielded different results when analysed by AFM and by TEM (Elazzouzi-Hafraoui *et al.*, 2008; Sacui *et al.*, 2014; Zia, Androsch, Radusch, & Ingoliç, 2008)Kvien et al., 2005). In general, objects appear larger in AFM compared to TEM analysis (Zia *et al.*, 2008) and different shapes are also observed (Hanley *et al.*, 1992). The major reasons for this may be the geometry of the tip in AFM, which is used for mechanical interaction with the specimen.

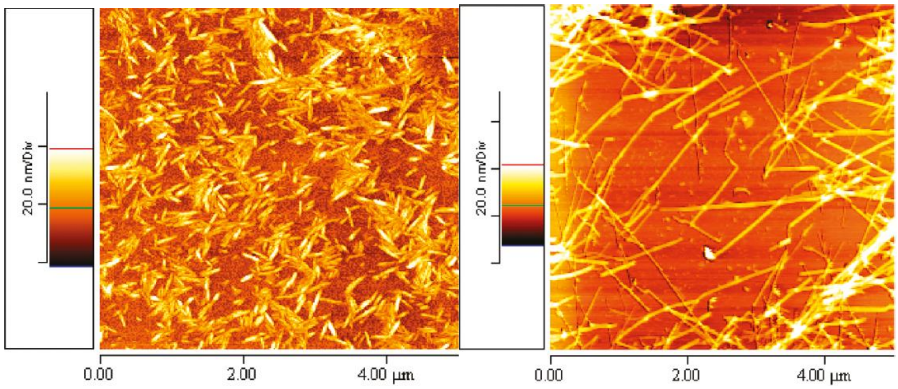

Figure 2.9 AFM image of cotton and tunicates CNCs (Rusli et al., 2011)

Table 2.4 summarizes the dimensions of CNCs found from different types of cellulose. The diameter of CNCs can be seen to depend on the nature of the cellulose source. The width is typically a few nanometres, while the length of CNCs ranges from tens of nanometres to a few micrometres. It is observed from Table 2.3 that the aspect ratio, which is defined as length-to-diameter ratio, also varies between different cellulose sources. For instance, the aspect ratio of cotton CNCs is 10 and about 67 for tunicate CNCs.

Table 2.5 Geometrical characteristic of CNCs from various sources: length, diameter and aspect ratio (reproduced from Kalia et al., 2011).

Source	Length, L (nm)	Diameter, D (nm)	L/D
Acacia pulp	100-250	5-15	--
Bacterial	100-several 1000	5-10 x 3-50	-
Banana rachis	500-1000	5	-
Capim duorado	300	4.5	67
Cassava bagasse	360-1700	2-11	-
Cladaphora	-	20 x 20	-
Coconut husk fibres	80-500	6	39
Cotton	100-300	5-15	10
Cotton seed linter	170-490	40-60	13-17
Date palm tree (rachis/leaflets)	260/180	6.1	43/30
Flax	100-500	10-30	15
Hemp	several 1000	30-100	-
MCC	150-300	3-7	-
Mulberry	400-500	20-40	-
Ramie	150-250	6-8	-
Sisal	215	5	42
Sugarcane bagasse	200-310	2-6	64
Tunicin	100-several 1000	10-20	67
Wheatstraw	150-300	5	45
Wood	100-300	3-5	50

2.2 Composites Materials

A composite material can be defined as a combination of two or more materials that results in better properties than those of the individual components used alone (Hull & Clyne, 1996). Generally, one or more discontinuous phases (stiffer and stronger) embedded within the continuous phase (comparatively softer) are used to form composites. The discontinuous phase is usually termed ‘reinforcing agents’, while the continuous phase is called the matrix. The matrix resin binds the reinforcement

materials by maintaining their shape and relative positions. The reinforcements, usually in fibre form, provide their special mechanical and physical properties to enhance the matrix properties. In a composite material, both matrix and reinforcement maintain their individual, physical and chemical properties; nevertheless together they produce a combination of qualities which the individual components alone could not have achieved (Taj, Khan, & Munawar, 2007). Composite materials can also be described as a material that integrates fibres which provides strength surrounded by a weaker matrix material which serves to transmit the load to fibres and their distribution (Gay & Tsai, 2002).

Based on the type of matrix, composite materials can be categorized into major classes which can be polymer matrix composites (PMCs), metal matrix composites (MMCs), ceramic matrix composites (CMCs), carbon-carbon composites (CCCs) and intermetallic composites (IMCs) (Al-Warid & Al-Maamori, 2016; Toozandehjani *et al*., 2019). Due to the superior mechanical properties of composite materials, there are a large number of commercial products or parts of products available on the market, for instance aircraft, automobiles, boats and furniture (Hull & Clyne, 1996). Among those types of composites, PMCs are well known for their widespread applications. They can be fabricated into complex, large shapes and have been accepted in a variety of commercial and aerospace applications (Schwartz, 1997).

2.2.1 Cellulose Reinforced Composites

Cellulose-based composites have been widely used for many decades. In 1941, a cotton polymer composite was first used by the military for radar domes on aircraft

(Piggott, 1980). Cellulose-based composites present many advantages compared to synthetic fibers, such as low density, high specific strength and modulus, cheaper cost, availability, and biodegradability (Wambua, Ivens, & Verpoest, 2003). The most common natural plants used in applications are bast fibers, such as hemp, jute, flax, kenaf, and sisal. Cellulose fibers have several major drawbacks as discussed in the previous section. Natural reinforcements such as cellulose and starch have a strong tendency for self-association because of their strongly interacting surface hydroxyl groups (De Souza Lima & Borsali, 2004). Some researchers (Bledzki & Gassan, 1999; Lu, Wang, & Drzal, 2008) have pointed out a problem of using cellulosic fibres in composites; the lack of good interfacial adhesion between the two components, which results in poor properties in the final product (Tserki, Matzinos, Kokkou, & Panayiotou, 2005). This lack of interfacial adhesion is because highly polar cellulosic fibres and less-polar polymer matrices are often poorly bonded.

The interface is described as a two-dimensional area between the fibre and matrix that possess the properties intermediate between the two phases (Paul *et al.,* 2008). Poor compatibility between the fibre and matrix could lead to a decline in mechanical properties. To achieve optimum mechanical properties of the composites, the fibre-matrix as well as fibre-fibre interactions need to be optimised. Compatibilisers such as maleic anhydride and polyoxyethylene have been used to improve chemical compatibility between the matrix and the filler in melt-compounding processes (Azouz *et al.*, 2012; Kosaka *et al.*, 2007; Qiu, Zhang, Endo, & Hirotsu, 2004). The effect of maleic anhydride polypropylene (MAPP) as a coupling agent on the performance of jute/polypropylene composites have been studied (Mohanty, Nayak,

Verma, & Tripathy, 2004). The compatibiliser with its polar groups improved the properties, 72.3% increase in flexural strength compared to untreated composites was noted. The use of compatibilisers has proven to be effective in enhancing the dispersion, adhesion and compatibility of the filler with the hydrophobic matrix. Images from a scanning electron microscopy study also supports the presence of MAPP leads better fiber matrix adhesion.

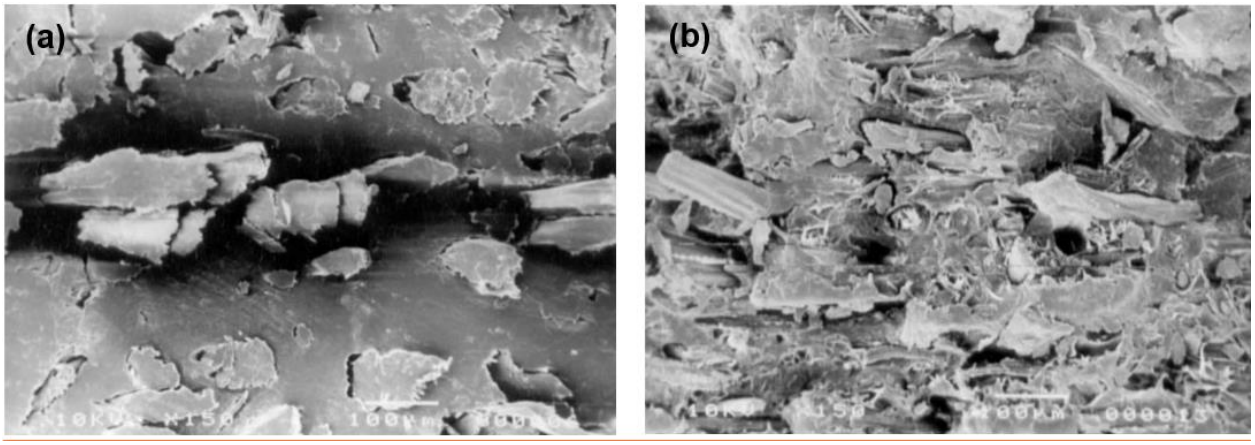

Figure 2.10 SEM Micrograph of (a) untreated jute/polypropylene composites sample and (b) treated jute/polypropylene composites (Mohanty et al., 2004)

Kim, Kim, Kim, & Yang, (2006) studied the effect on thermal properties of the addition of compatibilising agent; namely MAPE to rice husk flour (RHF) and low density polyethylene (LDPE) composites. With the incorporation of MAPE, storage modulus slightly increased compared to that of the non-treated composites. The melting temperature of the composites was not significantly changed but the crystallinity of MAPE-treated composites was slightly increased with increasing MAPE content. This enhancement of thermal stability and properties was attributed to an improvement in the interfacial adhesion and compatibility between the RHF and

LDPE matrix due to the treatment of compatibilising agent. Attenuated total reflectance (ATR-FTIR) analysis confirmed this result by demonstrating the changed chemical structures of the composites following the MAPE addition.

2.2.2 Nanocellulose Reinforced Composites

Nanocellulose reinforced composites or nanocomposites refer to multiphase materials where at least one of the constituent phase has one dimension less than 100 nm (Oksman *et al.*, 2006; Siqueira *et al.*, 2010). Nowadays, the incorporation of nanofiller in polymers has been an attractive scientific topic because of the improved properties at low filler contents (<10 wt.%) (Gong, Pyo, Mathew, & Oksman, 2011; Sapkota *et al.*, 2014; Spinella *et al.*, 2015). The first publications related to the use of CNCs as reinforcing fillers in polymer-based nanocomposites was reported in 1995 by Favier *et al.,* (1995a; 1995b). In these pioneering studies, they produced nanocomposite films by casting and evaporating a mixture of poly(styrene-co-butyl acrylate) in latex form and cellulose nanocrystals isolated from tunicates. By dynamic mechanical analysis (DMA) experiments in the shear mode, the authors observed a huge improvement in the storage modulus after adding CNCs into the host polymer even at low content. Since then, nano reinforcements have been the subject of a wide array of research efforts due to their high surface area, low cost, availability, renewability, light weight and unique morphology. Thus, they bring additional improvements and unique characteristics to the final product, at lower reinforcement content levels as compared to micro- and macro-sized materials. So far, incorporation of CNCs into a wide range of polymeric matrices was attempted, including synthetic and natural ones (such as starch, natural rubber, polylactic acid

(PLA), low density polyethylene (LDPE), polystyrene (PS), polyoxyethylene (POE), *etc*) (Kalia *et al.*, 2011; Mariano *et al*., 2014; Moon *et al*., 2011; Oksman *et al*., 2016).

Several researchers have reported improvements in the strength and modulus of polymer matrices with the addition of nanocellulose fibres (Mindaugas Bulota & Hughes, 2012; Lee, Park, & Kim, 2014; Spoljaric, Genovese, & Shanks, 2009). Other improved properties of cellulose nanocomposites with respect to the matrix polymer include better thermal properties (Lin, Huang, Chang, Feng, & Yu, 2011; Spoljaric *et al.*, 2009; Wang, Wang, & Shao, 2014), decreased moisture sensitivity (Boissard, Bourban, Tingaut, Zimmermann, & Manson, 2011; Syverud & Stenius, 2009; Tingaut, Zimmermann, & Lopez-Suevos, 2010) and improved barrier properties (Paralikar, Simonsen, & Lombardi, 2008). Due to the nano size of the reinforcement, highly transparent composites can also be prepared when well-dispersed CNCs are used as a polymer reinforcement.

2.2.3 Processing of Nanocelllulose Reinforced Composites

Nanocomposites have been processed by evaporation (Bulota & Hughes, 2012; Morán *et al.*, 2013), impregnation (Ifuku, Morooka, Morimoto, & Saimoto, 2010), extrusion (Boissard *et al.*, 2011; Marques *et al.*, 2015) and hot pressing (Gong *et al.*, 2011).

Solution processing is probably the most common method for the preparation of CNCs reinforced composites. In a typical process, the CNCs are firstly dispersed in a solvent, the CNCs dispersion is then mixed with the polymer solution by and finally

the composite is obtained by evaporation. Any polymers that are soluble can be processed using this method in theory and a small quantity of CNCs leads to a significant improvement in mechanical properties of the polymer in most cases (Alloin *et al.*, 2011).

Extrusion is an industrial method allowing the manufacture of a large range of products in short times due to the fact that the produced nanocomposites can be easily injection or compression-molded to different shapes (Gong *et al.*, 2011). Using extrusion to produce biopolymer-based nanocomposites could reduce manufacturing costs and make them competitive. Therefore, research into nanocomposites that have been produced using twin screw extrusion has been a focus of research in recent years (Bondeson & Oksman, 2007; Gong *et al.*, 2011; Mathew, Gong, Bjorngrim, & Wixe, 2011; Nicharat *et al.*, 2015). Extrusion or melt compounding has a direct impact on both the thermal and mechanical properties of the composite films because this process induces mechanical and temperature stresses and some possible orientation of the fibres (Alloin *et al.*, 2011). Good mechanical reinforcing efficiency has been observed in a range of composites that are fabricated using this technique (Spinella *et al.*, 2015).

Among these processes, slow wet casting processes such as casting/evaporation were reported to give highest mechanical performance compared to other processing techniques (Pereda *et al.*, 2014). During liquid evaporation, strong interaction between nanoparticles can settle and promote the formation through hydrogen bonding forces. In other hand, extrusion involves high shear rates that

would prevent the formation of the network. In the case of CNCs/latex composites, it has been shown that the efficiency of the processing methods is: extrusion < hot-pressing < evaporation (Hajji, Cavaille, Favier, Gauthier, & Vigier, 1996). Wet casting by direct water evaporation promote homogeneous formation of the CNCs network, as it can occur during slow evaporation process. In extrusion and hot pressing process, pressing pellets (randomly dispersed in a mold) from a freeze dried mixtures of CNCs and latex lead to heterogeneous at the macroscopic level.

In a recent study by Alloin *et al.*, (2011), tensile modulus of extruded composites was found around 2 MPa compared to 12 MPa for the cast/evaporated nanocomposite film with 6 wt.% of ramie cellulose nanocrystals. The rheological behavior for cast/evaporated films shows that viscoelastic and creep measurement have a solid-like behavior, which ascribed to the formation of a rigid cellulosic network. For extruded composites, the rheological behavior shows a liquid-like behavior, suggesting the absence of a strong mechanical network. However, the shape of the final product manufactured by the casting/evaporation method is restricted to a flat sheet or film. Also, these methods are both time consuming and produce a limited amount of material.

2.2.4 Mechanics of Nanocelllulose Reinforced Composites

Like all composite systems, the properties of nanocelllulose reinforced composites depends on the individual properties of the reinforcement and matrix, volume fraction, dispersion state and interfacial interaction between the phases. This section discusses how these factors influence the properties and how to optimize them in

the composites' structure. The properties of nanocomposites are dictated by some factors:

(a) The aspect ratio of the CNCs:

This ratio depends on the origin of the crystals and the higher it is the better the mechanical properties will be (Bras, Viet, Bruzzese, & Dufresne, 2011; Mueller *et al.*, 2015; Rusli *et al.*, 2011). CNCs from different origins will have diverse size distributions, surface properties and more importantly different aspect ratios. All of these have a fundamental influence on the mechanical properties of the final composition. Rusli *et al.* (2011) compared the stress transfer qualities in polymer composites reinforced with cellulose nanocrystals from tunicate and cotton. They observed a higher stress transfer in composites reinforced with tunicate cellulose nanocrystals, which have much higher aspect ratios. The investigation of aerogels made from cellulose nanofibers and poly(vinyl alcohol) (PVOH) as a polymeric binder has been reported (Mueller *et al.*, 2015). To cover a broad range of aspect ratios, high-aspect ratio CNCs isolated by sulfuric acid hydrolysis from the mantles of tunicates (80), intermediate-aspect ratio CNCs derived from the pseudostem of banana plants (25), and low- aspect ratio CNCs derived from microcrystalline cellulose (10) were dispersed in aqueous PVOH solutions and aerogels were prepared by freeze-drying. The data reveal that high-aspect ratio CNCs isolated from tunicates afford aerogels that show the least amount of shrinking upon freeze-drying and display the best mechanical properties. A higher aspect ratio can provide an increased reinforcement effect compared to nanofillers with lower aspect ratio, and therefore it is a key parameter with a strong influence on the mechanical properties

of CNCs-based nanocomposites. CNCs with higher aspect ratios is a desirable factor enabling a critical length for stress transfer from the matrix to the reinforcing phase (Khalil *et al.*, 2012). This is mainly because the larger specific area of higher aspect ratio of CNCs can more extensively interact with a matrix by increasing the contact surface area, thereby promoting a higher degree of interfacial interaction between fillers and a matrix (Aranguren, Marcovich, Salgueiro, & Somoza, 2013; Chen, Li, Hu, & Wang, 2014).

(b) The CNCs weight/volume fraction:

Like other composite systems, the properties of nanocomposites are also crucially determined by filler concentration. The preferred condition in most cellulose nanocomposites materials is that there is maximum interaction between the matrix and the reinforcement. Since the successful reinforcement of CNCs composites began with the work of Favier *et al*., (1995), CNCs have been widely studied and used to make nano-reinforced polymer composite materials. They used CNCs derived from tunicate, cotton, hemp, rice straw to reinforce polymer matrix with very low CNCs loading fractions of up to 6 vol.% (Fortunati *et al.,* 2012; Jun *et al.*, 2017; Liu, Martin, Moon, & Youngblood, 2015). Even at such low nanocellulose loading, they observed that the nanocomposites had significantly higher mechanical properties and thermal stability than the neat polymer. Theoretically, the higher loading of cellulose nanoparticles results in more rigid and compact compounds (Ng, Sin, Bee, Tee, & Rahmat, 2017). Practically, when the CNCs loading is increased beyond the optimum concentration (0.5 – 5 wt%), the reinforcing effect of CNCs might be suppressed and even deteriorated when CNCs lose their high aspect ratio due to their high tendency to agglomerate with each other (Dhar, Bhardwaj, Kumar

& Katiyar, 2015; Shahzad, 2015; Zarina & Ahmad, 2015). Excessive CNCs tend to be self-separated from the bulk composite as aggregates and agglomerated CNCs tend to act as defects to weaken the effective stress transfer from the matrix to fillers (Quazi *et al.*, 2013; Zhang *et al.*, 2011). This is attributed to hydrogen bonding forces or van der Waal's force developed between the matrix and CNCs, which have been weakened by sharing of energy for initiating the intra/intermolecular hydrogen bonding between hydroxyl groups on cellulose molecules (Aranguren *et al.*, 2013; Littunen, Hippi, Saarinen, & Seppälä, 2013). Consequently, poor stress transfer resulting in an uneven stress distribution throughout the matrix and fillers during tensile drawing and eventually reduced tensile strength (Espigulé *et al.*, 2013). Increased CNCs loadings could also decrease the plasticity of the polymer matrix and increase brittleness. The cracking sensitivity could be aggravated by filler-filler contacts in the composites leading any cracks being more readily propagated.

(c) The CNCs-matrix adhesion

In order for the stress to be effectively transferred to the reinforcement, good adhesion between CNCs and matrix is vital (Grunert & Winter, 2002; Heux, Chauve, & Bonini, 2000; Rusli *et al.*, 2011) and not all polymers will have good adhesion to cellulose. During loading, loads are not applied directly to the reinforcement but to the matrix. To have composites with excellent mechanical properties, the load must be transferred effectively from the matrix to the fillers. This is where the interphase comes into the picture. The interphase is a gradient region that extends from the matrix to the reinforcement surface and transfers the loads between the components. The interaction between the two phases, which have different polarity (hydrophobic and hydrophilic), can be improved using a coupling agent such as MAPP (Ma, Zhang, Meng, Anusonti-Inthra, & Wang, 2015; Peresin *et al.*, 2014; Zhang, Qiu, Yang, Endo, & Hirotsu, 2002), silane (Lu *et al.*, 2008) and PEO (Azouz *et al.*, 2012; Pereda *et al.*, 2014) to name a few. For example, polypropylene and cellulose have a limited interaction with each other because polypropylene consists of only carbon and hydrogen atoms in molecular chains, whereas a cellulose fibre is a hydrophilic material containing hydroxyl groups (-OH) (Beckermann & Pickering, 2008). The use of MAPP, therefore, is one of the most efficient ways to improve the interaction between a matrix and reinforcement phase since MAPP has both hydrophilic and hydrophobic properties on the same molecular chain. Whilst the hydrophobic part of MAPP is connected with a molecular chain of polypropylene, another part of MAPP, a polar part, interacts with a hydroxyl group of cellulose fibres (Beckermann & Pickering, 2008). Using this coupling agent to improve the interaction between two different components, however, is related to the volume

fraction of MAPP. Coating of CNCs with high molecular weight polyoxyethylene (PEO) prior to extrusion also showed encouraging results (Azouz *et al.*, 2012). Coating of the CNCs was performed in the polymer solution using water and dry polymer-coated cellulose nanocrystals were obtained by freeze-drying. Modified freeze dried CNCs were extruded with LDPE. Both improved dispersibility and thermal stability were observed compared to neat LDPE polymer (Azouz *et al.*, 2012).

(d) The CNCs dispersion

Other than interfacial adhesion, aspect ratio and volume fraction, critical to the mechanics of CNCs reinforced composites are the dispersibility of CNCs in the matrix. When the loading of CNCs is reached beyond the saturation level of dispersion, excessive nanocellulose tends to be self-separated from the bulk composite as aggregates. Fully dispersing CNCs within a composite structure has also proven to be a difficult task (Eichhorn, 2005). Chemical modification of CNCs such as esterification, acetylation, silylation and carbamination has been explored as a route for improving filler dispersion in hydrophobic polymers (Siró & Plackett, 2010a). Various methods have been used to characterise the CNCs dispersion in polymer matrix, which include SEM, TEM and Raman spectroscopy. Characterisation of the dispersion of CNCs in the matrix needs to be carried out to obtain information on the interfacial behaviour between fillers and matrix materials.

SEM has been used to study the topography of the fractured surfaces (usually obtained after mechanical testing) of the nanocomposites specimen and compared to the surface of the pure polymer. The addition of CNCs to polymers alters their

fracture mechanism. The fracture surface of thermoplastics is usually homogeneous, flat and smooth without voids. After CNCs are added, up till the optimum point, rigid CNCs act as obstacles for movement of dislocations and cracks and make them change path. As a result, the fracture surface is more chaotic than the matrix and usually CNCs appear like white dots whose concentration is a direct function of the filler content in the composites (Figure 2.11). After this point, the addition of more CNCs results in their agglomeration and inferior mechanical properties and this coincides with voids, wrinkles and nanocrystals being 'pulled out' of the polymer matrix.

In recent times it has also been possible to quantify the dispersion index of CNCs in a thermoplastic matrix using Raman spectroscopy (Agarwal, 2006). Further, using the technique of Raman mapping, it is possible to quantify a 'degree of mixing' between the CNCs and the matrix, something which has not been possible to do previously.

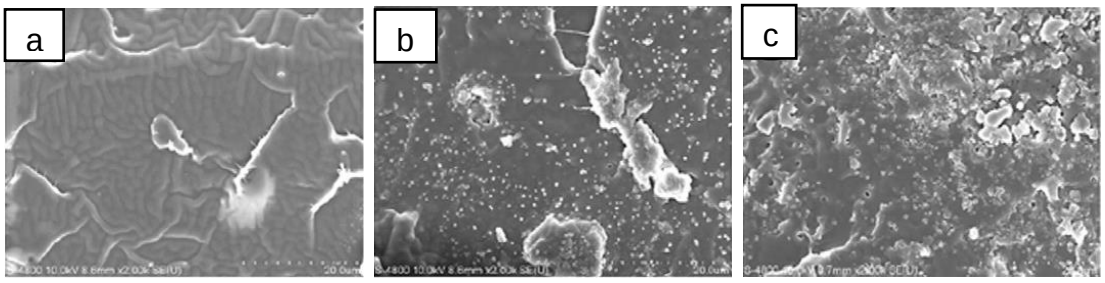

Figure 2.11 SEM images of fracture surfaces of PLA filled with different wt.% of CNCs (a) 0 (b) 2 (c) 10 (Lin et al., 2011).

(e) CNCs orientation

In composites, the alignment of reinforcing fillers in a matrix is one of the techniques used to improve the properties of composites when testing parallel or perpendicular to the direction of the CNCs' alignment. It has been reported that CNCs can be aligned by various methods, such as electric fields, magnetic fields and spin-coating (Bordel, Putaux, & Heux, 2006; Edgar & Gray, 2003; Kimura *et al.*, 2005; Kvien & Oksman, 2007; Yoshiharu, Shigenori, Masahisa, & Takeshi, 1997). Pullawan, Wilkinson, & Eichhorn, (2012) studied the orientation of CNCs derived from tunicates in an all-cellulose nanocomposite, through the application of a magnetic field. During solvent casting of the nanocomposite, a magnetic field was applied to induce their alignment. Production of the nanocomposites within the magnetic field was thought to align the CNCs, leading to enhanced stiffness and strength of the composites compared to unoriented CNCs samples. Gindl & Keckes, (2007) showed the significance of CNCs alignment on mechanical properties in their study of stretched solvent cast all-cellulose composites. The results showed that the tensile modulus of highly oriented CNCs/cellulose films along the stretching direction was higher (33.5 GPa) than the random orientation CNCs/cellulose films (9.9 GPa) (Gindl & Keckes, 2007).

2.2.5 Crystallinity of Nanocelllulose Reinforced Composites

Most of the studies in this field reported that the addition of CNCs does not seem to affect the melting temperature of the nanocomposites, as has been shown in the study of high and low density polyethylene (de Menezes *et al.*, 2009; Mokhena & Luyt, 2014), plasticised starch (Anglès & Dufresne, 2001; Mathew & Dufresne,

2002), poly(lactic) acid (Mindaugas Bulota & Hughes, 2012; Lin *et al.*, 2011), and polyvinyl alchohol (Lu *et al.*, 2008). Similar behaviour was reported for modified CNCs. However, the heat of fusion and degree of crystallinity were reported to increase with the content of the nanocellulose, whether modified or not (de Menezes *et al.*, 2009; Lee *et al.*, 2014; Lin *et al.*, 2011; Mokhena & Luyt, 2014). This behaviour was attributed to the cellulose crystalline structure, which make them act as nucleating agents in the polymer matrix and promote crystallization. The heat of fusion allows the determination of the degree of crystallinity (χ_c) of the composites. χ_c values can be obtained by dividing the heat of fusion of the material by that of the 100% crystalline matrix.

De Menezes *et al.* (2009) reported a significant increase in crystallinity with an increase in nanocellulose content regardless of the type of surface modification. They pointed out that the nanocellulose fibres acted as nucleating agents independent of their surface modification. However, the melting temperature (T_m) remained roughly constant between 103 and 105 °C. Lee *et al.*, (2014) reported that as the MCC content increased, the heat of fusion of PLA increased compared to pure PLA film. This indicated that the MCC had an effect on the crystallinity of the PLA composites film. Grunert & Winter (2002) also found that the heat of fusion increased with an increased silylated CNCs content, but stayed the same for the untreated sample. However, they reported that T_m increased with increasing silylated CNCs content as a result of stronger filler-matrix interactions. Bahar *et al.,* (2012) produced nanocomposites made of polypropylene and MCC. The melting and crystallization temperatures remained roughly constant with an increase in the

MAPP-modified nanocelluloses concentration. However, these authors found that the 15 wt.% MAPP-modified cellulose nanocomposites exhibited a 50% higher crystallinity than that of the neat polymer.

2.3 Raman Spectroscopy

Raman spectroscopy is a powerful technique for studying the structural and dynamic information on the molecular level. This technique possesses many advantages in materials characterization (Smith & Dent, 2005). It is widely used to provide information on chemical structure and physical forms, to identify substances from the characteristic spectral patterns and to determine quantitatively and semi-quantitatively the amount of substance in a sample. It is non-destructive technique and very small amount of samples and little or no sample-preparation is required for materials to be characterized by Raman spectroscopy. Additionally, the laser can be focused on a spot as small as 1 μm, and so it is possible to study the local properties of a material. Raman spectroscopy can be used in a whole range of physical states; for example as solids, liquids, and gaseous samples, in hot or cold states, in bulk, as microscopic particle or as surface layers (Paradkar, Sakhalkar, He, & Ellison, 2003; Quero *et al.*, 2011; Richard-lacroix & Pellerin, 2017; Rusli & Eichhorn, 2008; Smith & Dent, 2005).

2.3.1 Principle of Raman Spectroscopy

The Raman effect was first observed by the Indian physicist, Chandrasekhara Raman, together with his colleague K.S. Krishnan in 1928 (Raman, 1928; Raman & Krishnan, 1928). In their experiments they focused sunlight on either a purified liquid or a dust-free vapour sample using a telescope and a second lens. In order to detect the modified scattered radiation, they used the method of complementary light-filters. They observed, in addition to the elastic component of the radiation, a modified or inelastically scattered radiation, with an altered frequency. Since then, the phenomenon has been referred to as Raman spectroscopy. When a light wave, which can be considered as a stream of photons, interact with a sample and passes through a molecule, it can interact and distort the cloud of electrons round the nucleus. This incident light can either be absorbed, which forms the basis of infrared absorption spectroscopy, or be scattered either elastically (known as the Rayleigh scattering) or inelastically (Raman scattering). When a molecule interacts with an electromagnetic field, a transfer of energy from the field to the molecule occurs, according to the equation:

$$\Delta E = h v_o \qquad (2.1)$$

where ΔE is the difference in energy between the ground state and the excited states, h is Planck's constant (6.62×10^{-34} Js) and v_o is the frequency of light. A schematic of the origin of Raman scattering is shown in Figure 2.12. Most photons of the scattered light are elastically scattered, a process that is called Rayleigh

scattering. These scattered photons have the same wavelength as the incident photons (ν_o).

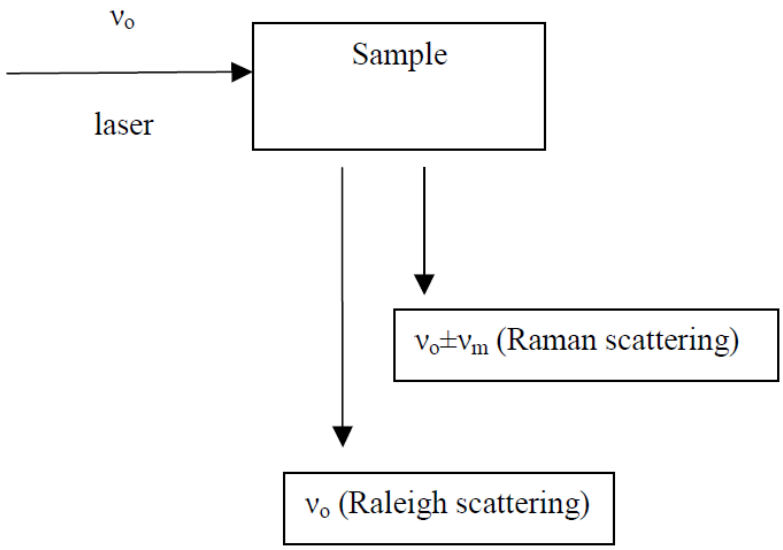

Figure 2.12 A schematic of the origin of Raman scattering (modified from Ferraro, John R., Nakamato, Kazuo Brown, (2003).

However, there is a small fraction of light (approximately 1 in 10^7 photons) which scatters at a different wavelength, usually lower than the frequency of the incident photons, $\nu_o \pm \nu_m$ where ν_m is a vibrational frequency of a molecule (Ferraro, John, Nakamato, Kazuo Brown, 2003). This inelastic scattering is called Raman scattering. Most of the inelastically scattered photons have a lower frequency than the incident photons, and this is referred to as *Stoke's* scattering. At the end of the interaction, the target molecule is promoted to a higher energy state. Sometimes the molecules are already in an excited state, and as soon as the photons are scattered, the molecule returns to the ground state. In that case the photons are scattered at a higher frequency than the incident photons. This is called *anti-Stoke's* scattering. In other words, the incident photons can excite the molecule to either higher (Stokes

Raman scattering) or to lower energy level (anti-Stokes Raman scattering), depending on whether the process starts with a molecule in the ground state or from a molecule in a vibrationally-excited state (Figure 2.13). Both Stoke's and anti-Stoke's scattering phenomena are more generally referred to as Raman scattering.

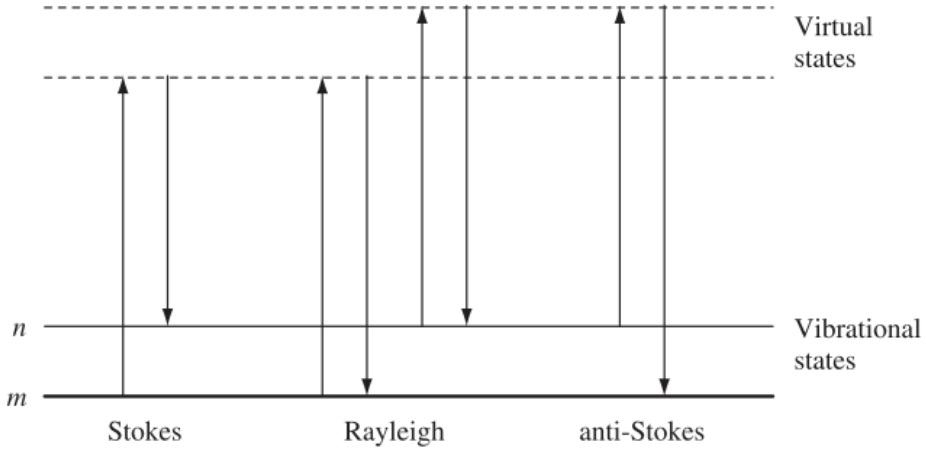

Figure 2.13 Diagram of energy level for Raman scattering; (a) Stokes Raman and (b) anti-Stokes Raman scattering (Smith & Dent, 2005).

Some of the first polymers to be studied were polystyrene and rubber samples (Gehman & Osterhof, 1936). After that, Raman spectroscopy was not initially widely used due to the lack of instrumental developments. In the early 1960s, a large number of instruments such as detectors, filters and microelectronics were developed. Later, with the introduction of powerful laser sources and charged-coupled devices (CCD), significant utilisation of Raman spectroscopy occurred. These studies allowed the recording of Raman spectra in microseconds (Bowley, Gardiner, Gerrard, Graves, & Louden, 1989).

Two theories can be used to describe Raman scattering; namely `classical theory' and `quantum theory'. This section contains information taken from (Ferraro, John

R., Nakamato, Kazuo Brown, (2003). According to the theory, Raman scattering is explained as follows. When the electric field of the incident light source interacts with a molecule, the electric field of the light causes a dipole moment in the molecule due to its polarisability. The generated dipole moment, *P* amount is expressed by the equation:

$$P = \alpha(q)E \tag{2.2}$$

where *α(q)* is the molecular polarisability and *E* is the electric field of the incident light. The electric field strength, E_s of the electromagnetic wave fluctuates with time, *t* according to the equation:

$$E_s = E_0 cos(2\pi v_0 t) \tag{2.3}$$

where E_0 is the vibrational amplitude, v_0 is the frequency of the incident light and *t* is time. Raman scattering involves energy transitions of the excited molecules to a different energy level from their initial energy level. If the molecule is vibrating with a certain frequency v_m, the nuclear displacement *q* is written as

$$q = q_0 cos(2\pi v_0 t) \tag{2.4}$$

where q_0 is the vibrational amplitude. For small amplitudes of vibration, *α(q)* can be written as a linear function of *q* according to the equation:

$$\alpha(q) = \alpha_0 + \left(\frac{\delta\alpha}{\delta q}\right)_0 q_0 \tag{2.5}$$

where α_o is the polarisability at equilibrium and $(\partial\alpha/\partial q)_o$ is the change rate of α with respect to the change in q at the equilibrium point. The combination of equations (2.2), (2.3), (2.4) and (2.5), leads to the equation

$$P = \alpha_0 E_0 cos(2\pi v_0 t) + \left(\frac{\delta\alpha}{\delta q}\right)_0 q_0 E_0 cos(2\pi v_0 t) cos(2\pi v_m t)$$

$$= \alpha_0 E_0 cos(2\pi v_0 t) + \frac{1}{2}\left(\frac{\delta\alpha}{\delta q}\right)_0 q_0 E_0 [cos(2\pi(v_0 + v_m)t) + cos(2\pi(v_0 - v_m)t)] \quad (2.6)$$

The first segment of Equation 2.6 represents the Raleigh scattering of frequency v_0 and the second part relates to the Raman scattering with frequency $v_0 + v_m$ (anti-Stokes) and $v_o - v_m$ (Stokes). It is important that the rate of change of polarisability (α) is not equal to zero in order for a particular vibrational mode to be Raman active.

The intensity of Stokes Raman scattering is observed to be higher than the anti-Stokes Raman scattering intensity. This contradicts the rule of classical electromagnetic theory where the intensity of the light is proportional to the fourth power of its wavenumber (Bowley *et al.*, 1989). Hence, the `quantum mechanical' theory of Raman scattering has been introduced to explain this behaviour. Tanaka & Young, (2006) described the vibrational energy level (ε_v) for a harmonic oscillation using the equation

$$\varepsilon_v = \left(v + \frac{1}{2}\right) v_m \quad (2.7)$$

where v is a vibrational quantum number. Energy transitions of v = 1, 2 . . . are allowed during Raman scattering. The probability of the transition is higher for v = 1 than other transitions as the v = 1 transition results in a small energy change. Normally, the initial state of the molecules is at the vibrational energy of the ground state (v = 0) except when the temperature is very high. The population of molecules with a vibrational energy (ε_v) can be elucidated using the Maxwell-Boltzman distribution law. The equation below further explains the correlation of the Stokes and anti-Stokes scattering intensities with the number of molecules with a vibrational energy:

$$\frac{\mathrm{I}_{Stokes}}{\mathrm{I}_{anti-Stokes}} = \left(\frac{v_0 - v_m}{v_0 + v_m}\right)^4 \frac{\mathrm{N}_v}{N_{v'}} = \left(\frac{v_0 - v_m}{v_0 + v_m}\right)^4 \exp\left(\frac{\varepsilon_v - \varepsilon_{v'}}{kT}\right) \quad (2.8)$$

where I is the intensity and N is the number of molecules with a vibrational energy. ε_v and $\varepsilon_{v'}$ are the energy levels of the molecule before and after transition respectively, v_o is the frequency of the incident light and v_m is the frequency of the vibration. k and T are the Boltzman's constant and temperature, respectively. At ambient temperature, it is expected that the probability of the vibrational energy transition from v = 0 to v = 1 is high during the Raman scattering. This explains why the intensity of the Stokes Raman scattering is higher compared to the anti-Stokes Raman scattering intensity.

2.3.2 Applications of Raman Spectroscopy for the Characterization of Cellulose

2.3.2.1 Band Assignments of Cellulose

Valonia ventricosa, a highly crystalline native cellulose was the first material to have several Raman bands assigned to particular elements of the molecular structure of cellulose (Blackwell, Vasko, & Koenig, 1970). It was shown that Raman spectroscopy is a powerful technique in determining the molecular conformation of cellulose. Later on, Wiley & Atalla (1987) carried out an assignment of cellulose Raman bands of two different types of native celluloses: namely *Valonia* and ramie fibres. It was found that the band intensities were dependent on the directions of the vibrational motions in the cellulose molecules, whether in stretching or bending mode. The C-C and glycosidic linkage stretching modes in the backbone of cellulose were assigned to the Raman band located at ~1095 cm^{-1}. Band assignments for Raman spectra of *Valonia* and ramie fibres are shown in Table 2.5. A later study by Edwards *et al.* (1997) on various types of cellulose fibre (ramie, jute, flax and cotton) however suggested that the Raman peak located approximately at ~1096 cm^{-1} can be assigned to glycosidic (C-O-C) bond stretching within the cellulose chain (Edwards *et al.*, 1997). In another study by Agarwal, Sabo, Reiner, Clemons, & Rudie, (2012), cellulose bands at 1098 cm^{-1} were used to visualize the spatial distribution of CNCs in the samples of the CNCs-polypropylene composites (Agarwal *et al.*, 2012). More recent work by Lewandowska, Inai, Ghita, & Eichhorn, (2018) on cotton CNCs reported the peak to be located at ~1100 cm^{-1} corresponding to the C–O ring stretching modes and the β-1,4 glycosidic linkage (C–O–C) stretching

modes between the glucose rings of the cellulose chains (Lewandowska *et al*., 2018). From these works, a typical band located at ~1095 to 1100 cm^{-1} is thought to correspond to the C-C, C-O and C-O-C stretching motions within the backbone of the cellulose molecular chain.

Table 2.6 Raman band assignments for the Raman spectra of Valonia and ramie fibres (Wiley and Atalla, 1987).

Raman band (cm^{-1})		Vibrational mode
Valonia	Ramie	
331	331	Heavy atom bending
344	344	Heavy atom bending
381	380	Heavy atom bending
437	437	Heavy atom bending
459	458	Heavy atom bending
520	519	Heavy atom bending
913	910	HCC and HCO bending at C6
968	969	Heavy atom (CC and CO)
997	995	Stretching
1034	1037	Stretching
1057	1057	Stretching
1095	1095	Stretching
1118	1117	Stretching
1123	1121	Stretching
1152	1151	Heavy atom stretching and HCC and HCO bending
1279	1275	HCC and HCO bending
1292	1291	HCC and HCO bending
1334	1331	HCC and HCO bending
1337	1337	HCC, HCO and HOC bending
1378	1378	HCC, HCO and HOC bending
1406	1407	HCC, HCO and HOC bending
1455	1456	HCH and HOC bending
1477	1475	HCH and HOC bending
2868	2866	CH and CH_2 stretching
2885	2889	CH and CH_2 stretching
2941	2943	CH and CH_2 stretching
2965	2963	CH and CH_2 stretching
3291	3286	OH stretching

3334	3335	OH stretching
3361	3363	OH stretching
3395	3402	OH stretching

2.3.2.2 Molecular Deformation of Cellulose

Raman spectroscopy can also be used to measure the molecular deformation or micromechanics of various types of cellulose I (hemp and flax) and II (Cordenka®, Enka® and Lyocell®) fibres, wood, paper and nanocelluloses (cellulose nanowhiskers and bacterial cellulose) (Eichhorn, Sirichaisit, & Young, 2001; Gierlinger, Schwanninger, Reinecke, & Burgert, 2006; Hsieh, Yano, Nogi, & Eichhorn, 2008; Quero et al., 2011). The first study involving the application of Raman spectroscopy to investigate molecular deformation of cellulose fibres was performed on regenerated cellulose fibres (Tencel®) (Hamad & Eichhorn, 1997). This study revealed that the two Raman bands initially located at ~895 and 1095 cm^{-1}, corresponding to the vibrational motion of C-O-C moieties, shifted towards a lower wavenumber under the application of external tensile deformation. This shift was thought to be due to molecular changes as a result of direct deformation of the backbone structure of the cellulose fibres (Eichhorn & Young, 2001; Kong & Eichhorn, 2005; Pullawan *et al.*, 2014; Šturcová *et al.*, 2005).

The explanation of why Raman band shifts occur upon the application of deformation of materials has been reviewed by Tashiro (1993) and Young (1995). Tashiro (1993) has interpreted the stress-induced change in the vibrational frequencies Raman bands in terms of the anharmonicity of the vibration as shown in Figure 2.14a. The

harmonic potential is shown as a dashed line. This can be modelled using equation called Morse function

$$U\ (\Delta r) = D[1 - \exp(-\eta\Delta r)] \tag{2.9}$$

where *U* is the potential energy, Δ*r* is the displacement of the interatomic distance *r* from the equilibrium value r_0 ($\Delta r = r - r_0$), *D* is the dissociation energy and *η* is a constant for a particular molecule. The force constant, *F* for the vibration is given by the second derivative of equation 2.1 with respect to Δ*r* as

$$F = \frac{d^2U}{d^2\Delta r} = 2D\eta^2\ [2\exp(-2\eta\Delta r) - \exp(-\eta\Delta r)] \tag{2.10}$$

From this equation, when a sample is subjected to tensile deformation, the interatomic separation distance is increased, resulting in the decrease of the force constant of the vibration as shown in Figure 2.14b. This results in a shift of the vibrational mode to a lower frequency, because the Raman wavenumber is proportional to the force constant of the vibration (Tashiro,1993).

(a)

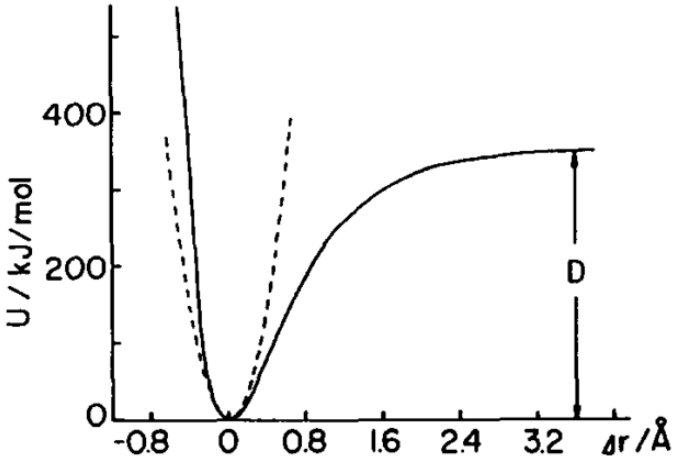

(b)

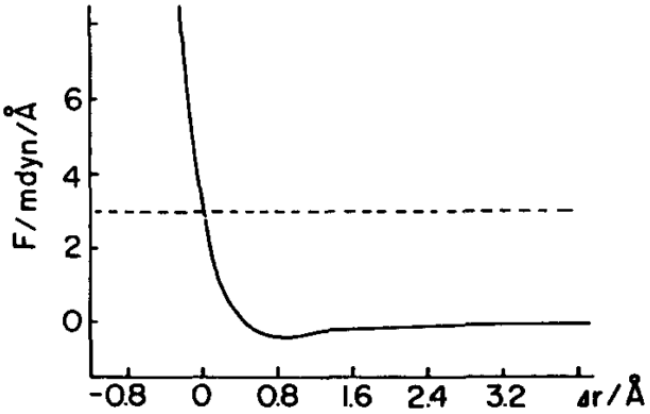

Figure 2.14 (a) Morse potential function and (b) its second derivative F with respect to the interatomic distance change Δr (Tashiro, 1993).

Another interesting study by Eichhorn *et al.,* (2001) reported the deformation mechanisms of pine wood using Raman spectroscopy. The wood samples were found to act like a typical unidirectional composite, with the lignin acting as the matrix while the cellulose acting as the reinforcement. The Raman spectra of wood samples showed two dominant peaks located ~1095 and ~1600 cm^{-1}, corresponding to C-C and C-O stretching of cellulose and the aryl stretching of lignin respectively. During tensile deformation, the downshifts of the Raman band located at 1095 cm^{-1} of the cellulose fibres were reported. In contrast, the band at ~1600 cm^{-1} belonging to lignin was found to be constant in position with the application of deformation. This may be because lignin serves as a low modulus and non-load bearing amorphous polymer. Thus, the position of Raman band located at ~1095 cm^{-1} was chosen to monitor molecular changes in these samples.

The study by Gierlinger *et al.*, (2006) also reported the molecular changes during tensile deformation of mechanically isolated fibers of spruce latewood. As shown in

Figure 2.15, along with increasing stress and strain of the wood samples, the band at 1097 cm^{-1} shifted to a lower wavenumber position, whereas the band at 1602 cm^{-1} remained at one position. These results were already reported by Eichhorn *et al.,* (2001), the function of cellulose and lignin in the wood "composite" structure. After the fiber failure, the Raman band located at 1097 cm^{-1} was found to return on its original position again, proving the elastic nature of the deformation.

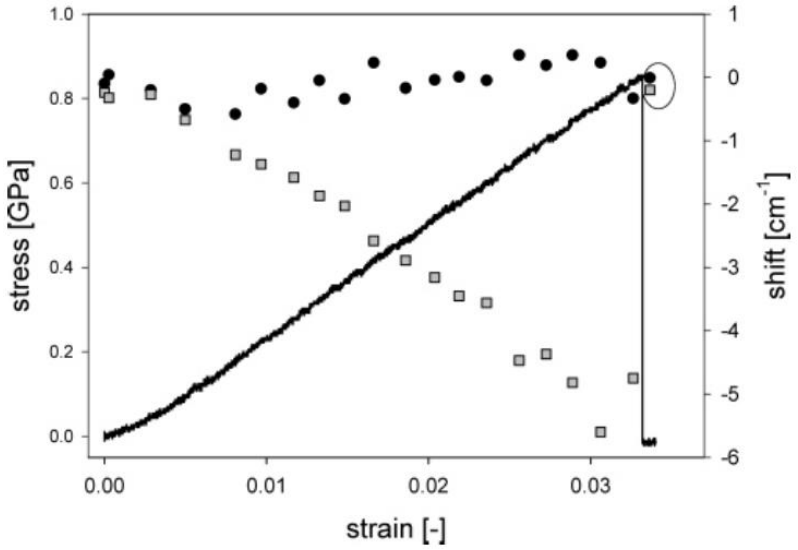

Figure 2.15 Stress-strain curve of a single spruce latewood fiber along with the calculated peak shift of the band at 1097 cm^{-1} (gray squares) and 1602 cm^{-1} (black circles) (Gierlinger et al., 2006).

Recently, Raman spectroscopy has been further used to investigate the effect of glyoxalisation treatment on the molecular deformation of bacterial cellulose (BC) networks (Quero *et al.*, 2011). The networks were functionalized by cross-linking cellulose polymer chains via covalent bonds through glyoxalisation. Higher Raman band shifts were observed for both wet and dry glyoxalised BC networks compared to unmodified samples, which is an indication of the cross-linking that has taken place (Quero *et al.,* 2011).

2.3.2.3 Crystallinity of Cellulose

Raman spectroscopy has been used to estimate the crystallinity of cellulose (Agarwal, Reiner, & Ralph, 2013; Chen *et al.*, 2015). In such measurements, the ratio of the intensity of cellulose Raman bands located at 380 cm^{-1} and 1096 cm^{-1} were used. Based on the application of the Raman method so far, this method has been proven to be reliable to measure the cellulose crystallinity of lignocellulose materials as long as proper correction for hemicellulose or syringyl lignin (if any) is carried out (Agarwal *et al.*, 2013; Chen *et al.*, 2015). Table 2.6 lists the X-Ray (Segal) and 380-Raman crystallinities of CNCs that were produced by acid hydrolysis under a variety of conditions where acid concentration, temperature, and time of hydrolysis varied. This table was adapted from the publication of Chen *et al.*, (2015). For most samples, compared to 380-Raman, the crystallinity data of X-Ray (Segal) were 44−54% higher. This is thought to be expected as the X-Ray (Segal) was affected by various types of lignin and hemicellulose (Chen *et al.*, 2015; Sunkyu Park, John O Baker, Michael E Himmel, Philip A Parilla, & David K Johnson, 2010). This issue may be one of the reasons why the results of crystallinity measurements by different researchers have been, at times, contradictory (Agarwal *et al.*, 2013; Sunkyu Park *et al.*, 2010). Therefore, the Raman method with corrections for influences of syringyl lignin and hemicellulose can be used to correctly estimate cellulose crystallinity.

Table 2.7 Comparisons of CNCs crystallinities (CrI) determined by X-ray Segal method and a Raman method (Chen et al., 2015).

CNCs sample (acid concentration, temperature, time)	*CrI* - X-Ray (Segal)	*CrI* – Raman (I_{380}/I_{1096})
(56, 70, 90)	74.3 ± 0.0	55.4
(58, 56, 60)	73.6 ± 0.4	48.4
(58, 56, 120)	72.8 ± 0.5	50.4
(58, 56, 180)	75.5 ± 0.7	57.0
(58, 56, 210)	73.4 ± 2.1	50.0
(62, 40, 75)	78.5 ± 0.1	51.8
(62, 40, 105)	77.4 ± 0.5	50.2
(62, 50, 60)	75.4 ± 0.1	50.3
(62, 50, 75)	76.0 ± 0.6	51.4
(62, 60, 30)	73.4 ± 0.0	51.8
(62, 60, 60)	76.1 ± 0.5	53.6
(64, 45, 15)	68.5 ± 1.3	39.8
(64, 45, 45)	72.0 ± 0.2	54.0
(64, 45, 75)	73.9 ± 1.7	54.4
(64, 45, 105)	75.4 ± 0.1	54.9

2.3.3 Applications of Raman Spectroscopy for the Characterization of Cellulose Reinforced Composites

Raman spectroscopy has been proven to be a powerful technique to characterise CNCs reinforced composites. This technique has advantages over the other techniques in that the rich information it can provide, the capability of studying the

composites structure on the molecular scale and simple sample-preparation. In fact, Raman spectroscopy has been employed to study almost all aspects that influence the mechanical properties of nanocomposites.

2.3.3.1 Dispersion of Cellulose in Cellulose Reinforced Composites

A number of researchers have used Raman imaging to investigate woody tissue. The distribution of lignin and cellulose was mapped simultaneously by selecting Raman bands that are specific to these cell wall components (Agarwal, 2006; Zhang *et al.*, 2015). This approach has been used in the investigation of nanocellulose composites as well. In a study conducted by Zhang *et al.*, (2015), a Raman imaging data set was collected from a 55.5 μm × 47.5 μm cross-section of poplar tension wood. Cluster analysis was used to systematically assign the obtained spectra into different groups based on similarities in Principal Component Analysis (PCA) scores. Several thousand spectra were successfully classified into five groups in accordance with different morphological regions, namely, cell corner (CC), compound middle lamella (CML), secondary wall (SW), gelatinous layer (G-layer), and cell lumen as shown in Figure 2.16.

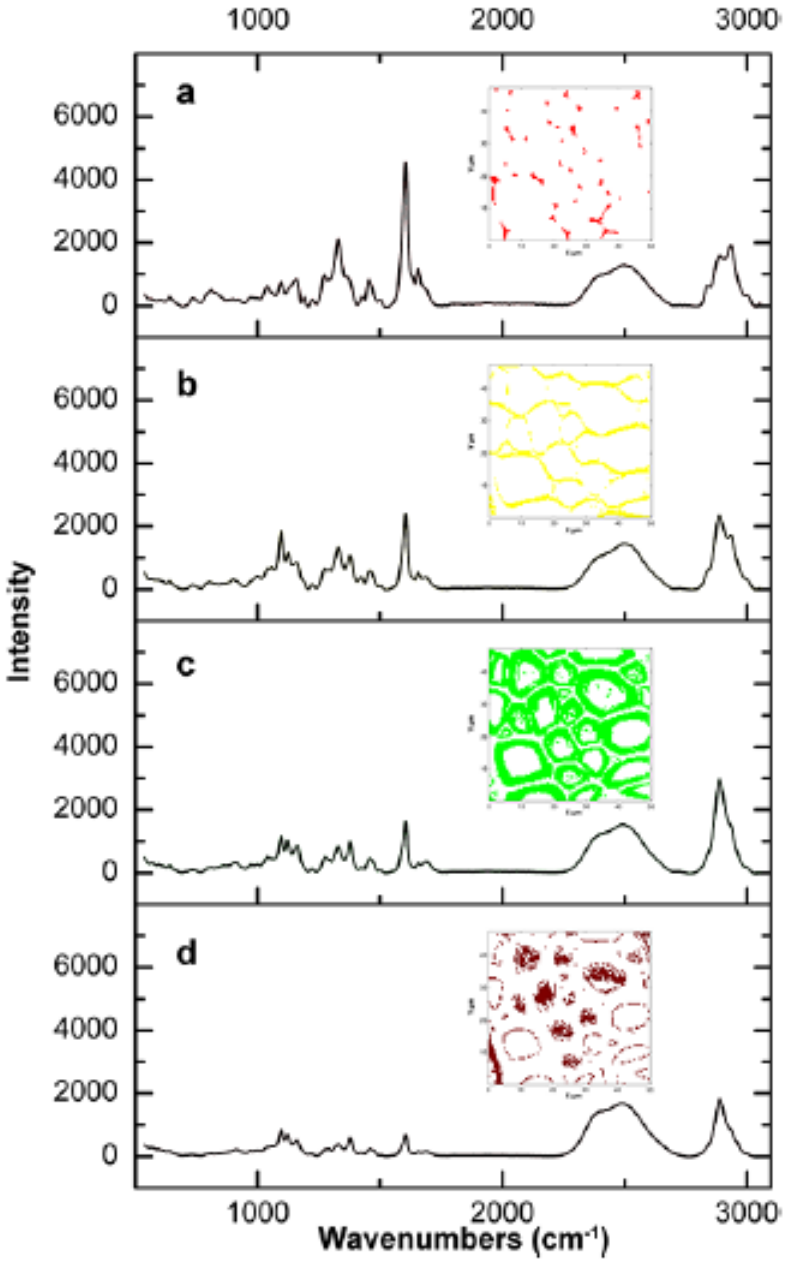

Figure 2.16 Average spectra of different cell wall layers in poplar tension wood calculated by PCA and cluster analysis: (a) CC, (b) CML, (c) SW, and (d) G-layer (Zhang et al., 2015).

Two of the principal roles played by polymer processing equipment such as extruders are that of mixing and dispersion of the reinforcing phase. Raman spectroscopy provides a qualitative but convenient way to assess the mixing and dispersion of cellulose in composites. Very limited studies on spatial quantification

of the dispersion of cellulose in matrices have been reported. A study by Agarwal *et al.,* (2012) demonstrated the usefulness of the Raman mapping technique for evaluating the dispersion of CNCs in a polymer matrix at the microscopic level. Raman spectroscopy was used to characterize the distribution of CNCs in extruded CNCs-polypropylene composites. Two nanocomposites were produced. One of the two investigated composites contained MAPP which was used as a coupling agent. Raman bands located at 1098 cm^{-1} and 1120 cm^{-1} for cellulose and polypropylene, respectively were used to visualize the spatial distribution of CNCs in the polypropylene matrix as shown in Figure 2.17. The intensity scale for each Raman map appears on the right of the image. High, medium, and very low component concentrations are indicated as red, green, and blue regions, respectively. The figure clearly shows that the CNCs were poorly dispersed in the polypropylene. The CNCs rich-regions were present as aggregates and the polypropylene-abundant regions were present as continuous phases. Nevertheless, for the CNCs/MAPP-polypropylene sample, the incorporation of the coupling agents into the composites improved the CNCs dispersion in the composites.

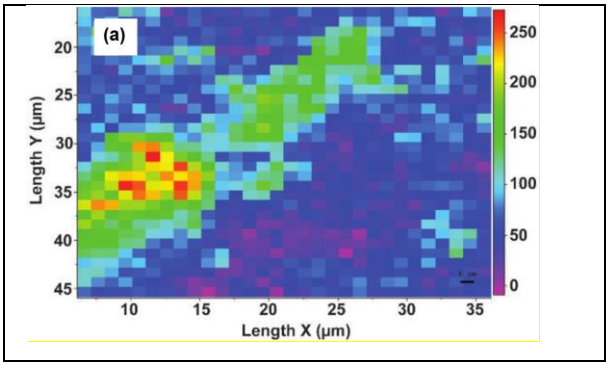

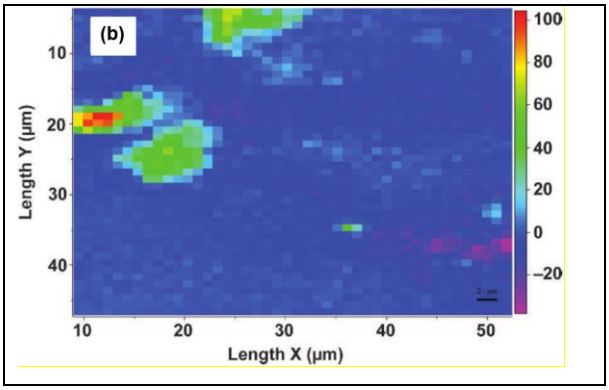

Figure 2.17 Raman images (false color) of spatial distributions of composite components: (a) CNCs in CNCs-polypropylene sample and (b) CNCs in CNCs/MAPP-polypropylene sample. Note the different scale bar values in different images (a = 1 µm and b = 2 µm). The intensity scale for each Raman map appears on the right of the image. High, medium, and very low component concentrations are indicated as red, green, and blue regions, respectively. Some locations show negative values and arise from the manner in which intensities were calculated for the images (Agarwal et al., 2012).

2.3.3.2 Stress Transfer Mechanism in Cellulose Reinforced Composites

Raman spectroscopy has been used to understand the molecular deformation of cellulose reinforced composites and the interfacial behavior between the reinforcement and the matrix. The use of Raman spectroscopy to understand the stress transfer mechanism in bacterial cellulose (BC) / poly(Lactic acid) (PLA) laminated composite was reported by Quero *et al.* (2012). In this work, maleic anhydride was grafted along the PLA backbone structure to produce maleated PLA (MAPLA). Increased molecular deformation was observed for BC/MAPLA (-1.2 ± 0.3 $cm^{-1}\%^{-1}$) compared to BC/PLA (-0.6 ± 0.1 $cm^{-1}\%^{-1}$). This suggest that grafting maleic

anhydride to the PLA enhanced the stress transfer at the interface between BC and PLA.

The use of Raman spectroscopy to understand the stress transfer mechanism in tunicates CNCs reinforced composites was reported by (Šturcová *et al.*, 2005). In this work, tCNCs embedded in an epoxy resin and the shift in the peak position of the Raman band located at 1095 cm^{-1} was detected. The observed shift was an indication of the stress transfer mechanism in the nanocomposite, resulting in the molecular deformation along the cellulose backbone structure. Subsequently, the stress transfer mechanism of tCNCs and cCNCs reinforced epoxy composites by using Raman spectroscopy was reported (Rusli *et al.*, 2011). As the composite beam is deformed in tension, the position of the 1095 cm^{-1} Raman band from both type of CNCs reinforced composite was observed to shift towards a lower wave number position. Higher Raman band shifts as a function of strain were observed for tCNCs/epoxy nanocomposites compared to cCNCs/epoxy composites, indicating the stress transfer efficiency in these nanocomposites. This is attributed to the high aspect ratio of tCNCs compared to cCNCs (as previously discussed in Section 2.2.4).

.

Pullawan *et al.*, (2014) reported the use of Raman spectroscopy to study the deformation of all-cellulose composites (CNCs reinforced microcrystalline cellulose composites) produced by solution casting. Even though both reinforcement and matrix phase of these all-cellulose nanocomposites were derived from cellulose, it was possible to observe the single-phase composited by obtaining a “fingerprint” Raman spectrum of each component. CNCs showed a dominant peak located at

1095 cm^{-1} whereas the MCC matrix exhibited peak located at both 1095 cm^{-1} and 895 cm^{-1}. It was found that as the volume fraction of the CNCs increased, the shift in the peak position of the Raman band located at 1095 cm^{-1} with respect to tensile strain were found to also increase, indicating an enhancement in the stress transfer efficiency from the matrix to the reinforcement phase. On the other hand the value of shift of the Raman band located at 895 cm^{-1} as a function of strain of the pure matrix was found to be similar for all nanocomposites with different volume fraction of CNCs. This suggest that although the stress transfer may occur within the matrix itself, the enhancement of the stress transfer efficiency of the nanocomposites resulted from the addition of CNCs.

Most of the studies of CNCs reinforced nanocomposites has been applied to thermoset or solution cast matrix system. It is therefore timely to investigate the micromechanical properties of a thermoplastic matrix system produced by melt compounding using the Raman spectroscopy technique. This has not been reported before and will offer a unique insight into the interfaces that are present in these materials.

CHAPTER 3

EXPERIMENTAL METHODOLOGY

The details of materials used in this study and the methods used to prepare CNCs and nanocomposites are provided in this chapter. Also, the techniques used to characterise the properties of CNCs and nanocomposites are included.

3.1 Introduction

In the first part of the study, Whatman filter aid as a source of cotton cellulose was purchased from Sigma Aldrich and tunicates (*Styela Clava*) were purchased from Loch Fyne Seafarms Ltd. The cellulosic materials used in this study (cotton and tunicate) were prepared at the Physics Building, Streatham Campus, University of Exeter. Sulfuric acid (98%) was obtained from Sigma Aldrich (Dorset, UK) and used as a hydrolysis agent. High density polyethylene (Arboblend HDPE) was purchased from Tecnaro GmbH and used as a matrix material. Compatibilising agent: maleic anhydride grafted polyethylene (A-C 575A, MAPE copolymer) and poly(ethylene oxide) (PEO) (M_w = 5 x 10^6 g mol^{-1}) was provided by Honeywell (Heverlee, Belgium) and Sigma Aldrich (Dorset, UK), respectively.

In this study the flow chart of the process and experimental methodology are schematically depicted in Figure 3.1.

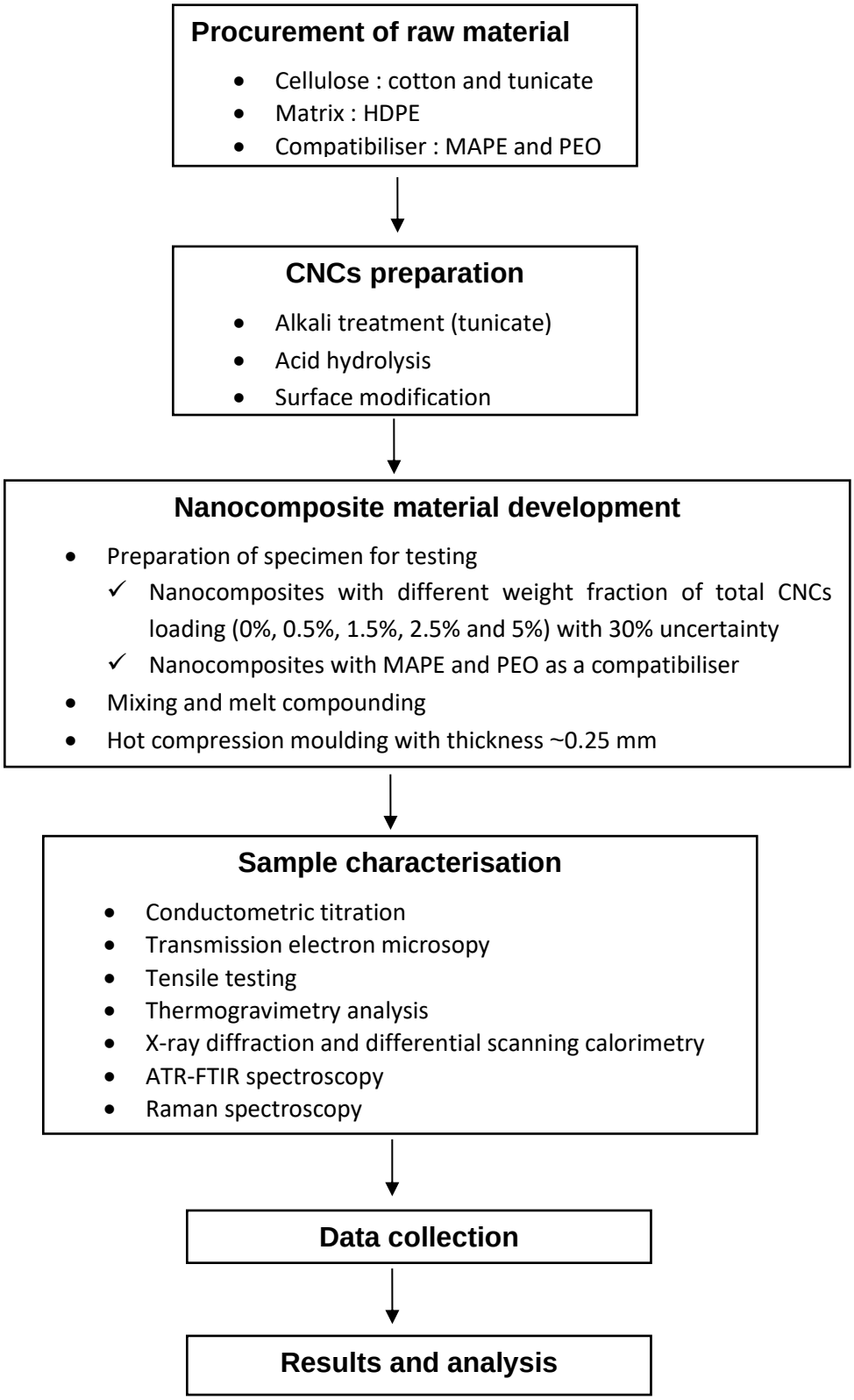

Figure 3.1 Flow chart of the methodology for experiments

3.2 Production of Cellulose Nanocrystals (CNCs)

3.2.1 Cotton Cellulose Nanocrystals

Cotton CNCs (cCNCs) were prepared from sulfuric acid (H_2SO_4) hydrolysis of Whatman filter aid according to the method described by Clift *et al.*, (2011) with slight modifications. Whatman no.1 filter paper was shredded into the Waring blender and 250 ml of deionised water was added. This mixture was then blended at high speed until a pulp was formed. Acid hydrolysis of this pulp was carried out using 64% sulfuric acid concentration. The resulting suspension was held at 50 °C under mechanical stirring for 3.5 hours to allow hydrolysis to take place. After hydrolysis, the mixture was cooled at room temperature and washed via centrifugation at 3400 rpm for 15 minutes and repeated until the solution had a pH 4. The solution was then dialyzed against distilled water until the solution reached pH 7. The cCNCs dispersion was completed by an ultrasonic treatment using a Branson sonifier for two 3 min cycles (20% power). The suspensions were then centrifuged at 10 000 rpm for 5 minutes to remove the larger pieces. The cCNCs were then be kept as an aqueous dispersion or dried by lypholization.

3.2.2 Tunicate Cellulose Nanocrystals

For tunicates cellulose extraction the sea squirts were first gutted. Then the incrustations on the outer walls of the tunicates were removed by heating in aqueous potassium hydroxide (3 L, 5% w/w per 500 g of tunicate walls, 80 °C, 6 h), followed by mechanical agitation, scrubbing, and one more treatment with aqueous

potassium hydroxide (3 L, 5% w/w, 80 °C, 72 h); this protocol represents a minor modification of the procedure reported by Khandelwal & Windle, (2013). After washing the raw cellulose with water to obtain a neutral solution, water (3 L), acetic acid (2.5 ml), and sodium hypochloric solution (4% chlorine, 5 ml) were added, and the temperature was raised to 60 °C. In one hour intervals, additional portions of acetic acid (5 ml) and sodium hypochlorite solution (>4% chlorine, 10 ml) were added until the material's colour changed from pinkish to pure white (usually two or three additions were required, depending on the particular batch of tunicates). Finally, the bleached walls were washed with de-ionised water and the tunicate cellulose obtained was oven dried (60 °C, 24 h) till further use.

Tunicate CNCs (tCNCs) were prepared by sulfuric acid hydrolysis of tunicates as described by Jorfi, Roberts, Foster, & Weder, (2013) *w*ith minor modifications. Dried bleached tunicates were shredded into the Waring blender with 500 ml deionised water until a pulp was formed. Sulfuric acid concentration and reaction temperature were 64% and 60 °C, respectively. The suspension was heated for 1 hour while continually stirring to allow hydrolysis to take place. After hydrolysis, the dispersion was cooled, centrifuged, dialysed, sonicated and freeze dried with the same procedure used for cCNCs. The percentage yield of CNCs obtained from tunicate and cotton were 34%.

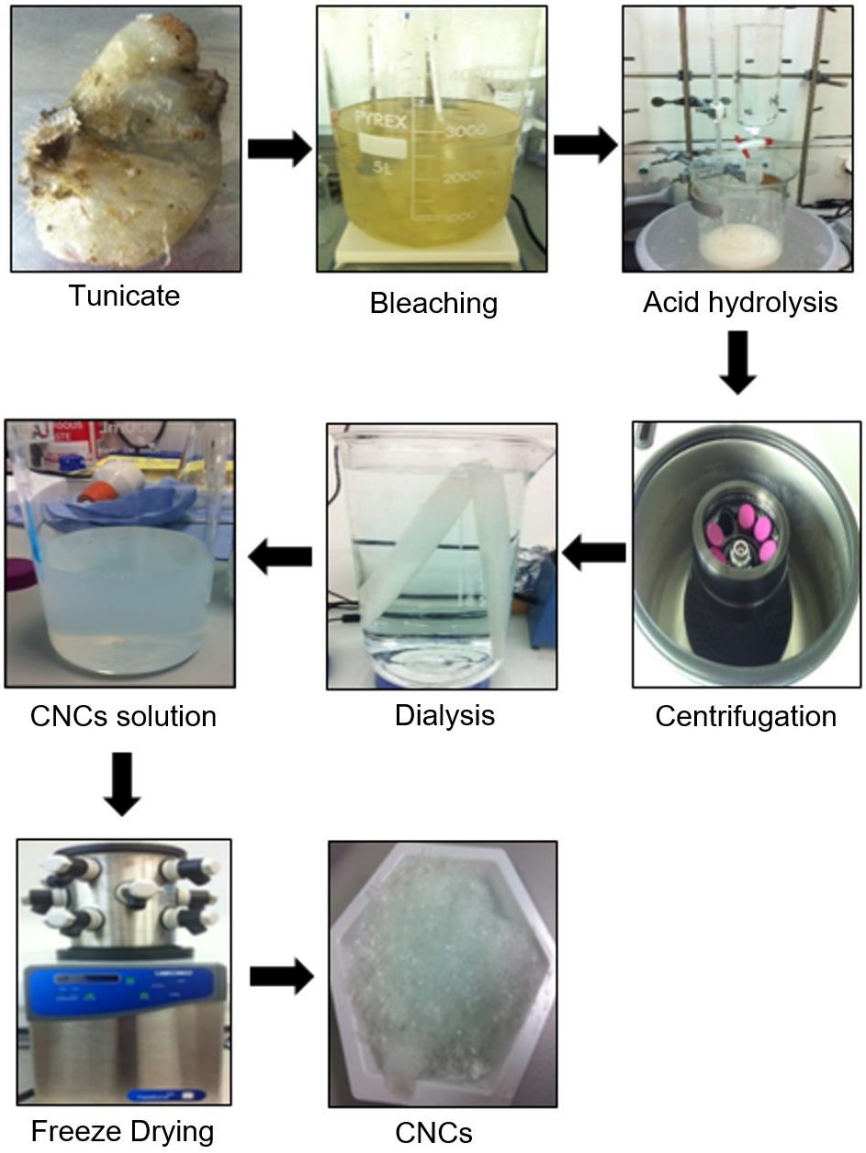

Figure 3.2 Preparation procedure of tCNCs from tunicates via an acid hydrolysis process.

3.3 Nanocellulose Surface Modification

Aqueous polymer solutions were obtained by adding PEO in distilled water (1.25 wt.%) and mechanically stirring at room temperature. The solution was protected from photo-oxidation by covering with aluminium foil (Bossard, El, Aprea, Alloin, & Dufresne, 2010). This solution was then gently stirred at 500 rpm for 4 days. After

the aqueous PEO solutions were prepared, cCNCs or tCNCs in aqueous suspension form were added; 50:50 PEO:dry content CNCs amount based on the amount of PEO. Then, distilled water was added to ensure the resulting suspension of PEO had an overall PEO concentration of 1 wt.%. These suspensions were then freeze dried before compounding and extrusion. Freeze drying was necessary to eliminate water from the materials before compounding, and to also assist the adsorption of PEO onto the surface of the CNCs.

3.4 Preparation of Nanocomposites

3.4.1 Melt Compounding

The fillers (cCNCs and tCNCs), compatibilisers (MAPE and PEO) and HDPE matrix were mixed in a mortar for 8 min. This mixture was then dried in a vacuum oven at a temperature of 60 °C for 24 h to remove humidity. Nanocomposites were prepared by mixing HDPE and CNCs either with or without compatibiliser (CNCs content ranging from 0 to 5 wt.% based on HDPE content).

CNCs reinforced HDPE nanocomposites were prepared by melt compounding using a counter rotating, intermeshing twin screw extruder (Haake, MiniLab Rheomex CTW5, Thermo Fisher Scientific). The screws are double-flighted, 109.5 mm in length and conical with a screw diameter of 14 mm at the beginning and 5 mm at the end, as shown in Figure 3.3. Feeding was performed by adding 6 g of material batchwise into the feeder and then manually pressing into the extruder using a cylinder. The screw speed was set 70 rpm for 7 min and the component was melt

processed at 160 °C. The nanocomposites were extruded in a filament form with a diameter of ~2 mm.

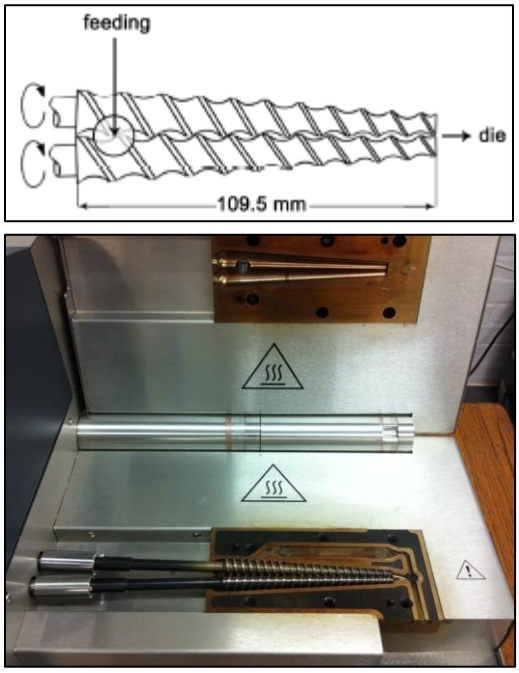

Figure 3.3 Schematic representation of the twin screw extruder.

3.4.2 Hot Compression Moulding

Hot compression moulding was used for preparation of the composite sheets for mechanical testing. The extruded strips of nanocomposite were then cut into small pieces. These pieces were then fabricated into composite films of dimensions 100 × 55 × 0.25 mm, by placing them in an aluminium mould and then into the hot press. The hot plate was preheated at 160 °C, for 2 minutes. Pressing of the composites was carried out at a pressure of 2 MPa for 7 minutes and a cooling time of 20 minutes.

.

3.5 Materials Characterisation Procedures

3.5.1 Conductometric Titration

The conductometric titration method was used to determine the concentration of surface charges on CNCs after the hydrolysis process (Abitbol, Marway, & Cranston, 2014; Araki, Wada, Kuga, & Okano, 1999). 30 mg of the CNCs were suspended into 20 ml distilled water and sonicated for two 1 min cycles (10% power). Then 20 ml of 1 mM aqueous hydrochloric acid (HCl) was added into the suspension and stirred continuously. The suspensions were titrated with 1 mM sodium hydroxide (NaOH); this procedure represents a minor modification of the procedure reported by Jorfi *et. al.,* (2013). The resistance of the suspension was monitored with a conductivity benchtop meter (Oaklon CON 2700), while repeating the titration three times. The concentration of sulfate groups was calculated using the equation

$$\frac{\text{mmol of } SO_4^-}{\text{kg of cellulose}} = \frac{C_{NaOH}\, x\, V_{NaOH}}{W_{CNCs}}\, x\, 10^6 \qquad (3.1)$$

where C_{NaOH} is the concentration of the base (1 mM), V_{NaOH} is the volume of NaOH used to titrate the weak acid, and W_{CNCs} is the weight of tCNCs and cCNCs employed for the measurement (g).

3.5.2 Transmission Electron Microscopy

Transmission electron microscopy (TEM) was used to determine the dimensions of the cCNCs and tCNCs, using a JOEL-200FX TEM operating at an accelerating voltage of 200 kV. A drop of 0.01% aqueous CNCs suspension was deposited on

the carbon-coated grids and allowed to dry at room temperature. Then, all samples were stained with a 2 wt.% solution of uranyl acetate prior to observation. Image J software was used to process the TEM images.

3.5.3 Attenuated Total Reflection Infrared Spectroscopy

The infrared spectra were recorded using an Alpha FTIR system with an attenuated total reflection (ATR) setup. This set up allowed collecting IR spectral data from the films in reflectance rather than traditional transmission mode. The spectra were collected at a resolution of 2 cm^{-1} in the range of 400 cm^{-1} and 4000 cm^{-1}. A total of 24 scans were used to obtain each spectrum. At least three replicate samples were analyzed.

3.5.4 X-ray Diffraction

X-ray diffraction (XRD) was used to measure the crystallinity of the CNCs. The CNCs were analysed in an X-ray diffractometer (Philips X'Pert-MPD) using 1.54 Å Copper X-ray source Kα radiation, with a 2θ step size of 0.05º over the range 10 - 45º. The crystallinity index of CNCs was calculated using an area method. Segal's method for crystallinity index was also used for comparison (Segal *et al.* 1959).

(i) Area method

This method used a computer routine (Diffrac.eva V4.2) which calculates based on the area under the XRD spectrum using the equation:

$$CrI = \frac{A_c}{A_c + A_a}\, x\, 100\% \qquad (3.2)$$

where A_c and A_a are the total crystalline and total amorphous areas, respectively, between 10 and 40°.

(ii) Segal`s method

This method uses the intensity of the 002 reflection compared to the intensity of the amorphous background. The crystallinity index (*CrI*) of cellulose can be defined by the following equation (Segal *et al.* 1959):

$$CrI = \frac{(I_{002} - I_{am})}{I_{002}} \; x \; 100\% \qquad (3.3)$$

where I_{002} is the maximum intensity (in arbitrary units) of the 002 lattice diffraction, typically located in the range 2θ = 21-23º for cellulose, and I_{am} is the intensity of the amorphous fraction (Fareez et al., 2018; French & Santiago Cintrón, 2013; Nam, French, Condon, & Concha, 2016). The XRD pattern of cCNCs displays peaks relating to diffraction planes 101, 10ī, 002 and 040 as shown in Figure 3.4.

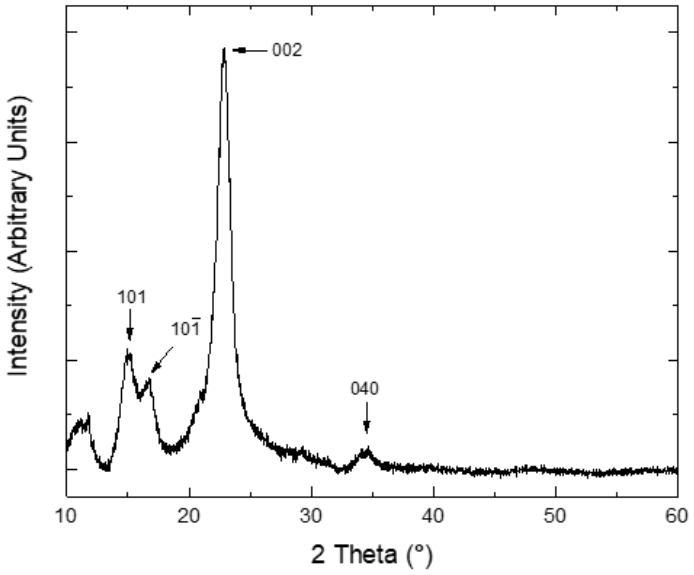

Figure 3.4 A typical X–ray pattern for cCNCs highlighting peaks located at 101, 10ī, 002 and 040.

3.5.5 Differential Scanning Calorimetry

A Mettler Toledo (DSC721e) differential scanning calorimeter (DSC) was used to investigate the thermal properties of HDPE and CNCs reinforced HDPE nanocomposites. Samples having a weight of 10 - 12 mg were enclosed in hermitic aluminium pans. They were heated under a nitrogen flow of 50 ml min^{-1} from 25 to 200 °C at a heating rate of 10 °C min^{-1}, kept at this temperature for 5 min to erase the thermal history, cooled to 25 °C at the same rate, and reheated under the same conditions to eliminate any thermal history effects. The cold crystallisation temperature, melt temperature and enthalpy of melting were determined from the second heating scan of the samples. The melting enthalpies (ΔH_m) and temperatures (T_m) were determined from the second heating curve, while the crystallization enthalpies (ΔH_c) and temperatures (T_c) of the samples were determined from the first cooling curve. Three individual measurements were performed to ensure reproducibility. Crystallinities of the HDPE specimen and CNCs reinforced composites were calculated by the following equation:

$$X_c(\%) = \frac{\Delta H_m}{(1-\emptyset)\Delta H_m^{\circ}} \text{ x } 100\% \qquad (3.4)$$

where X_c is the crystallinity, ΔH_m is the enthalpy of melting, $\Delta H°_m$ is the enthalpy corresponding to the melting of 100% crystalline HDPE (293.6 Jg^{-1}) (Wunderlich, 1990) and ∅ is the weight fraction of filler.

3.5.6 Thermogravimetric Analysis

A thermogravimetric analysis (TGA) equipment (Mettler Toledo TGA/DSC1, STAR^e) system was used to investigate the thermal stabilities of HDPE and CNCs reinforced HDPE nanocomposites. Samples with masses in the range of 10 to 12 mg were heated under a nitrogen flow of 50 ml min^{-1} from 30 to 600 ºC at a heating rate of 10 ºC min^{-1}, and the corresponding mass loss was recorded. Experiments were performed in triplicate for each sample and averages and standard deviations are presented. The onset of degradation temperature defined as temperature at which 5% mass loss occurred (Teja, Ramana, Sriramulu, & Rao, 2016; Yildirim & Shaler, 2017).

3.5.7 Statistical Analysis

Statistical analysis for comparison between nanocomposites was carried out by one-way ANOVA with Tukey's post-test. All statistical analyses were performed using IBM SPSS Statistic Version 22; *p*-values of less than 0.05 (95% confidence) were considered to be significantly different.

3.6 Mechanical Testing of the Nanocomposites

Tensile testing is the most frequently used test method to characterize the mechanical properties of materials. These tests were performed on rectangular specimens from thin films of uniform thickness. Tensile stress, strain, and Young's modulus were determined from load-elongation curves. The experiments were

carried out using a Lloyd Universal Testing Machine according to the ASTM D 882-02 standard. Seven samples were tested for every weight fraction. A specimen size of 50 × 5 × 0.25 mm was used for all tests. A testing speed of 10 mm min^{-1} and a load cell of 500 N was used in all cases.

Before the tensile testing start, the Lloyd machine was set to tensile testing mode and the dimensions of the specimen were programmed into the Lloyd machine`s computer. The test specimen was positioned vertically and grips were tightened evenly and firmly to prevent any slippage (Figure 3.5). The cross-head speed for testing was entered and the load was then applied to the specimen. The elongation of the specimen was continued until the rupture of the specimen was observed.

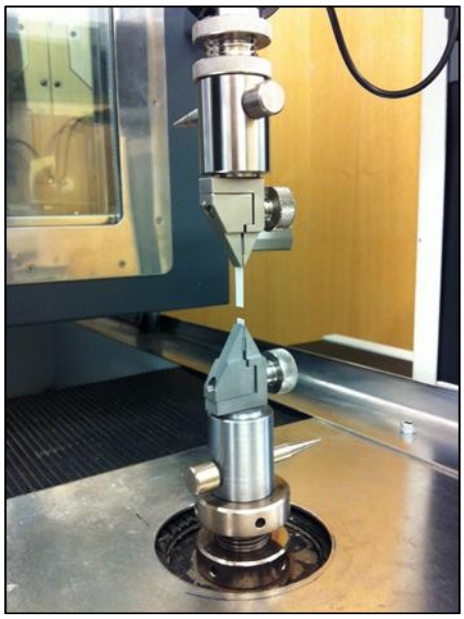

Figure 3.5 Experimental set-up of the tensile testing.

Stress σ, strain ε and Young's modulus E were calculated using the following equations;

$$\sigma = \frac{F}{A} \tag{3.5}$$

$$\varepsilon = \frac{\delta}{L} \tag{3.6}$$

$$E = \frac{\sigma}{\varepsilon} \tag{3.7}$$

where *F* is the force applied, *A* is the cross-sectional area of the sample, L is the original length of the sample, *δ* is the sample's deformed length and *E* is the Young's modulus of the sample.

3.7 Raman Spectroscopy and Imaging

Raman spectroscopy was used for three purposes: i) to study the composition of the materials, ii) to detect stress transfer from the matrix to the CNCs and iii) to investigate the mixing and aggregation of CNCs in the HDPE matrix.

3.7.1 General Description of Raman Spectrometer

In order to detect the stress transfer in the composites, a Renishaw system 1000 Raman spectrometer coupled to a 25 mW, 785 nm near-infrared laser was used to record spectra from the nanocomposites. Figure 3.6 shows a schematic of the optical arrangement of a Renishaw system 1000 Raman spectrometer, which was used in this study.

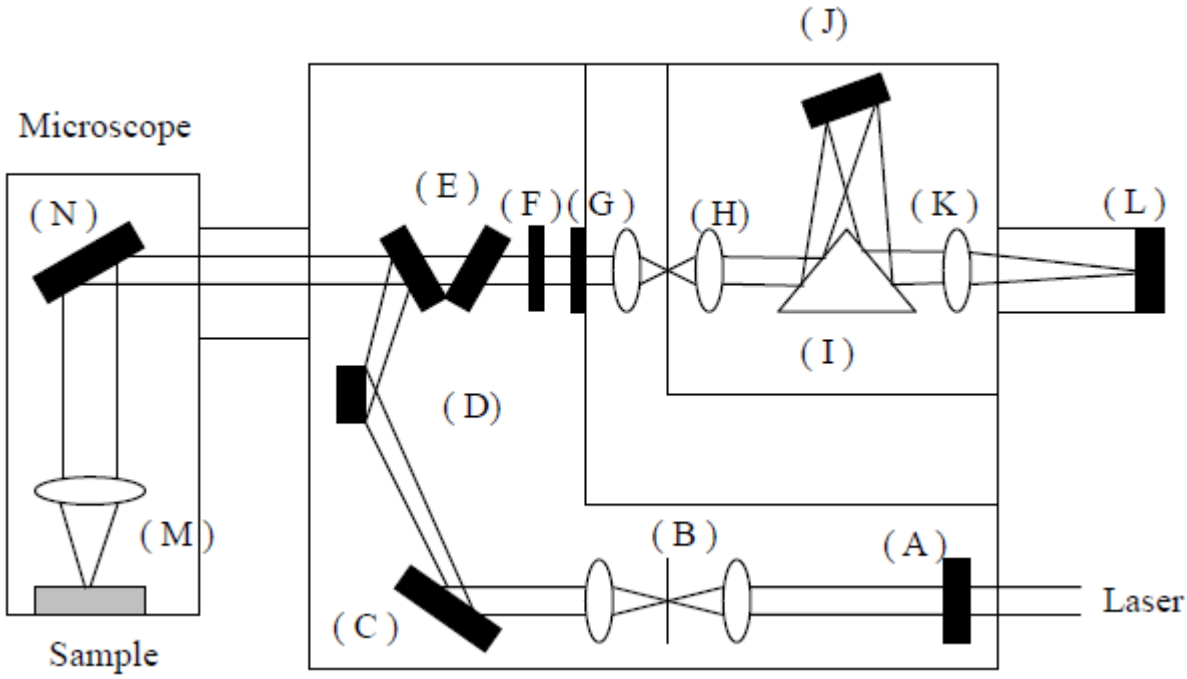

Figure 3.6 Schematic diagram of a Reinshaw Raman spectrometer (Renishawservicemanual, 1997)

The incident light (laser beam) passes through the monochromator (A) which filters the undesired wavelengths and allow only the monochromatic and polarised beam to enter the system. Then, this laser beam passes through an objective lens and a pinhole (B), ensuring that the incident beam is circular. The beam is subsequently reflected by two mirrors (C and D) onto the holographic notch filter (E). The holographic notch filter serves as a beam diverter, which reflects the laser beam to the optical microscope (M), and the beam is then focused on the sample surface (N). Subsequently, the scattered light returns back the same way to the holographic notch filter (E). The elastically Rayleigh scattered light is filtered out by this filter, whereas the Raman scattered light having different vibrational frequencies (Raman scattering light) is allowed to pass through it. Inserting a 1/2 wave plate (F) and/or a polariser (G) in the system depends on which polarisation configuration is needed to be used. The scattered light then passes through the slit (H), and reflects onto the

isosceles triangle mirror (I) to the diffraction grating assembly (J), which splits the scattered light into constituent frequencies. This radiation then passes through a focusing lens (K), and individual frequencies are detected by a charge-coupled device (CCD) detector (L), which transforms the optical signals into electrical signals.

3.7.2 Calibration of Raman Spectrometer

The Raman band position requires calibration via the use of a silicon standard, whose characteristic peak is located at 520.00 ± 0.1 cm^{-1} as shown in Figure 3.7. It is performed to verify the accuracy and consistency of the recorded data. The calibration procedure was performed using 100 % laser power at the silicon sample surface with an exposure time of 10 s with 1 accumulation. A single peak spectrum was fitted to determine the peak position of the band. An arbitrary value of this peak position was chosen, and if the position deviated from this, a day-to-day occurrence, then the software was reprogrammed to take this into account allowing consistent measurements to be taken.

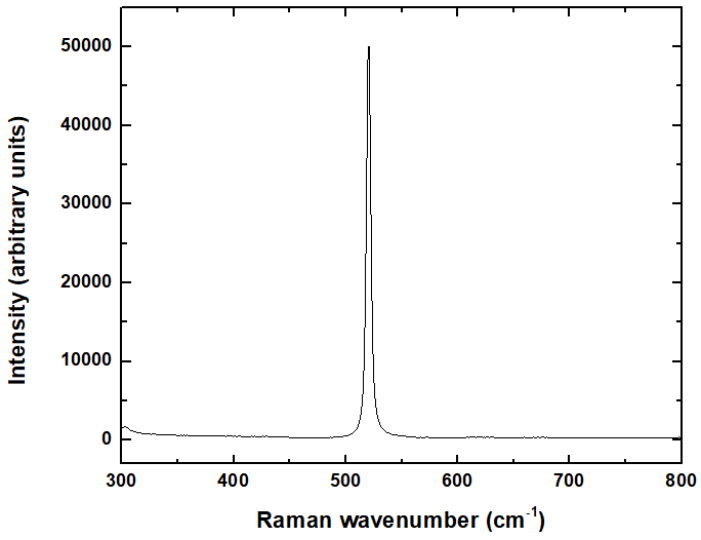

Figure 3.7 A typical Raman spectrum of a silicon standard, used for the calibration of the Raman spectrometer.

3.7.3 Micromechanical Investigation of Nanocomposites

Raman micromechanical deformation studies were performed on individual nanocomposite samples, with gauge lengths of 10 mm, fixed onto a deformation rig (Deben, MICROTEST). The details of this testing rig are shown in Figure 3.8. Spectra were obtained from the nanocomposites during incremental tensile testing on this deformation rig, which fitted directly onto the microscope stage of the Raman spectrometer. The load applied to the sample was recorded using the load cell connected to the fixed block, which is connected to a controller box. The nanocomposite samples were secured on a tensile deformation rig equipped with a 200 N load cell (Figure 3.10) and fitted directly onto the microscope stage. The laser beam was polarised parallel to the nanocomposite sample's axis, and an exposure time of 30 s with two accumulations (total time = 60 s), was used to obtain a spectrum at each strain increment (0.5%). Raman spectra were recorded in the range of 950 to 1550 cm^{-1}. The full power of the laser was used to maximize the signal obtained from the sample when focused on the surface of the sample. Three Raman spectra were recorded from the same spot for each strain increment and at least three samples were tested for each material. Raman bands located at ~1095 and ~1132 cm^{-1} were all fitted using a Lorentzian function, using the Origin software, to determine the peak position as a function of strain. The experimental set-up used for this investigation is illustrated in Figure 3.9.

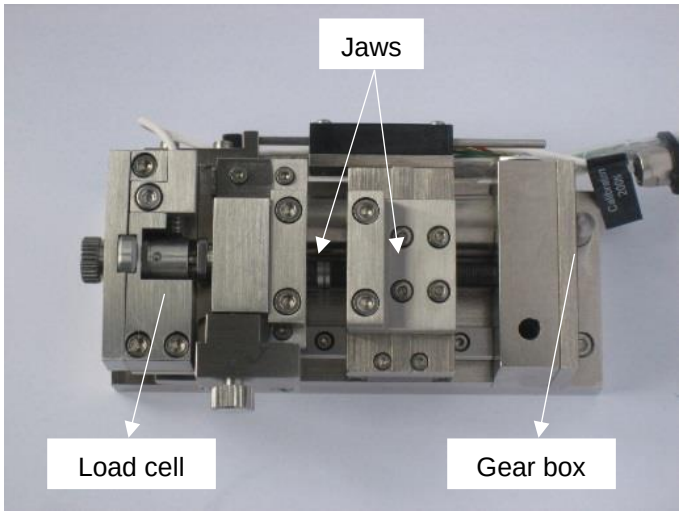

Figure 3.8 The Deben rig used to conduct tensile deformation of nanocomposites (200 N load cell).

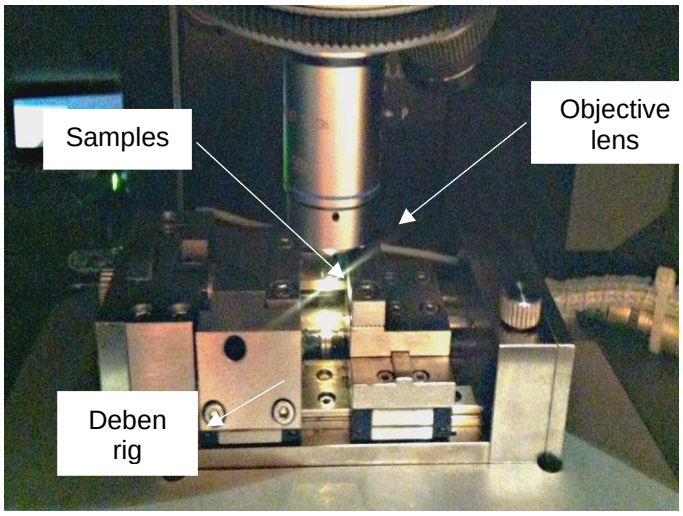

Figure 3.9 Experimental setup of the micromechanical testing with Raman spectroscopy used in this study.

3.7.4 Raman Mapping of Nanocomposites

To investigate mixing and dispersion of the CNCs in the polymer matrix, Raman mapping measurements were performed on the cross-sections of the composite filaments, which were cryo-microtomed prior to measurements. Raman

spectroscopy was performed using a confocal Raman microscope, Alpha300 (WITec) equipped with a thermoelectrically cooled CCD detector (cooled to – 61 °C). A 532 nm wavelength laser was used for excitation and a 50× objective lens was used for backscattered light collection. Single Raman spectra of each component in the nanocomposites were recorded using an exposure time of 60 s and two accumulations. Raman images were recorded within an area of 50 × 50 μm^2 with a step size of 0.2 µm in both *x*- and *y*- directions with an exposure time of 0.1 s and one accumulation. A total of 62500 Raman spectra were measured for each map. WITec Project Plus software was used to analyze Raman images and to convert them into chemical images. These chemical images were subsequently analyzed using Image-J software to estimate the area in μm^2 and the percentage of the area related to each component of the chemical image. The average number of maps per composites was three. Extraction of the objects using Image-J was performed using an automated threshold with the algorithm 'IsoData'. This algorithm sets one or two (upper and lower) cut-off values separating specific pixel intensities from each other.

CHAPTER 4

CELLULOSE NANOCRYSTALS

In this study, both cCNCs and tCNCs were prepared by using sulfuric acid as the hydrolysing agent. The use of sulfuric acid provides highly stable aqueous suspensions. This is because the esterification reaction between sulfuric acid and hydroxyl groups of cellulose under controlled hydrolysis produces negatively charged sulfate ester groups on the surface of CNCs (Beck-Candanedo *et al.*, 2005). Figure 4.1 shows the chemical structure and esterification of the hydroxyl groups of cellulose structure in sulfuric acid hydrolysis of cotton and tunicate cellulose.

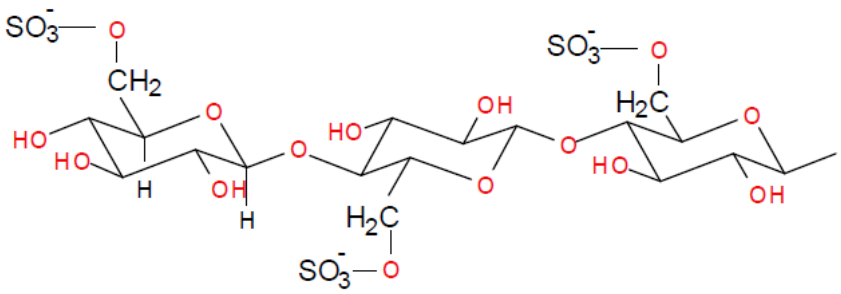

Figure 4.1 Chemical structure and esterification of hydroxyl group of cellulose structure in sulfuric acid hydrolysis.

4.1 Characterisation of CNCs

The TEM images of the CNCs presented in Figure 4.2 revealed a rod-like morphology. The addition of 2% uranyl acetate solution provided some contrast for the image. Due to acid hydrolysis, it is thought that the amorphous regions of the cellulose structure were hydrolysed, and the crystalline region remained unaffected to produce rod-like CNCs. Comparing Figures 4.2 (a) and (b), it clearly shows that tCNCs are longer and narrower than cCNCs.

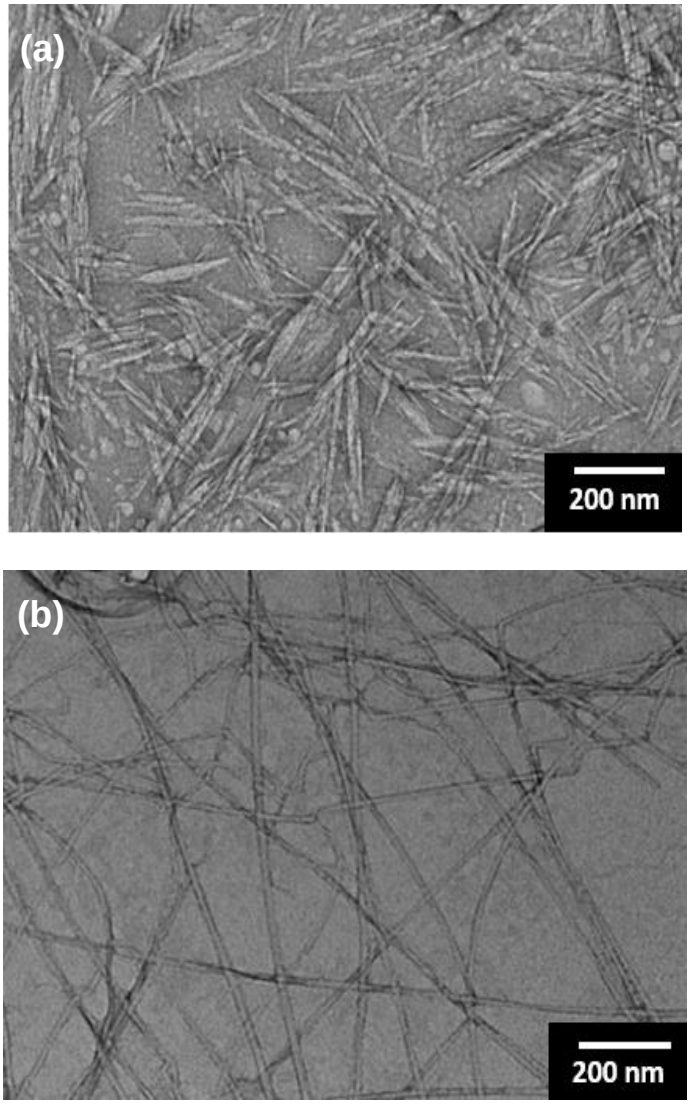

Figure 4.2 Typical TEM images of (a) cCNCs and (b) tCNCs

Image J software was used to analyze the lengths and diameters of CNCs from TEM images. Fifty measurements of the widths and lengths of CNCs were recorded and averaged; the width and length distribution histograms of cCNCs and tCNCs are shown in Figures 4.3 and 4.4, respectively. The cCNCs have widths ranging from 5 to 35 nm and lengths from 52.1 to 312.8 nm. The average width and length of the cCNCs is approximately 14.3 ± 3.6 nm and 173.5 ± 38.3 nm, giving an aspect ratio of 16.3 ± 5.7. The aspect ratios was calculated using the average for each CNCs.

In the case of tCNCs, both straight and kinked tCNCs were measured. The average length of a kinked tCNCs was measured by summing the length of its constitutive segments separating defects, as described by Elazzouzi-Hafraoui *et al.*, (2008). The widths of tCNCs ranged from 3.5 to 17.8 nm and their lengths from 220.1 to 2197.5 nm. The average widths and lengths are found to be 10.1 ± 2.5 nm and 1260 ± 480.3 nm, giving an aspect ratio of 60.7 ± 30.7. These results are summarised in Table 4.1. Since tCNCs have a much longer length, the aspect ratio is higher than for cCNCs. The presented errors are standard deviations from the mean, which are quite high because of the difficulty of measuring the dimensions of both cCNCs and tCNCs due to them overlapping each other and their aggregation.

Table 4.1 Dimensions and aspect ratio of cCNCs and tCNCs.

Samples	Width (nm)	Length (nm)	Aspect ratio
H_2SO_4 hydrolysed cCNCs	14.3 ± 3.6	165.5 ± 38.3	16.3 ± 5.7
H_2SO_4 hydrolysed tCNCs	10.1 ± 2.5	1460 ± 480.3	60.7 ± 30.7

(a)

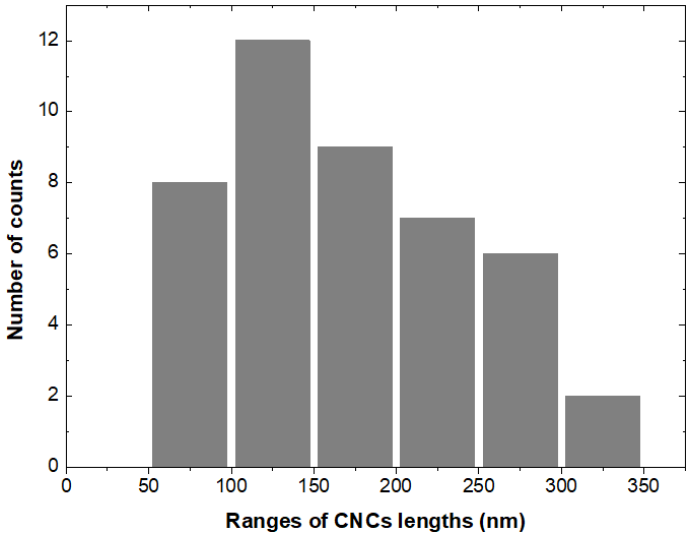

(b)

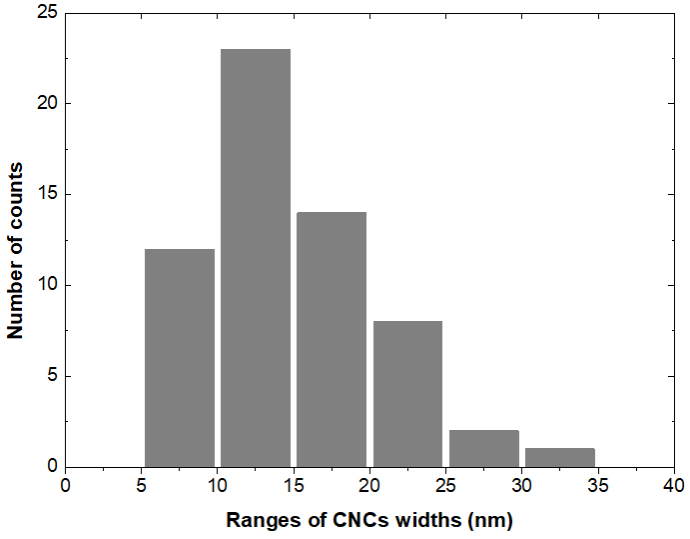

Figure 4.3 (a) Distributions of the lengths of cCNCs (nm) and (b) distribution of the widths of cCNCs (nm).

(a)

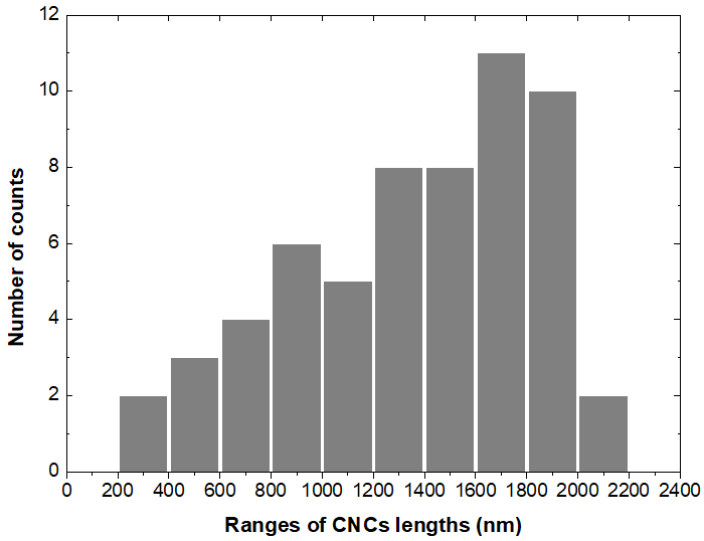

(b)

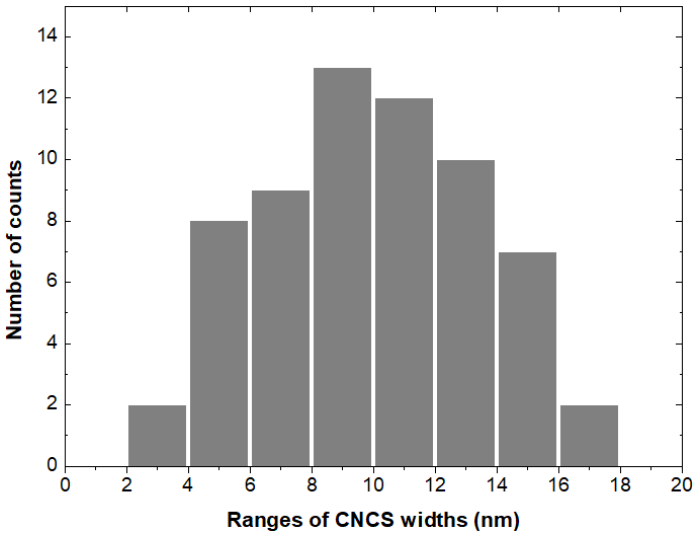

Figure 4.4 (a) Distribution of the lengths of tCNCs (nm) and (b) distribution of the widths of tCNCs (nm).

4.2 Conductometric Titration of CNCs Suspension

In this study, both cCNCs and tCNCs were prepared by using sulfuric acid as the hydrolysing agent. The esterification reaction between sulfuric acid and hydroxyl groups of cellulose under controlled hydrolysis process produces negatively charged sulfate ester groups on the surface of cellulose nanocrystals. Conductometric titration was performed to determine the concentration of the sulfate groups on the surface of the CNCs (Jorfi *et al.*, 2013). The titration curve of the sulfuric acid hydrolysed cCNCs and tCNCs suspensions are shown in Figure 4.5. The curve can be divided into three parts. The first part of the curve is associated with neutralization of strong acid groups present on the surface of the CNCs; resulting in conductivity decreases as NaOH is added. The second interval is a state of little change which relates to the neutralization of weak acid groups corresponding to the sulfate-ester surface groups. Finally, the third interval shows an increase in conductivity after the neutralization is completed. This is because there is an increase in Na+ and OH− ions in the solution. The three regions were separately fitted with linear regressions, and the volume of NaOH used to titrate the sulfate-ester groups was determined by the volume comprised within the points at which the linear fits intersect one another. To assess the accuracy of this titration volume with regard to other weakly acidic species being in solution, such as dissolved CO_2, a blank titration was performed without CNCs being present in solution. This volume was subtracted from the volumes determined for titrations containing cCNCs and tCNCs to further calculate the sulfate charge density.

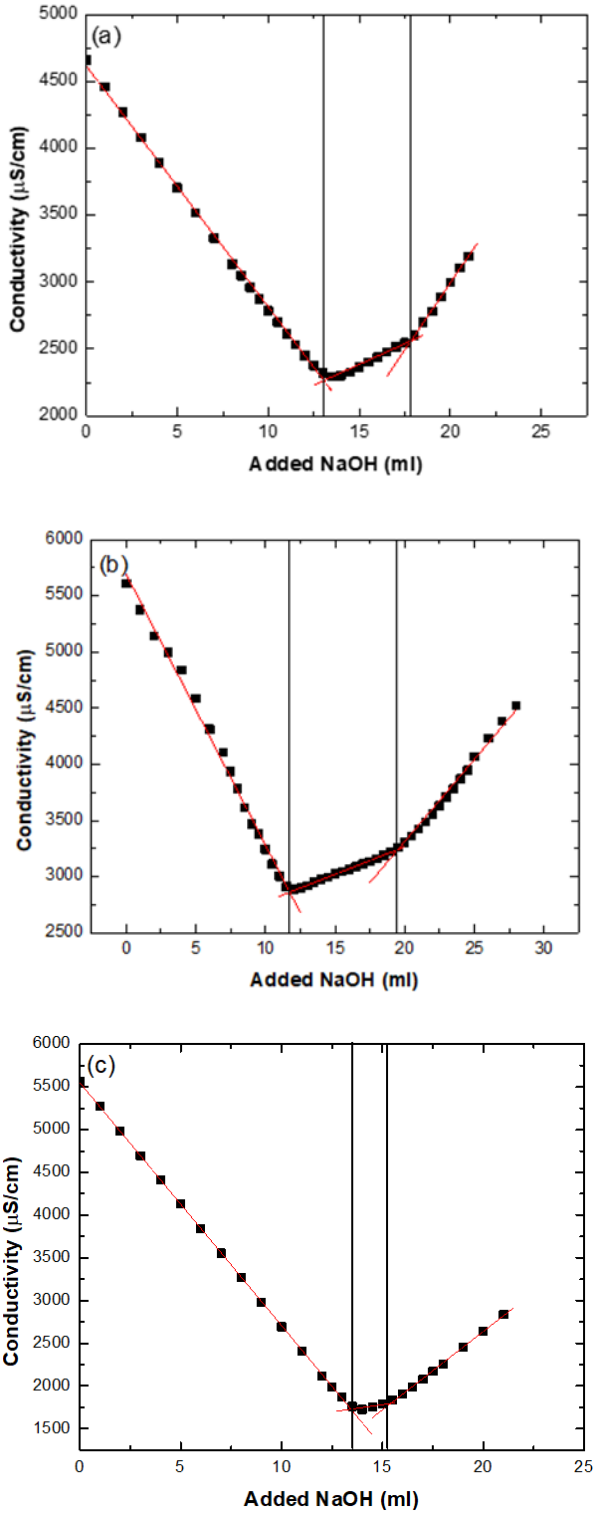

Figure 4.5 A typical conductometric titration curve of a sulfuric acid hydrolysed (a) cCNCs, (b) tCNCs and (c) blank titration without CNCs.

Table 4.2 Concentration of sulfate groups in CNCs, calculated from the added volume of NaOH by using Equation 3.1 as described in Section 3.1.3.

Samples	Concentration of negatively charged sulfate groups (mmol SO_4^-/kg cellulose)			
	This work	(Jorfi *et al.*, 2013)	(Rusli *et al.*, 2011)	(Shanmuganathan, Capadona, Rowan, & Weder, 2010).
H_2SO_4 hydrolysed cCNCs	40 ± 2.6	25	38	31
H_2SO_4 hydrolysed tCNCs	64 ± 3.9	75	-	85

In addition to exhibiting a lower aspect ratio than the tCNCs, the charge density on the surface of cCNCs (40 mmol/kg) is lower than that of tCNCs (64 mmol/kg), which is in agreement with a previous study (Jorfi *et al.*, 2013; Rusli *et al.*, 2011; Shanmuganathan *et al.*, 2010). Furthermore, the treatment conditions such as temperature of hydrolysis and acid concentration are very important in the esterification of hydroxyl groups by sulfate ions (Bondeson *et al.*, 2006; Roman & Winter, 2004). As the acid concentration and temperature of hydrolysis for tCNCs were higher than cCNCs in this study, a significant increase of sulfate groups was observed.

4.3 Crystallinity Index

The crystallinity index of CNCs was investigated using X-ray diffraction. Typical X-ray diffraction patterns recorded from cCNCs and tCNCs are shown in Figure 4.6.

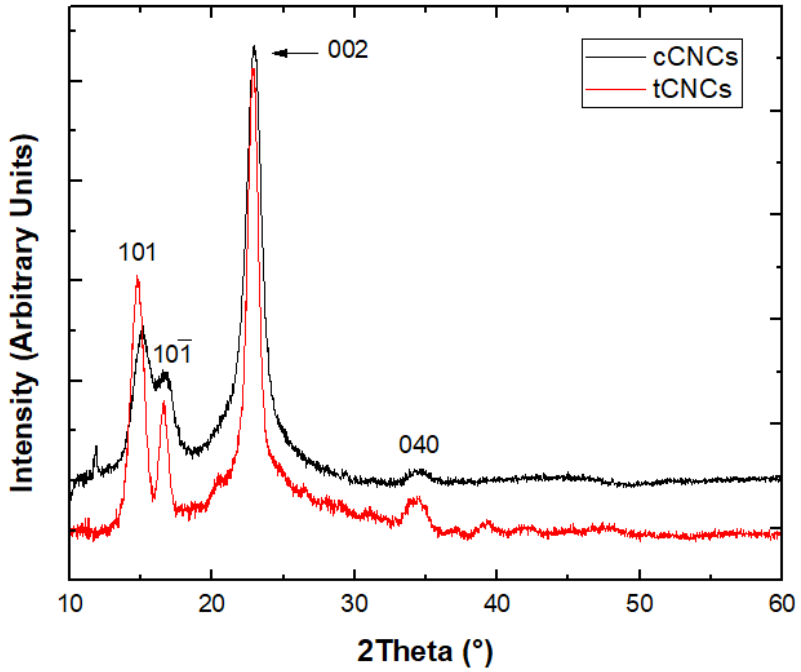

Figure 4.6 Typical X-ray diffraction patterns of cCNCs and tCNCs.

The crystallinity index (CI) of both CNCs was calculated using two methods; namely the area method and the peak height method, as described in Section 3.5.4.

4.3.1 Area Method

CI was derived according to the ratio of the total of the crystalline area to the sum of the total crystalline area and amorphous area as explained in Section 3.5.4. Using this method, the CI (%) of the cCNCs and tCNCs are found to be 67.1 ± 2.5 and 72.7 ± 2.1 respectively.

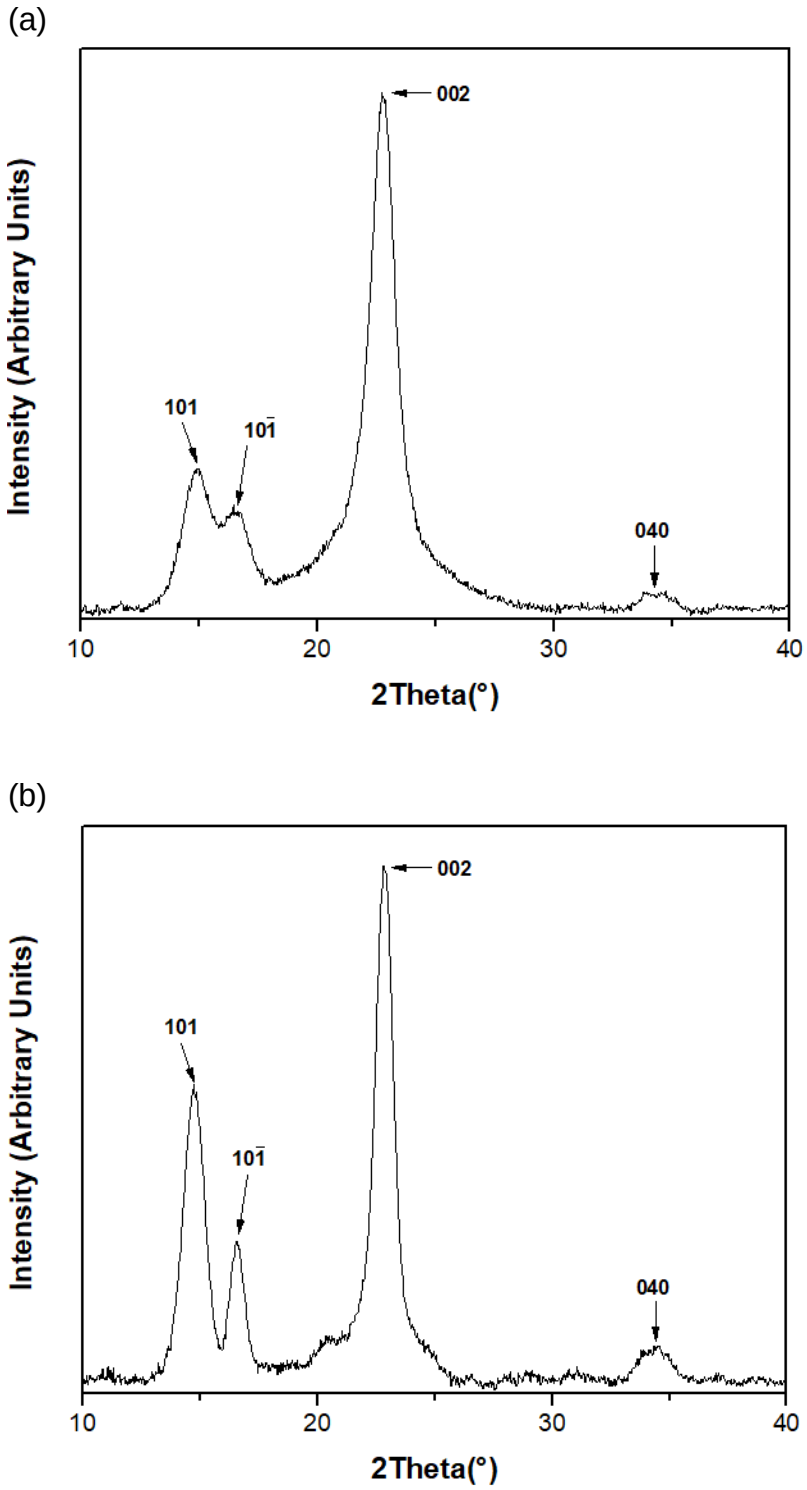

Figure 4.7 Typical X-ray diffraction patterns for (a) cCNCs and (b) tCNCs with highlighted peaks located at 101, 10ī, 002 and 040.

4.3.2 Peak Height Method

This method, developed by Segal and coworkers, used the height of the (002) Bragg peak and the height of the minimum (I_{am}) which is between the (10ī) and (002) peaks, as shown in Figure 4.7. The CI (%) of the cCNCs is found to be about 80.4 ± 1.5, which is lower compared to a value of 86.6 ± 1 for tCNCs. The CI of CNCs obtained using Segal`s peak height method is significantly higher than those calculated using area method, for both cCNCs and tCNCs (See Table 4.3). Similar results were also presented in the literature (Ahvenainen, Kontro, & Svedstrom, 2016; Ju, Bowden, Brown, & Zhang, 2015; Sunkyu *et al.*, 2010). The values obtained from Segal`s peak height method should be considered as a relative difference in samples and comparisons of values obtained from different samples of crystallites sizes should be avoided (Ahvenainen *et al.*, 2016). Since this work compares cellulose from different sources, it can be assumed that crystallinity index based on Segal`s method is not valid for this work. The area method is preferred for the rest of this work.

Table 4.3 Crystallinity index (CI) of cCNCs and tCNCs obtained using area method and peak height method.

Source of CNCs	Crystallinity Index (%)	
	Area method	Peak height method
cCNCs	67.1 ± 2.5	80.4 ± 1.5
tCNCs	72.7 ± 2.1	86.6 ± 1

The diffraction pattern for cCNCs displays four well-defined Bragg peaks located at 2θ = 14.9, 16.6, 22.9 and 34.5°, whilst the peaks for the tCNCs have slightly different positions at 2θ = 15, 16.9, 22.92 and 34.9°. These peaks correspond to the 101,10ī,

002 and 040 planes of the cellulose I crystal (Sugiyama *et al.,* 1991). The value of the interlayer distances and the crystal size of the CNCs were obtained using Bragg's law and Scherrer's equation. The value of the interlayer distances in the crystal, *d*, were calculated using Bragg`s law and equation;

$$n\lambda = 2dsin\theta \tag{4.1}$$

where *n* is an integer, λ is the wavelength of the radiation, and θ is the angle of incidence of the beam. The lateral crystallite size (*L*(002)) corresponding to the structural order of the 002 reflection was calculated from the integral breadth of the peak according to Scherrer's equation (Scherrer 1918)

$$L_{002} = \frac{K\lambda}{\beta cos\theta} \tag{4.2}$$

where L_{002} is the crystal dimension from the 002 lattice plane of diffraction, λ is the wavelength of the X-rays used, *K* is Scherrer's constant (0.91), *β* is the full width at half maximum (FWHM) of the 002 reflection in radians and *θ* is the Bragg angle in degrees. The values of interlayer distances and crystal sizes of the CNCs are reported in Table 4.4. Generally, hydrolysed tCNCs indicated higher crystallinity index and crystallite size compared to both hydrolysed cCNCs, which is in agreement with a previous study (Elazzouzi-Hafraoui *et al.*, 2008).

Table 4.4 Full width at half maximum (FWHM), the calculated interlayer distance (d(002)) and crystallite size (L(002)) of 002 reflection for cCNCs and tCNCs.

Reflection	FWHM (°)	$d_{(002)}$ (Å)	$L_{(002)}$ (Å)
cCNCs	1.25 ± 0.1	7.24 ± 0.0	62.1 ± 0.8
tCNCs	1.05 ± 0.1	7.1 ± 0.1	73.3 ± 1.4

4.4 Raman Spectroscopy

Figure 4.8 shows typical Raman spectra for both cCNCs and tCNCs. Both spectra from cCNCs and tCNCs exhibit a very intense Raman band located[1] at ~1100 cm^{-1}, corresponding to the C–O ring stretching or glycosidic linkage (C–O–C) mode in the backbone of the cellulose molecule (Agarwal *et al.*, 2012; Lewandowska & Eichhorn, 2016; Sacui *et al.*, 2014). It is therefore possible to use the position of this Raman band to monitor the chain deformation of the CNCs in the nanocomposites and it can also be used to identify this material within a polymer matrix. Additional verification of the presence of CNCs results from the presence of bands located in the range ~250-600 cm^{-1} assigned to skeletal-bending modes involving the C-C-C, C-O-C, O-C-C and skeletal stretching modes of C-C and C-O (Szymańska-Chargot, Cybulska, & Zdunek, 2011; Wiley & Atalla, 1987).

[1] The Raman system uses two different optical set-ups for the micromechanics analysis and Raman mapping. This results in two different band positions for the peak located at ~1095 cm^{-1} (785 nm laser) and ~1100 cm^{-1} (532 nm laser).

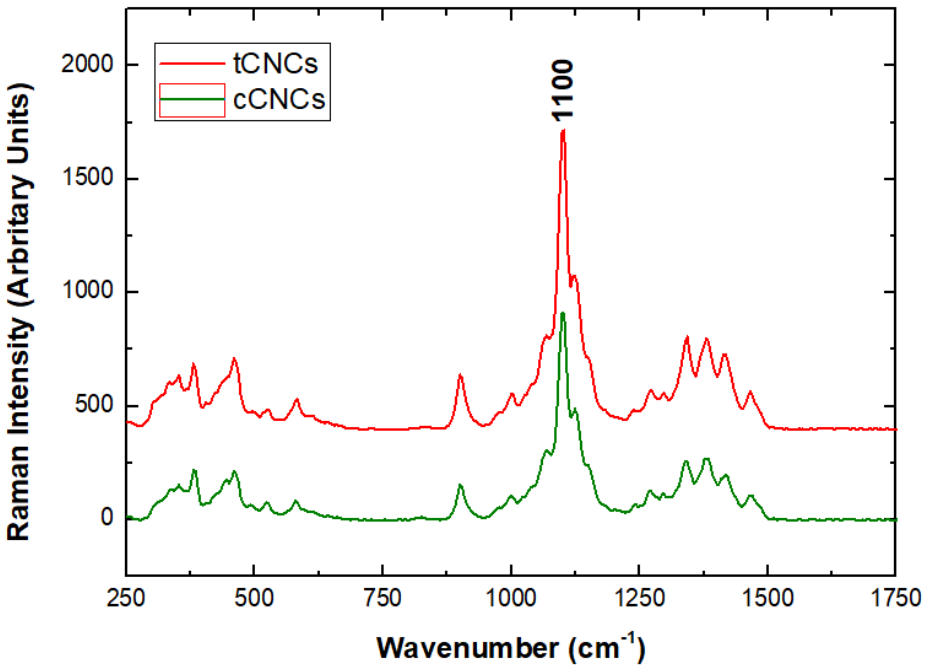

Figure 4.8 Typical Raman spectra for cCNCs and tCNCs highlighting the position of the Raman band located at ~1100 cm^{-1}.

4.5 Characterisation of PEO/CNCs

4.5.1 Raman Spectroscopy

For comparison, the Raman bands of PEO, PEO/cCNCs, PEO/tCNCs, cCNCs and tCNCs are shown in Figure 4.9. The functional group of PEO exhibits the following distinctive Raman band in the wavenumber region of 200 – 1750 cm^{-1}; C-O-C and O-C-C bending at 279 cm^{-1}; CH_2 rocking at 847 cm^{-1}; C-O-C stretching at 864 cm^{-1}, 1068 cm^{-1} and 1147 cm^{-1}; and CH_2 rocking at 1238 and 1284 cm^{-1} and CH_2 bending at 1482 cm^{-1} (Koduru *et al.*, 2017; Maxfield & Shepherd, 1975; Richard-lacroix &

Pellerin, 2017). These bands appear in both spectra for PEO/cCNCs and PEO/tCNCs, indicating the presence of PEO at the surface of CNCs.

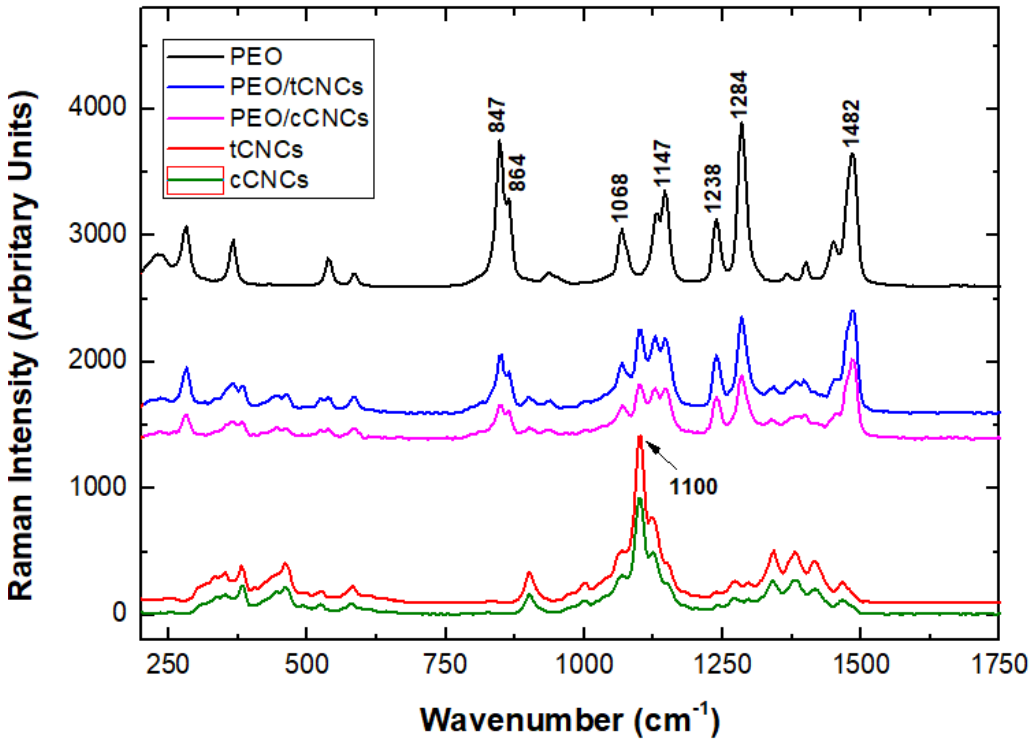

Figure 4.9 Typical Raman spectra for PEO, PEO/cCNCs, PEO/tCNCs, cCNCs, and tCNCs.

4.5.2 ATR-FTIR Spectroscopy

Figure 4.10 reports FTIR spectra of PEO, cCNCs, tCNCs, PEO/cCNCs and PEO/tCNCs. The bands for PEO are located at ~842, ~947.8 and ~960.4 cm^{-1} are ascribed to the vibrations of CH_2 and C-O-C groups, likewise, the bands located at ~1095 and ~1146 cm^{-1} are due to C-O group asymmetric stretching vibrations, and the intense band located at ~2885 cm^{-1} is attributed to the symmetric and asymmetric C-H stretching (Hoffmann & Rabolt, 1996; Kakade *et al.*, 2007).

In the CNCs' spectra, the hydrogen bonding within the cellulose chain, and between chains, associated with the O–H group appears within the region ~2995 to ~3600 cm^{-1}. In addition, the small band located at ~1640 cm^{-1} is also associated with this bonding (Zhang *et al.*, 2014). The band located at ~2889 cm^{-1} is attributed to the asymmetric stretching vibration of C–H (Zhang, Zhang, Gao, & Piao, 2013). The band located at ~1160 cm^{-1} is due to C–O–C asymmetric stretch vibrations of cellulose while the bands located around ~1056 cm^{-1} are associated with C-O stretching (Abidi, Cabrales, & Haigler, 2014).

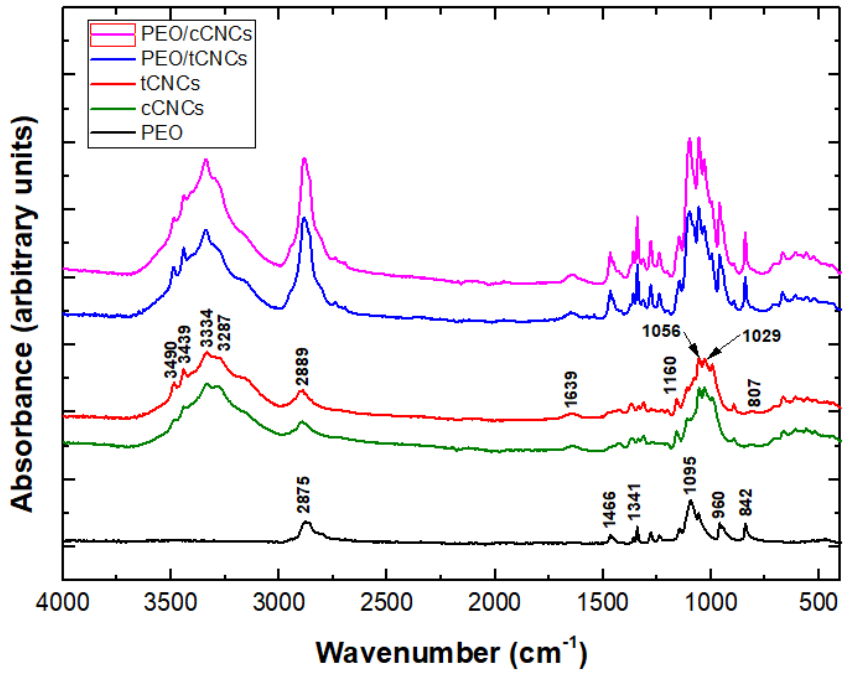

Figure 4.10 ATR-FTIR spectra for PEO, PEO/cCNCs, PEO/tCNCs, cCNCs, and tCNCs.

Being a polymer with a hydrophilic oxygen atom and hydrophobic ethylene group aligned alternatively along its chain, PEO has the ability to form hydrogen bonds with proton donors such as OH groups on CNCs. In the PEO spectra, changes of the strong characteristic triplet of PEO (i.e., ~1144, ~1095, and ~1058 cm^{-1}) that ascribed to C−O−C stretching are noted (Figure 4.11). The intensities and

frequencies of the triplet are influenced by the crystallinity of PEO and the intermolecular interactions (*e.g.*, hydrogen bonding) between C−O−C and other materials such as OH groups in CNCs (Xu *et al.*, 2013). The peak located at ~1095 cm^{-1} in the spectrum of pure PEO is attributed to C−O stretching. However, the presence of cCNCs or tCNCs in the PEO/CNCs nanocomposites upshifts the peak by approximately 5 cm^{-1}. Changes in the intensity ratio of the ~1144 cm^{-1} to ~1095 cm^{-1} bands are also observed. In both spectra of PEO/cCNCs and PEO/tCNCs, the intensity ratio of these two peaks are increase to 94% and 117% respectively, compared to the pure PEO spectrum. This is an indication that hydrogen bonding is established between PEO and the CNCs. Table 4.2 shows the relative peak height of FTIR spectra of PEO, PEO/cCNCs and PEO/tCNCs.

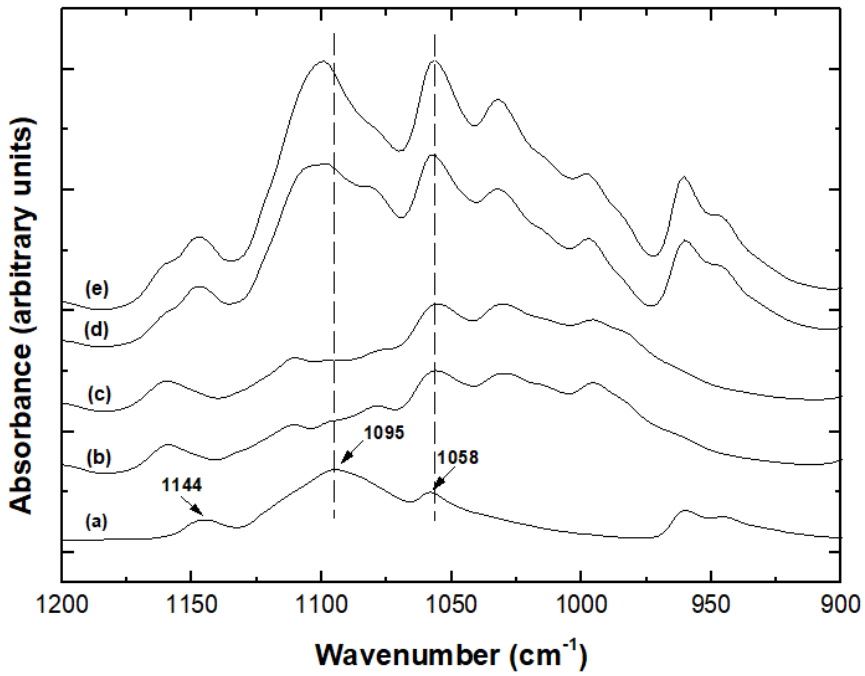

Figure 4.11 Typical ATR-FTIR spectra in the region of functional group of (a) PEO, (b) tCNCs, (c) cCNCs, (d) PEO/tCNCs and (e) PEO/cCNCs.

Table 4.5 Relative peak height of ATR-FTIR spectra of PEO, PEO/cCNCs and PEO/tCNCs.

Sample	~1144 cm^{-1}	~1095 cm^{-1}	Peak Height Ratio (~1095 cm^{-1}/~1144 cm^{-1})
PEO	0.05	0.15	0.34
PEO/cCNCs	0.25	0.38	0.66
PEO/tCNCs	0.59	0.79	0.74

4.5.3 Thermal Stability

One of the important issues for the melt processing of sulfuric acid hydrolysed CNCs reinforced polymer nanocomposites is their thermal stability. Figure 4.12 shows the TGA thermograms obtained from CNCs, PEO and PEO/CNCs. From the TGA curve of both cotton and tunicate CNCs, an initial weight loss is observed upon heating at around 60°C to 100 °C. It is attributed to the removal of moisture in the material, due to the hydrophilic character of cellulose. The degradation onset temperature of cCNCs (defined as temperature at which 5% mass loss occurred) is observed to occur at 210 °C and the maximum degradation is 355 °C. The degradation onset temperature of tCNCs is observed at a lower temperature (160 °C) and the maximum degradation is 325 °C. This earlier onset of degradation probably occurs due to a density of sulfate half-ester groups on the surface of tCNCs compared to cCNCs. It has been reported that the presence of sulfate half ester groups resulting from the sulfuric acid hydrolysis process lowers the thermal stability of CNCs (Roman & Winter, 2004). Another possible reason is higher surface area of tCNCs, which result in greater exposure to heat (Yildirim & Shaler, 2017).

Pure PEO had much higher thermal stability than CNCs, with an onset degradation temperature of 325 °C. The PEO-CNCs composite showed intermediate behavior with an onset degradation temperature of 230 °C for PEO/cCNCs and 210 °C for PEO/tCNCs. This increased thermal stability is probably due to the protecting role of interacting PEO chains that shield the sulfate half ester groups on the CNCs. PEO is a polar polymeric chain, with known hydrogen bond interactions occurring between the primary hydroxyls at the C6 position in model cellulose compounds (not cellulose itself though) and the ether oxygen in the PEO chain (Kondo *et al.*, 1994; Xu *et al.,* 2013). It is thought that a shielding of the sulfate half ester groups takes place, although a separate interaction with this group and the ether oxygen in PEO may also occur.

(a) (b)

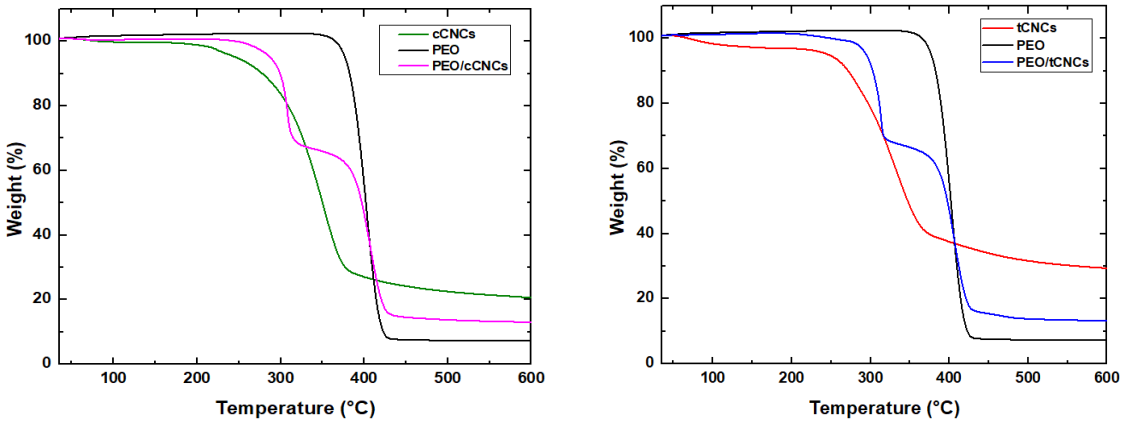

Figure 4.12 TGA curves of (a) cCNCs, PEO and PEO/cCNCs and (b) tCNCs, PEO and PEO/tCNCs.

4.5.4 X-ray Diffraction

The freeze-dried samples were characterized using X-ray diffraction. Diffraction patterns for CNCs, PEO and PEO/CNCs are shown in Figure 4.13. The diffraction pattern for pure PEO displays four well defined peak at 2θ = 19.2°, 23.3°, 26.2°, and 26.9° (Koduru *et al.*, 2017). Pure cCNCs displays four well-defined Bragg peaks located at 2θ = 14.9, 16.6, 22.9 and 34.5°, whilst the peaks of tCNCs have slightly different positions at 2θ = 15, 16.9, 22.92 and 34.9°. Meanwhile, in the case of PEO/cCNCs and PEO/tCNCs samples, new prominent diffraction peaks observed at 2θ = 19.2°, 2θ = 23.5° and around 2θ = 26-27° are ascribed to PEO chains present in the PEO/CNCs samples (Lin & Dufresne, 2013). The crystallinity index of PEO/cCNCs and PEO/tCNCs was obtained using the area method as described in Section 3.5.4. The CI (%) of the PEO/cCNCs and PEO/tCNCs were found to be about 80.9 ± 4 and 86 ± 2 %, respectively. These values are almost similar to the CI value of cCNCs and tCNCs in Table 4.3, suggesting that PEO does not affect the crystallinity of the CNCs.

(a) (b)

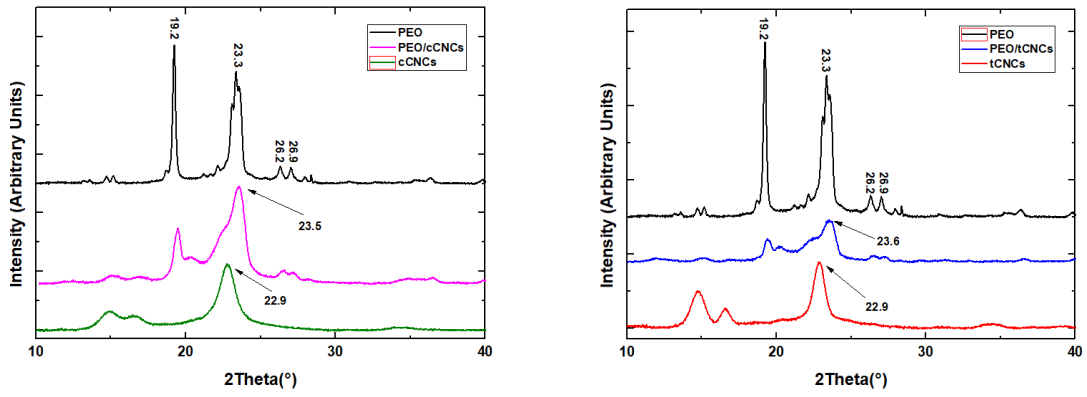

Figure 4.13 Typical X-ray diffraction patterns for (a) cCNCs, PEO and PEO/cCNCs and (b) tCNCs, PEO and PEO/tCNCs.

4.5.5 Differential Scanning Calorimetry

The crystallisation behaviour of PEO in the PEO/CNCs composite was investigated using DSC analysis. The DSC thermograms in Figure 4.14 shows the heat flux in the samples on heating and cooling on the second heating cycle. The percentage crystallization of PEO (Table 2) showed that the crystallinity of PEO (~79%) was comparable to a value published in the literature (Xu *et al.*, 2013). The addition of both cCNCs and tCNCs leads to a decrease in the crystallinity of PEO to 60% and 62.5% for PEO/cCNCs and PEO/tCNCs respectively.

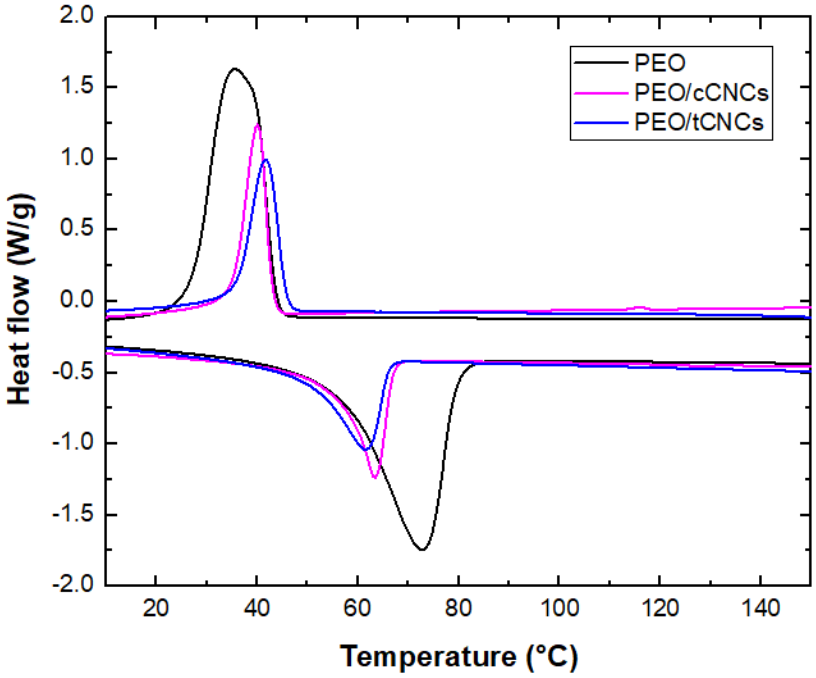

Figure 4.14 Typical DSC thermograms for PEO, PEO/cCNCs and PEO/tCNCs obtained from the second heating cycle.

Table 4.6 Melting characteristic of PEO, PEO/cCNCs and PEO/tCNCs investigated using DSC data.

Samples	2nd heating cycle		
	ΔH_m (Jg^{-1})[a]	T_m (°C)	χ_c (%)
PEO	148.4 ± 0.3	72.7 ± 1.5	79 ± 0.6
PEO/cCNCs	56.3 ± 1.1	63.5 ± 1.8	60 ± 1.6
PEO/tCNCs	57.8 ± 0.9	61.6 ± 1.9	62.5 ± 1.2

[a]ΔH_m is based on PEO weight. Heat of fusion of 100% crystallinity PEO is 188 Jg^{-1} (Rocco, Pereira, & Felisberti, 2001; Xu et al., 2013).

4.7 Conclusions

In this study, tunicate and cotton CNCs have been successfully produced using acid hydrolysis. The negative charges on the surface of the CNCs have been introduced by the sulfuric acid hydrolysis and have been detected using conductometric titration. Conductometric titration results revealed that the concentration of sulfate groups on the surface of tCNCs (64 ± 3.9 $mmolkg^{-1}$) is higher than for cCNCs (40 ± 3.2 $mmolkg^{-1}$). According to TEM images, tunicate CNCs are longer and narrower than cotton CNCs. Analysis of the resulting CNCs indicated rod-like particles with an average aspect ratio of 16.3 ± 6.2 and 60.7 ± 40.8 for cotton and tunicate CNCs, respectively. The crystallinity and crystal size were investigated using X-ray diffraction. The crystallinity of tCNCs is found to be higher than cCNCs. Clear Raman spectra can be obtained from cotton and tunicate CNCs where the peaks initially highlighted at approximately 1100 cm^{-1}, correspond to the C-O ring stretching or the glycosidic linkage (C-O-C) stretching mode in the backbone of cellulose molecule. Additional verification of the presence of CNCs results from the bands found at 250-600 cm^{-1},

assigned to the skeletal bending modes involving the CCC, COC, OCC and skeletal stretching modes of CC and CO (Wiley & Atalla, 1987). Raman spectroscopy is also used to confirm the presence of PEO in the PEO/CNCs and intermolecular interaction established between PEO and the CNCs. Improved thermal stability and reduced thermal degradation of the CNCs were observed showing the compatibilising action of PEO. PEO did not affect the degree of crystallinity of both cCNCs and tCNCs. However, the addition of CNCs leads to a decrease of crystallinity of PEO from 79% to 60% and 62.5% for PEO/cCNCs and PEO/tCNCs respectively.

CHAPTER 5

CRYSTALLINITY, MECHANICAL AND THERMAL PROPERTIES OF CELLULOSE NANOCRYSTAL REINFORCED POLYETHYLENE NANOCOMPOSITES

In this section, nanocomposites were prepared using HDPE as a matrix reinforced with cCNCs and tCNCs by a melt-compounding process. Nanocomposites were also prepared using maleic anhydride polyethylene (MAPE) and poly(ethylene oxide) (PEO) as compatibilisers to compare the effect of their addition on crystallinity, mechanical and thermal properties.

Figure 5.1 shows images of compression moulded films composed of neat HDPE, HDPE-CNCs, HDPE-MAPE/CNCs and HDPE-PEO/CNCs of cotton and tunicates reinforced HDPE nanocomposites. Visually, the pure HDPE film are optically white and transparent. When adding CNCs into the matrix, the films becomes brownish and darker as the increase of the CNCs concentration. These are obviously attributed to the incorporation of cotton CNCs and possibly reveal their degradation, as well as their inhomogeneous dispersion within the HDPE matrix. The degradation of CNCs is ascribed to their low thermal stability, as evidenced from TGA experiments in Section 4.5.3. Lack of dispersion is ascribed to the polar nature of cellulose inducing their self-aggregation when blended with a highly non-polar polymer such as HDPE. Similar observations were reported for tunicate CNCs reinforced HDPE nanocomposites films.

(a)

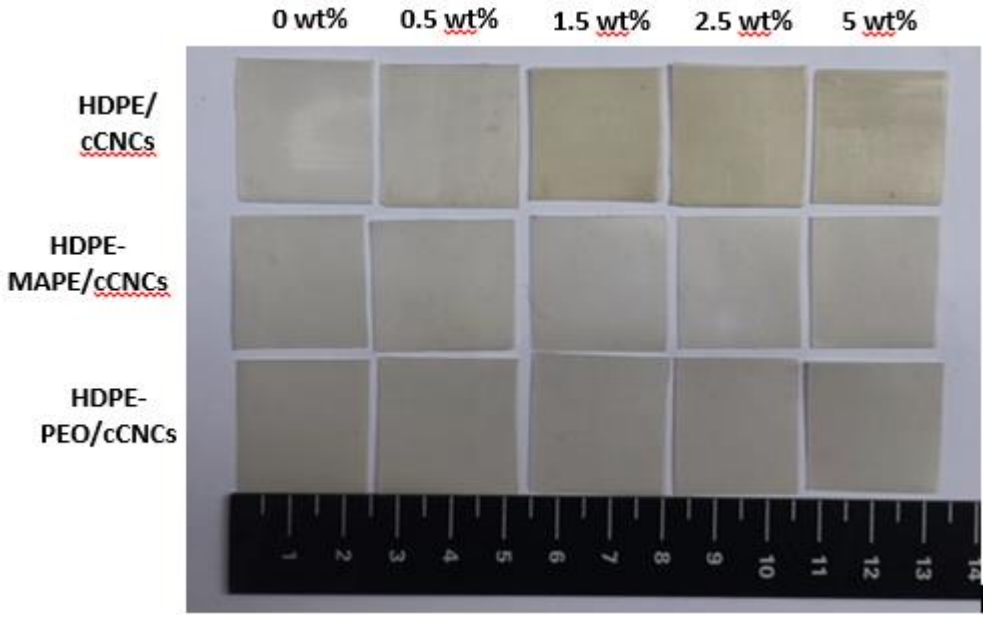

(b)

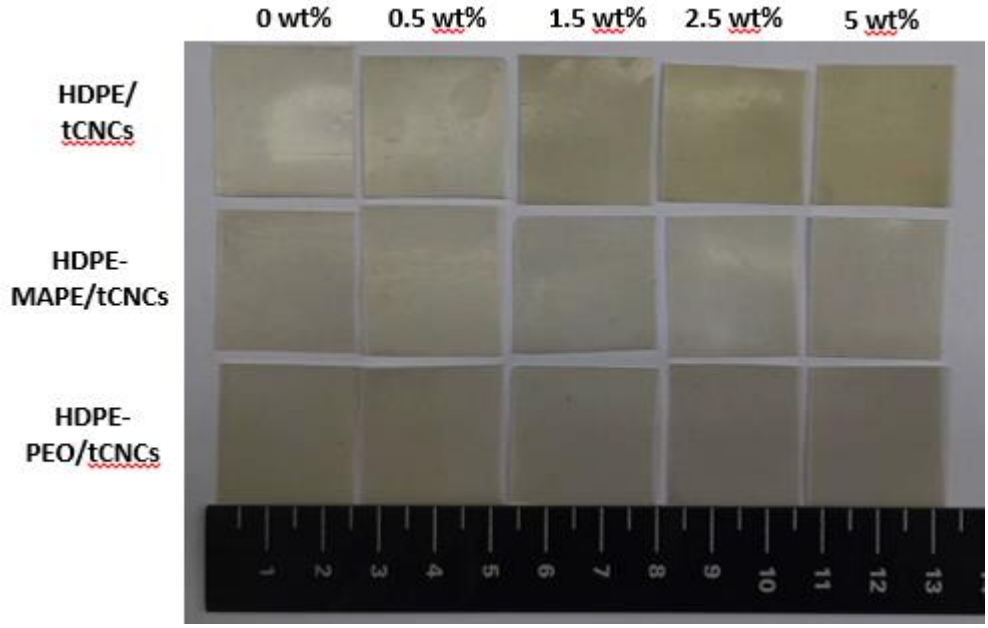

Figure 5.1 Images of the nanocomposite samples post-processing; (a) cCNCs reinforced HDPE nanocomposites and (b) tCNCs reinforced HDPE nanocomposites at weight fractions of 0, 0.5, 1.5, 2.5, 5 wt.%. Scale bar is in centimetres.

The addition of MAPE and PEO compatibilisers changes the images of the nanocomposite films. They appeared much more homogeneous and less thermally degraded. This can be ascribed to the compatibilising role of PEO chains and the latter observation correlates with TGA experiments. HDPE/CNCs nanocomposites also suffer from serious embrittlement when compared to the rest of the nanocomposites samples. This embrittlement led to the lower tensile properties of the nanocomposites.

5.1 Raman Spectroscopy

Figure 5.2 shows typical Raman spectra of HDPE, HDPE-cCNCs1.5, HDPE-MAPE/cCNCs1.5 and HDPE-PEO/cCNCs1.5 nanocomposites. A comparison between the typical Raman spectra for pure components enables the identification of unique bands, which can be used to distinguish these components in melt compounded nanocomposites. The main band corresponding to HDPE is narrow and located at ~1301 cm^{-1} and ~1464 cm^{-1} corresponding to CH_2 twisting and rocking modes in the crystalline phases of the polymer (Cherukupalli & Ogale, 2004; Sato, Shimoyama, Kamiya, Amari, Sasic, *et al.*, 2002). Additionally, the Raman bands located at ~1068 cm^{-1} and ~1133 cm^{-1} are assigned to C-C stretching modes representative of crystalline and amorphous phases of HDPE. The Raman spectrum of MAPE used in the preparation of these composite specimens exhibit the same bands as HDPE (A E Lewandowska & Eichhorn, 2016). Verification of the presence of PEO is based on the appearance of Raman bands located at ~847 cm^{-1}, ~860 cm^{-1}, ~1285 cm^{-1} and ~1483 cm^{-1} as mentioned in Section 4.5.1. In the CNCs reinforced

HDPE composites, besides the intense Raman band located at ~1101 cm^{-1}, bands centered at ~383 cm^{-1} and ~462 cm^{-1} are assigned to skeletal-bending modes involving C-C-C, C-O-C, O-C-C moieties. Skeletal stretching modes of C-C and C-O were additionally used to verify the presence of CNCs in the nanocomposites (Szymańska-Chargot *et al.*, 2011; Wiley & Atalla, 1987). These unique Raman bands for each component appear in both spectra for HDPE-MAPE/cCNCs and HDPE-PEO/cCNCs nanocomposites, indicating the presence of cCNCs and PEO in the HDPE matrix.

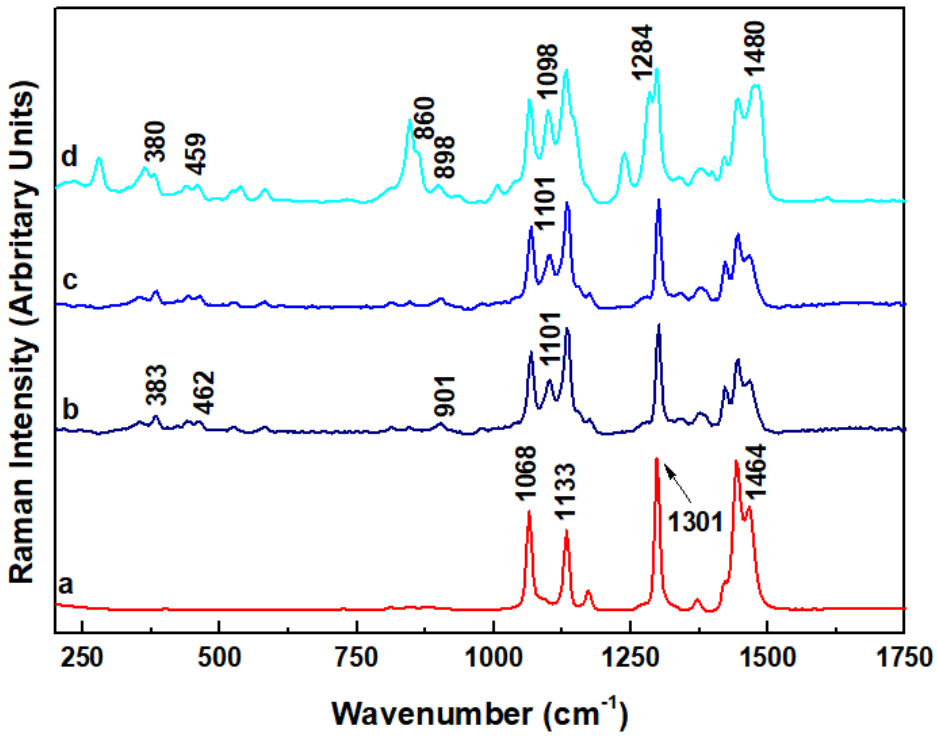

Figure 5.2 Typical Raman spectra of (a) HDPE, (b) HDPE-cCNCs1.5, (c) HDPE-MAPE/cCNCs1.5 and (d) HDPE-PEO/cCNCs1.5.

It is possible to detect a shift in the position of the Raman bands, which is thought to derive from an interaction between the filler and the compatibiliser. In the case of

maleated polyethylene, an interaction is thought to be due to an esterification reaction and/or hydrogen bonding between the maleic anhydride groups (–COOH and –C=O) and the hydroxyl groups (–OH) of the cellulose (Qiu *et al.*, 2004; Xu *et al., 2013)*. It is revealed that the formation of ester bonds between crystalline cellulose and maleic anhydride in the solid state is primarily due to the mechanochemical activation of cellulose through milling, being only slightly dependent on the chemical structure of maleic anhydride (Qiu *et al.*, 2004). As shown in Figure 5.2, the shift of Raman bands corresponding to CNCs in the HDPE-MAPE/cCNCs composite is the same as for the reference spectrum for HDPE/cCNCs. The interfacial interaction between CNCs and MAPE will be further discussed in Section 5.2. In the case of poly(ethylene oxide), hydrogen bond interaction is expected to occur between the primary hydroxyls at the C6 position in cellulose, and the ether oxygen in the PEO chain (Kondo & Sawatari, 1994). The bands located in the region ~800 cm^{-1} to ~1200 cm^{-1} have been investigated in most detail as these arise from combinations of chain backbone modes, in particular the (C-O-C) stretching vibration, and the ethylene rocking modes and are most likely to be susceptible to hydrogen bonding effects (Maxfield & Shepherd, 1975). The PEO Raman band located at ~864 cm^{-1} is found to shift towards a lower wavenumber position (~860 cm^{-1}) in the HDPE-PEO/cCNCs composites while the band located at ~847 cm^{-1} remained unchanged. The Raman band located at ~864 cm^{-1} corresponds to a combination of symmetric CH_2 rocking and symmetric C-O-C stretching modes (Koduru *et al.*, 2017; Richard-lacroix & Pellerin, 2017). The vibration of this band is expected to be sensitive to hydrophobic as well as hydrogen bonding interactions, since it involves the oxygen atom in the PEO backbone chain (Maxfield & Shepherd,

1975). Additionally, the formation of hydrogen bonds is also supported by a shift of the Raman band located at ~1068 cm^{-1}, which is also related to the symmetric C-O-C stretching mode of the backbone chain (Maxfield & Shepherd, 1975). This Raman band however overlaps with the bands characteristic of HDPE and CNCs, which makes it difficult to assign its exact position. A shift in the position of the Raman bands corresponding to CNCs in the CNCs/PEO/HDPE composites is also observed. Bands centered at ~901 and ~1101 cm^{-1} shifted towards lower number positions (899 cm^{-1} and 1098 cm^{-1} respectively). Although, these bands correspond to the vibrational modes not directly involved in the formation of hydrogen bonds, their position is sensitive to the deformation of the of cellulose chains, which may arise from their formation. Additionally, there is a shift in the Raman band position, initially located at ~383 cm^{-1}, which arises from bonds that are in the same orientation as the moieties giving rise to the band located at ~1101 cm^{-1} (Agarwal & Atalla, 1986). This shift indicates the effects of the CNCs on the PEO matrix through hydrogen bonding.

5.2 ATR-FTIR Spectroscopy

To further investigate the esterification reaction between CNCs and MAPE, the formation of interfacial bonds in the system was further corroborated using infrared spectroscopy. This technique is commonly used for ester analysis in cellulose reinforced polymer composites (Carlborn & Matuana, 2006; Paunikallio, Kasanen, Suvanto, & Pakkanen, 2003; Spinella *et al.*, 2015).

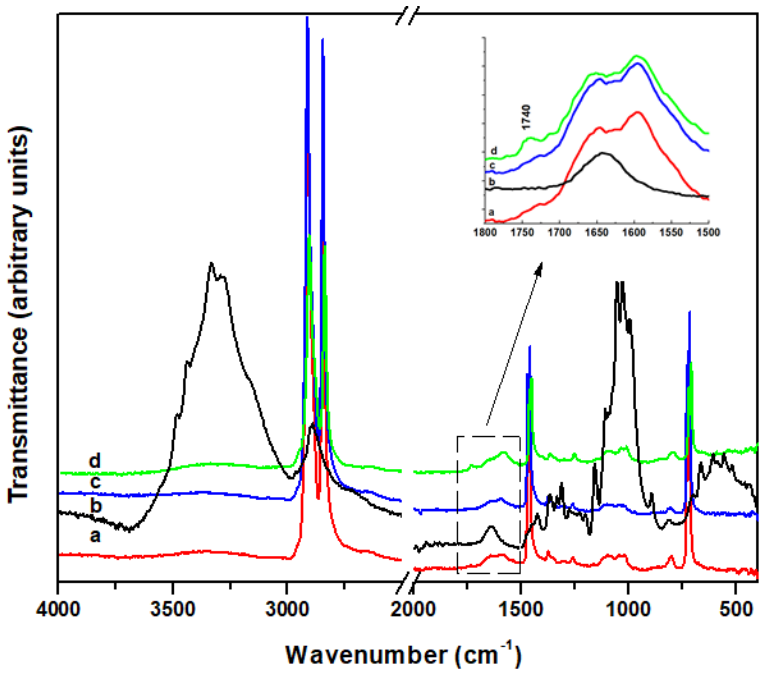

Figure 5.3 ATR-FTIR spectra of cCNCs reinforced HDPE nanocomposites (a) neat HDPE, (b) cCNCs (c) HDPE-cCNCs1.5 and (d) HDPE-MAPE/cCNCs1.5.

The ATR-FTIR spectra of HDPE, HDPE-cCNCs1.5 and HDPE-MAPE/cCNCs1.5 nanocomposites are presented in Figure 5.3. In comparison to HDPE and HDPE-cCNCs1.5 nanocomposites, the appearance of an absorption band at 1740 cm^{-1} can be seen in the HDPE-MAPE/cCNCs1.5 nanocomposite spectra. This is assigned to the C=O stretching of the carbonyl group in the ester bond by an esterification reaction of the hydrophobic MAPE onto hydroxyl group of CNCs (Kim *et al.*, 2006; Smita Mohanty, Verma, & Nayak, 2006; Qiu *et al.*, 2004). Figure 5.4A shows the typical ATR-IR spectra obtained from HDPE, HDPE- MAPE/cCNCs0.5, HDPE-MAPE/cCNCs1.5, HDPE-MAPE/cCNCs2.5 and HDPE-MAPE/cCNCs5. To estimate the extent of the ester band,I_1 was normalised against the intensity of the absorption band (I_2) corresponding to the CH_2 deformation, which is located around 1462 cm^{-1} (Martinez-Romo, González-Mota, Soto-Bernal, & Rosales-Candelas, 2015). The

percentage of the intensity ratios (I_1/I_2) are shown in Figure 5.4B. From these results, the incorporation of CNCs increases the intensity ratio of the nanocomposites. Thus, the degree of esterification was strongly determined by the amount of the nanocellulose present; more CNCs led to higher free hydroxyl rich surface of CNCs forming ester bonds with MAPE. Similar observations were reported for tCNCs reinforced HDPE composites samples.

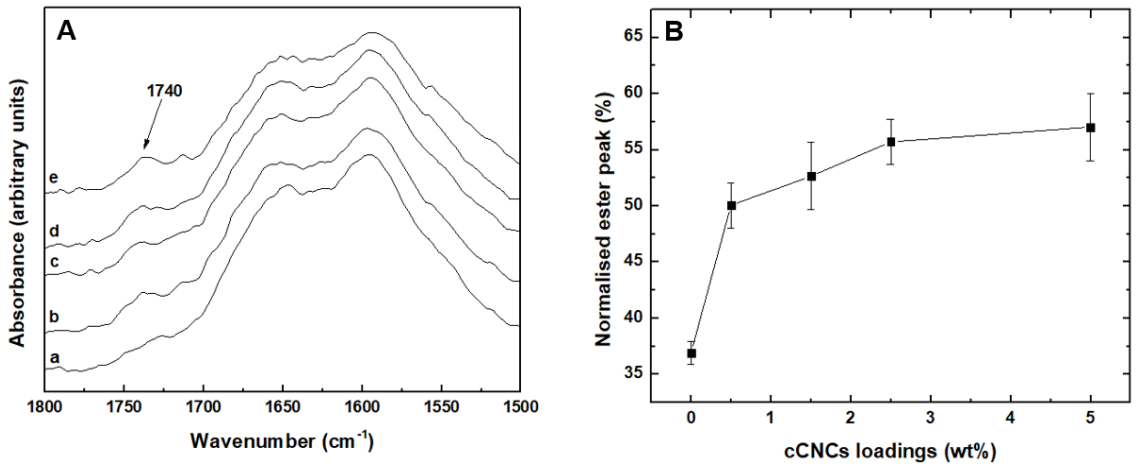

Figure 5.4 (A)Typical ATR-FTIR spectra obtained from (a) HDPE, (b) HDPE-MAPE/cCNCs0.5, (c) HDPE-MAPE/cCNCs1.5, (d) HDPE-MAPE/cCNCs2.5, (e) HDPE-MAPE/cCNCs5 and (B) Intensity ratio of HDPE-MAPE/cCNCs nanocomposites at different cCNCs loadings.

5.3 Crystallisation and Melt Behaviour of the Nanocomposites

5.3.1 Crystallisation and Melt Behaviour of cCNCs Reinforced HDPE Nanocomposites

Crystallinity of the matrix, as affected by the incorporation of the filler material, is an important characteristic influencing the mechanical properties of nanocomposites.

The crystallisation behaviour of HDPE in the nanocomposites was investigated using DSC. The DSC curves of HDPE and HDPE-cCNCs nanocomposites at weight fractions of 0.5 wt.%, 1.5 wt.%, 2.5 wt.% and 5 wt.% cCNCs are shown in Figure 5.5. Characteristic temperatures such as the crystallization temperature (T_c) and the melt temperature (T_m) are tabulated in Table 5.1, along with the degree of crystallinity of the matrix and the nanocomposites. From Table 5.1, the cooling curves showed that HDPE crystallised at 116°C and the inclusion of cCNCs and compatibilisers did not change the crystallization temperature of the nanocomposites. Pure HDPE undergoes melting at 130°C; it was observed that the melting temperature of the composites did not seem to be affected by the addition of the cCNCs and compatibilisers.

The percentage crystallinity of the matrix showed that the crystallinity of the HDPE (~62%) has comparable values to those reported in the literature (Araujo *et al.*, 2008; Kodjie *et al.*, 2006). The addition of cCNCs to the matrix increases the crystallinity of the samples at low filler loadings. The crystallisation of matrix in the nanocomposites was found to increase, as expected probably due to the crystal nucleation of polymer influenced by the presence of CNCs crystallites. A similar effect has been reported in the literature (de Menezes *et al.*, 2009; Nagalakshmaiah *et al.*, 2016; Pereda *et al.*, 2014). This effect is typically observed for CNCs reinforced semi-crystalline polymers and is generally attributed to a nucleating effect of the cellulosic nanoparticle (Hossain *et al.*, 2012). However, for higher cCNCs contents (2.5 and 5 wt.%), the degree of crystallinity of HDPE decreased and exhibited lower

values than that of the neat matrix. This could possibly be the result of aggregation of the cCNCs and a limited filler/matrix interface.

Table 5.1 Crystallisation temperature (T_c), melting temperature (T_m) and the crystallinity (χ_c) for HDPE, HDPE-MAPE, HDPE-PEO, HDPE-cCNCs, HDPE-MAPE/cCNCs and HDPE-PEO/cCNCs at weight fractions of 0.5, 1.5, 2.5, 5 wt.%. Error reports are standard deviations from the mean.

Material	First heating data		Second heating data		
	T_m (°C)	χ_c (%)	T_c (°C)	T_m (°C)	χ_c (%)
HDPE	131.6 ± 0.6	60.9 ± 0.5	116.4 ± 0.1	130.5 ± 0.7	61.7 ± 0.6
HDPE-MAPE	131.9 ± 0.8	61.6 ± 0.8	116.4 ± 0.4	131.2 ± 0.6	62.2 ± 0.6
HDPE-PEO	131.7 ± 0.6	61.9 ± 0.6	116.3 ± 0.3	131.1 ± 0.8	62.7 ± 0.8
HDPE-cCNCs0.5	131.1 ± 0.3	62.7 ± 0.7	116.4 ± 0.3	130.2 ± 0.4	63 ± 0.5
HDPE-cCNCs1.5	131.8 ± 0.4	63.5 ± 0.3	116.7 ± 0.1	130.6 ± 0.7	64.8 ± 0.5
HDPE-cCNCs2.5	131.2 ± 0.2	57.9 ± 0.6	116.5 ± 0.2	130.5 ± 0.5	59.3 ± 0.7
HDPE-cCNCs5	131.3 ± 0.5	56.9 ± 0.4	116.2 ± 0.1	131.2 ± 0.4	58.9 ± 0.2
HDPE-MAPE/cCNCs0.5	132.4 ± 0.6	63.5 ± 0.6	116.7 ± 0.4	130.4 ± 0.7	64.8 ± 0.8
HDPE-MAPE/cCNCs1.5	131.7 ± 0.5	65.1 ± 0.4	117.1 ± 0.1	129.7 ± 0.1	66 ± 0.7
HDPE-MAPE/cCNCs2.5	132.1 ± 0.6	63.3 ± 0.7	116.9 ± 0.2	129.9 ± 0.4	64.3 ± 0.5
HDPE-MAPE/cCNCs5	132.1 ± 0.7	62.7 ± 0.6	116.7 ± 0.1	130.1 ± 0.5	63.4 ± 0.5
HDPE-PEO/cCNCs0.5	131.6 ± 0.8	64.8 ± 0.4	116.9 ± 0.1	130.8 ± 0.3	65.9 ± 0.5
HDPE-PEO/cCNCs1.5	131.3 ± 0.5	65.8 ± 0.4	117.4 ± 0.4	131.2 ± 0.2	66.9 ± 0.5
HDPE-PEO/cCNCs2.5	132.2 ± 0.6	64.1 ± 0.3	116.8 ± 0.1	131.3 ± 0.5	65 ± 0.2
HDPE-PEO/cCNCs5	132.6 ± 0.4	63.8 ± 0.2	116.9 ± 0.1	131.2 ± 0.3	64.5 ± 0.7

With the addition of compatibilisers, an increase in crystallinity was observed in HDPE-MAPE/cCNCs and HDPE-PEO/cCNCs nanocomposites compared to HDPE-cCNCs nanocomposites. This behaviour is in agreement with previous work for polyethylene film reinforced with unmodified-CNCs and PEO-modified CNCs composites (Pereda *et al.*, 2014). Statistical significances (P-values) based on *t*-tests have been calculated to compare the crystallinity values of HDPE, HDPE-cCNCs,

HDPE-MAPE/cCNCs and HDPE-PEO/cCNCs nanocomposites. If an acceptable level of significance is $p < 0.05$ (>95% confidence), the P-values of the crystallinity of the nanocomposites with the same CNCs loadings (1.5 wt.%) are 0.04 for HDPE-cCNCs1.5, 0.03 for HDPE-MAPE/cCNCs1.5 and 0.03 for HDPE-PEO/cCNCs1.5 with respect to the HDPE. Therefore, it can be concluded that the presence of filler and both compatibilisers significantly enhances the crystallinity of the nanocomposites. At higher cCNCs contents (2.5 wt.% and 5 wt.%), the degree of crystallinity of HDPE-MAPE/cCNCs and HDPE-PEO/cCNCs exhibited higher values than that of HDPE-cCNCs nanocomposites.

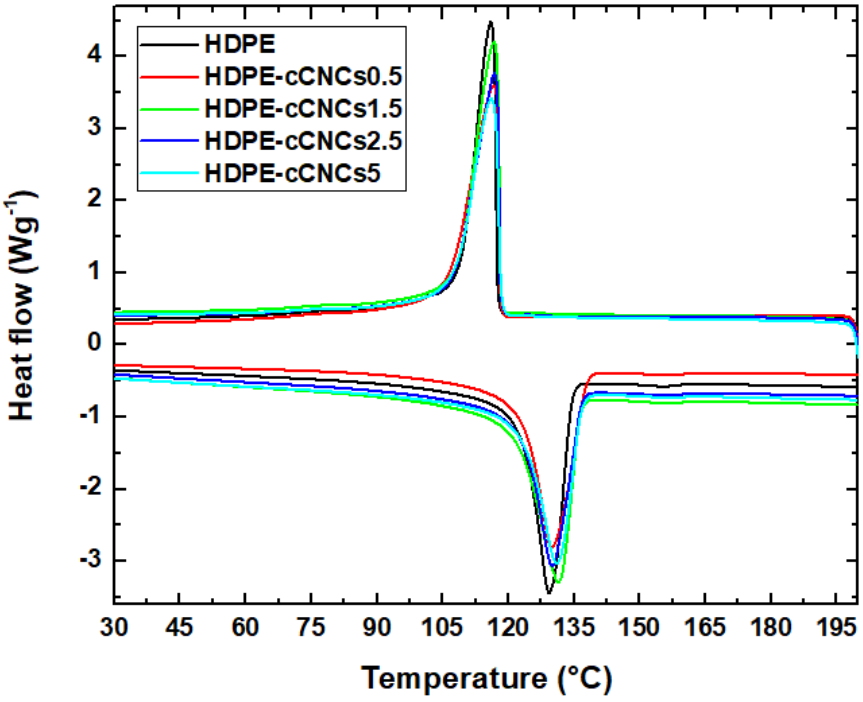

Figure 5.5 Differential scanning calorimetry curves for the second heating cycle and one cooling cycle of HDPE and HDPE-cCNCs nanocomposites at weight fractions of 0.5 wt.%, 1.5 wt.%, 2.5 wt.% and 5 wt.% cCNCs.

5.3.2 Crystallisation and Melt Behaviour of tCNCs Reinforced HDPE Nanocomposites

The DSC curves of HDPE and HDPE-tCNCs nanocomposites at weight fractions of 0.5 wt.%, 1.5 wt.%, 2.5 wt.% and 5 wt.% tCNCs are shown in Figure 5.6. Characteristic temperatures, such as crystallization temperature (T_c) and melt temperature (T_m) are tabulated in Table 5.2, along with the degree of crystallinity of the matrix and the nanocomposites. Similar results with cCNCs reinforced HDPE were observed; the addition of tCNCs into the matrix did not affect the values of T_c and T_m for these nanocomposites. The degree of crystallinity of the HDPE matrix was found to increase with an increase in the tCNCs content. Similarly, the crystallinity did not increase at a weight fraction of 2.5 wt.% and 5 wt.% for both cCNCs and tCNCs samples. This was possibly due to aggregation of both forms of CNCs at higher weight fractions. As it can be seen, the crystallinity of the samples reinforced with tCNCs is slightly higher than the cCNCs samples, reflecting a higher crystallinity of tCNCs (72.7%) compared to cCNCs (67.1%), as shown in Section 4.3.2.

Table 5.2 Crystallisation temperature (T_c), melting temperature (T_m) and the crystallinity ($\mathcal{X}_c$) for HDPE, HDPE-MAPE, HDPE-PEO, HDPE-tCNCs, HDPE-MAPE/tCNCs and HDPE-PEO/tCNCs at weight fractions of 0.5, 1.5, 2.5, 5 wt.%. Error reports are standard deviations from the mean.

Material	First heating data		Second heating data		
	T_m (°C)	$\mathcal{X}_c$ (%)	T_c (°C)	T_m (°C)	$\mathcal{X}_c$ (%)
HDPE	131.6 ± 0.6	60.9 ± 0.5	116.4 ± 0.1	130.5 ± 0.3	61.7 ± 0.6
HDPE-MAPE	131.9 ± 0.8	61.6 ± 0.8	116.4 ± 0.4	131.2 ± 0.6	62.2 ± 0.6
HDPE-PEO	131.7 ± 0.6	61.9 ± 0.6	116.3 ± 0.3	131.1 ± 0.8	62.7 ± 0.8
HDPE-tCNCs0.5	132.2 ± 0.4	63.6 ± 0.5	117.2 ± 0.3	131.6 ± 0.3	64.2 ± 0.5

HDPE-tCNCs1.5	132.1 ± 0.6	64.5 ± 0.3	116.7 ± 0.7	132.3 ± 0.4	65.4 ± 0.6
HDPE-tCNCs2.5	131.2 ± 0.5	62.2 ± 0.5	116.7 ± 0.2	132.4 ± 0.5	64.5 ± 0.4
HDPE-cCNCs5	131.7 ± 0.5	60.9 ± 0.6	116.7 ± 0.5	132 ± 0.4	62 ± 0.4
HDPE-MAPE/tCNCs0.5	132.2 ± 0.5	64.1 ± 0.6	117.1 ± 0.4	132.1 ± 0.7	65.1 ± 0.2
HDPE-MAPE/tCNCs1.5	131.7 ± 0.5	65.2 ± 0.4	117.2 ± 0.2	131.2 ± 0.4	66.1 ± 0.2
HDPE-MAPE/tCNCs2.5	131.9 ± 0.3	64.7 ± 0.5	117.5 ± 0.3	131.7 ± 0.5	66 ± 0.4
HDPE-MAPE/tCNCs5	131.1 ± 0.7	63.7 ± 0.5	117.4 ± 0.1	131.1 ± 0.2	65.1 ± 0.4
HDPE-PEO/tCNCs0.5	132.4 ± 0.6	65.5 ± 0.4	117.3 ± 0.4	132.1 ± 0.2	66.4 ± 0.5
HDPE-PEO/tCNCs1.5	131.7 ± 0.5	67.7 ± 0.5	117.1 ± 0.7	131.5 ± 0.5	68.2 ± 0.2
HDPE-PEO/tCNCs2.5	132.1 ± 0.2	66.3 ± 0.4	117.4 ± 0.4	132.2 ± 0.2	67 ± 0.5
HDPE-PEO/tCNCs5	132.4 ± 0.7	64.7 ± 0.6	117.1± 0.1	131 ± 0.3	66.5 ± 0.5

Similarly, the addition of tCNCs and both compatibilisers increases in crystallinity of nanocomposites compared to HDPE matrix. The P-values of the crystallinity of the nanocomposites with the same tCNCs loadings (1.5 wt.%) are 0.03 for HDPE-tCNCs, 0.03 for HDPE-MAPE/tCNCs and 0.02 for HDPE-PEO/tCNCs with respect to the HDPE. The crystallinity of tCNCs reinforced HDPE nanocomposites are noted to have a higher crystallinity than the cCNCs reinforced HDPE nanocomposites owing to the greater nucleating effect of tCNCs on the matrix. This is thought to be mainly credited to their higher aspect ratio (~60.7 vs ~16.3), resulting in an increased surface area interacting with the polymer. The crystallinity of nanocellulose is critical because it is directly related to modulus, and an increased modulus is often desirable in the preparation of composites. TCNCs have been shown to have higher modulus compared to cCNCs (Iwamoto *et al.*, 2009; Rusli & Eichhorn, 2008; Šturcová *et al.*, 2005). It has also been shown that the higher modulus fibres, the more crystalline the sample and that the crystalline domains are often more oriented (Rusli & Eichhorn, 2008).

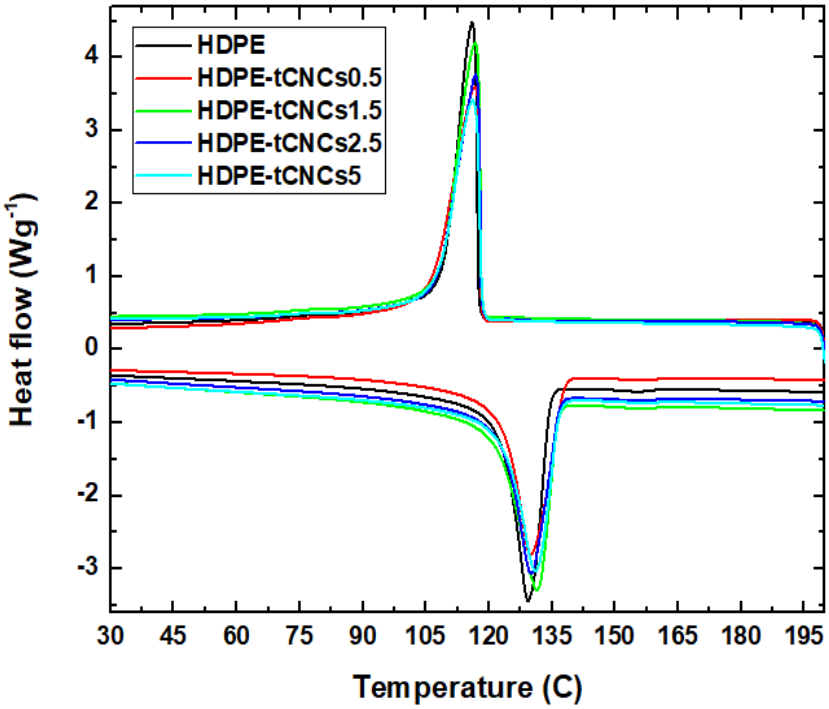

Figure 5.6 Differential scanning calorimetry curves for the second heating cycle and one cooling cycle of HDPE and HDPE-tCNCs nanocomposites at weight fractions of 0.5 wt.%, 1.5 wt.%, 2.5 wt.% and 5 wt.% tCNCs.

5.4 Thermal Degradation Behaviour of the Nanocomposites

5.4.1 Thermal Degradation Behaviour of cCNCs Reinforced HDPE Nanocomposites

Weight losses and derivatives of the weight (DTG) thermographs of the HDPE, HDPE-cCNCs, HDPE-MAPE/cCNCs and HDPE-PEO/cCNCs nanocomposites are shown in Figure 5.7 and 5.8. The HDPE weight loss occurred in a one-step degradation process from 400 to 520 °C (Figure 5.7a). This result is confirmed by the presence of only one peak at 483.8 °C on the DTG curve (Figure 5.8a). The

single step weight loss process of HDPE has also been observed previously (Araujo *et al.*, 2008; Kodjie *et al*., 2006; Smita Mohanty *et al.*, 2006). The thermal degradation of all HDPE-cCNCs, HDPE-MAPE/cCNCs and HDPE-PEO/cCNCs nanocomposites composites occurred in a two-step process (Figure 5.7). The first degradation step, from 200 to 400 °C, can be attributed to the decomposition of the cellulose fibres and is confirmed by the presence of two peaks on the DTG curve (Figure 5.8). The second degradation step, from 400 to 520 °C, can be assigned to the decomposition of the HDPE polymeric matrix. Similar findings have also been observed previously (Haddar, Elloumi, Koubaa, & Bradai, 2017; Smita Mohanty, Verma, Nayak, & Tripathy, 2004). All TGA curves shows the increasing mass as a function of temperature before the degradation step.

Table 3 shows the initial degradation temperature (T_{onset}) and the maximum degradation temperature (DTG_{max}) for HDPE, HDPE-cCNCs, HDPE-MAPE/cCNCs and HDPE-PEO/cCNCs nanocomposites. The onset of degradation of HDPE was observed at 455.4 °C (defined as temperature at which 5% mass loss occurred), with maximum degradation occurring at 483.8 °C. The onset degradation temperature of the nanocomposites was found to decrease as the cCNCs loadings increase compared to the pure polymer matrix. The low degradation temperatures of cCNCs are due to the cellulose component which have low decomposition temperatures. As a result; filler content with low degradation temperatures reduces thermal stability of the nanocomposites. A similar effect has been reported in the literature (Ambrosio-Martin, Fabra, Lopez-Rubio, & Lagaron, 2015; Mokhena & Luyt, 2014). These nanocomposites also exhibited a decrease in the onset degradation temperature

with the addition of CNCs. Another possibility is due to the presence of sulfate half ester groups on the cCNCs, resulting in significantly lower onset degradation temperatures of cCNCs compared to the matrix, as presented in Section 4.5.3. On the other hand, addition of MAPE and PEO compatibiliser to the nanocomposite with different filler loading levels (0, 1.5, 2.5 and 0.5 wt.%) decreased the onset degradation temperature of the nanocomposite samples.

It is worth noticing that the onset degradation temperature of the HDPE-PEO composites increases from 446.1 °C to 450.8 °C when reinforced with 0.5 wt.% cCNCs. This increase is possibly due to an improved heat resistance of cCNCs when compatibilised with PEO, as presented in Section 4.5.3. A protecting role of the interacting PEO chains, shielding the surface sulfate groups of cCNCs is suspected to be a reason for this. At higher cCNCs concentrations, a decrease in the onset degradation temperature of nanocomposites was observed. This is expected, since the CNCs should decompose before the HDPE matrix. At lower loadings of cCNCs (0.5 wt.%), the onset degradation temperature of the HDPE-MAPE/cCNCs nanocomposites was found not to be affected by the addition of cCNCs compared to HDPE-MAPE composites. Similar to HDPE-PEO/cCNCs, the addition of cCNCs at higher loadings leads to a decreased onset degradation temperature of nanocomposites. All nanocomposites exhibited similar maximum degradation temperatures as the HDPE matrix. There appears to have little effect on this temperature either, with an increase in the cCNCs contents or with the addition of compatibilisers on the thermal stability of the nanocomposites.

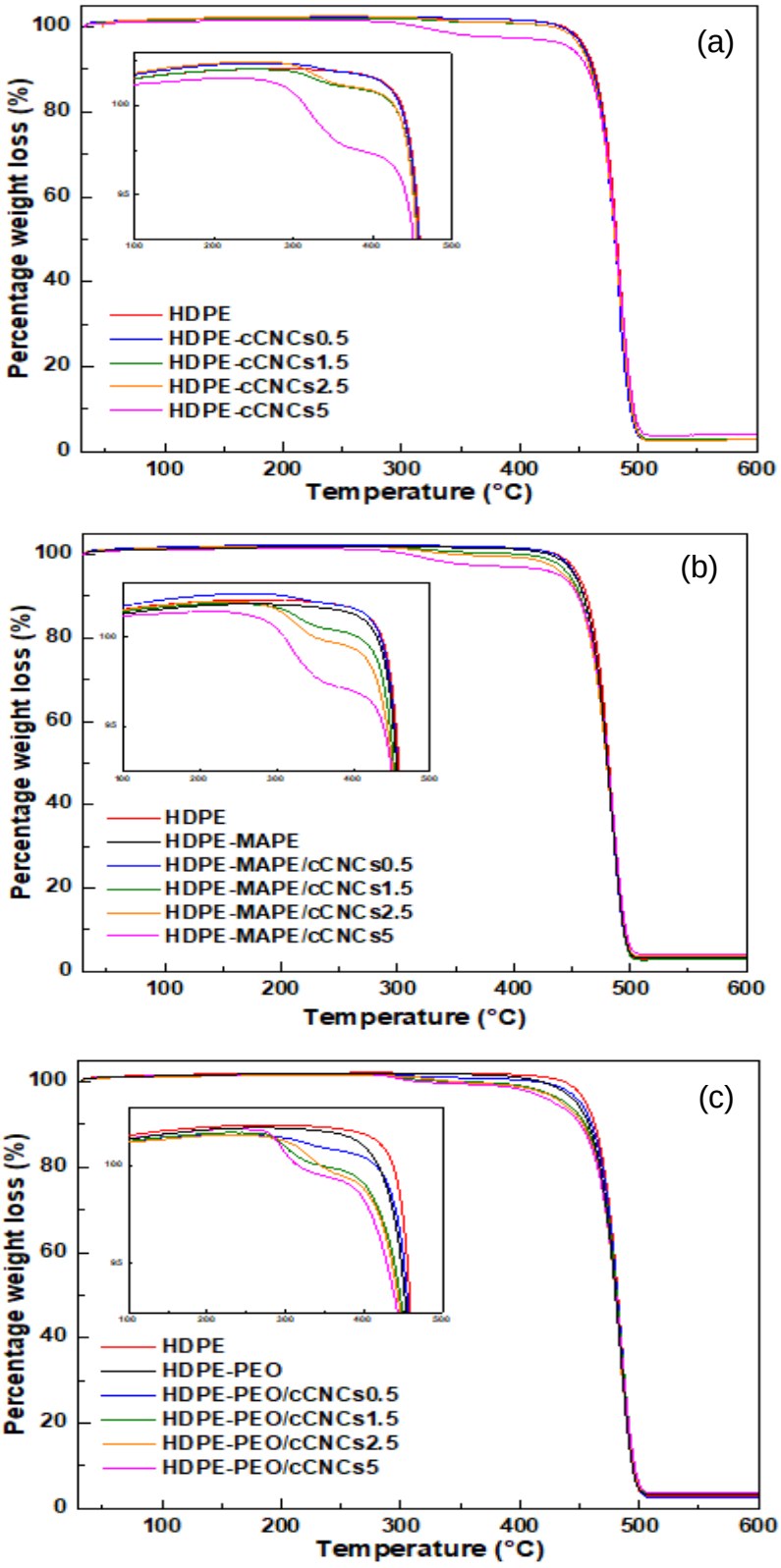

Figure 5.7 TGA curves of (a) HDPE-cCNCs, (b) HDPE-MAPE/cCNCs and (c) HDPE-PEO/cCNCs nanocomposites at weight fractions of 0.5, 1.5, 2.5, 5 wt.%.

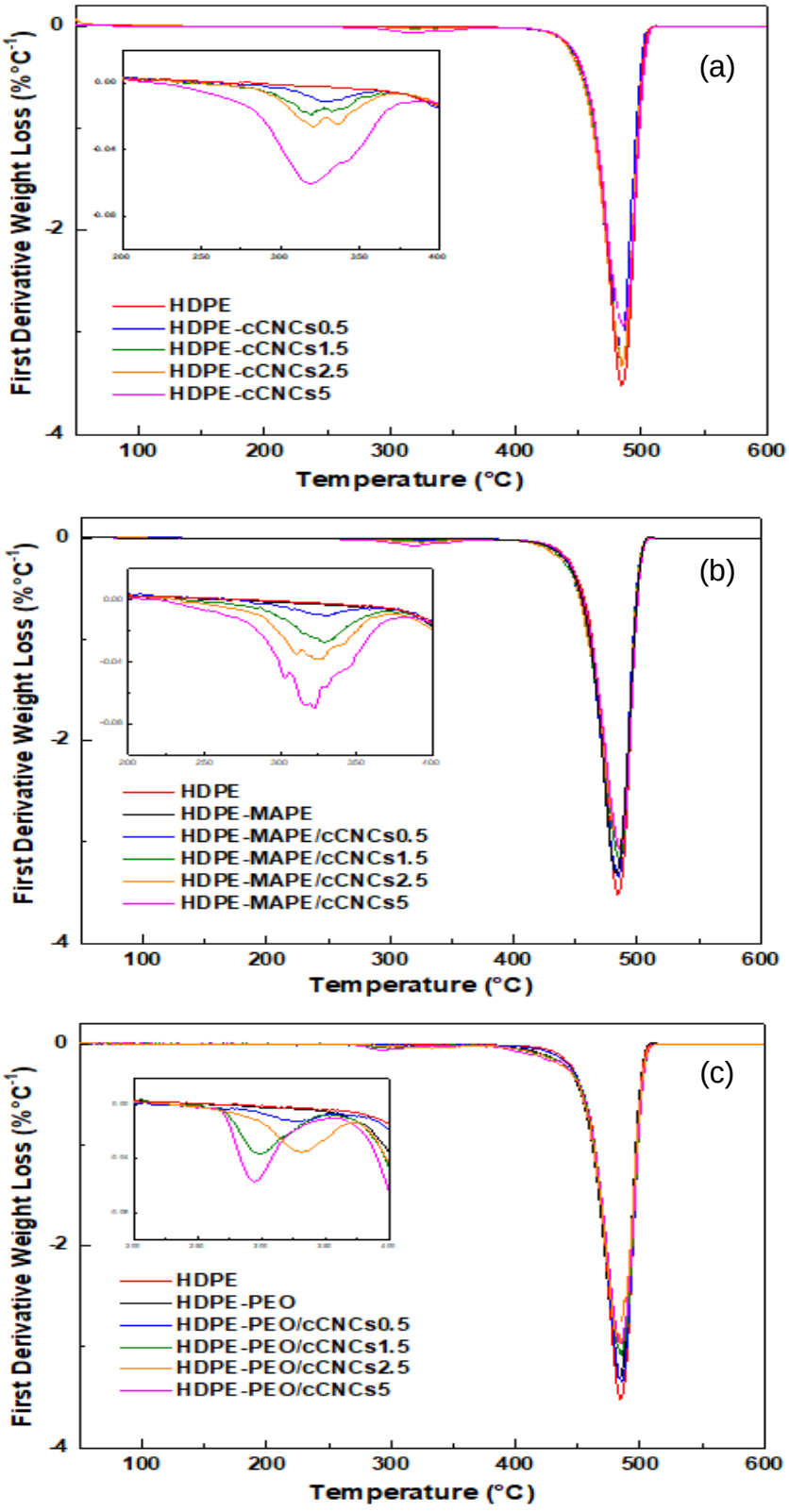

Figure 5.8 DTG curves of (a) HDPE-cCNCs, (b) HDPE-MAPE/cCNCs and (c) HDPE-PEO/cCNCs nanocomposites at weight fractions of 0.5, 1.5, 2.5, 5 wt.%.

Table 5.3 Onset degradation and maximum degradation temperature of HDPE-cCNCs, HDPE-MAPE/cCNCs and HDPE-PEO/cCNCs nanocomposites at weight fractions of 0.5, 1.5, 2.5, 5 wt.%.

Material	T_{onset} (°C)	DTG_{max} (°C) in first degradation step	DTG_{max} (°C) in second degradation step
HDPE	455.4 ± 1.7	-	483.8 ± 0.8
HDPE-MAPE	452.5 ± 2.1	-	484.4 ± 0.5
HDPE-PEO	446.1 ± 1.5	-	484.1 ± 0.9
HDPE-cCNCs0.5	454.0 ± 2.4	328.2 ± 0.7	484 ± 0.8
HDPE-cCNCs1.5	451.9 ± 1.8	326 ± 0.9	483.3 ± 1.3
HDPE-cCNCs2.5	451.1 ± 1.4	323 ± 1.2	482.8 ± 0.7
HDPE-cCNCs5	442.3 ± 1.9	318.3 ± 1.6	483.1 ± 0.9
HDPE-MAPE/cCNCs0.5	452.9 ± 1.9	330.8 ± 0.8	484.6 ± 0.5
HDPE-MAPE/cCNCs1.5	447.9 ± 1.2	328.2 ± 0.8	483.8 ± 0.8
HDPE-MAPE/cCNCs2.5	444.2 ± 1.8	325 ± 1.5	483.3 ± 0.4
HDPE-MAPE/cCNCs5	439.0 ± 1.9	321 ± 1.2	483.2 ± 0.5
HDPE-PEO/cCNCs0.5	450.8 ± 2.3	326.4 ± 0.9	484.1 ± 0.9
HDPE-PEO/cCNCs1.5	439.2 ± 1.6	330 ± 1.2	483.4 ± 0.5
HDPE-PEO/cCNCs2.5	435.6 ± 1.8	299.2 ± 1.1	484 ± 0.8
HDPE-PEO/cCNCs5	429.1 ± 1.7	294 ± 1.3	483 ± 0.7

5.4.2 Thermal Degradation Behaviour of tCNCs Reinforced HDPE Nanocomposites

Weight losses and derivatives of the weight (DTG) thermographs of the HDPE, HDPE-tCNCs, HDPE-MAPE/tCNCs and HDPE-PEO/tCNCs nanocomposites are shown in Figure 5.9 and 5.10. The thermal degradation of all HDPE-tCNCs, HDPE-MAPE/tCNCs and HDPE-PEO/tCNCs nanocomposites composites occurred in a two-step degradation process (Figure 5.9). The first degradation step, from 200 to 400 °C, can be attributed to the decomposition of the cellulose fibres and is confirmed by the presence of two peaks on the DTG curve (Figure 5.10). The second degradation step, from 400 to 520 °C, can be assigned to the decomposition of the HDPE polymeric matrix.

Table 4 shows the initial degradation temperature (T_{onset}) and the maximum degradation temperature (DTG_{max}) for HDPE, HDPE-tCNCs, HDPE-MAPE/tCNCs and HDPE-PEO/tCNCs nanocomposites. As seen from the results, the addition of tCNCs and both compatibilisers to the HDPE matrix leads to a reduction in the onset temperature of the nanocomposites; similar results have been reported for cCNCs reinforced HDPE nanocomposites. As already mentioned, the onset degradation temperature of nanocomposites decreased probably due to the lower onset degradation temperatures for tCNCs, HDPE-MAPE and HDPE-PEO themselves, compared to HDPE. The onset degradation temperature of the HDPE-PEO/tCNCs nanocomposites increases from 446.1 °C to 451.0 °C compared to the HDPE-PEO when reinforced with 0.5 wt.% tCNCs. At higher concentrations, a decrease in the onset degradation temperature of nanocomposites was observed. The maximum

degradation temperature of the nanocomposites on the other hand was not affected by the addition of tCNCs, and both compatibilisers, when compared to neat HDPE.

In comparison, the onset degradation temperature of tCNCs reinforced HDPE nanocomposites are noted to have higher values than the cCNCs reinforced HDPE nanocomposites. This increase is thought to be due to the higher crystallinity and aspect ratio of tCNCs compared to cCNCs (as presented in Section 4.5 and 4.6), leading to better reinforcing effects and interactions between the filler and matrix (Um *et al.*, 2004)

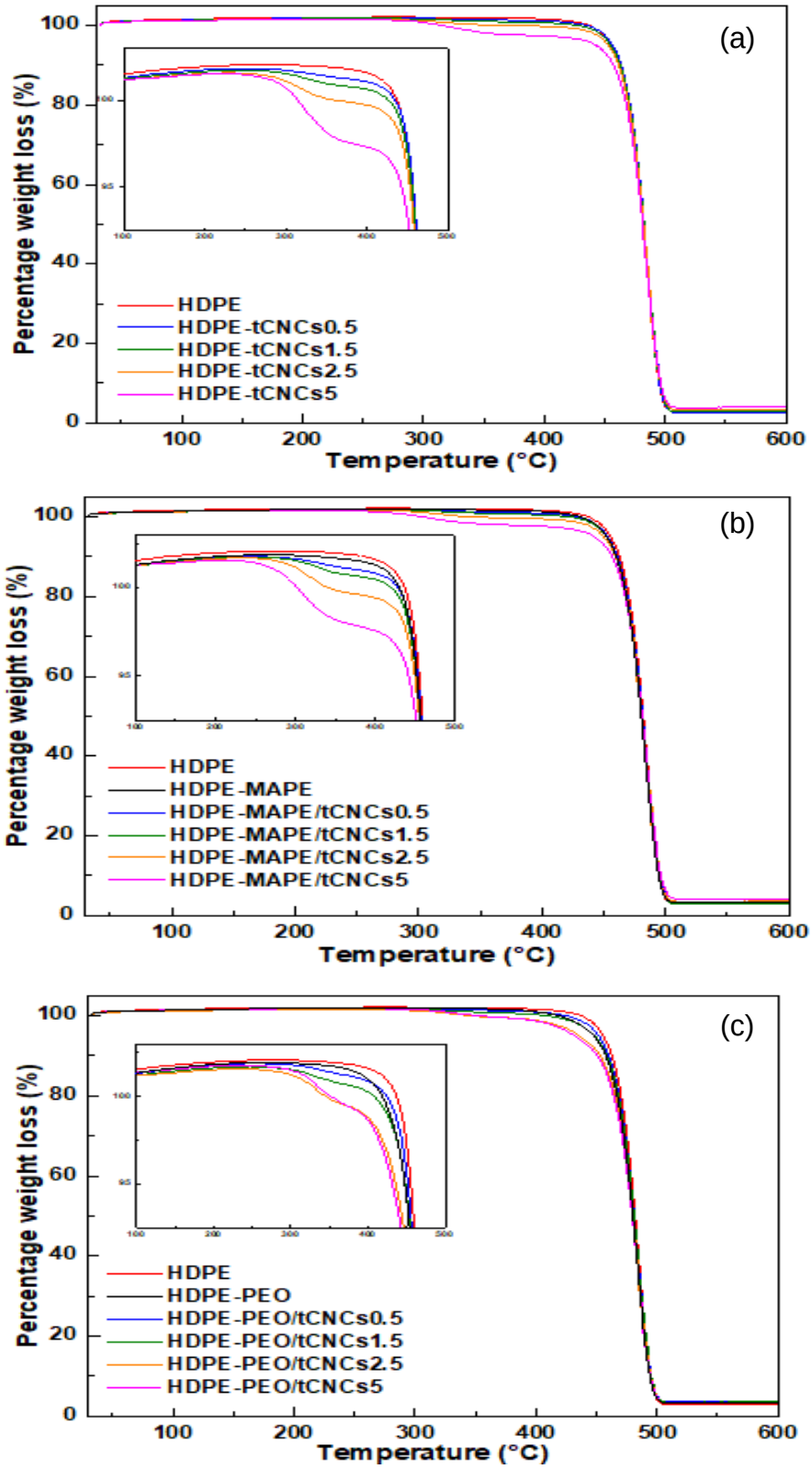

Figure 5.9 TGA curves of (a) HDPE-tCNCs, (b) HDPE-MAPE/tCNCs and (c) HDPE-PEO/tCNCs nanocomposites at weight fractions of 0.5, 1.5, 2.5, 5 wt.%.

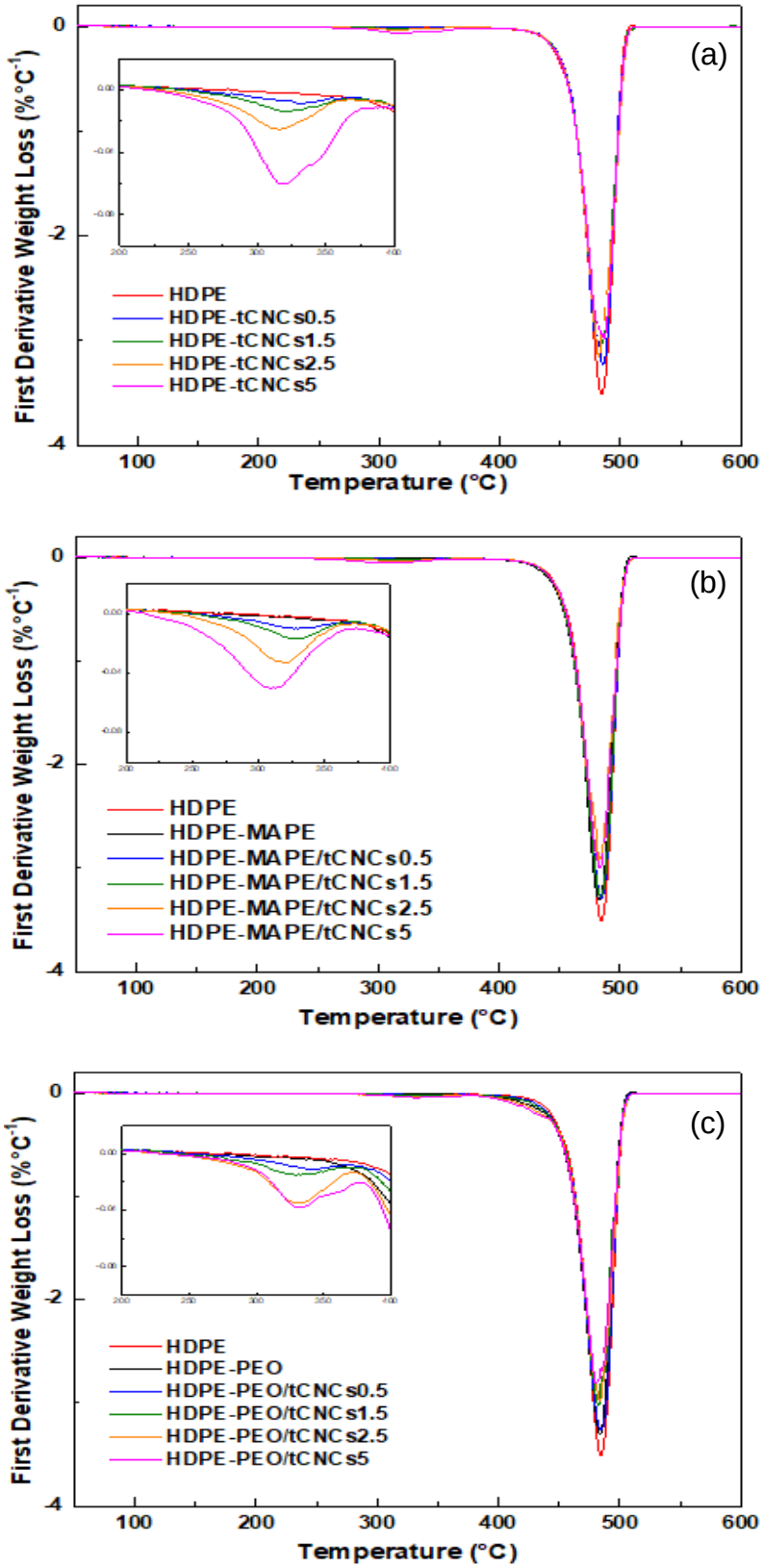

Figure 5.10 DTG curves of (a) HDPE-tCNCs, (b) HDPE-MAPE/tCNCs and (c) HDPE-PEO/tCNCs nanocomposites at weight fractions of 0.5, 1.5, 2.5, 5 wt.%.

Table 5.4 Onset degradation and maximum degradation temperature of HDPE-tCNCs, HDPE-MAPE/tCNCs and HDPE-PEO/tCNCs nanocomposites at weight fractions of 0.5, 1.5, 2.5, 5 wt.%.

Material	T_{onset} (°C)	DTG_{max} (°C) in first degradation step	DTG_{max} (°C) in second degradation step
HDPE	455.4 ± 1.7	-	483.8 ± 0.8
HDPE-MAPE	452.5 ± 2.1	-	484.4 ± 0.5
HDPE-PEO	446.1 ± 1.5	-	484.1 ± 0.9
HDPE-tCNCs0.5	456.3 ± 2.3	328 ± 0.8	484 ± 0.5
HDPE-tCNCs1.5	454.3 ± 2.4	321.4 ± 1.1	483.3 ± 0.8
HDPE-tCNCs2.5	452.8 ± 1.9	317.2 ± 1.1	483.6 ± 0.4
HDPE-cCNCs5	442.8 ± 2.5	316.7 ± 1.6	483.2 ± 0.9
HDPE-MAPE/tCNCs0.5	452.9 ± 1.9	327.8 ± 0.7	484.5 ± 0.9
HDPE-MAPE/tCNCs1.5	452.1 ± 2.4	325 ± 1.0	484.1 ± 1.2
HDPE-MAPE/tCNCs2.5	449.7 ± 2.1	318.2 ± 0.9	484.4 ± 0.5
HDPE-MAPE/tCNCs5	442.3 ± 2.5	310 ± 1.5	483.2 ± 0.7
HDPE-PEO/tCNCs0.5	451.0 ± 2.1	339.7 ± 0.9	484.1 ± 1
HDPE-PEO/tCNCs1.5	447.8 ± 1.9	333.9 ± 1.1	483.4 ± 0.8
HDPE-PEO/tCNCs2.5	435.6 ± 2.5	331.4 ± 0.9	484 ± 0.6
HDPE-PEO/tCNCs5	431.6 ± 2.6	331 ± 1.2	483.4 ± 0.7

5.5 Mechanical Properties of Nanocomposites

5.5.1 Stress Strain Behaviour of cCNCs Reinforced HDPE Nanocomposites

Typical stress-strain curves of HDPE and HDPE-cCNC composites films with a variation of weight fractions of cCNCs from 0.5 wt.% to 5 wt.% are shown in Figure

5.11a. Figure 5.11b display the typical stress-strain curves of HDPE, HDPE-MAPE, HDPE-PEO, HDPE-cCNCs, HDPE-MAPE/cCNCs and HDPE-PEO/cCNCs at weight fractions of 1.5 wt.% cCNCs. All curves indicate characteristic non-linear stress-strain behaviour. This non-linearity is typical for a polymer film, as has been previously reported for polymer films made using this method (Morais, Gadioli, De Paoli, & Paoli, 2016). Detailed mechanical properties are reported in Table 5.5. In order to measure the stiffness of the materials, Young's moduli were obtained from the slope of the initially linear portion of the stress-strain curve, up to a value of about 1% strain. The mechanical properties of a film of pure matrix material are similar to values obtained in previous work (Haddar *et al.*, 2017; Kahar, Sarifuddin, & Ismail, 2017; Sepet, Tarakcioglu, & Misra, 2016). One can observe that the addition of compatibilising agent does not seem to affect the Young`s modulus and tensile strength of the HDPE. However, a significant drop in strain at break was seen in HDPE-MAPE and PEO-MAPE composites, as shown in Table 5.5

Tensile tests of unmodified HDPE-cCNCs nanocomposite samples reveal an increase in Young's modulus and tensile strength with an increase in the weight fractions of cotton CNCs, whereas the strain at break (%) decreased. The mean values of the moduli of the nanocomposites increase by 3.4% and 6% (compared to the HDPE modulus) when reinforced with 0.5 wt.% and 1.5 wt.% cCNCs, respectively. As predicted, based on the rule-of-mixtures for composite materials, the introduction of stiff cCNCs into a softer HDPE polymer matrix improves the Young's modulus of the composite. Tensile strength increased considerably with respect to the matrix film (20.2 ± 0.3 MPa), reaching values of 21.2 ± 0.3 MPa (0.5

wt.% cCNCs) and 21.5 ± 0.5 MPa (1.5 wt.% cCNCs). The addition of high stiffness/strength cCNCs to the matrix leads to an increase in the mechanical properties of the nanocomposites as a result of stress transfer. As can be seen, a decrease in Young's modulus and tensile strength was observed for the nanocomposite specimens with 2.5 and 5 wt.% cCNCs loadings, which follows the decrease in crystallinity noted previously (see Table 5.1). The aggregation of cCNCs at higher concentrations could reduce the interaction between the matrix and cCNCs, thereby reducing their mechanical properties.

Two compatibilisers; MAPE and PEO have been added to the neat HDPE and HDPE-cCNCs nanocomposites; the impact of these compatibilising agents on the mechanical properties of nanocomposites were discussed. The Young's modulus and tensile strength of the HDPE-MAPE/cCNCs1.5 nanocomposites improved by 13.6% and 11%, respectively compared to HDPE-MAPE, and improved by 12.6% and 15.8%, respectively compared to neat HDPE. When comparing with HDPE-cCNCs1.5, the HDPE-MAPE/cCNCs1.5 nanocomposites showed a higher Young's modulus and tensile strength; increases of 6.5% and 8.8%, respectively. In the case of HDPE-PEO/cCNCs1.5, the Young's modulus and tensile strength of the nanocomposites increased by 26.5% and 13.7%, respectively compared to HDPE-PEO, and improved by 28.6% and 23.3%, respectively compared to neat HDPE. The HDPE-PEO/cCNCs1.5 nanocomposites showed a higher Young's modulus and tensile strength; by 21.4% and 15.8%, respectively compared to HDPE-cCNCs1.5. Statistical significance (p-values) based on t-tests have been calculated for the tensile modulus and strength of the HDPE-cCNCs, HDPE-MAPE/cCNCs and HDPE-

PEO/cCNCs. Based on these tests (significance is for $p < 0.05$), the p-values of the tensile modulus and strength with the same CNCs loadings (1.5 wt.%) but for different compatibilisers are 0.02, 0.04 (modulus, strength) for HDPE-MAPE/cCNCs and 0.02, 0.02 (modulus, strength) for HDPE-PEO/cCNCs with respect to the HDPE-cCNCs. Therefore, it can be concluded that the presence of compatibilisers significantly enhances the tensile properties of the materials, which could be attributed to better interfacial adhesion and better stress transfer from the matrix to the reinforcement.

The tensile modulus and strength of the HDPE-MAPE/cCNCs and HDPE-PEO/cCNCs also increased with an increasing cCNCs content up to a 1.5 wt.% loading. However, above 1.5 wt.% of cCNCs, Young's modulus and tensile strength continuously decrease. This indicates that at 1.5 wt. % of cCNCs is an optimum filler loading into the HDPE matrix. A significant decrease in the strain at break (%) was observed for all the cCNCs based nanocomposites compared to pure polymer alone, indicating increased brittleness of the composites after incorporating the cCNC fillers into the matrix. HDPE-MAPE/cCNCs and HDPE-PEO/cCNCs composites were however found to have higher strain at break values than nanocomposites designed using uncompatibilised HDPE.

(a)

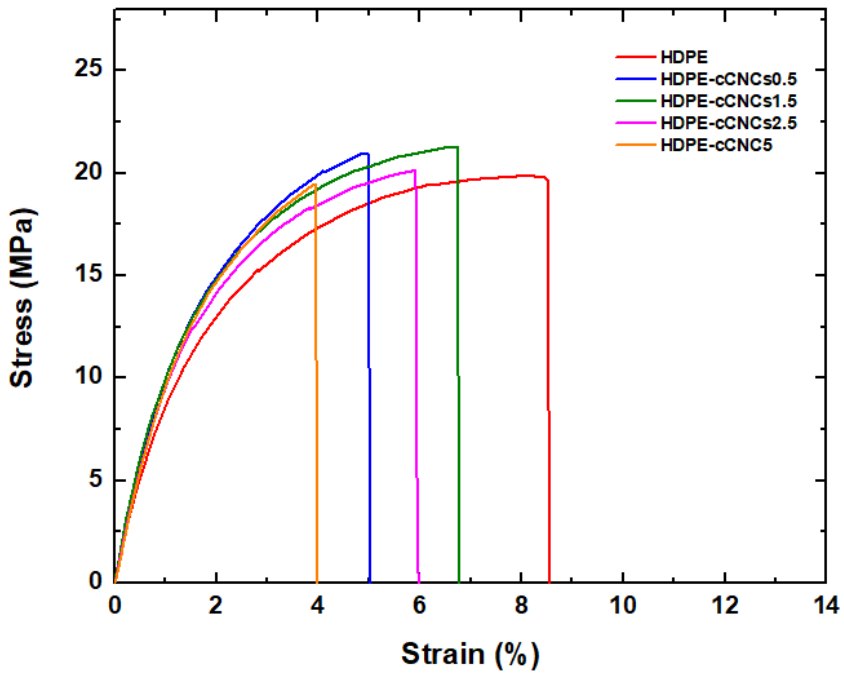

(b)

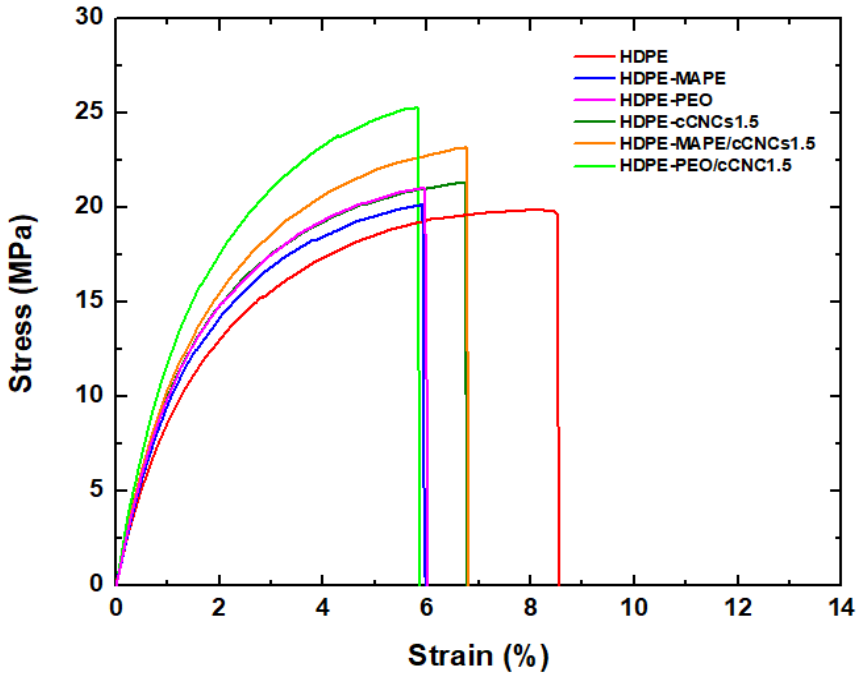

Figure 5.11 Typical stress-strain curves of (a) the composites films with HDPE and HDPE-cCNCs with a variation of weight fraction of cCNCs from 0.5 wt.% to 5 wt.%, (b) the composites films with HDPE, HDPE-MAPE, HDPE-PEO, HDPE-cCNCs, HDPE-MAPE/cCNCs and HDPE-PEO/cCNCs at weight fractions of 1.5 wt.% cCNCs.

Table 5.5 Mechanical properties of the composites films for HDPE, HDPE-cCNCs, HDPE-MAPE/cCNCs and HDPE-PEO/cCNCs at weight fractions of 0.5, 1.5, 2.5, 5 wt.%. Error reports are standard deviations from the mean.

Material	Young`s modulus (GPa)	Tensile strength (MPa)	Strain at break (%)
HDPE	1.19 ± 0.0	20.2 ± 0.3	10 ± 0.6
HDPE/MAPE	1.18 ± 0.0	21.1 ± 0.3	5.3 ± 0.8
HDPE/PEO	1.21 ± 0.0	21.9 ± 0.4	6.2 ± 0.6
HDPE-cCNCs0.5	1.23 ± 0.0	21.2 ± 0.3	5.3 ± 1.0
HDPE-cCNCs1.5	1.26 ± 0.0	21.5 ± 0.5	5.4 ± 1.1
HDPE-cCNCs2.5	1.22 ± 0.0	20.1 ± 0.6	4.6 ± 0.5
HDPE-cCNCs5	1.21 ± 0.0	19.9 ± 0.6	4.1 ± 1.1
HDPE-MAPE/cCNCs0.5	1.26 ± 0.0	22.2 ± 0.4	7.0 ± 0.8
HDPE-MAPE/cCNCs1.5	1.34 ± 0.1	23.4 ± 0.5	6.2 ± 0.4
HDPE-MAPE/cCNCs2.5	1.30 ± 0.0	21.4 ± 0.4	6.2 ± 0.7
HDPE-MAPE/cCNCs5	1.26 ± 0.0	20.9 ± 0.4	5.7 ± 1.1
HDPE-PEO/cCNCs0.5	1.47 ± 0.0	23.8 ± 0.5	9.1 ± 0.2
HDPE-PEO/cCNCs1.5	1.53 ± 0.1	24.9 ± 0.6	8.3 ± 0.4
HDPE-PEO/cCNCs2.5	1.40 ± 0.0	24 ± 0.4	7.7 ± 0.1
HDPE-PEO/cCNCs5	1.31 ± 0.0	22 ± 1.1	7.3 ± 0.5

5.5.2 Stress Strain Behaviour of tCNCs Reinforced HDPE Nanocomposites

Typical stress strain curves of the HDPE and nanocomposites samples produced from tunicates CNCs in HDPE are shown in Figure 5.12. The detailed mechanical properties are reported in Table 5.6. The mean values of the Young's modulus of the nanocomposites increases by 14.3% and 19.3% (compared to the HDPE Young's modulus) when reinforced with 0.5 wt.% and 1.5 wt.% tunicates CNCs, respectively. The HDPE-tCNCs0.5 and HDPE-tCNCs1.5 nanocomposites showed slightly increase tensile strength, increasing from 20.2 ± 0.3 MPa (neat HDPE) to 22.2 ± 0.5 MPa and 22.9 ± 0.7 MPa respectively. The mechanical properties of nanocomposites containing more than 1.5 wt.% tCNCs however decreased, suggesting an aggregation of CNCs within the nanocomposites.

Similar to cCNCs reinforced HDPE nanocomposites, the addition of compatibilisers; MAPE and PEO to the HDPE-tCNCs increased the Young's modulus and tensile strength of the nanocomposites (see Figure 5.11b and Table 5.5). The Young's modulus and tensile strength of the HDPE-MAPE/tCNCs1.5 nanocomposites improved by 25.4% and 27.0%, respectively compared to HDPE-MAPE, and improved by 24.4% and 32.7%, respectively compared to neat HDPE. When comparing with HDPE-tCNCs1.5, the HDPE-MAPE/tCNCs1.5 nanocomposites showed a higher Young's modulus and tensile strength; increases of 4.2% and 17% were found, respectively. In the case of HDPE-PEO/tCNCs1.5, the Young's modulus and tensile strength of the nanocomposites increased by 39.7% and 30.6%, respectively compared to HDPE-PEO, and improved by 42% and 37%, respectively compared to neat HDPE. The HDPE-PEO/tCNCs1.5 nanocomposites showed a

higher Young's modulus and tensile strength; increases of 19% and 23.1%, respectively compared to HDPE-tCNCs1.5. Based on t-tests ($p < 0.05$ being statistically significant), the p-values of the tensile modulus and strength with the same tCNCs loadings (1.5 wt.%) but for different compatibilisers were 0.02, 0.03 (modulus, strength) for HDPE-MAPE/tCNCs and 0.02, 0.03 (modulus, strength) for HDPE-PEO/tCNCs with respect to the HDPE-tCNCs. A significant decrease in the strain at break (%) was observed for all the tCNCs based nanocomposites compared to pure polymer alone, indicating increased brittleness of the composites after incorporating the tCNCs fillers into the matrix.

The mechanical properties of the nanocomposite films reinforced with tunicates CNCs are higher than those reinforced with cotton CNCs. tCNCs reinforced HDPE nanocomposites led to higher strength and modulus than cCNCs reinforced HDPE nanocomposites at the same CNCs concentration. This is thought to be due to the enhanced reinforcing effect of tCNCs, due to their much larger aspect ratios (60.7 ± 30.7) compared to cCNCs (16.3 ± 5.7) (see Section 4.3). Tunicate CNCs are thought to more extensively interact with the matrix due to an increasing contact surface area, thus promoting a higher degree of interfacial interaction. The modulus of a single tCNC appears to be higher than a cCNCs (Rusli & Eichhorn, 2008; Šturcová *et al.*, 2005). This could be due to the higher crystallinity and aspect ratio of the CNCs produced from tunicate cellulose. For example, surface charge is important because this determines the manner in which nanocellulose interacts with itself (CNCs-CNCs interactions) and with polymers via ionic, hydrogen bonding, and hydrophobic interactions (Rusli *et al.*, 2011; Sacui *et al.*, 2014). The higher stiffness of tCNCs would translate to an enhanced stiffening of the composites compared to cCNCs.

This demonstrates that the origin of the starting raw lignocellulosic material governs the resulting reinforcing effect via its aspect ratio, surface charge, stiffness and crystallinity index.

For nanocomposites prepared using both cotton and tunicates HDPE-CNCs, the mechanical properties values obtained using the HDPE-PEO/tCNCs nanocomposites are higher than those obtained using HDPE-MAPE/cCNCs. This may be due to increased stress transfer between the HDPE-PEO/tCNCs composites compared to the HDPE-MAPE/cCNCs composites; this will be explored in more detail in Chapter 6.

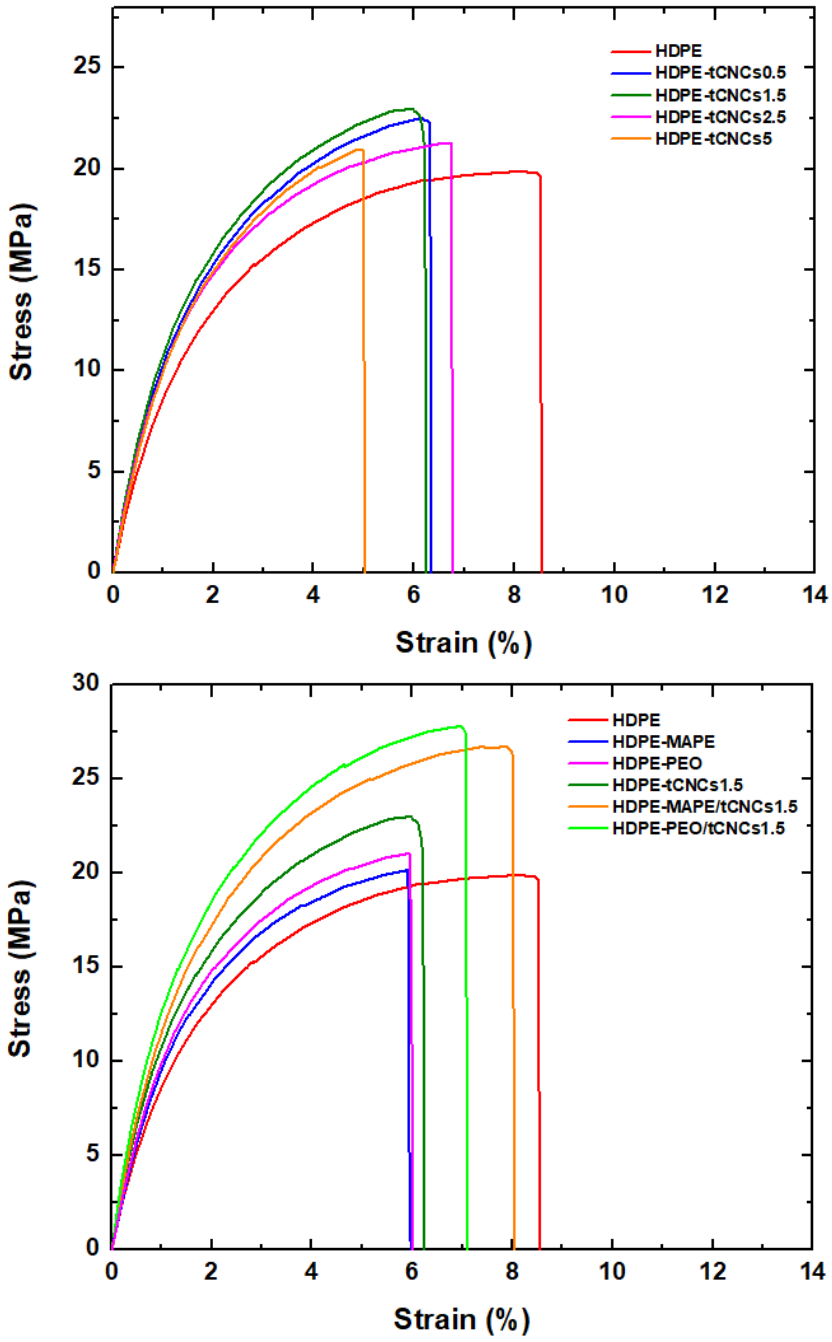

Figure 5.12 Typical stress-strain curves of (a) the composites films with HDPE and HDPE-tCNCs with a variation of weight fraction of tCNCs from 0.5 wt.% to 5 wt.%, (b) the composites films with HDPE, HDPE-MAPE, HDPE-PEO, HDPE-tCNCs, HDPE-MAPE/tCNCs and HDPE-PEO/tCNCs at weight fractions of 1.5 wt.% tCNCs.

Table 5.6 Mechanical properties of the composites films for HDPE, HDPE-tCNCs, HDPE-MAPE/tCNCs and HDPE-PEO/tCNCs at weight fractions of 0.5, 1.5, 2.5, 5 wt.%. Error reports are standard deviations from the mean.

Material	Young`s modulus (GPa)	Tensile strength (MPa)	Strain at break (%)
HDPE	1.19 ± 0.0	20.2 ± 0.3	10 ± 0.6
HDPE/MAPE	1.18 ± 0.0	21.1 ± 0.3	5.3 ± 0.8
HDPE/PEO	1.21 ± 0.0	21.6 ± 0.4	6.2 ± 0.6
HDPE-tCNCs0.5	1.36 ± 0.0	22.2 ± 0.5	6.4 ± 1.4
HDPE-tCNCs1.5	1.42 ± 0.0	22.9 ±0.7	6.4 ± 1.2
HDPE-tCNCs2.5	1.3 ± 0.0	21.8 ±0.7	5.97 ± 0.4
HDPE-tCNCs5	1.25 ± 0.0	20.3 ±0.7	4.5 ± 0.7
HDPE-MAPE/tCNCs0.5	1.4 ± 0.0	25 ± 0.6	7.3 ± 1.1
HDPE-MAPE/tCNCs1.5	1.48 ± 0.0	26.8 ± 0.2	7.2 ± 1.0
HDPE-MAPE/tCNCs2.5	1.39 ± 0.0	24.4 ± 0.4	7 ± 0.2
HDPE-MAPE/tCNCs5	1.34 ± 0.0	23.4 ± 0.3	7.6 ± 1.1
HDPE-PEO/tCNCs0.5	1.56 ± 0.0	26.1 ± 0.3	6.6 ± 1.6
HDPE-PEO/tCNCs1.5	1.69 ± 0.0	28.2 ± 0.9	8 ± 1.0
HDPE-PEO/tCNCs2.5	1.55 ± 0.0	26.7 ± 0.2	6.6 ± 0.9
HDPE-PEO/tCNCs5	1.47 ± 0.0	24.7 ± 0.7	6.9 ± 1.2

5.6 Conclusions

The use of CNCs and compatibilising agents to produce CNCs reinforced HDPE nanocomposites with improved stiffness and strength has been reported in this chapter. Raman spectroscopy has been shown to be a powerful tool to obtain Raman spectrum of each constituent, which in itself is unique molecular level information. Using Raman spectroscopy, identification of each component material in CNCs reinforced HDPE nanocomposites can be simply accomplished. The Raman band initially located at ~1100 cm^{-1} belonging to the cellulose has been shown detectable throughout the HDPE matrix. Raman spectroscopy has also demonstrated that PEO interacts with the CNCs through hydrogen bonding. Using infrared spectroscopy, the appearance of an absorption band located at ~1740 cm^{-1} can be seen in the HDPE-MAPE/CNCs nanocomposite spectra as a result of the esterification reaction of the hydrophobic MAPE onto the hydroxyl groups of CNCs. The thermal characterization of the HDPE matrix and nanocomposites using DSC showed that the addition of CNCs and compatibilising agent to the matrix increase crystallinity of the samples at low filler loadings. Unfortunately, the thermal stability of the nanocomposites was found to decrease as the CNCs loading increased and the incorporation of compatibilising agent to the nanocomposites reduced the onset degradation temperature. The preparation of composites using HDPE matrix and 1.5 wt.% of cCNCs and tCNCs as reinforcement, resulted in Young`s modulus being improved by 6% and 19.6% respectively when compared to polymer alone. This is attributed to the presence of stiff CNCs in the matrix. The tensile strength of the HDPE-cCNCs1.5 and HDPE-tCNCs1.5 nanocomposites samples slightly increase

compared to HDPE matrix at lower loadings, and continue decrease at higher loadings. This suggest that poor interfacial adhesion between matrix and reinforcement leads to aggregation of CNCs at higher loadings. The preparation of nanocomposites using MAPE and PEO as compatibilisers in HDPE-tCNCs1.5 nanocomposites resulted in an improvement of both Young`s modulus (19% higher) and tensile strength (23.1% higher) compared to the HDPE-tCNCs1.5 nanocomposites. The addition of compatibilisers to the nanocomposites enables enhanced matrix-fibre stress transfer leading to better composites performance.

CHAPTER 6

MICROMECHANICS OF CELLULOSE NANOCRYSTALS REINFORCED HDPE USING RAMAN SPECTROSCOPY

In this chapter, Raman spectroscopy has been performed on mechanically deformed CNCs reinforced HDPE matrix composite samples to better understand their molecular deformation and stress transfer properties. The main purpose is to understand the mechanical properties of the nanocomposites reported in Section 5.5.

6.1 Molecular Deformation

Raman spectroscopy is a useful tool for the quantification of stress transfer between a polymer matrix and a stiff cellulose fibre reinforcement. The use of this technique for cellulosic materials and other polymers has already been reported previously in the literature (Eichhorn & Young, 2004; Rusli *et al.*, 2011; Šturcová *et al.*, 2005; Tanpichai, Sampson, & Eichhorn, 2014). The principle of the technique is that a shift in the position of a characteristic Raman band of the polymer is followed, towards a lower wavenumber, upon the application of a tensile deformation. These types of shift in the position of Raman band are thought to be due to direct molecular stressing of the backbone of the polymer (Eichhorn & Young, 2001). The shifts observed are defined as the deviation of the Raman band position from that of an undeformed specimen, according to the equation

$$\Delta v = v - v_0 \quad (6.1)$$

where Δv is the Raman band shift (note; Δv is negative), v is the Raman band position after tensile deformation and v_0 is the Raman band position of the undeformed specimen.

Typical Raman spectra for HDPE-PEO/cCNCs1.5 and HDPE-PEO/tCNCs1.5 nanocomposites are shown in Figure 6.1. As discussed in Section 5.1, it is possible to distinguish between the filler and the matrix in the nanocomposites using specific Raman bands. Cellulosic material exhibit a characteristic Raman band located[2] at ~1095 cm^{-1} that can be attributed to the C-C and C-O stretching modes. These bands have been used to monitor peak shifts by many researchers (Bulota, Tanpichai, Hughes, & Eichhorn, 2012; Pullawan *et al.*, 2014; Rusli *et al.*, 2011; Šturcová *et al.*, 2005). In the case of HDPE matrix, the Raman band located at ~1063 cm^{-1} and ~1132 cm^{-1} are assigned to the C-C stretching modes. The shifts in the positions of these C-C stretching modes have been used to detect the load sharing on polymer chains (Kida, Oku, Hiejima, & Nitta, 2015; Prasad & Grubb, 1989; Tashiro, Wu, & Kobayashi, 1988). The Raman bands located at ~1298 cm^{-1} and ~1313 cm^{-1} are assigned to the CH_2 twisting modes of the crystalline and amorphous chains, respectively. These bands are commonly used as an internal standard to estimate crystallinity and molecular orientation (Dothée, Berjot, & Marx, 1988; W. Lin, Cossar, Dang, & Teh, 2007; Paradkar *et al.*, 2003). Three distinctive band around 1400 –

[2] The Raman system uses two different optical set-ups for the micromechanics analysis and Raman mapping. This results in two different band positions for the peak located at ~1095 cm^{-1} (785 nm laser) and ~1100 cm^{-1} (532 nm laser).

1500 cm^{-1} are assigned to CH_2 bending modes and have been used to estimate the crystallinity of polyethylene (Migler, Kotula, & Hight Walker, 2015). A study has been carried out by Kida *et al.*, (2016) on HDPE during tensile deformation to compare the shift factor (slope of the shift) of several Raman bands. They showed that the Raman band corresponding to C-C twisting modes and CH_2 twisting modes exhibit smaller shift factors than for C-C stretching modes. This result indicated that the torsional motion of the chain and vibrational of the CH_2 groups are less affected by tensile stress. Thus, the Raman band located at ~1132 cm^{-1}, which corresponds to C-C stretching modes, has been used to follow the Raman band shifts in HDPE matrix.

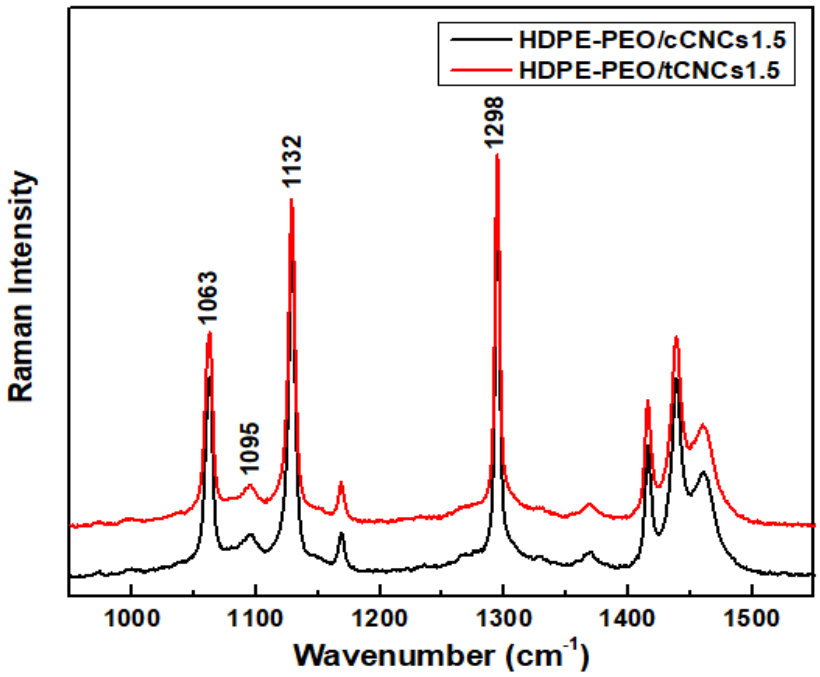

Figure 6.1 Typical Raman spectra of HDPE-PEO/cCNCs1.5 and HDPE-PEO/cCNCs1.5.

When tensile deformation was applied to the composites produced in Section 3.4, the Raman bands initially located at ~1095 cm^{-1} and ~1132 cm^{-1} were observed to

shift towards a lower wavenumber position. Figure 6.2 and Figure 6.3 reports typical shifts in the position of Raman bands initially located at (a) ~1095 cm^{-1} and (b) ~1132 cm^{-1} before (0%) and after tensile deformation (12%) of HDPE-PEO/cCNCs1.5 and HDPE-PEO/tCNCs1.5 nanocomposites respectively. As seen from the graph, after tensile deformation, the shift of Raman band initially located at ~1095 cm^{-1} for both nanocomposites are noticeable; while very little shift can be seen for the Raman band initially located at ~1132 cm^{-1}. The shifts in the position of the Raman band initially located at ~1095 cm^{-1} indicates that stress transfers between the HDPE matrix and the CNCs in the composites, resulting in a direct deformation along the molecular backbone of the cellulose polymer (Eichhorn & Young, 2001; Gierlinger *et al.*, 2006; Pullawan *et al.*, 2014; Šturcová *et al.*, 2005) . On the other hand, smaller shifts of the Raman band initially located at ~1132 cm^{-1} shows that there is possibly some load sharing within the matrix itself (Kida *et al.*, 2016; Pullawan *et al.*, 2014).

Similar shifts towards a lower wavenumber position have also been observed for HDPE-cCNCs, HDPE-tCNCs, HDPE-MAPE/cCNCs and HDPE-MAPE/tCNCs nanocomposites. The shifts in the positions of these two Raman bands have been used to study the interfacial micromechanics of the nanocomposites and will be discussed in this Chapter. The origin of these stress-induced Raman band shifts has already been discussed in Section 2.4.3.

(a)

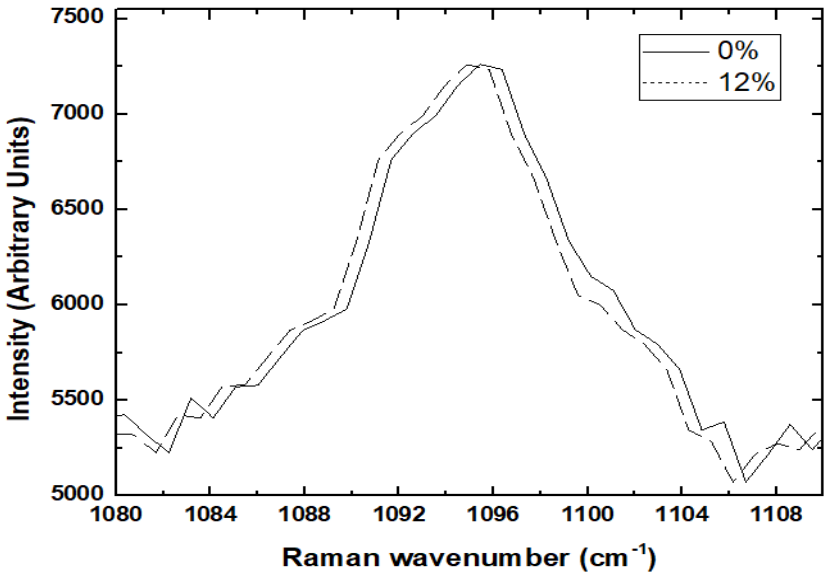

(b)

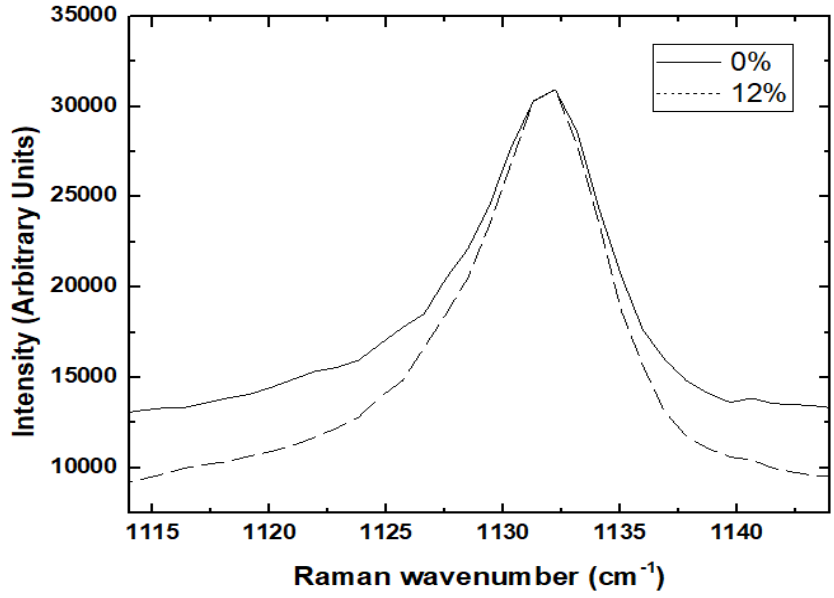

Figure 6.2 Typical shifts in the positions of the Raman bands located approximately at (a) ~1095 cm^{-1} and (b) ~1132 cm^{-1} before (0%) and after tensile deformation (12%) of a HDPE-PEO/cCNCs1.5 nanocomposite.

(a)

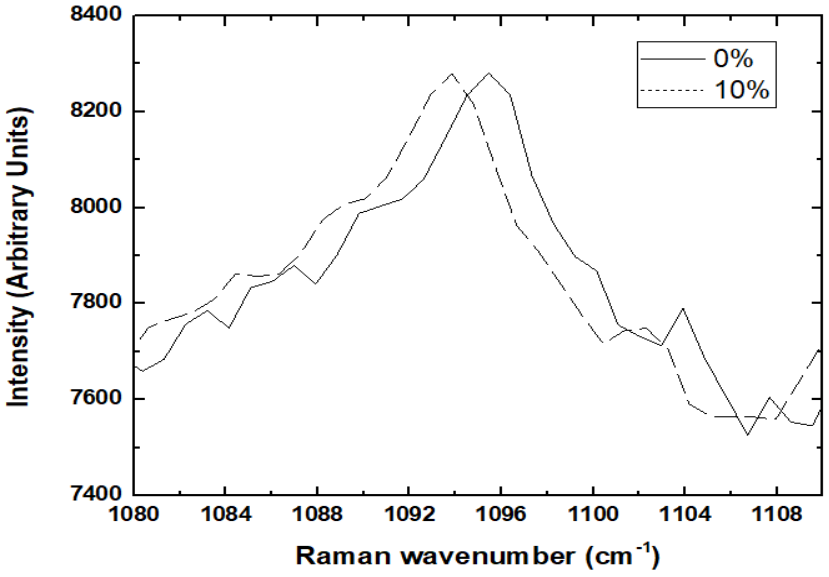

(b)

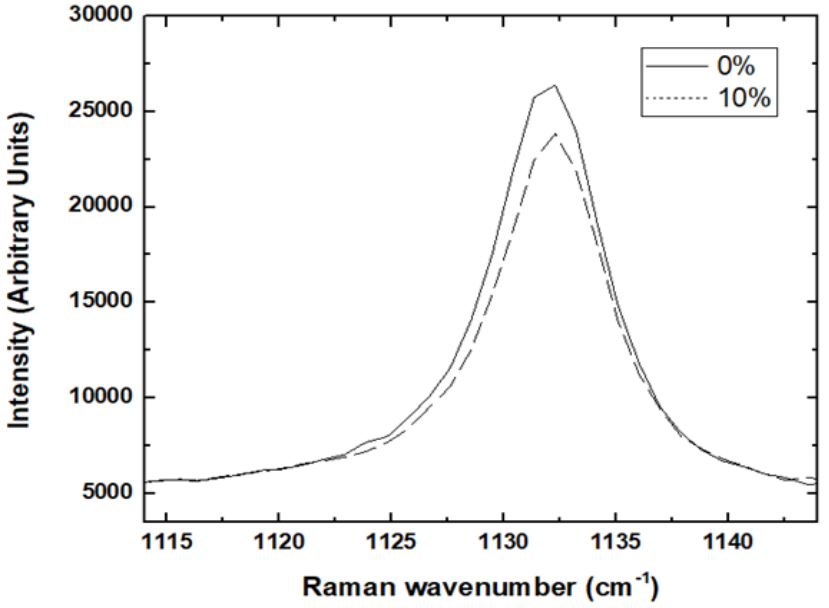

Figure 6.3 Typical shifts in the positions of the Raman bands located approximately at (a) ~1095 cm^{-1} and (b) ~1132 cm^{-1} before (0%) and after tensile deformation (10%) of a HDPE-PEO/tCNCs1.5 nanocomposite.

6.2 Effect of Compatibiliser

6.2.1 Effect of Compatibiliser on the cCNCs Reinforced HDPE Nanocomposites

A comparison between the shifts in the position of the Raman bands initially located at ~1095 cm^{-1} and ~1132 cm^{-1} as a function of tensile strain are shown in Figure 6.4; data for pure HDPE, HDPE-cCNCs, HDPE-MAPE/cCNCs and HDPE-PEO/cCNCs with 1.5 wt.% cCNCs are reported. As seen from these data, the profiles of these shifts are linear for the pure polymer and HDPE-cCNCs samples. However, the data for the HDPE-MAPE/cCNCs and HDPE-PEO/cCNCs samples have a non-linear shape, and most closely reflect the shape of the stress strain curves shown in Section 5.5. The non-linearity occurs at higher strain, and may be due to a breakdown in the interface between the softer phase of the compatibiliser (MAPE and PEO) and the HDPE. Scatter in the data is more pronounced for cCNCs reinforced HDPE nanocomposites because of the weaker signals obtained from these materials compared to pure HDPE matrix.

The initial gradient of the shifts in these data are fitted with an equation of the form (note; Δv is negative)

$$\Delta v = -k_1\varepsilon + k_2\varepsilon^2 \qquad 6.2$$

where k_1 and k_2 are constants and ε is strain. This equation is similar in form to an equation proposed by Nissan (Nissan, 1956)

$$\sigma = E\varepsilon - K\varepsilon^2 \qquad 6.3$$

where σ is stress, E is elastic modulus and K is a constant. This use of these equations can be justified since the magnitude of the Raman band shift is proportional to the stress of the cellulose fibres (Pullawan *et al.*, 2014; Tanpichai *et al.*, 2014). The initial gradient of the shifts in these data were determined by fitting with this equation and then determining the first differential of this function. The value of this function gives the initial gradient to the shifts, whose magnitude is an indication of the stiffness of the composites, and thereby the level of stress transfer taking place within the material. Stress transfer mechanism in a material is thought to occur via hydrogen bonding between the fibrils in the network. In the composite, stress transfer is also thought to occur *via* this mechanism, occurring between the less stiff matrix to the reinforcing CNCs (Rusli, Shanmuganathan, Rowan, Weder, & Eichhorn, 2010). If there is an intact interface between the matrix and the reinforcing phase, a shift in a band representing the latter will occur to a greater or lesser extent depending on the stress transfer efficiency. However, it is true to say that a very stiff phase could be debonded from the matrix and therefore very little shift would occur in this instance. It is also true that orientation of the matrix phase, or a change in crystallinity, leading to a stiffer composite, without an increase in these initial gradients, may also occur if the interface is not intact.

The initial gradients of the fit to the shift data for the Raman band initially located at ~1095 cm^{-1} for HDPE-cCNCs, HDPE-MAPE/cCNCs and HDPE-PEO/cCNCs have been found to be -0.04, -0.07 and −0.07 $cm^{-1}\%^{-1}$ respectively. The initial gradients of the fit to the shift data for Raman band initially located at ~1095 cm^{-1} for HDPE-MAPE/cCNCs and HDPE-PEO/cCNCs are found to be higher than for HDPE-cCNCs

nanocomposites, an indication of the enhanced stress transfer taking place due to compatibilisation. The higher shift rate of a Raman band initially located at ~1095 cm^{-1} with respect to strain for the nanocomposites with the addition of compatibilisers (MAPE and PEO) suggests the compatibiliser initiates a better interaction between the matrix and the reinforcement in this composite. This indicates that the HDPE-MAPE/cCNCs and HDPE-PEO/cCNCs interface is stronger than the HDPE-cCNCs sample. This is in agreement with the results from the mechanical properties data in Section 5.5; the mechanical properties of nanocomposites made from HDPE-MAPE/cCNCs and HDPE-PEO/cCNCs nanocomposites were higher than those produced from HDPE-cCNCs nanocomposites. No significant difference has been however obtained for gradients of the fit to the shifts data for Raman band initially located at ~1095 cm^{-1} between HDPE-MAPE/cCNCs and HDPE-PEO/cCNCs nanocomposites.

During deformation of the nanocomposite samples, the position of the Raman band initially located at ~1132 cm^{-1} was also recorded. The gradients of a fit to the data for shifts in the positions of Raman bands located at ~1132 cm^{-1} for pure HDPE, HDPE-cCNCs, HDPE MAPE/cCNCs and HDPE-PEO/cCNCs samples are small (-0.02 $cm^{-1}\%^{-1}$), but non-zero. Shifts in this same Raman band for deformed polyethylene have been previously observed (Kida *et al.*, 2016; Prasad & Grubb, 1989). This result suggests that some load is borne by the matrix, but the majority of the stress is transferred from the lower stiffness HDPE matrix to the cCNCs, which is typical for fibre reinforced composites of this type. These shifts also suggest some load sharing between the two phases. The gradient of a fit to the shifts in the

positions of Raman bands located at ~1132 cm^{-1} for all samples appears to be the same (see Figure 6.4b). This indicates that the improvement of the stress transfer comes from the addition of cCNCs and also the compatibilisers.

(a)

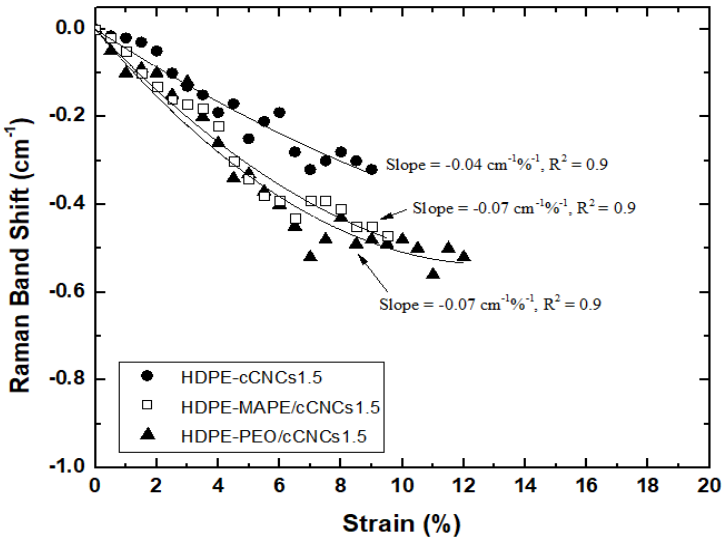

(b)

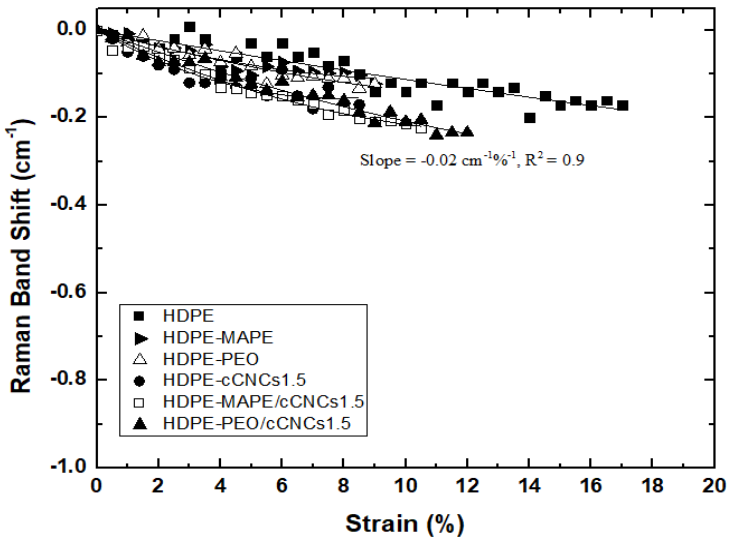

Figure 6.4 Shifts in the positions of Raman bands as a function of tensile strain initially located at (a) ~1095 cm^{-1} and (b) ~1132 cm^{-1} for the pure HDPE, HDPE-MAPE, HDPE-PEO, HDPE-cCNCs, HDPE-MAPE/cCNCs and HDPE-PEO/cCNCs samples with 1.5 wt.% cCNCs. Data are fitted with Equation 6.2 (solid line).

6.2.2 Effect of Compatibiliser on the tCNCs Reinforced HDPE Nanocomposites

Figure 6.5 reports the initial gradients of the fit to the shift data in the position of the Raman bands initially located at ~1095 and ~1132 cm^{-1} as a function of tensile strain for pure HDPE, HDPE-tCNCs, HDPE-MAPE/tCNCs and HDPE-PEO/tCNCs with 1.5 wt.% tCNCs. The initial gradients of the Raman band shift located at ~1095 cm^{-1} for HDPE-tCNCs, HDPE-MAPE/tCNCs and HDPE-PEO/tCNCs have been found to be -0.07, -0.12 and −0.17 $cm^{-1}\%^{-1}$ respectively. Similarly with cCNCs reinforced HDPE nanocomposites, the HDPE-MAPE/tCNCs and HDPE-PEO/tCNCs nanocomposite has better stress transfer efficiency than the HDPE-tCNCs nanocomposite. This indicates that the addition of MAPE and PEO is sufficient to provide a stronger interface between the filler and matrix in these nanocomposites. A comparison between the addition of two different types of compatibiliser (MAPE and PEO) in the tCNCs reinforced HDPE nanocomposites showed that the stress transfer of HDPE-PEO/tCNCs nanocomposites is higher than HDPE-MAPE/tCNCs nanocomposites. This difference is thought to be due to the enhanced interaction between PEO and CNCs *via* hydrogen bonding, as demonstrated by Raman spectroscopy in Section 4.4. These interactions have an impact on improving the interface between the CNCs and the matrix, leading to increase stress transfer in the composites prepared using PEO as a compatibiliser.

To quantitatively analyze the interfacial shear stress, it was calculated using the modified shear-lag equation (Newcomb *et al.*, 2014)

$$\tau_i = \frac{nE_f\varepsilon_i}{2}\tanh(ns) \quad 6.4$$

and $$n = \sqrt{\frac{G_m}{E_f \ln\left(\frac{R}{r}\right)}}, \quad 6.5$$

where E_f is the tCNCs modulus, ε_i is the strain at the fibre−matrix interface, G_m is the matrix shear modulus, which was determined from an elastic modulus and a Poisson's ratio of 0.33 (Bellan, Kameoka, & Craighead, 2005), *s* is the aspect ratio of tCNCs (60.7), and *r* is the tCNCs radius (5 nm) and *R* is the average distance to the next tCNCs, which is calculated using the equation (Chang *et al.*, 2017)

$$R = 2r\sqrt{\frac{\pi[(100-f_m).\rho + f_m.\rho]}{2\sqrt{3}.f_m.\rho}} \quad 6.6$$

where f_m is the weight percentage of tCNCs and ρ is the density of tCNCs. *R* is calculated to be 77 nm, tCNCs modulus is taken as 143 GPa (Rusli & Eichhorn, 2008) and the elongation at the fibre−matrix interface which was calculated from maximum shift of nanocomposites and Raman band shift of individual CNCs of -1.46 $cm^{-1}\%^{-1}$ (Eichhorn *et al.*, 2001). An interfacial shear stress value of 1.18 MPa was obtained for HDPE-tCNCs1.5 which is lower than shear stresses of 2.10 MPa and 2.91 MPa obtained for HDPE-MAPE/tCNCs1.5 and HDPE-PEO/tCNCs1.5 respectively. This low value indicates inefficient and poor stress transfer between tCNCs and HDPE matrix. This study is in agreement with previous work reported for CNCs reinforced with polymer composites (Chang *et al.*, 2017; Wanasekara & Eichhorn, 2017). Their study concluded that higher interfacial shear stress indicates a higher stress transfer between the fibre and matrix.

It is noted that the initial gradients of the fit to the shift data for the Raman band initially located at ~1095 cm^{-1} for tCNCs-based nanocomposites are found to be higher than cCNCs-based nanocomposites. The difference in the slopes of these curves could be explained on the basis that there is increased stress transfer in tCNCs-based nanocomposites compared to cCNCs-based nanocomposites. The higher stress transfer observed for tCNCs-based nanocomposites indicates that there is a stronger interaction between HDPE and the tCNCs than for cCNCs nanocomposites. This can be explained by the differences in surface charges and aspect ratio between different cellulose sources (Rusli *et al.*, 2011). It was found that the tCNCs have higher surface charge (64 ± 3.9 mmol kg^{-1}) than cCNCs (40 ± 2.6 mmol kg^{-1}) as reported in Section 4.2. A lower surface charge can promote the lyophilization-induced self-assembling behavior of nanoparticles (Han, Zhou, Wu, Liu, & Wu, 2013), leading to aggregation of the CNCs and poor dispersibility within the matrix. This aggregation could reduce the effective aspect ratio of the reinforcing phase, and also the surface area that is in contact with the matrix phase, resulting in a reduction in stress transfer (Rusli *et al.*, 2011). By assuming cylindrical geometries for the CNCs as shown in Section 4.4, and using the CNCs dimensions (diameter and length) given in Section 4.4, the surface area to volume ratio of the CNCs can be calculated (Rusli *et al.*, 2011). The surface area to volume ratio of tCNCs (0.42) was found higher than cCNCs (0.28). In addition, the degree of crystallinity of tCNCs was found higher compared to cCNCs. In a highly crystalline cellulose samples, the crystallite domains are highly oriented, and that the chain stretching contributes more to the overall stress leading to greater shifts in the position of Raman bands.

(a)

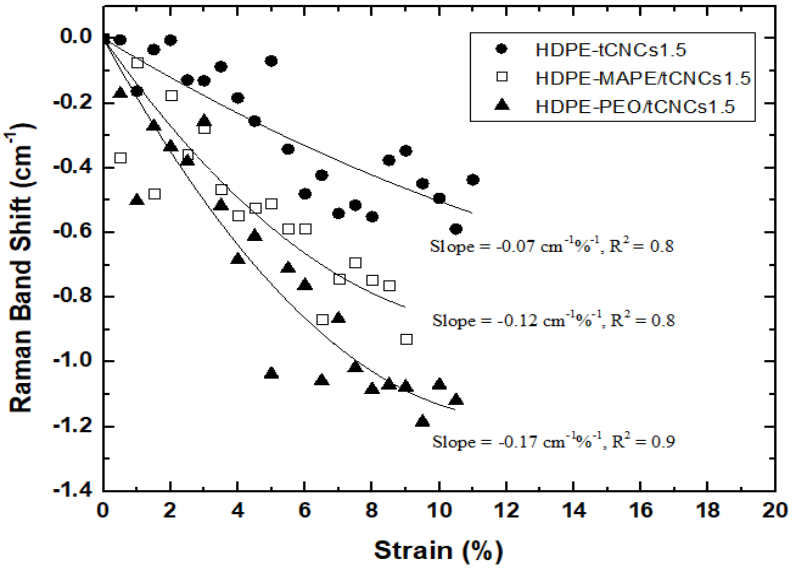

(b)

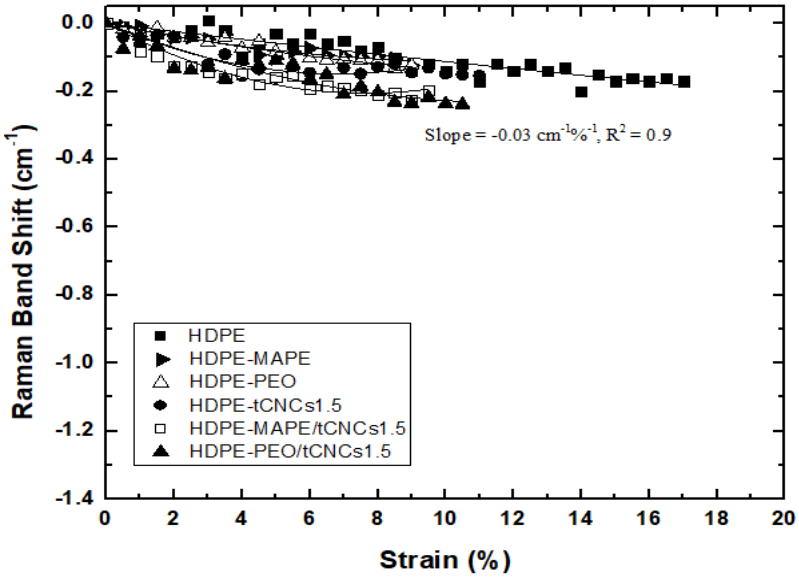

Figure 6.5 Shifts in the positions of Raman bands initially located at (a) ~1095 cm^{-1} and (b) ~1132 cm^{-1} as a function of tensile strain for the pure HDPE, HDPE-MAPE, HDPE-PEO, HDPE-tCNCs, HDPE-MAPE/tCNCs and HDPE-PEO/tCNCs samples with 1.5 wt.% tCNCs. Data are fitted with Equation 6.2 (solid line).

6.3 Effect of Weight Fraction of CNCs

6.3.1 Effect of Weight Fraction of cCNCs on the Micromechanical Properties of the CNCs Reinforced HDPE Nanocomposites

The Raman band located initially at ~1095 cm^{-1} undergoes a stress induced shift towards a lower wavenumber position upon tensile deformation. The shift in this band position has been used to follow the local micromechanics of the interface in the nanocomposites. The effect of the weight fraction of cCNCs on the rate of shift in the position of Raman band initially located at ~1095 cm^{-1} as a function of strain for the HDPE-cCNCs, HDPE-MAPE/cCNCs and HDPE-PEO/cCNCs nanocomposites with 0.5, 1.5, 2.5 and 5 wt.% cCNCs is shown in Figure 6.4. The shift profiles are linear for the HDPE-cCNC samples. However, the profile of the shifts for the HDPE-MAPE/cCNCs and HDPE-PEO/cCNCs samples have a non-linear shape (similar to Figure 6.4a), and most closely reflect the shape of the stress strain curves shown in Section 5.5. The non-linear fit to these data are reported in Table 5.6; the initial gradient were calculated following the method described in Section 6.2.1. As the loading of cCNCs increases from 0.5 wt.% to 1.5 wt.%, the initial shift rate with respect to strain for the Raman band located initially at ~1095 cm^{-1} increases. An increase in the gradient with respect to strain is an indication of the progressive increase in the stiffening of the nanocomposites due to the presence of high modulus cCNCs since the band shift rate with respect to strain has previously been shown to be proportional to the modulus (Eichhorn *et al.*, 2001; Eichhorn & Young, 2001).The largest initial gradients in the position of Raman band initially located at ~1095 cm^{-1} for HDPE-cCNCs, HDPE-MAPE/cCNCs and HDPE-

PEO/cCNCs nanocomposites are found at a low loading of cCNCs (at a weight fraction of 1.5 wt.%) which follows the mechanical properties and crystallinity data obtained for these materials. However, above a loading of 1.5 wt.% of cCNCs, the shift rate continuously decreases with an increasing cCNCs content. This is in agreement with the mechanical properties and crystallinity data (see Section 5.5.1 and Section 5.3.1). A decrease in the initial gradient with respect to strain has been found for all nanocomposites, and is thought to be due to the aggregation of cCNCs at higher weight fractions (Pullawan *et al.*, 2014). Aggregation of the fillers limit the surface area that is in contact with the matrix phase, resulting in a reduction in stress transfer.

The initial gradient of the Raman band located initially located at ~1095 cm^{-1} for the HDPE-PEO/cCNCs1.5 nanocomposites (-0.07 $cm^{-1}\%^{-1}$) is lower than the one obtained by Pullawan *et al.* (2014) for cCNCs reinforced lithium chloride/N,N-dimethyl acetamide dissolved cellulose (-0.5 $cm^{-1}\%^{-1}$ for 5 vol% cCNCs loadings). There are two possible reasons for this; firstly the aspect ratio of cCNCs obtained in this study may be lower than those used by Pullawan *et al.*, (2014) (17.2). The lower aspect ratio of the filler leads to aggregation, resulting in poor stress transfer from HDPE matrix to cCNCs. Secondly, the influence of processing method (melt compounding) used in this study leads to a decrease in mechanical properties compared to the solution casting method used by Pullawan *et al.*, (2014). Sapkota, Kumar, Weder, & Foster, (2015) showed that solution-cast cCNCs/PVAc nanocomposites exhibit higher mechanical reinforcement than materials produced by reprocessing of solution-cast cCNCs/PVAc in a screw extruder. This can be

explained by the reduction of the lengths of cCNCs by high shear melt-mixing in a twin screw extruder that leads to a lower surface area contact with the polymer matrix. Stress transfer between the matrix and CNCs is dependent upon a multitude of factors. These include, but are not limited to, the type of matrix and CNCs used in the formation of the nanocomposite, the interfacial bonding between matrix and CNCs, and the amount and degree of mixing of the CNCs within the matrix. Because of these factors, the direct comparison of the stress transfer between different nanocomposites has not yet been fully realized.

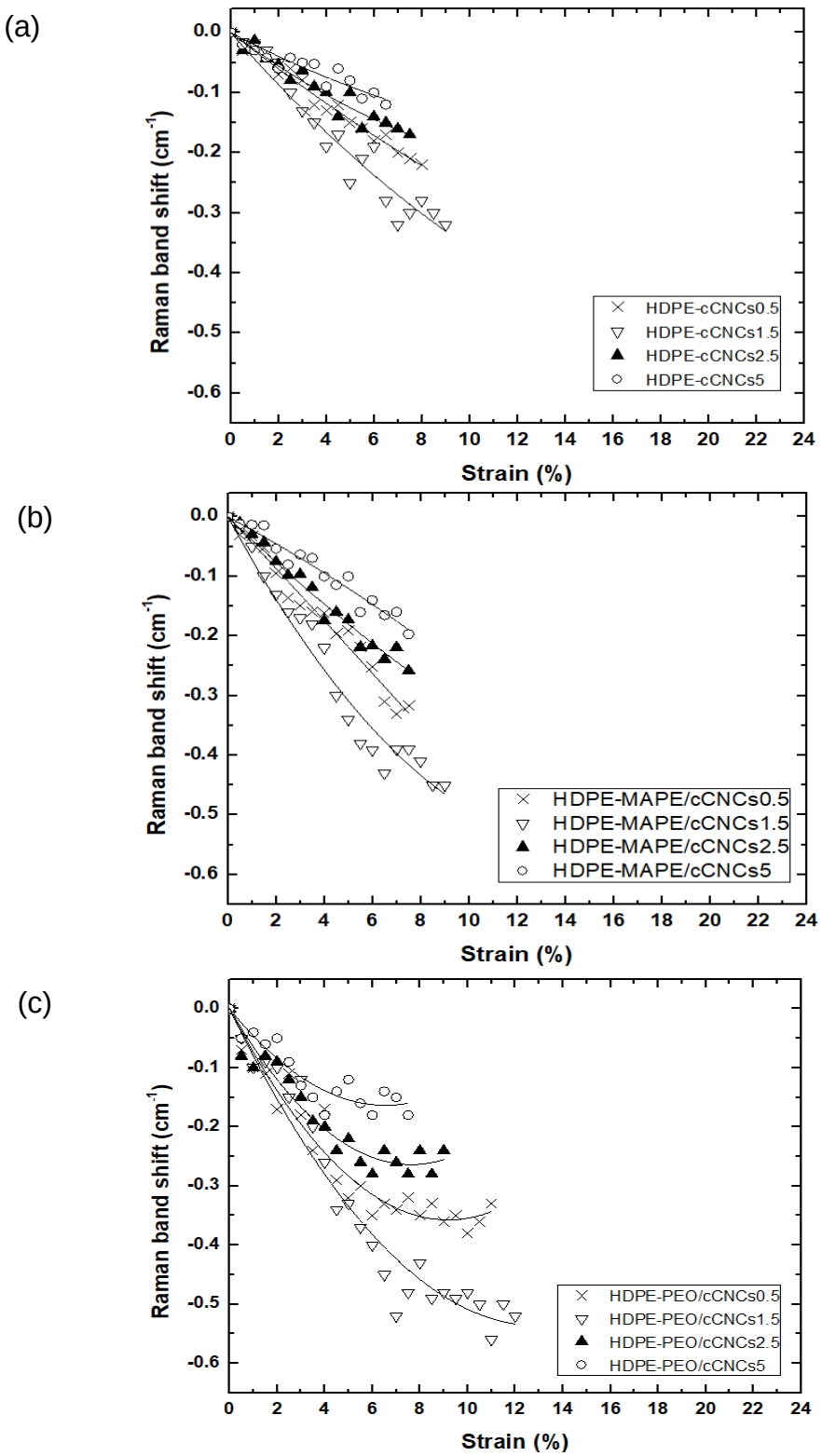

Figure 6.6 Typical shifts in the Raman band initially located at ~1095 cm^{-1} for (a) HDPE-cCNCs, (b) HDPE-MAPE/cCNCs and (c) HDPE/PEO-cCNCs nanocomposites at different cCNCs weight fractions of 0.5, 1.5, 2.5 and 5 wt.%. Data are fitted with Equation 6.2 (solid line).

Table 6.1 Initial gradients of the nonlinear fits to shifts in the position of Raman bands initially located at ~1095 cm^{-1} for HDPE-cCNCs, HDPE-MAPE/cCNCs and HDPE-PEO/cCNCs nanocomposite samples with different cCNCs weight fractions (0.5, 1.5, 2.5 and 5 wt.%).

Material	Gradients to fit ($cm^{-1}\%^{-1}$)	R^2
HDPE-cCNCs0.5	-0.03 ± 0.00	0.8 ± 0.04
HDPE-cCNCs1.5	-0.04 ± 0.00	0.9 ± 0.05
HDPE-cCNCs2.5	-0.03 ± 0.00	0.9 ± 0.03
HDPE-cCNCs5	-0.03 ± 0.00	0.8 ± 0.07
HDPE-MAPE/cCNCs0.5	-0.05 ± 0.00	0.9 ± 0.03
HDPE-MAPE/cCNCs1.5	-0.07 ± 0.01	0.9 ± 0.06
HDPE-MAPE/cCNCs2.5	-0.05 ± 0.00	0.8 ± 0.05
HDPE-MAPE/cCNCs5	-0.03 ± 0.00	0.8 ± 0.04
HDPE-PEO/cCNCs0.5	-0.06 ± 0.00	0.9 ± 0.05
HDPE-PEO/cCNCs1.5	-0.07 ± 0.00	0.9 ± 0.06
HDPE-PEO/cCNCs2.5	-0.06 ± 0.00	0.8 ± 0.02
HDPE-PEO/cCNCs5	-0.04 ± 0.00	0.9 ± 0.04

6.3.2 Effect of Weight Fraction of tCNCs on the Micromechanical Properties of the CNCs Reinforced HDPE Nanocomposites

In a comparative study, the effect of the weight fraction of tCNCs on the micromechanics of nanocomposites was also investigated. Typical shifts in the position of the Raman band initially located at ~1095 cm^{-1} upon tensile deformation of HDPE-tCNCs, HDPE-MAPE/tCNCs and HDPE-PEO/tCNCs are shown in Figure 6.5. Except for the HDPE-tCNCs, the shift profiles are non-linear, and reflect the stress-strain curves in Section 5.5. The initial gradients of fits to these data are

reported in Table 6.2. Similar to cCNCs-based nanocomposites, the largest initial gradients for HDPE-tCNCs, HDPE-MAPE/tCNCs and HDPE-PEO/tCNCs nanocomposites are found at a low loading of tCNCs; at a weight fraction of 1.5 wt.%. The shift rate of tCNCs-based nanocomposites decreases at tCNCs weight fractions of 2.5 and 5 wt.%; as a result of the aggregation of tCNCs at higher loadings. From the results, it is clear that tCNCs based nanocomposites exhibit a higher gradient and an increased stress transfer efficiency compared to cCNCs based nanocomposites; again, this could be due to the higher aspect ratio and surface functionality of the tCNCs. This supports the results from the mechanical properties data in Section 5.5; the mechanical properties of tCNCs-based nanocomposites were higher than those nanocomposites produced from cCNCs. It has been shown that the shift in the position of Raman band related to direct chain stretching of cellulose (Šturcová *et al.*, 2005). In less oriented crystallite domains, crystallite reorientation dominate the deformation of low crystallinity and modulus cCNCs. The smaller shifts in the position of Raman bands has been found in low crystallinity-based nanocomposites and are believed to be as a result of less contribution of chain stretching to the overall stress.

(a)

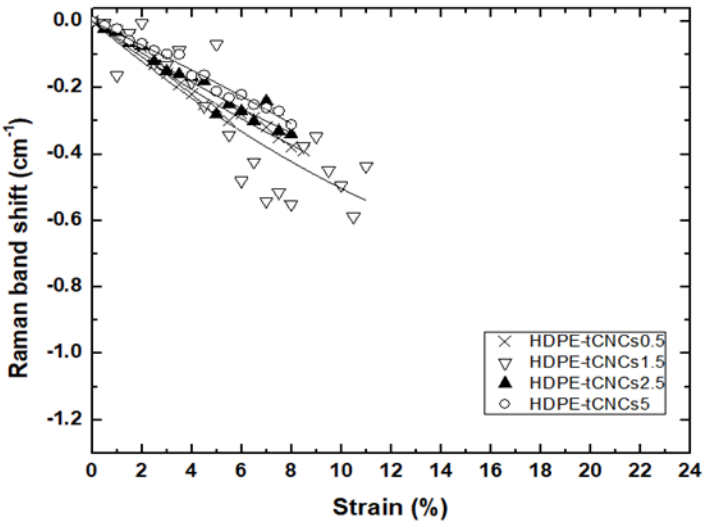

(b)

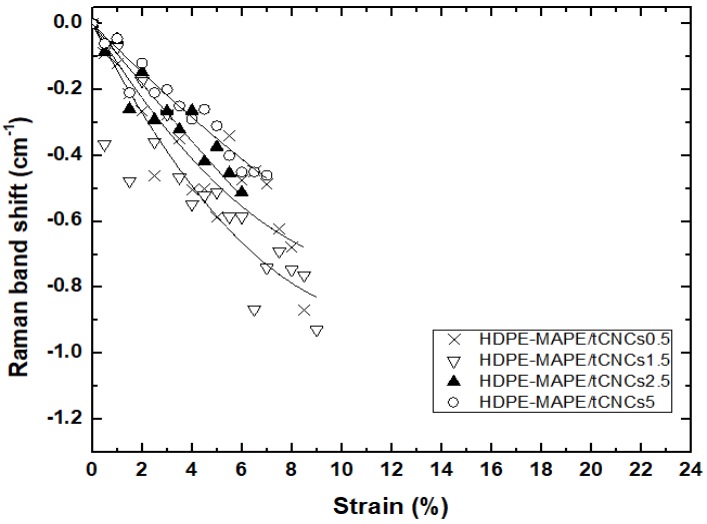

(c)

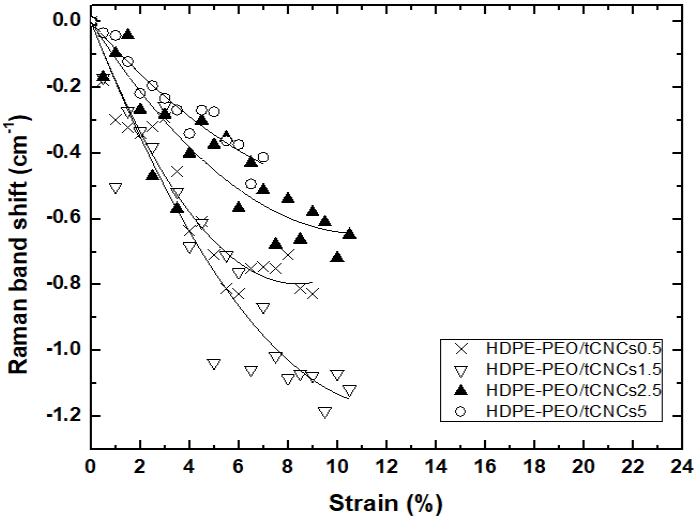

Figure 6.7 Typical shifts in the position of a Raman band initially located at ~1095 cm^{-1} for (a) HDPE-tCNCs, (b) HDPE-MAPE/tCNCs and (c) HDPE/PEO-tCNCs nanocomposites at different weight fractions of tCNCs; 0.5, 1.5, 2.5 and 5 wt.%. Data are fitted with Equation 6.2 (solid line).

Table 6.2 Initial gradients of the nonlinear fits to shifts in the position of Raman bands initially located at ~1095 cm^{-1} for HDPE-tCNCs, HDPE-MAPE/tCNCs and HDPE-PEO/tCNCs nanocomposite samples with different tCNCs weight fractions (0.5, 1.5, 2.5 and 5 wt.%).

Material	Gradients to fit ($cm^{-1}\%^{-1}$)	R^2
HDPE-tCNCs0.5	-0.06 ± 0.01	0.8 ± 0.02
HDPE-tCNCs1.5	-0.07 ± 0.0	0.9 ± 0.03
HDPE-tCNCs2.5	-0.05 ± 0.0	0.9 ± 0.01
HDPE-tCNCs5	-0.04 ± 0.0	0.9 ± 0.02
HDPE-MAPE/tCNCs0.5	-0.11 ± 0.01	0.8 ± 0.03
HDPE-MAPE/tCNCs1.5	-0.14 ± 0.01	0.9 ± 0.03
HDPE-MAPE/tCNCs2.5	-0.09 ± 0.01	0.8 ± 0.05
HDPE-MAPE/tCNCs5	-0.07 ± 0.01	0.9 ± 0.02
HDPE-PEO/tCNCs0.5	-0.16 ± 0.01	0.8 ± 0.03
HDPE-PEO/tCNCs1.5	-0.17 ± 0.02	0.8 ± 0.04
HDPE-PEO/tCNCs2.5	-0.11 ± 0.01	0.9 ± 0.02
HDPE-PEO/tCNCs5	-0.09 ± 0.01	0.9 ± 0.02

6.4 Conclusions

The Raman technique has been used to investigate the micromechanics of cellulose nanocrystal reinforced HDPE matrix composites. Raman Spectroscopy is able to provide information on deformation of both phases – the CNCs and the matrix. Shifts in the positions of the two Raman bands initially located at ~1095 cm^{-1} and ~1132 cm^{-1} have been used to follow the local micromechanics of the interface in CNCs and the HDPE matrix respectively. The Raman band located at ~1095 cm^{-1} corresponds to the cellulose backbone polymer chain whereas the band located at ~1132 cm^{-1} corresponds to the HDPE matrix. The peak position of the Raman band initially located at ~1095 cm^{-1} for the cellulose nanocrystal reinforced HDPE matrix composite was found to shift towards a lower wavenumber when the composites were subjected to tensile deformation. These shifts indicate that stress transfers between the CNCs and the HDPE matrix in the composites, resulting in a direct deformation along the molecular backbone of the cellulose polymer. In comparison, very little shift (non-zero) was seen for the Raman band initially located at ~1132 cm^{-1}, which indicates possible load sharing within the matrix itself. Raman spectroscopy also revealed an improvement of the stress transfer at the interface of nanocomposites designed with the addition of the MAPE and PEO compatibilisers. The initial gradients of the fit to the shift data for the Raman band initially located at ~1095 cm^{-1} for cellulose nanocrystal reinforced HDPE matrix composite designed using MAPE and PEO was found to be higher compared to unmodified cellulose nanocrystal reinforced HDPE matrix composites. This confirms that the addition of MAPE and PEO facilitates stress transfer in this form of nanocomposites. An

interfacial shear stress calculated for the HDPE-tCNCs1.5 nanocomposites was found to be lower than values for the HDPE-MAPE/tCNCs1.5 and HDPE-PEO/tCNCs1.5 samples. The largest initial gradients in the position of Raman band initially located at ~1095 cm^{-1} for of cellulose nanocrystal reinforced HDPE matrix composites are found at a low loading of CNCs (at a weight fraction of 1.5 wt.% CNCs) which follows the mechanical properties and crystallinity data obtained for these materials. However, above a loading of 1.5 wt.% of CNCs, the shift rate continuously decreases with an increasing CNCs content as a result of the aggregation of the CNCs at higher weight fractions. Aggregation of the fillers limit the surface area that is in contact with the matrix phase, resulting in a reduction in stress transfer. It was also shown that the stress transfer in tCNCs-based nanocomposites are found to be better compared to the cCNCs-based nanocomposites. The low surface charges and aspect ratio characteristics of cCNCs is thought to contribute the smaller shift of the Raman band compare with the tCNCs.

CHAPTER 7

QUANTITATIVE ANALYSIS OF THE MIXING AND AGGREGATION OF CELLULOSE NANOCRYSTALS IN THERMOPLASTIC COMPOSITES USING RAMAN IMAGING

In this chapter, Raman imaging and chemical images are used to study the morphology of agglomerates of CNCs in the HDPE matrix. The effect of a compatibiliser and a quantification of the degree of mixing and aggregation between the components is also presented. Since a quantification of the morphology of agglomerated CNCs and their degree of mixing has not been previously reported, this chapter gives new prospects for inspecting the reinforcement mechanism for cotton and tunicate CNCs-based polymer nanocomposites.

7.1 Raman Spectra of Nanocomposite Components

The interfacial region where the intimate interaction between CNCs, the compatibiliser and the HDPE matrix takes place can be investigated by a combination of Raman mapping with chemical images and image analysis. The Raman mapping approach requires an unambiguous differentiation of all the components in the polymer nanocomposites. Characteristic Raman bands are used for distinguishing these components in Raman images. Typical reference Raman spectra for HDPE, MAPE, PEO, CNCs and CNCs-PEO are shown in Figure 7.1. To visualize the appearance of the CNCs, three most intense Raman bands located at

~382cm^{-1}, ~1100 cm^{-1} and ~1381 cm^{-1} were used to confirm the appearance of CNCs in the Raman images (Agarwal *et al.*, 2012; Wiley & Atalla, 1987). The most intense Raman band, characteristic of the CNCs, is located[3] at ~1100 cm^{-1} and has been previously assigned to the C-O ring stretching and the β-1,4 glycosidic linkage (C-O-C) stretching modes between the glucose rings of the cellulose chains (Gierlinger *et al.*, 2006; Wiley & Atalla, 1987). The Raman band located at ~382 cm^{-1} falls within the region 250-600 cm^{-1}, which has been assigned to skeletal-bending modes involving the C-C-C, C-O-C, O-C-C, O-C-O and skeletal stretching modes of C-C and C-O moieties (Wiley & Atalla, 1987). Additionally, the Raman band located at ~1381 cm^{-1} falls within the region 1180-1550 cm^{-1}, which has been assigned to bending modes involving the C-C-H, O-C-H and C-O-H moieties (Wiley & Atalla, 1987).

HDPE bands located at ~1301 cm^{-1} and ~1464 cm^{-1}, which have been assigned to CH_2 twisting modes and CH_2 rocking modes in the crystalline phase of the polymer were used to visualize the presence of HDPE matrix in the Raman images (Cherukupalli & Ogale, 2004; Sato, Shimoyama, Kamiya, Amari, Aic, *et al.*, 2002). Verification of the presence of PEO is based on two distinctive Raman bands located at ~847 cm^{-1} and ~864 cm^{-1} correspond to CH_2 rocking modes and C-O-C stretching mode, respectively (Maxfield & Shepherd, 1975). Furthermore, Raman bands centered at ~1285 cm^{-1} and ~1483 cm^{-1}, assigned to CH_2 twisting modes and CH_2

[3]The Raman system uses two different optical set-ups for the micromechanic analysis and Raman mapping. This results in two different band positions for the peak located at ~1095 cm^{-1} (785 nm laser) and ~1100 cm^{-1} (532 nm laser).

scissoring modes, were additionally used in the analysis to distinguish PEO and HDPE (Maxfield & Shepherd, 1975). As shown in Section 5.1, a Raman spectrum for MAPE exhibits the same bands as pure polyethylene. A comparison between the typical Raman spectra for pure components enables the identification of unique bands, which can be used to distinguish these components in subsequent images.

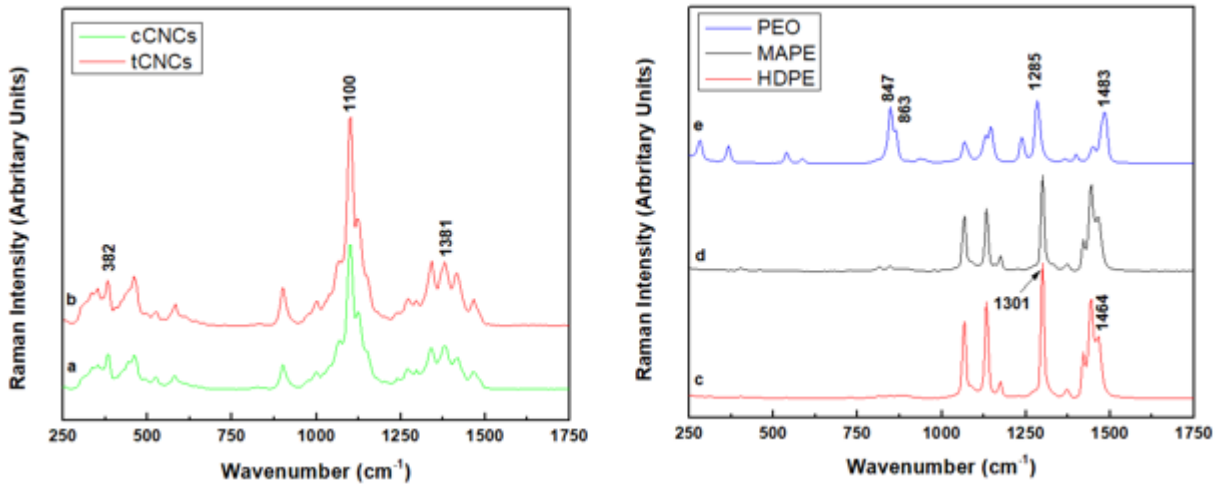

Figure 7.1 Typical Raman spectra of pure nanocomposite components: (a) cCNCs, (b) tCNCs, (c) high-density polyethylene (HDPE), (d) maleated polyethylene (MAPE) and (e) poly(ethylene oxide) (PEO).

7.2 Raman Imaging of cCNCs Reinforced HDPE Nanocomposites

7.2.1 Raman Images of Spatial Mixing of Nanocomposites Components

The conversion of Raman spectra to Raman images provides an evaluation of the spatial distribution of CNCs in the HDPE matrix. Figure 7.2 (also Figure A1, A2 and A3 in Appendix) illustrates the Raman images collected from cross sectional areas

of composites films of HDPE-cCNCs1.5, HDPE-MAPE/cCNCs1.5 and HDPE-PEO/cCNCs1.5 nanocomposites. As seen from the figure, it is not possible to discriminate single CNCs on the nanometer scale (typically cCNCs are 165.5 ± 38.3 nm long and 14.3 ± 3.6 nm in width, and tCNCs are 1460 ± 480.3 nm long and 10.1 ± 2.5 nm nm in width based on TEM images – as shown in Section 4.1) because of the limitations of the lateral resolution of the laser spot (~388 nm). These images do additionally present features of the surface morphology associated with the presence of cellulose aggregates and the process of microtome cutting. The Raman images for the HDPE-cCNCs composites were constructed by plotting the intensity of the band at ~1100 cm^{-1}, corresponding to the backbone vibrations of cellulose, and the band located at ~1301 cm^{-1} corresponding to the CH_2 twisting mode of HDPE. These two bands to illustrate the regions containing cCNCs and HDPE components, respectively, as shown in Figure 7.2. In the figure, a bright yellow colour indicates a high intensity of the specific Raman band. Conversely, a dark colour corresponds to a low intensity of the specific Raman band. In Figure 7.2 (A, C and E), the bright yellow areas are indicative of a region of aggregated CNCs. The bright yellow areas in Figure 7.2 (B, E and F) shows the presence of the HDPE matrix, related to the relatively high intensity of the Raman band located at ~1301 cm^{-1}. A brown colour indicates areas where the absence of the selected Raman band or their intensity is significantly low. From the figure, it can be summarized that Raman images based on cellulose and HDPE bands were almost complementary to each other; the region where the cellulose intensity is close to zero, the HDPE intensity was relatively high, and *vice versa*. These images further reveal the tendency of the cCNCs to form aggregate structures with irregular shapes in the volume of the HDPE matrix. The

shapes of these aggregates are irregular, independent of the presence of MAPE and the PEO compatibiliser. These results are in agreement with two independent studies (Agarwal *et al.*, 2012; Mukherjee *et al.*, 2017). Both studies show a clear transition interface between the thermoplastic matrix-abundant and CNCs-abundant regions, indicating the tendency of CNCs to form aggregate structures rather than being dispersed in thermoplastic matrices. Similar results have been reported by Agarwal *et al.,* (2012) in their study of the impact of coupling agent on the dispersion of extruded composite films of polypropylene reinforced with CNCs. Their work reported that although the dispersion was slightly improved with the addition of the MAPP, a clear transition interface between the PP-abundant and CNCs-abundant regions was observed, indicating that the CNCs remained poorly dispersed.

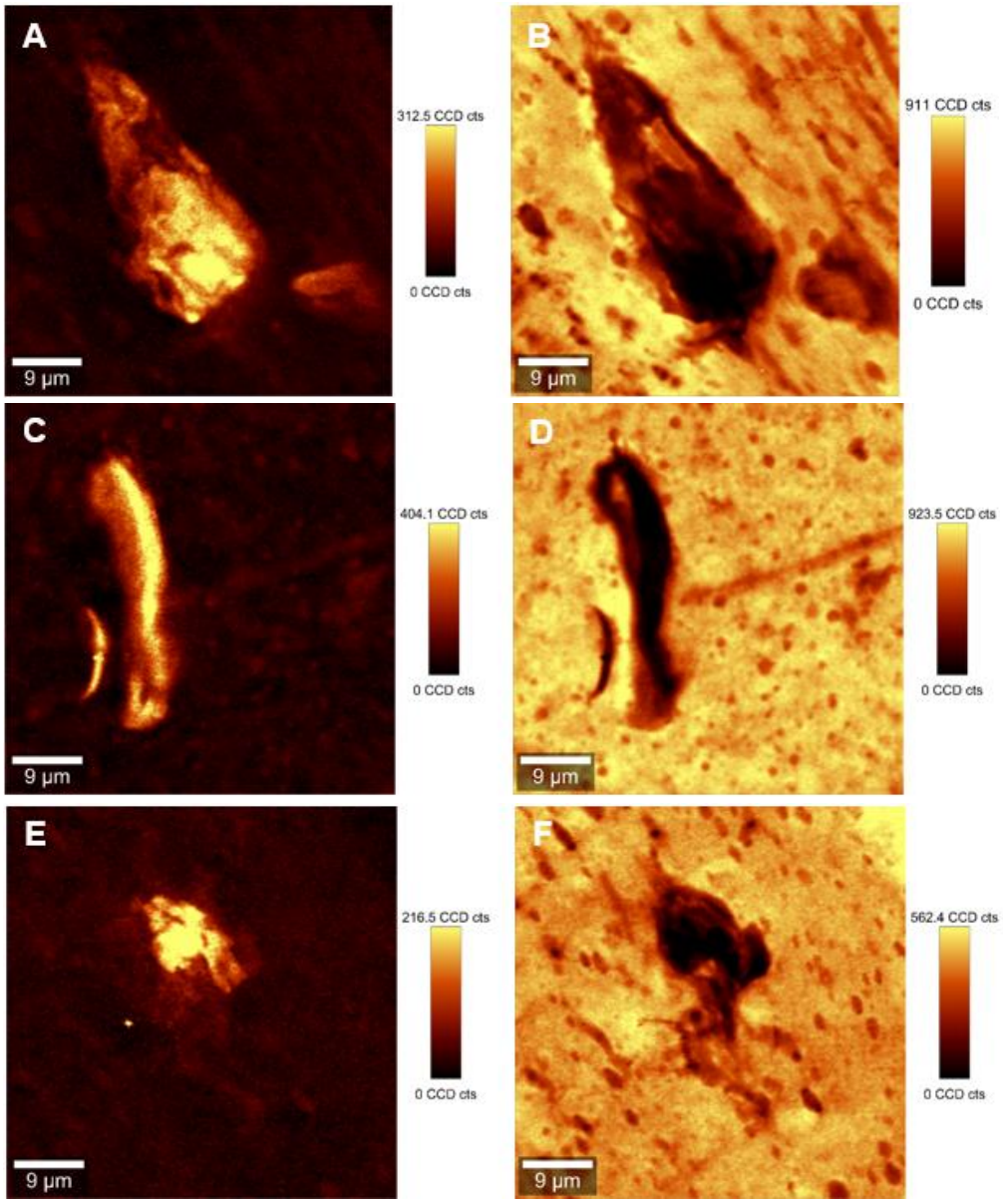

Figure 7.2 Typical Raman images of HDPE-cCNCs1.5 (A and B), HDPE-MAPE/cCNCs1.5 (C and D) and HDPE-PEO/cCNCs1.5 (E and F) composites depicting the intensity of a Raman band located at ~1100 cm^{-1} (A, C, and E) and ~1301 cm^{-1} (B, D, and F).

7.2.2 Chemical Images of Spatial Mixing of Nanocomposites Components

The degree of mixing between CNCs, compatibilisers and HDPE can be evaluated from the chemical images extracted from Raman images. Figure 7.3 shows the chemical images of HDPE-cCNCs, HDPE-MAPE/cCNCs and HDPE-PEO/cCNCs nanocomposites at a loading of 1.5 wt.% CNCs, as derived from Figure 7.2. These chemical images show spatially the gradual changes in the concentration between filler, compatibiliser and matrix in the composites (Figures A, C and E), while the Raman spectra reflect the changes in the relative intensity of their respective Raman bands (Figure B, D and F). The chemical images disclose seven regions (red, navy, blue, cyan, lime, green and dark green colours) that represent average Raman bands for each specific area and also demonstrate the areas of mixing between the components. The red area in the chemical images is characteristic of the HDPE spectrum (also coloured in red) present the most intense band for the CH_2 twisting mode located at ~1299 cm^{-1}. The average Raman spectrum obtained for HDPE is similar to the pure HDPE used for the melt compounding process as shown in Figure 7.3. The mixing region is shown as a scale of blue colours (navy, blue, cyan), whereas the aggregation region is shown as a scale of green colours (lime, green, dark green).

For HDPE-cCNCs and HDPE-MAPE/cCNCs nanocomposites, a region of mixing between the CNCs and HDPE is noted. This is evident as a gradual decrease in the intensity of Raman bands corresponding to the HDPE band (~1299 cm^{-1}) and a gradual increase of the intensity of the band associated with cellulose (~1100 cm^{-1}). The existence of the Raman band located at ~1100 cm^{-1} confirms the presence of

the CNCs in the mixing region (Figure 7.3 B and D; navy colour). The scale of the colours change from ‘navy’ to ‘cyan’, moving inward to the core of the aggregates. The regions rich in cellulose are depicted with colour scale changes from a lime to dark green, corresponding to an increase in the concentration of CNCs. Additionally, the presence of the cellulose is further confirmed by the presence of well-resolved regions of skeletal-bending modes, with intense Raman bands located at ~383 cm^{-1} and bending modes with a band located at ~1382 cm^{-1}. The intensity of Raman bands corresponding to cellulose gradually increases inward to the core of the aggregates. Raman bands corresponding only to the presence of cellulose dominate the core of the aggregate structures in the HDPE-cCNCs and HDPE-MAPE/cCNCs nanocomposites; they overlap with the Raman bands characteristic for HDPE, apart from the most intense band for the CH_2 twisting mode located at ~1299 cm^{-1} (Figure 7.3 A, C and B, D; dark green).

In the case of HDPE-PEO/cCNCs nanocomposites, the core of the aggregate structures for the composite specimens consists mainly of a PEO/cCNCs phase, which is confirmed by the presence of typical Raman bands located at ~380 cm^{-1} and ~1098 cm^{-1} as well as bands corresponding to CH_2 rocking modes and to COC stretching modes located at ~847 cm^{-1} and ~864 cm^{-1} and the CH_2 twisting and scissoring modes at ~1285 cm^{-1} and ~1483 cm^{-1} characteristic of PEO (Figure 7.3 E and F; dark green). It was shown in Section 5.2 the Raman band corresponding to CNCs located at ~1100 cm^{-1} shifts in position to ~1098 cm^{-1} suggesting the presence of an interaction between the CNCs and PEO. The Raman band located at ~1299 cm^{-1}, which is typical of HDPE, appears as a shoulder on the Raman band associated with PEO (at ~1285 cm^{-1}). Changes in the concentration between the

PEO/cCNCs phase and the HDPE matrix were assessed using the ratio of the Raman bands typical for each component; namely $I_{1299/1284}$ and $I_{1464/1480}$. It was found that these intensity ratios gradually decreased moving out from the core to the outer edge of the aggregates. The dark green colours correspond to regions rich in the PEO/cCNCs phase; a decrease in the concentration of this phase is reflected by a change from a deeper to a lighter colour. The mixing region is shown as a scale of blue colours, where the increase of this colour corresponds to an increase in the concentration of the HDPE matrix. The existence of a PEO/cCNCs phase in the entire aggregate area is confirmed by the Raman bands located at ~1098 cm^{-1} (CNCs) and ~847 cm^{-1} and ~860 cm^{-1} (PEO) (Figure 6.2 E and F, dark green - navy).

The estimation of the boundary between the aggregated and mixed phases is very important for the quantification of the degree of mixing between the filler, compatibiliser and matrix. The determination of the boundaries between different phases within the composites has been enabled by calculating the intensity ratio of the Raman band corresponding to polyethylene (~1301 cm^{-1}) to that of the CNCs (~1381 cm^{-1}) for HDPE-cCNCs and HDPE-MAPE/cCNCs nanocomposites (Table 7.1) and the Raman band characteristic of poly(ethylene oxide) (~1285 cm^{-1}) for HDPE-PEO/cCNCs nanocomposites (Table 7.2). The intensities of these Raman bands have been assessed by deconvolution using a Lorentzian function. The boundary between the aggregated and mixed phases in the HDPE-cCNCs, HDPE-MAPE/cCNCs and HDPE-PEO/cCNCs composites are estimated to be 1.1, 1.3 and 1.0 respectively, using the $I_{1301/1381}$ and

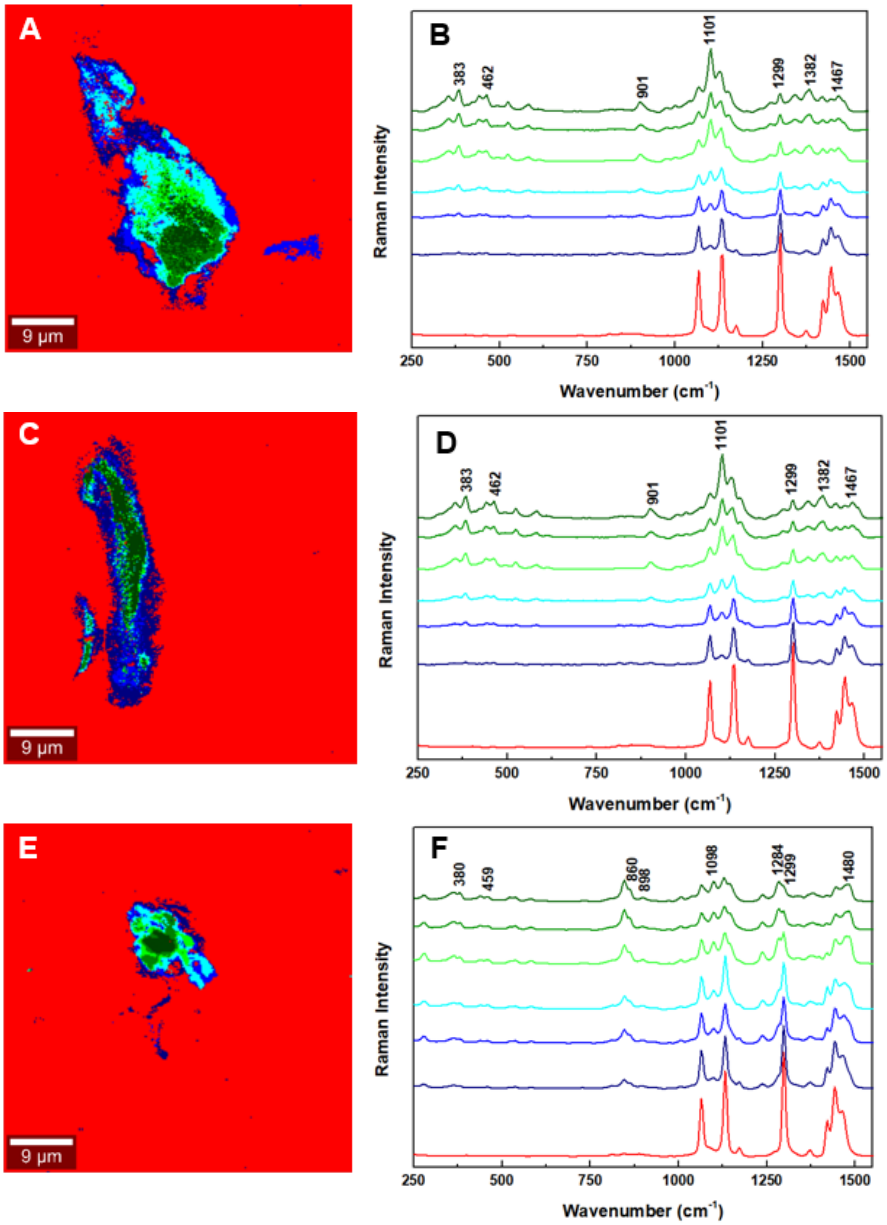

Figure 7.3 Typical chemical images of HDPE-cCNCs composites depicting the composition of a mapped cross-section: (A) HDPE-cCNCs1.5 (C) HDPE-MAPE/cCNCs1.5 and (E) HDPE-PEO/cCNCs1.5. Raman spectra corresponding to mixing components with the chemical images, where (B) HDPE-cCNCs1.5 (D) HDPE-MAPE/cCNCs1.5 and (F) HDPE-PEO/cCNCs1.5.

Table 7.1 Intensity of selected Raman bands and the intensity ratio used for description of the boundary of mixing degree levels of HDPE-cCNCs1.5 and HDPE-MAPE/cCNCs1.5 nanocomposites.

Composite	Raman Band Intensity		Intensity Ratio
HDPE-cCNCs1.5	1301 [cm^{-1}]	1381 [cm^{-1}]	1301/1381
Dark Green	130	170	0.8
Green	121	133	0.9
Lime	149	140	1.1
Cyan	155	70	2.2
Blue	210	20	10.5
Navy	344	16	21.5
HDPE-MAPE/cCNCs1.5	1301 [cm^{-1}]	1381 [cm^{-1}]	1301/1381
Dark Green	139	164	0.9
Green	124	120	1.0
Lime	154	123	1.3
Cyan	160	61	2.6
Blue	229	21	10.9
Navy	349	15	23.9

Table 7.2 Intensity of selected Raman bands and the intensity ratio used for description of the boundary of mixing degree levels of HDPE-PEO/cCNCs nanocomposites.

Composite	Raman Band Intensity		Intensity Ratio
HDPE-PEO/cCNCs1.5	1301 [cm^{-1}]	1285 [cm^{-1}]	1301/1285
Dark Green	110	176	0.6
Green	131	184	0.7
Lime	221	226	1.0
Cyan	358	168	2.1
Blue	388	131	3.0
Navy	545	65	8.4

$I_{1301/1285}$ ratios. Therefore, all regions with an intensity ratio <1 are considered to be aggregated, while those with an intensity ratio >1 are considered to be mixed. For example, in the case of HDPE-cCNCs and HDPE-MAPE/cCNCs nanocomposites, the blue scale colour (cyan, blue and navy) are mixed as the intensity of the Raman band corresponding to CNCs (~1381 cm^{-1}) are much lower than that of the intensity of the Raman band corresponding to HDPE (~1301 cm^{-1}).

7.2.3 Quantification of the Degree of Mixing

The chemical images analysis approach allows a quantitative assessment of the degree of mixing between the cCNCs and HDPE. Figure 7.4 (A, C and E) shows chemical images of the region corresponding to the composition of the HDPE-cCNCs, HDPE-MAPE/cCNCs and HDPE-PEO/cCNCs nanocomposites. The chemical images disclose three regions that represent the average Raman band for each specific area and also demonstrate the mixing area between the components. The red colour dominates these images, and confirms the presence of the polyethylene matrix. The areas corresponding to the cellulose aggregates are depicted in green (intensity ratio < 1) and the area considered to exhibit good mixing are assigned to blue colours (intensity ratio >1). The Raman spectra assigned to all three regions of the chemical images are presented in Figure 7.4 (B, D and F). Their detailed analysis provides additional information related to the interfacial adhesion between the filler and matrix.

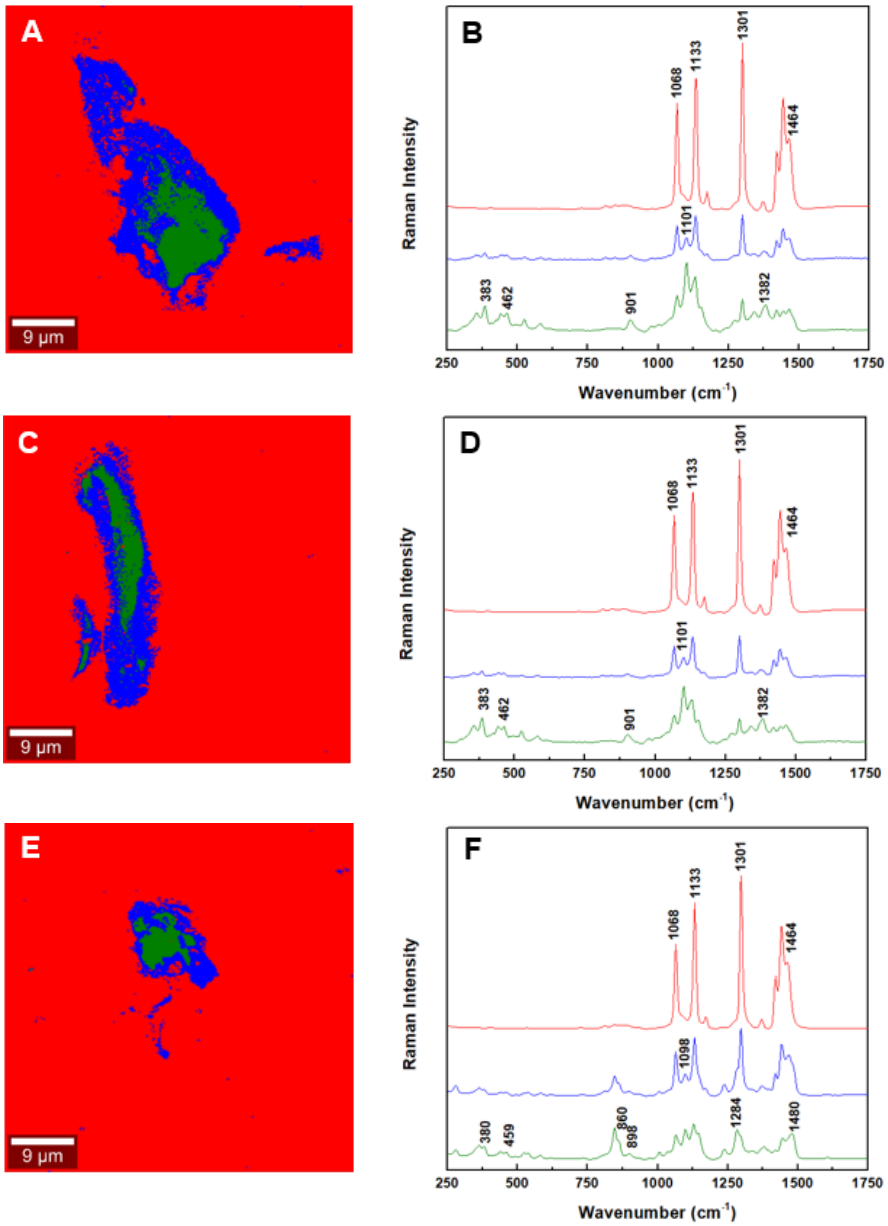

Figure 7.4 Typical chemical images of (A) HDPE-cCNCs1.5 (C) HDPE-MAPE/cCNCs1.5 and (E) HDPE-PEO/cCNCs1.5 composites depicting the general chemical composition of a mapped cross-section from Figure 5. Typical Raman spectra of bands observed within the mixing zone of the chemical images of (B) HDPE-cCNCs1.5 (D) HDPE-MAPE/cCNCs1.5 and (F) HDPE-PEO/cCNCs1.5.

Figures 7.5 (A,C,E) and 7.5 (B,D,F) illustrate the grayscale images of the blue and green areas respectively obtained from the chemical images of HDPE-cCNCs1.5,

HDPE-MAPE/cCNCs1.5 and HDPE-PEO/cCNCs1.5 composites. The grayscale images consist of a white region which corresponding to the object and a black region corresponding to the background. The conversion of the chemical images to the greyscale combined with a splitting between each colour allows the extraction of the objects and a quantification of their respective areas. Tables 7.3 and 7.4 present the areas corresponding to the matrix, the mixing of the matrix with the filler and the filler aggregation within the chemical images, as estimated using Image-J software. The total area of the Raman images is 2500 μm^2. Figure 7.6 illustrates the dependence of the degree of mixing and degree of aggregation as a function of cCNCs loadings for HDPE-cCNCs, HDPE-MAPE/cCNCs and HDPE-PEO/cCNCs composites. The average ratio of Blue/(Red + Blue + Green) areas can be used as an indication of the degree of mixing. From Figure 7.6 A, the average value of the degree of mixing show a high standard deviation suggesting that the nanocomposites prepared using MAPE and PEO as compatibilisers (HDPE-MAPE/cCNCs and HDPE-PEO/cCNCs) do not exhibit a correlation between the degree of mixing and CNCs loadings. On the other hand, the average ratio of Green/(Red + Blue + Green) areas can be used to quantify the degree of aggregation between the fillers and matrix (Figure 7.6 B). At 1.5 wt.% cCNCs loadings, the degree of aggregation is much higher for HDPE/cCNCs than for HDPE-MAPE/cCNCs and HDPE-PEO/cCNCs. The degree of aggregation of HDPE/cCNCs1.5 composites decrease from 0.06 to 0.02 and 0.01 for HDPE-MAPE/cCNCs1.5 and HDPE-PEO/cCNCs1.5 respectively. This suggests that the addition of the compatibilising agents reduces the tendency of cCNCs to agglomerate during the melt compounding with the HDPE matrix. The decrease in agglomeration with the addition of a

compatibiliser supports the increases in mechanical properties of the nanocomposites at this level of loading. This suggests that less aggregation, and therefore more dispersion of the CNCs, is likely to lead to stronger and stiffer nanocomposites. Similar trends were observed for a study of CNCs-polypropylene (PP) composites using maleated PP (MAPP) as a coupling agent (Agarwal *et al.*, 2012). From Raman mapping and analysis, the dispersion index for the CNCs_MAPP_PP composites was significantly higher than for CNCs_PP composites. Furthermore, this agrees with the increases in the tensile strength and modulus for CNCs_MAPP_PP composites compared to CNCs_PP composites. This is thought to be as a result of an improved CNCs-PP interface and better dispersion of the reinforcing phase. It is worthwhile noting that all nanocomposites samples exhibit large agglomerate structures. These agglomerate structures decrease the overall observed area corresponding to the presence of CNCs, and prevent the use of Raman images as a means to estimate of the stoichiometric ratio of components. Hence, they are useful for identifying the composition, quantifying the degree of mixing, and the degree of aggregation between components. Both of those variables (degree of mixing and degree of aggregation) were found to be independent of the cCNCs loading for the all nanocomposite samples. It is worth noting that the spatial resolution of the Raman images is limited by the size of the laser spot, which depends on the laser wavelength, objective lens and associated optics. In this study, it is not possible to detect the aggregates structure smaller than ~2 μm but one cannot exclude the presence of smaller aggregates structure below detection limit of this technique.

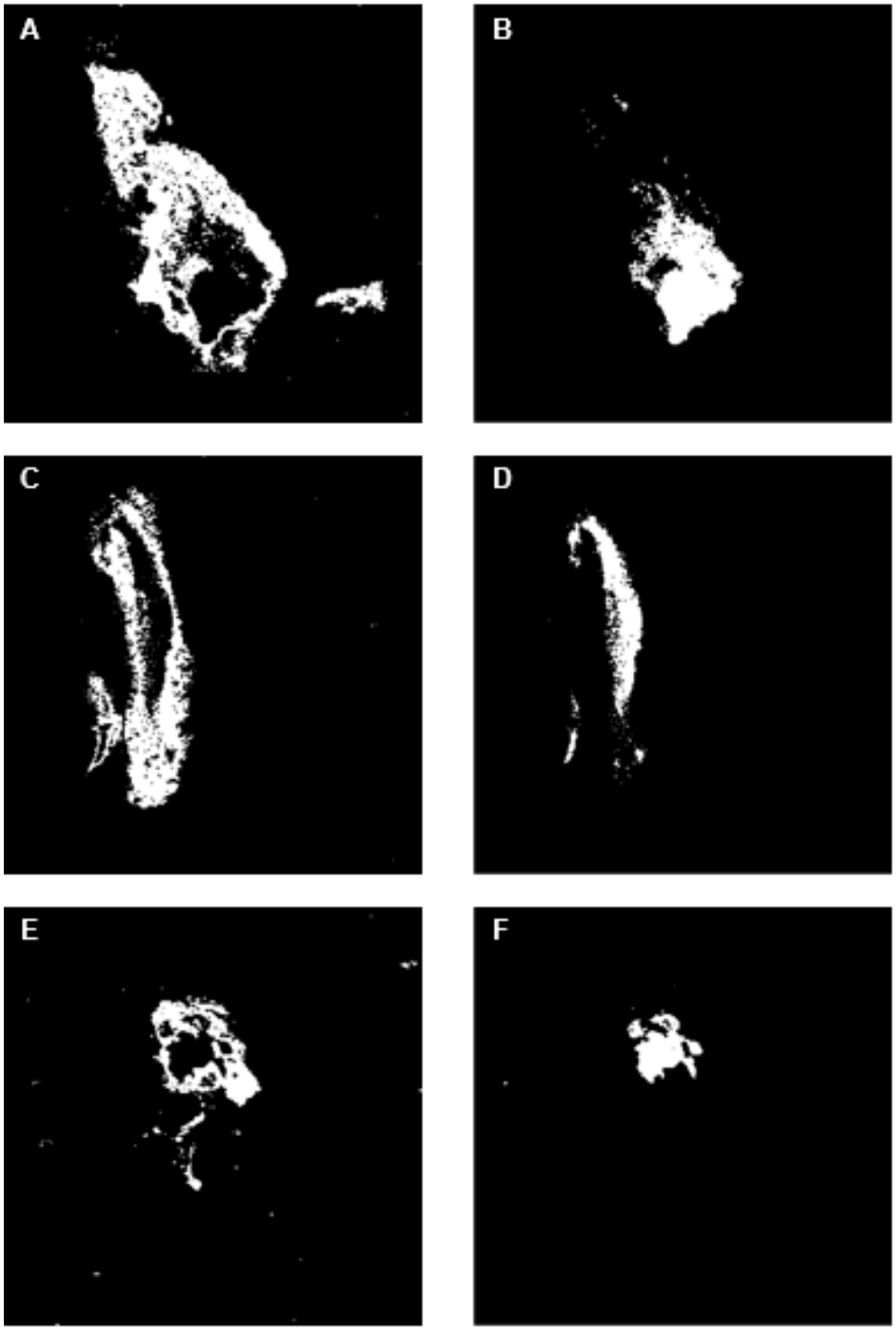

Figure 7.5 Grayscale images corresponding to blue area (A, C, E) and green area (B, D, F) at chemical images of HDPE-cCNCs1.5, HDPE-MAPE/cCNCs1.5 and HDPE-PEO/cCNCs1.5.

Table 7.3 Average area fraction of the component of chemical maps quantified for HDPE-cCNCs and HDPE-MAPE/cCNCs composites using Image-J software.

Composite	Area fraction			Ratio of fraction	
	Red (R)* [μm^2]	Blue (B)* [μm^2]	Green (G)* [μm^2]	B/(R+B+G)	G/(R+B+G)
HDPE-cCNCs0.5	2359±106	79±22	55±29	0.03±0.01	0.02±0.01
HDPE-cCNCs1.5	2169±109	176±97	147±58	0.08±0.04	0.06±0.02
HDPE-cCNCs2.5	2224±123	124±55	152±128	0.05±0.02	0.06±0.05
HDPE-cCNCs5	2075±152	269±130	148±101	0.11±0.05	0.06±0.04
HDPE-MAPE/cCNCs0.5	2364±112	81±75	51±26	0.03±0.03	0.02±0.01
HDPE-MAPE/cCNCs1.5	2280±102	174±110	55±28	0.07±0.04	0.02±0.01
HDPE-MAPE/cCNCs2.5	2276±96	151±125	74±55	0.06±0.05	0.03±0.02
HDPE-MAPE/cCNCs5	2090±124	258±102	146±98	0.10±0.04	0.06±0.04

* Red – fraction area corresponding to HDPE;
* Blue – fraction area corresponding to cCNCs + HDPE;
* Green - fraction area corresponding to cCNCs.

Table 7.4 Average area fraction of the component of chemical maps quantified for HDPE-PEO/cCNCs composites using Image-J software.

Composite	Area fraction			Ratio of fraction	
	Red (R)* [μm^2]	Blue (B)* [μm^2]	Green (G)* [μm^2]	B/(R+B+G)	G/(R+B+G)
HDPE-PEO/cCNCs0.5	2415±97	55±24	28±22	0.02±0.01	0.01±0.01
HDPE-PEO/cCNCs1.5	2320±99	152±89	35±24	0.06±0.04	0.01±0.01
HDPE-PEO/cCNCs2.5	2390±121	77±56	29±28	0.03±0.02	0.01±0.01
HDPE-PEO/cCNCs5	2194±108	201±126	101±54	0.08±0.05	0.04±0.02

* Red – fraction area corresponding to HDPE;
* Blue – fraction area corresponding to cCNCs + PEO + HDPE;
* Green - fraction area corresponding to cCNCs + PEO

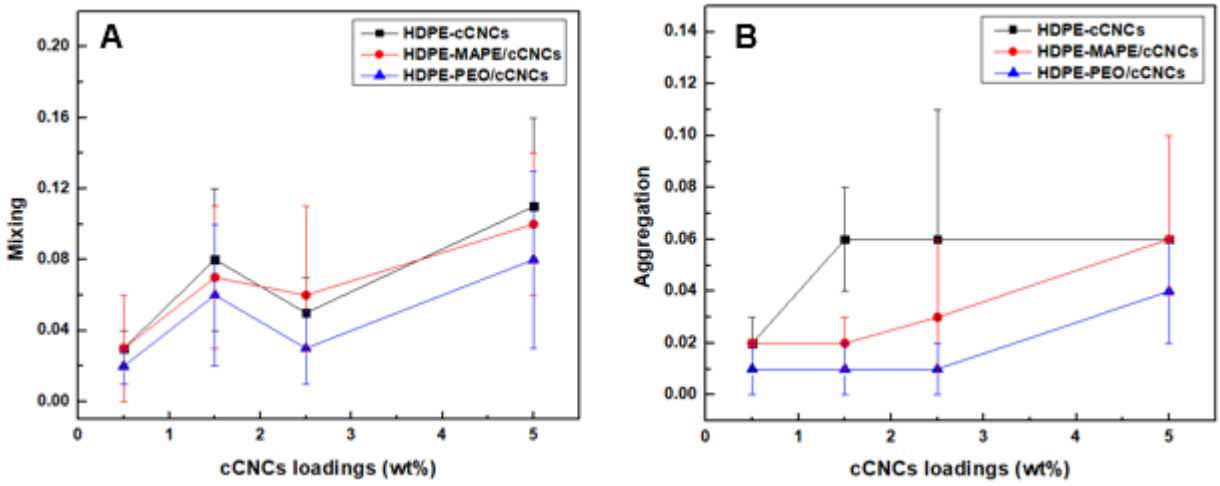

Figure 7.6 (A) degree of mixing and (B) degree of aggregation of cCNCs in HDPE-cCNCs, HDPE-MAPE/cCNCs and HDPE-PEO/cCNCs composites at 0.5, 1.5, 2.5 and 5 wt.% cCNCs loadings.

7.3 Raman Imaging of tCNCs Reinforced HDPE Nanocomposites

7.3.1 Raman Images of Spatial Mixing of Nanocomposites Components

Figure 7.7 (also Figure A4, A5 and A6 in the Appendix) presents typical images from HDPE-tCNCs, HDPE-MAPE/tCNCs and HDPE-PEO/tCNCs composite samples. The same colour scale was used for the tCNCs based nanocomposites, as for cCNCs based nanocomposites; a bright yellow colour corresponds to the highest intensity of the selected Raman bands while a deep brown colour to the areas where these bands show a significantly low intensity or are not detectable. The bright yellow colour in Figures 7.7 (A) and (C) indicates a high intensity, attributed to a Raman band located at ~1100 cm^{-1} due to the presence of tCNCs. These images further reveal the tendency of tCNCs to form aggregates, independent of the compatibiliser and source of cellulose used for their preparation. Similar to cCNCs based nanocomposites, tCNCs are aggregated in the volume of HDPE matrix with random shapes. The intensity of the yellow colour changes across the aggregates, suggesting a variability in the concentrations of tCNCs. A deep brown colour surrounding the tCNCs' aggregates indicates the absence of the Raman band located at ~1100 cm^{-1}, and therefore a lack of tCNCs in this area (Figure 7.7 A and C). These regions turn to a bright yellow, when the intensity of a Raman band located at ~1301 cm^{-1}, corresponding to CH_2 twisting mode in polyethylene, is observed (Figure 7.7 B and D). The intensity of the Raman band indicative of HDPE reduces to a 'light brown' colour in the areas assigned to aggregates of tCNCs. This colour change indicates the existence of a region where mixing of the filler (tCNCs) and matrix (HDPE) takes place.

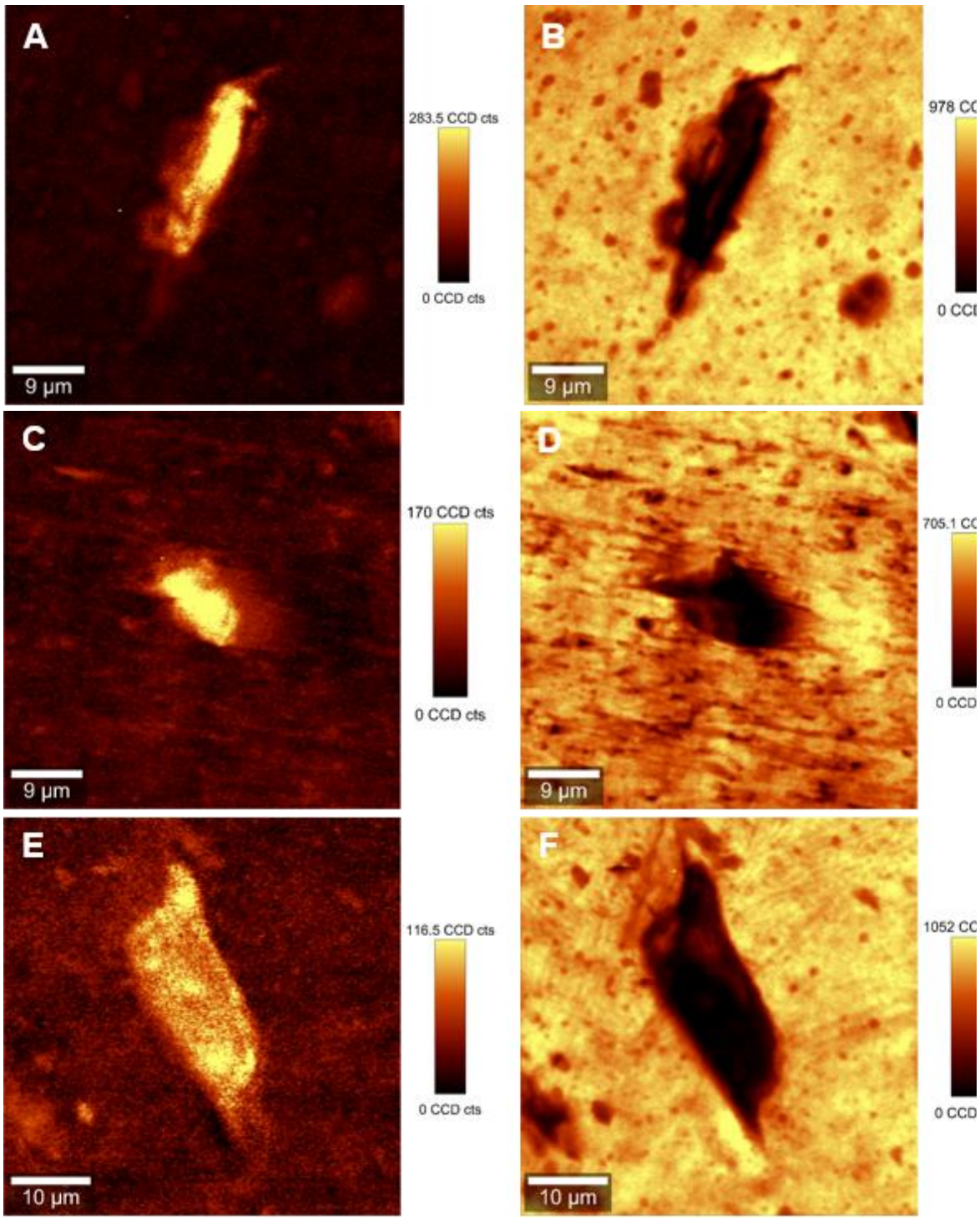

Figure 7.7 Typical Raman images of HDPE-tCNCs1.5 (A and B), HDPE-MAPE/tCNCs1.5 (C and D) and HDPE-PEO/tCNCs1.5 (E and F) composites depicting the intensity of a Raman band located at ~1100 cm^{-1} (A, C, and E) and ~1301 cm^{-1} (B, D, and F).

7.3.2 Chemical Images of Spatial Mixing of Nanocomposites Components

Figure 7.8 illustrates the phase changes in the concentration between filler, compatibiliser and matrix in the composites for the HDPE-CNCs, HDPE-MAPE/tCNCs and HDPE-PEO/tCNCs composite samples. These chemical images show spatially, the changes in the concentration of composite components (Fig. 7.8 A and C), while the Raman spectra reflect the changes in the relative intensities of their respective Raman bands (Fig. 7.8 B and D). For the HDPE-CNCs and HDPE-MAPE/tCNCs composite samples, the core of the aggregates contains only cellulose. Raman bands corresponding only to the presence of cellulose dominate the core of the aggregate structures in these composites. Raman bands associated with these structures overlap with those characteristic for HDPE, apart from the most intense band for the CH_2 twisting mode located at ~1299 cm^{-1} (Figure 7.8A and B; dark green). Additionally, in the core of the aggregates, there are well resolved regions of cellulose skeletal-bending modes, with intense Raman bands located at ~383 cm^{-1} and bending modes with a band located at ~1382 cm^{-1}. The core of the aggregates for which the regions rich in cellulose are depicted with a dark green colours, changes to ‘green’ and ‘lime’ colours, corresponding to a reduction in the intensities of the Raman bands corresponding to cellulose. The intensity of the Raman bands corresponding to the cellulose concentration gradually decrease outwards from the core of the aggregates. A region of mixing between the tCNCs and HPDE is depicted as a blue scale of colours; this scale changes from a ‘cyan’ to a ‘navy’ colour, moving out from the core of the aggregates, matching the gradual increase in the intensity of the Raman bands corresponding to HDPE. The existence of the most intense cellulose Raman band, located at ~1101 cm^{-1}, confirms the

presence of CNCs in the mixing region (Fig. 7.8 A and B, navy). The core of the aggregate structures for the HDPE-PEO/tCNCs composite samples consists mainly of a CNCs-PEO phase. This is confirmed by the presence of typical cellulose Raman bands for cellulose and PEO. Raman bands located at ~380 cm^{-1} and 1098 cm^{-1} confirm the appearance of the cellulose in the core of the aggregate structures. Raman bands corresponding to CH_2 rocking modes and to COC stretching modes located at ~847 cm^{-1} and ~864 cm^{-1} and the CH_2 twisting and scissoring modes at ~1285 cm^{-1} and ~1483 cm^{-1} are characteristic of PEO (Fig. 7.8 C and D; dark green).

Similar to the cCNCs based composite, changes in the concentration between the PEO/tCNCs phase and the HDPE matrix were assessed using the ratio of the typical Raman bands for PEO and HDPE; namely $I_{1299/1284}$ and $I_{1464/1480}$. The existence of tCNCs in the entire aggregate structure is confirmed by the presence of Raman bands located at ~1098 cm^{-1}, while two Raman bands at ~847 cm^{-1} and ~860 cm^{-1} confirmed the presence of PEO (Fig. 7.8 C and D, dark green - navy). The determination of the boundaries between the different phases within the composites was enabled by calculating the intensity ratio of the Raman band corresponding to polyethylene (~1301 cm^{-1}) to that of the CNCs (~1381 cm^{-1}) for HDPE-tCNCs and HDPE-MAPE/tCNCs composites, and the PEO (~1285 cm^{-1}) for HDPE-PEO/tCNCs composites (Table 5 and 6). Similar to cCNCs based composites, all regions with an intensity ratio <1 were considered to be aggregated, while those with an intensity ratio >1 were considered to be mixed. From Table 7.5 and Table 7.6, the boundary between the aggregated and mixed phases in the CNCs/MAPE/HDPE and CNCs/PEO/HDPE.

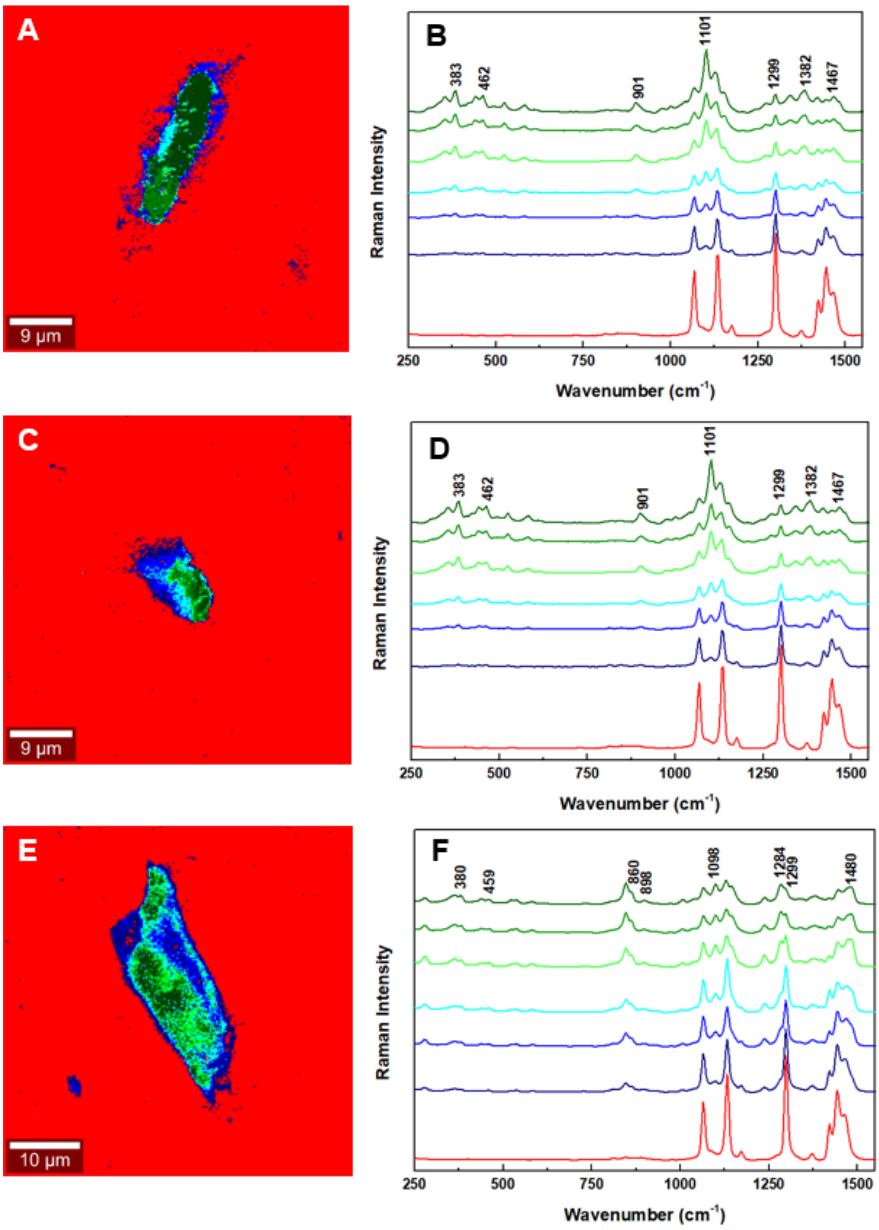

Figure 7.8 Typical chemical images of HDPE-tCNCs composites depicting the composition of a mapped cross-section: (A) HDPE-tCNCs1.5 (C) HDPE-MAPE/tCNCs1.5 and (E) HDPE-PEO/tCNCs1.5. Raman spectra corresponding to mixing components with the chemical images, where (B) HDPE-tCNCs1.5 (D) HDPE-MAPE/tCNCs1.5 and (F) HDPE-PEO/tCNCs1.5.

Table 7.5 Intensity of selected Raman bands and the intensity ratio used for description of the boundary of mixing degree levels of HDPE-tCNCs1.5 and HDPE-MAPE/tCNCs1.5 nanocomposites.

Composite	Raman Band Intensity		Intensity Ratio
HDPE-tCNCs1.5	1301 [cm^{-1}]	1381 [cm^{-1}]	1301/1381
Dark Green	142	174	0.8
Green	133	141	0.9
Lime	151	133	1.1
Cyan	161	65	2.5
Blue	212	19	11.2
Navy	341	17	20.6
HDPE-MAPE/tCNCs1.5	1301 [cm^{-1}]	1381 [cm^{-1}]	1301/1381
Dark Green	148	167	0.9
Green	136	130	1.1
Lime	157	119	1.3
Cyan	168	55	3.1
Blue	215	18	11.9
Navy	351	14	25.1

Table 7.6 Intensity of selected Raman bands and the intensity ratio used for description of the boundary of mixing degree levels of HDPE-PEO/tCNCs nanocomposites.

Composite	Raman Band Intensity		Intensity Ratio
HDPE-PEO/tCNCs1.5	1301 [cm^{-1}]	1285 [cm^{-1}]	1301/1285
Dark Green	112	171	0.7
Green	138	169	0.8
Lime	228	213	1.1
Cyan	341	183	1.9
Blue	391	130	3.0

Navy	557	64	8.8

composites are estimated to be 1.3 and 1.1 respectively, using the $I_{1301/1381}$ and $I_{1301/1285}$ ratios.

7.3.3 Quantification of the Degree of Mixing

Figure 7.9 (as well as Figures A5 and A6) show the chemical images extracted from the Raman images for the HDPE-tCNCs, HDPE-MAPE/tCNCs and HDPE-MAPE/tCNCs composites. A red colour dominates these images, which is related to the presence of HDPE matrix. The areas corresponding to the cellulose aggregates are depicted in green and blue colours. Similar to cCNCs based composites, the boundary between the aggregated (green) and mixed (blue) regions is distinguished by intensity ratios; the $I_{1301/1381}$ ratio for HDPE-MAPE/CNCs and the $I_{1301/1285}$ ratio for HDPE-PEO/CNCs. The Raman spectra assigned to all three regions of the chemical images are presented in Figure 7.9 B and D. Their detailed analysis provides additional information related to the interfacial adhesion between the filler and the compatibilisers. Figure 7.10 (A,C,E) and Figure 7.10 (B,D,F) present grayscale images of the blue and green areas respectively obtained from the chemical images of HDPE-cCNCs1.5, HDPE-MAPE/cCNCs1.5 and HDPE-PEO/cCNCs1.5 composites. As shown in Section 7.2.3, the conversion of the chemical images to a greyscale combined with a splitting between each of the colours allows the extraction of the objects and a quantification of their respective areas. Table 7.7 and Table 7.8 shows the quantified areas corresponding to each of the Raman images estimated using Image-J software. Similar to cCNCs based composites, the degree of mixing

can be calculated from the average ratio of fillers + HDPE matrix area to total area (Blue/(Red + Blue + Green)). On the other hand, the average ratio of fillers area to total area (Green/(Red + Blue + Green)) can be used as an indicator of degree of aggregation. Figure 7.11 illustrates the dependence of the degree of mixing and degree of aggregation as a function of tCNCs loadings for HDPE-tCNCs, HDPE-MAPE/tCNCs and HDPE-PEO/tCNCs composites.At 1.5 wt.% tCNCs loading, the addition of MAPE and PEO as a compatibiliser to the HDPE-tCNCs composites reduces the degree of aggregation of HDPE-tCNCs composites by 57%. Again, it appears that at this loading the addition of MAPE and PEO to the HDPE-tCNCs composites reduces the tendency of CNCs to aggregate during the melt compounding process. PEO and MAPE has shown to have an interaction with the CNCs through hydrogen bonding and esterification (see Section 5.1 and 5.2 respectively). These interfacial interactions have an impact on the degree of aggregation of the CNCs in the HDPE matrix, leading to nanocomposites with enhanced mechanical properties. The average value of the degree of mixing for tCNCs based composites shows a high standard deviation between each of the samples suggesting that no correlation between the degree of mixing and type of compatibiliser. Additionally, both the degree of mixing and degree of aggregation are independent of the tCNCs loadings for all nanocomposites samples; a similar trend is noted for cCNCs based nanocomposites.

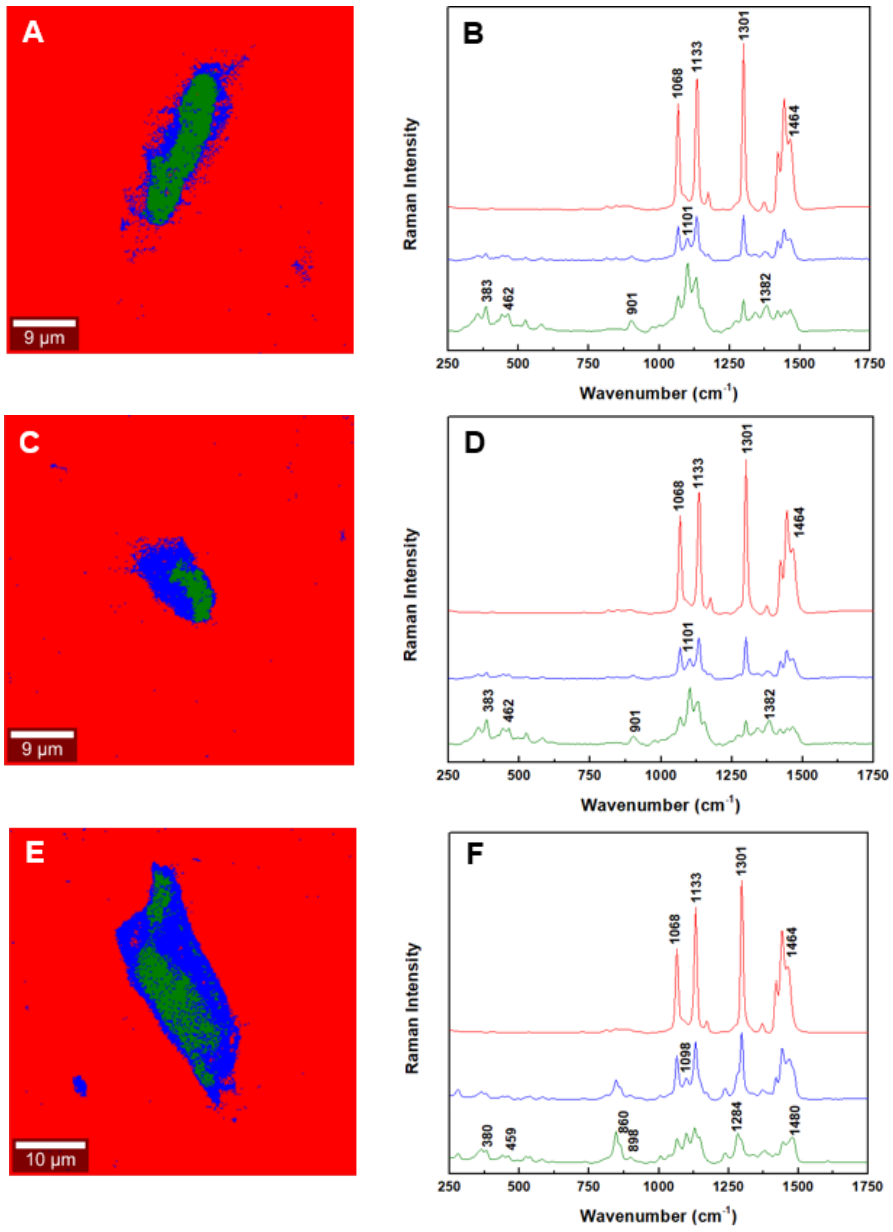

Figure 7.9 Typical chemical images of (A) HDPE-tCNCs1.5 (C) HDPE-MAPE/tCNCs1.5 and (E) HDPE-PEO/tCNCs1.5 composites depicting the general chemical composition of a mapped cross-section from Figure 5. Typical Raman spectra of bands observed within the mixing zone of the chemical images of (A) HDPE-tCNCs1.5 (C) HDPE-MAPE/tCNCs1.5 and (E) HDPE-PEO/tCNCs1.5.

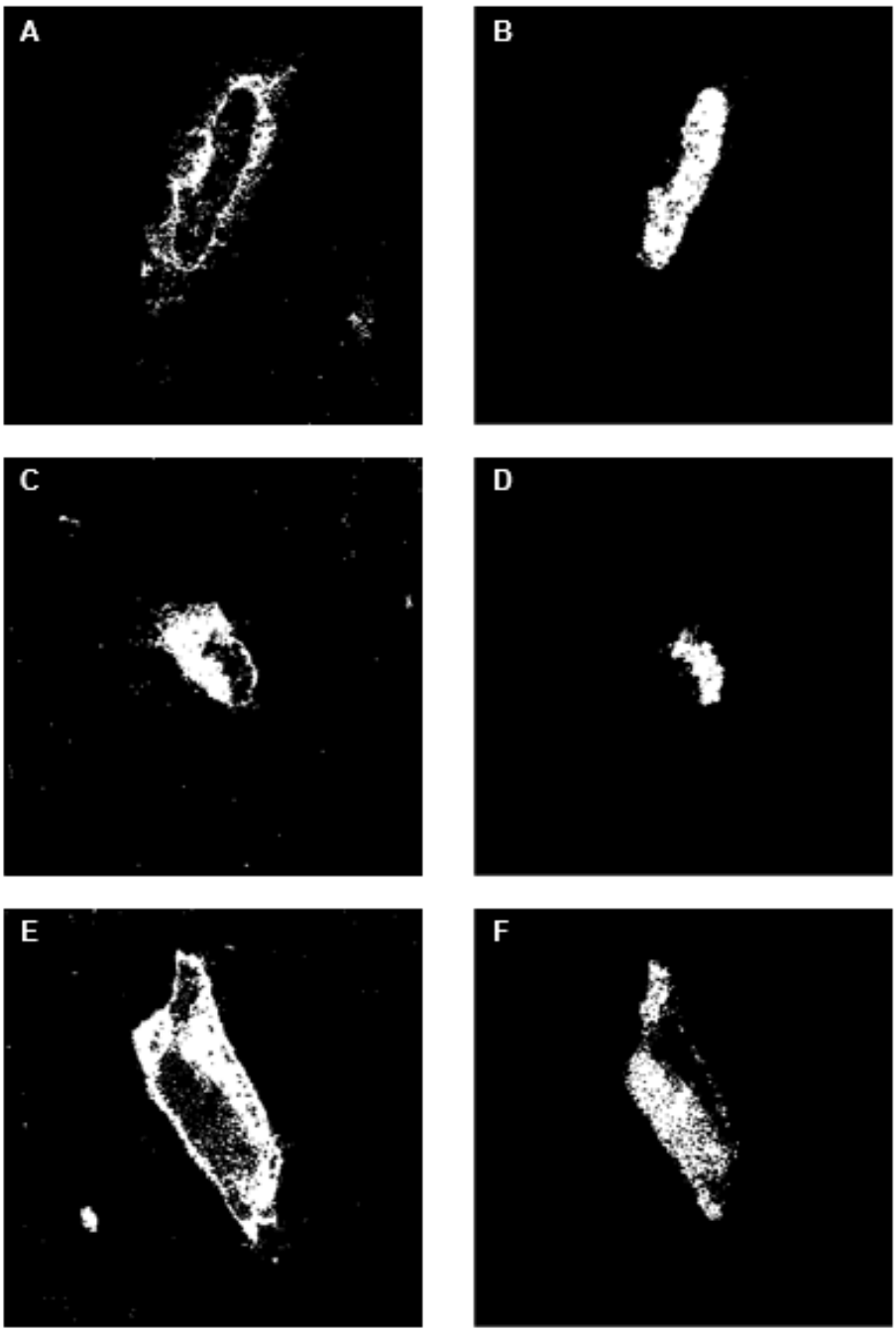

Figure 7.10 Grayscale images corresponding to blue area (A, C, E) and green area (B, D, F) at chemical images of HDPE-tCNCs1.5, HDPE-MAPE/tCNCs1.5 and HDPE-PEO/tCNCs1.5.

Table 7.7 Average area fraction of the component of chemical maps quantified for HDPE-tCNCs and HDPE-MAPE/tCNCs composites using Image-J software.

Composite	Area fraction			Ratio of fraction	
	Red (R)* [μm^2]	Blue (B)* [μm^2]	Green (G)* [μm^2]	B/(R+B+G)	G/(R+B+G)
HDPE-tCNCs0.5	2388±122	55±26	58±29	0.02±0.01	0.02±0.01
HDPE-tCNCs1.5	2219±117	101±82	179±55	0.04±0.03	0.07±0.02
HDPE-tCNCs2.5	2260±124	78±31	159±59	0.03±0.01	0.06±0.02
HDPE-tCNCs5	2110±136	229±133	157±61	0.09±0.05	0.06±0.02
HDPE-MAPE/tCNCs0.5	2370±133	77±54	51±29	0.03±0.02	0.02±0.01
HDPE-MAPE/tCNCs1.5	2261±126	154±102	79±59	0.06±0.04	0.03±0.02
HDPE-MAPE/tCNCs2.5	2252±119	161±84	84±27	0.06±0.03	0.03±0.01
HDPE-MAPE/tCNCs5	2211±129	248±105	133±62	0.10±0.04	0.05±0.02

* Red – fraction area corresponding to HDPE;
* Blue – fraction area corresponding to tCNCs + HDPE;
* Green - fraction area corresponding to tCNCs

Table 7.8 Average area fraction of the component of chemical maps quantified for HDPE-PEO/tCNCs composites using Image-J software.

Composite	Area fraction			Ratio of fraction	
	Red (R)* [μm^2]	Blue (B)* [μm^2]	Green (G)* [μm^2]	B/(R+B+G)	G/(R+B+G)
HDPE-PEO/tCNCs0.5	2396±121	76±24	25±22	0.03±0.01	0.01±0.01
HDPE-PEO/tCNCs1.5	2287±127	131±79	79±23	0.05±0.03	0.03±0.01
HDPE-PEO/tCNCs2.5	2292±133	154±54	55±51	0.06±0.02	0.02±0.02
HDPE-PEO/tCNCs5	2162±±124	249±133	83±71	0.09±0.05	0.03±0.03

* Red – fraction area corresponding to HDPE;
* Blue – fraction area corresponding to tCNCs + PEO + HDPE;
* Green - fraction area corresponding to tCNCs + PEO

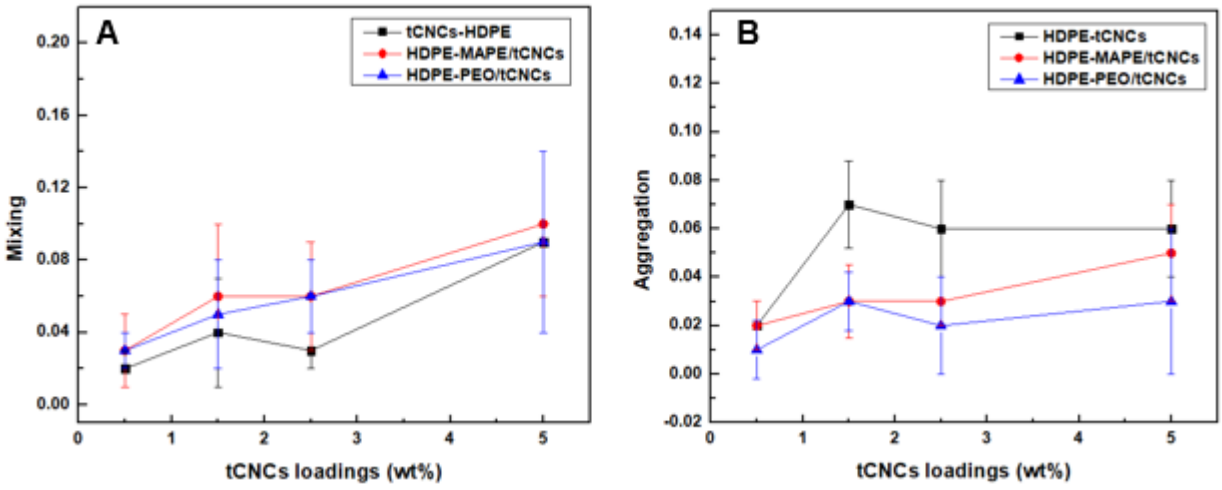

Figure 7.11 (A) degree of mixing and (B) degree of aggregation of tCNCs in HDPE-CNCs, HDPE/MAPE-tCNCs and HDPE/PEO-tCNCs composites at 0.5, 1.5, 2.5 and 5 wt.% tCNCs loadings.

7.4 Conclusions

In this chapter, Raman spectroscopy has been used to study the composition of CNC based nanocomposites. Through a combination of Raman images and chemical 'fingerprints' from these images, the degree of mixing and aggregation between components can be quantified. Detailed analysis provides additional information related to the interfacial adhesion between the filler and the matrix as well as the effect of the addition of compatibilisers. The boundary between the mixed and aggregated phases in HDPE-CNCs and HDPE-MAPE/CNCs nancomposites samples can be estimated using the intensity ratio of the Raman band corresponding to HDPE to the Raman band corresponding to cellulose. Meanwhile, the intensity ratio of a Raman band corresponding to HDPE to a band corresponding to PEO was used for HDPE-PEO/CNCs nanocomposites samples. The conversion of the chemical images to a greyscale image, combined with a splitting between each colour allows the extraction of the objects and a quantification of their respective areas. The area of fraction of the HDPE matrix, the mixing between the filler and matrix as well as the aggregation of the filler within matrix was quantified using Image-J software. Raman maps based on CNCs and HDPE Raman bands located at ~1100 cm^{-1} and ~1301 cm^{-1} respectively revealed that the CNCs were aggregated independent of the presence of MAPE and PEO compatibiliser, and also source of CNCs used in their production. The results showed that the CNCs mixed to varying degrees in the HDPE matrix. The degree of mixing and degree of aggregation are found to be independent of the CNCs loading for the all nanocomposites samples due to high error bar in the data analysis. The composites prepared using MAPE and

PEO as compatibilisers in the HDPE-cCNCs and HDPE-tCNCs composites at 1.5 wt.% CNCs loadings decrease the degree of aggregation of nanocomposites samples. It appears that the optimum loading of CNCs in the MAPE and PEO compatibilised composites is close to 1.5 wt.%; above this loading CNCs aggregation is observed. In conclusion, the obtained results show that the use of Raman spectroscopic imaging coupled with proper methods for analysis of the obtained spectra gives an effective tool for quantitative and reliable estimation of degree of mixing and aggregation of fillers in melt compounded HDPE.

CHAPTER 8

CONCLUSIONS

8.1 Summary

In this study, two types of CNCs obtained from cotton and tunicates have been used as sources of cellulose to produce CNCs reinforced HDPE composites by melt compounding. Two types of compatibiliser; MAPE and PEO were also used and compared. The results of this study demonstrate the effect of several factors on the interfacial behavior between nanocellulose fillers and thermoplastic polymer matrix. Raman spectroscopy has been used as a tool to study the interfaces between CNCs and the HDPE matrix. Standard mechanical testing methods could not be used to obtain the same amount of information for these materials due to the size constraint of nano-sized fillers. Raman mapping combined with chemical images has also been used to quantify the degree of mixing and degree of aggregation of CNCs in the HDPE matrix.

The two types of CNCs (cotton and tunicate) were characterised in terms of morphology and chemical composition. Observations using TEM revealed rod-like shaped particles, and their dimensions and aspect ratios. Tunicate-sourced CNCs have higher aspect ratios, which is attributed to their longer lengths and smaller diameters compared to cotton-sourced CNCs. The concentrations of the sulfate

groups on the surface of tunicate CNCs (64 mmol kg^{-1}) was found to be significantly higher than for cotton CNCs (40 mmol kg^{-1}). This is believed to be the result of different treatment conditions such as hydrolysis temperature and the concentration of the acid used in the hydrolysis process. A comparison between cotton and tunicate CNCs indicates that the crystallinity of tunicates is higher than for cotton CNCs. Cotton and tunicate CNCs are also found to exhibit an intense Raman band initially located at ~1100 cm^{-1}. The position of this band was shown to be sensitive to the effect of chain deformation upon the application of tensile deformation. Raman spectroscopy and FT-IR spectroscopy were used to confirm the presence of PEO in the PEO/CNCs and the intermolecular interaction established between PEO and the CNCs. Improved thermal stability of the cCNCs and tCNCs was observed showing the compatibilising action of PEO. However, the addition of CNCs leads to a decrease in the crystallinity of PEO; from 79% to 60% and 63% for cCNCs and tCNCs respectively.

In Chapter 5, CNCs reinforced HDPE composites with different sources of CNCs and compatibilisers were successfully prepared using a melt compounding method. The properties of the nanocomposites are influenced by several significant factors. These properties were compared with those of pure HDPE matrix and nanocomposites prepared without the presence of compatibilisers. The Raman technique has been used to study the components in the composites. It has been shown that the single components of the composites can be observed by obtaining a ‘fingerprint’ Raman spectrum of the HDPE matrix which is distinct from the reinforcing component. A shift in the position of characteristic Raman bands indicates the formation of hydrogen bonding between PEO compatibiliser and CNCs,

which in turn is thought to affect the properties of the nanocomposites. ATR-FTIR confirm the esterification reaction between hydrophobic MAPE and hydrophilic CNCs as an ester carbonyl peak (~1740 cm^{-1}) was observed in compatibilised nanocomposites sample.

When CNCs were melt compounded into the HDPE matrix, an enhanced modulus and strength of the resulting materials was observed, as compared to neat HDPE matrix. This enhancement is attributed to the presence of stiff CNCs in the matrix. An increase in tensile properties of nanocomposites was obtained with an increase in the weight fraction of CNCs, up to a 1.5 wt.% loading. After this point, a continuous decrease in tensile modulus and strength was reported, which is possibly due to the aggregation of CNCs at higher concentrations, leading to a reduction in the interaction between the matrix and CNCs.

The mechanical properties of the HDPE-cCNCs and HDPE-tCNCs composites revealed a significant improvement of Young`s modulus and strength when MAPE and PEO were used as a compatibiliser. This was attributed to better interfacial adhesion between the HDPE and the CNCs as a result of the formation of hydrogen bonding and esterification reaction between compatibiliser and CNCs. The application of a compatibiliser improved the mechanical properties without the need for any complex chemical modification of the CNCs.

The crystallization behavior of HDPE in the nanocomposites was investigated using DSC analysis. The addition of CNCs to the matrix material increased the crystallinity

of the samples at low filler loadings. It is thought that the nucleation effect of CNCs leads to an increase of crystallinity of the composites at low filler loadings. However, above a 1.5 wt.% CNCs concentration, the crystallinity started to decrease, possibly due to their aggregation and thereby a limited filler/matrix interface. With the addition of a compatibiliser, an increase in crystallinity was observed for the HDPE-MAPE/CNCs and HDPE-PEO/CNCs nanocomposites compared to HDPE-CNCs nanocomposites. The thermal stability of the nanocomposites was found to decrease as the CNCs loading increased compared to the pure polymer matrix. A filler content with a low degradation temperature was expected to reduce the thermal stability of the nanocomposites. The addition of MAPE and PEO compatibilisers to the nanocomposite decreased the onset degradation temperature. This was posssibly due to the low onset degradation temperature observed for the CNCs fillers, and HDPE-MAPE and HDPE-PEO themselves, compared to pure HDPE.

On the whole, polymer nanocomposites containing tCNCs consistently exhibited enhanced mechanical properties compared to cCNCs; this is thought to be mainly credited to their longer lengths and smaller widths (because this determines surface area and aspect ratio), modulus, and crystallinity. However, compared to tunicate, cotton is a more readily available source of cellulose for mass production of CNCs.

In Chapter 6, Raman spectroscopy was used to investigate the molecular deformation and stress transfer properties of CNCs reinforced HDPE composites. A shift in the position of Raman band initially located at ~1095 cm^{-1}, corresponding to the vibrations of the cellulose backbone polymer chain was followed under tensile

deformation. Meanwhile, a shift in the position of Raman band initially located at ~1132 cm^{-1}, corresponding to the C-C stretching modes of HDPE, has also been followed. The peak position of the Raman band initially located at ~1095 cm^{-1} for the CNCs reinforced HDPE matrix composite was found to shift towards a lower wavenumber when the composites were subjected to tensile deformation. These shifts indicate that stress transfers between the HDPE matrix and the CNCs in the composites, resulting in a direct deformation along the molecular backbone of the cellulose polymer. In comparison, very little shift (non-zero) was seen for the Raman band initially located at ~1132 cm^{-1}, which indicates possible load sharing within the matrix itself. The gradient of shift in the position of the Raman band initially located at ~1095 cm^{-1} increased with increasing CNCs loading up to 1.5 wt.%. Above this value, a continuous decrease in the gradient was reported. This is thought to be due to aggregation of the CNCs, thereby limiting the surface area that is in contact with the matrix phase, resulting in a reduction in stress transfer. The addition of PEO and MAPE as a compatibiliser to HDPE-CNCs composites has been found to facilitate the stress transfer process of HDPE-CNCs nanocomposites. This has been attributed to role of the compatibiliser to facilitate better interfacial interaction through hydrogen bonding and esterification between CNCs and HDPE matrix as shown in Section 5.3. No significant difference was however observed between the stress transfer properties of HDPE-PEO/cCNCs and HDPE-MAPE/cCNCs nanocomposites. However, HDPE-PEO/tCNCs nanocomposites exhibit a higher stress transfer compared to HDPE-MAPE/tCNCs nanocomposites. The gradient of shift of cCNCs based nanocomposites are found to be lower than the tCNCs based nanocomposites regardless of CNCs loading and the type of compatibiliser. The

lower stress transfer observed for cCNCs based nanocomposites could be explained by differences in aspect ratio and surface charges as shown in Sections 4.3 and 4.4 respectively.

In Chapter 7, the combination of the Raman spectroscopy technique; imaging and chemical analysis has been used to study the morphology of CNCs reinforced HDPE composites. The conversion of Raman spectra to chemical images and a quantitative evaluation of the composite components yields a degree of mixing and aggregation between components. Furthermore, the role and effectiveness of MAPE and PEO as compatibilisers and their interaction with CNCs in the melt compounding process has been evaluated. The distribution of celluloses in Raman images was verified by the intensity of two unique Raman band located at ~382 cm^{-1} and ~1101 cm^{-1}. Meanwhile, the presence of HDPE in the Raman images was confirmed by the Raman band located at ~1296 cm^{-1}. CNCs are found to form irregular agglomerated 'islands' within the HDPE independent of the filler loading, presence of MAPE and PEO compatibiliser and also source of CNCs used in composites production. Raman microscopy has been demonstrated to be able to quantify the degree of mixing and degree of aggregation between CNCs and HDPE. The chemical images show spatially the gradual changes in the concentration of the components within the composites, based on the changes in the relative intensity of their respective Raman bands. The chemical images reveal three major areas present in the CNCs reinforced HDPE composites; a pure CNCs phase, a PEO/CNCs phase and a matrix phase. An evaluation of the chemical images revealed that the region richest in CNCs or CNCs-PEO phases is relatively small compared to the aggregate structure size. The areas corresponding to pure HDPE matrix dominate the chemical maps of

the composites with different loadings (red area). One significant region of the maps, with reference to the composite preparation, is the ‘blue area’ which is associated with mixing between the CNCs and the matrix phases. A Raman spectrum corresponding to this region exhibits bands characteristic of CNCs, compatibilisers and HDPE, suggesting a good mixing of the components. The ratio of the fraction of the blue area (fillers and matrix) to the total area of the Raman images was able to quantify the effectiveness of the degree of mixing. Meanwhile, the ratio of the fraction of the green areas (fillers) to the total area of the Raman images quantifies the degree of aggregation. Both these parameters are found to be independent of the loading of the CNCs, which is mainly due to the large errors associated with the data. The limitation of the spatial resolution of the Raman images has limited the observation of aggregate structures smaller than 2 μm^2, but their presence cannot be excluded in the samples. In contrast to this, a decrease in the average degree of aggregation was observed for composites prepared using MAPE and PEO as compatibilisers in the HDPE-cCNCs and HDPE-tCNCs composites at 1.5 wt.% CNCs loadings. PEO and MAPE have been shown to have an interaction with the CNCs through hydrogen bonding and esterification respectively. These interfacial interactions have an impact on the aggregation of the CNCs in the HDPE matrix, leading to better composites prepared with PEO and MAPE as compatibilisers. It appears that the optimum loading of CNCs in the MAPE and PEO compatibilised composites is close to 1.5 wt.%; above this loading, the addition of the compatibilising agents seem unable to reduce the cCNCs agglomeration during melt compounding. In conclusion, it has been demonstrated that Raman spectroscopy is a versatile tool to provide rich and detail information about the morphology of CNCs

in a HDPE matrix supported by a detailed chemical quantification and morphological feature of the material.

To conclude, this study revealed that it is possible to optimize the mechanical properties and stress transfer of CNCs reinforced HDPE composites using high aspect ratio and crystallinity CNCs. Also, the use of a compatibiliser enhances the fibre-matrix interface and reduces the aggregation of the CNCs. The lack of a route towards large scale production, both due to supply of raw materials and the low yield, are the main drawbacks to using tunicate cellulose for this purpose compared to other sources.

8.2 Future work

The use of another acid for hydrolysis such as phosphoric or hydrochloric acid may be an alternative to the use of sulfuric acid. Hydrolysis with sulfuric acid causes the introduction of a considerable amount of negatively charged sulfate half- ester groups on the CNCs surfaces which catalyze the degradation of cellulose, especially at higher temperatures. The use of alternative acids could increase the thermal stability of CNCs and allow the formation of melt mixed CNCs reinforced polymer nanocomposites at higher temperature, mixing speed and time.

In order to improve the mechanical properties of CNCs reinforced polymer composites, the use of more highly oriented CNCs would be interesting. The alignment of CNCs in composites can be carried out under externally applied

magnetic field (Li *et al.*, 2010; Pullawan *et al.*, 2012). The alignment behaviour of CNCs under magnetic fields depends on the magnetic anisotropy of the CNCs. Thus, the tensile properties of samples can be observed both in the perpendicular and parallel direction of the samples to the tensile axis. The highest levels of stiffness and strength are obtained for composites when the reinforcing fibres are aligned in one direction. The networks of aligned CNCs also can be fabricated using an electrospinning technique, and composites are subsequently prepared using compression moulding (Park, Kang, Kim, & Jin, 2007; Rojas, Montero, & Forest, 2009). The ability to align the CNCs offers an interesting fabrication parameter to tailor properties, which could be incorporated into composite materials.

Compatibilisers have been proven to enhance the mechanical properties of the composites; however, it can be expected that there should exist an optimum concentration whereby the compatibilisers content should facilitate better CNCs and matrix interface. The mechanical properties of CNCs reinforced nanocomposites should be improved even further by optimizing the balance between compatibiliser, filler and matrix. Another interesting direction of research using the compatibiliser would be its effect of the environment on the properties of compatibilised nanocomposites. As the CNCs reinforced thermoplastic composite material can be used as a packaging product, the effect of water and moisture on the mechanical properties of composites is an important issue which should be investigated. It has been reported that the stress transfer of cellulose reinforced composite materials can be affected by water and the strength and modulus of the composites has been reported to significantly decrease (Mendez *et al.*, 2011; Rusli *et al.*, 2010). The use

of the compatibiliser for the production of CNCs reinforced thermoplastic composites could improve the water uptake resistance of the nanocomposites.

From this study, Raman spectroscopy was found to be versatile and powerful technique for studying the interfaces of the composite materials. It is however important to mention the limitations of this tool. From the instrumentation of view, the limitation for studying nanomaterials results from the spatial resolution of the images, which is limited by the size of laser spot. This resolution depends on the laser wavelength, objective lens and associated optics. The need to carry out capability at nano-meter resolved Raman spectroscopy on CNCs and the composites can be achieved by using the tip-enhanced Raman spectroscopy (TERS).

The use of a bio-sourced and biodegradable matrix to produce biocomposites material would be also very interesting. But on the other hand, the composites properties would be likely to be more sensitive to moisture. If the composites are fully biodegradable, another suggestion for future work would be to study the influence of aging on the stress transfer under composting condition.

CHAPTER 9

REFERENCES

Abidi, N., Cabrales, L., & Haigler, C. H. (2014). Changes in the cell wall and cellulose content of developing cotton fibers investigated by FTIR spectroscopy. *Carbohydrate Polymers*, *100*, 9–16. https://doi.org/10.1016/j.carbpol.2013.01.074

Abitbol, T., Marway, H., & Cranston, E. D. (2014). Surface modification of cellulose nanocrystals with cetyltrimethylammonium bromide. *Special Issue: Nanocellulose Nordic Pulp & Paper Research Journal*, *29*(1), 46–57.

Agarwal, U. P. (2006). Raman imaging to investigate ultrastructure and composition of plant cell walls : distribution of lignin and cellulose in black spruce wood (Picea mariana). *Planta*, *224*, 1141–1153.

Agarwal, U. P. (2017). Raman spectroscopy of CNC-and CNF-based nanocomposites. In *Handbook of Nanocellulose and Cellulose Nanocomposites* (First Edition). Wiley-VCHVerlag GmbH& Co. KGaA. https://doi.org/10.1002/9783527689972.ch18

Agarwal, U. P., & Atalla, R. H. (1986). In-situ Raman microprobe studies of plant cell walls: Macromolecular organization and compositional variability in the secondary wall of Picea mariana (Mill.) B.S.P. *Planta*, *169*(3), 325–332. https://doi.org/10.1007/BF00392127

Agarwal, U. P., Reiner, R. R., & Ralph, S. A. (2013). Estimation of cellulose crystallinity of lignocelluloses using near-IR FT-Raman spectroscopy and comparison of the Raman and Segal-WAXS methods. *Journal of Agricultural and Food Chemistry*, *61*(1), 103–113. https://doi.org/10.1021/jf304465k

Agarwal, U. P., Sabo, R., Reiner, R. S., Clemons, C. M., & Rudie, A. W. (2012). Spatially resolved characterization of cellulose nanocrystal-polypropylene composite by confocal raman microscopy. *Applied Spectroscopy*, *66*(7), 750–756. https://doi.org/10.1366/11-06563

Ahvenainen, P., Kontro, I., & Svedstrom, K. (2016). Comparison of sample crystallinity determination methods by X-ray diffraction for challenging cellulose I materials. *Cellulose*, *23*, 1073–1086. https://doi.org/10.1007/s10570-016-0881-6

Akil, H. M., Omar, M. F., Mazuki, A. A. M., Safiee, S., Ishak, Z. A. M., & Abu Bakar, A. (2011). Kenaf fiber reinforced composites: A review. *Materials and Design*, *32*(8–9), 4107–4121. https://doi.org/10.1016/j.matdes.2011.04.008

Al-Warid, D. A., & Al-Maamori, M. H. (2016). Study the effect of adding dust of cement in some of the mechanical properties of SBR composites. *World Scientific News*, *32*, 13.

Alloin, F., D'Aprea, A., Dufresne, A., Kissi, N. El, & Bossard, F. (2011). Poly(oxyethylene) and ramie whiskers based nanocomposites: influence of processing: extrusion and casting/evaporation. *Cellulose*, *18*, 957–973.

Ambrosio-Martin, J., Fabra, M. J., Lopez-Rubio, A., & Lagaron, J. M. (2015). Melt polycondensation to improve the dispersion of bacterial cellulose into polylactide via melt compounding: enhanced barrier and mechanical properties.

Biomacromolecules, *22*(11), 1201–1226. https://doi.org/10.1007/s10570-014-0523-9

Anglès, M. N., & Dufresne, A. (2001). Plasticized starch / tunicin whiskers nanocomposite materials . 2 . mechanical behavior. *Macromolecules*, *34*, 2921–2931. https://doi.org/10.1021/ma001555h

Araki, J., Wada, M., Kuga, S., & Okano, T. (1999). Influence of surface charge on viscosity behavior of cellulose microcrystal suspension. *Journal of Wood Science*, *45*(3), 258–261. https://doi.org/10.1007/BF01177736

Aranguren, M. I., Marcovich, N. E., Salgueiro, W., & Somoza, A. (2013). Effect of the nano-cellulose content on the properties of reinforced polyurethanes. A study using mechanical tests and positron anihilation spectroscopy. *Polymer Testing*, *32*(1), 115–122. https://doi.org/10.1016/j.polymertesting.2012.08.014

Araujo, J. R., Waldman, W. R., & De Paoli, M. A. (2008). Thermal properties of high density polyethylene composites with natural fibres: Coupling agent effect. *Polymer Degradation and Stability*, *93*(10), 1770–1775. https://doi.org/10.1016/j.polymdegradstab.2008.07.021

Ashori, A., Babaee, M., Jonoobi, M., & Hamzeh, Y. (2014). Solvent-free acetylation of cellulose nanofibers for improving compatibility and dispersion. *Carbohydrate Polymers*, *102*(1), 369–375. http://dx.doi.org/10.1016/j.carbpol.2013.11.067

Ashori, A., Harun, J., Raverty, W., & Yusoff, M. N. M. (2006). Chemical and morphological characteristics of Malaysian cultivated kenaf (Hibiscus cannabinus) fiber. *Polymer - Plastics Technology and Engineering*, *45*(1), 131–134. https://doi.org/10.1080/03602550500373782

Azouz, K. Ben, Ramires, E. C., Van Den Fonteyne, W., El Kissi, N., & Dufresne, A. (2012). Simple method for the melt extrusion of a cellulose nanocrystal reinforced hydrophobic polymer. *ACS Macro Letters*, *1*(1), 236–240. https://doi.org/dx.doi.org/10.1021/mz2001737

Bahar, E., Ucar, N., Onen, A., Wang, Y., Z, M. O., Ayaz, O., … Demir, A. (2012). Thermal and mechanical properties of polypropylene nanocomposite materials reinforced with cellulose nano whiskers. *Journal of Applied Polymer Science*, *125*(4), 2882–2889. https://doi.org/10.1002/app.36445

Beck-Candanedo, S., Roman, M., & Gray, D. G. (2005). Effect of reaction conditions on the properties and behavior of wood cellulose nanocrystal suspensions. *Biomacromolecules*, *6*(2), 1048–1054. https://doi.org/10.1021/bm049300p

Beckermann, G. W., & Pickering, K. L. (2008). Engineering and evaluation of hemp fibre reinforced polypropylene composites: Fibre treatment and matrix modification. *Composites Part A: Applied Science and Manufacturing*, *39*(6), 979–988. https://doi.org/10.1016/j.compositesa.2008.03.010

Bellan, L. M., Kameoka, J., & Craighead, H. G. (2005). Measurement of the Young's moduli of individual polyethylene oxide and glass nanofibres. *Nanotechnology*, *16*(8), 1095–1099. https://doi.org/10.1088/0957-4484/16/8/017

Blackwell, J., Vasko, P. D., & Koenig, J. L. (1970). Infrared and raman spectra of the cellulose from the cell wall of valonia ventricosa. *Journal of Applied Physics*, *41*(11), 4375–4379. https://doi.org/10.1063/1.1658470

Bledzki, A. K., & Gassan, J. (1999). Composites-reinforced with cellulose based fibres. *Progress in Polymer Science*, *24*, 221–274. https://doi.org/10.1016/S0079-6700(98)00018-5

Boissard, C. I. R., Bourban, P.-E., Tingaut, P., Zimmermann, T., & Manson, J.-A. E.

(2011). Water of functionalized microfibrillated cellulose as foaming agent for the elaboration of poly(lactic acid) biocomposites. *Journal of Reinforced Plastics and Composites*, *30*(8), 709–719.

Bondeson, D., Mathew, A., & Oksman, K. (2006). Optimization of the isolation of nanocrystals from microcrystalline cellulose by acid hydrolysis. *Cellulose*, *13*, 171–180. https://doi.org/10.1007/s10570-006-9061-4

Bondeson, D., & Oksman, K. (2007). Polylactic acid/cellulose whisker nanocomposites modified by polyvinyl alcohol. *Composites Part A: Applied Science and Manufacturing*, *38*(12), 2486–2492. https://doi.org/10.1016/j.compositesa.2007.08.001

Bordel, D., Putaux, J. L., & Heux, L. (2006). Orientation of native cellulose in an electric field. *Langmuir*, *22*(11), 4899–4901. https://doi.org/10.1021/la0600402

Bossard, F., El, N., Aprea, A. D., Alloin, F., & Dufresne, J. S. A. (2010). Influence of dispersion procedure on rheological properties of aqueous solutions of high molecular weight PEO. *Rheologica Acta*, *49*(5), 529–540. https://doi.org/10.1007/s00397-009-0402-8

Bowley, H. J., Gardiner, D. J., Gerrard, D. L., Graves, P. R., & Louden, J. D. (1989). *Practical Raman Spectroscopy*. London, Springer-Verlag.

Bras, J., Viet, D., Bruzzese, C., & Dufresne, A. (2011). Correlation between stiffness of sheets prepared from cellulose whiskers and nanoparticles dimensions. *Carbohydrate Polymers*, *84*(1), 211–215. http://dx.doi.org/10.1016/j.carbpol.2010.11.022

Brett, C. T., & Waldron, K. W. (1996). Physiology and biochemistry of plant cell walls. *Plant Science*, *123*(1–2), 211. https://doi.org/10.1016/s0168-9452(96)04565-7

Bulota, M., & Hughes, M. (2012). Toughening mechanisms in poly(lactic) acid reinforced with TEMPO-oxidized cellulose. *Journal of Materials Science*, *47*(14), 5517–5523. https://doi.org/10.1007/s10853-012-6443-x

Bulota, M., Jääskeläinen, a. S., Paltakari, J., & Hughes, M. (2011). Properties of biocomposites: Influence of preparation method, testing environment and a comparison with theoretical models. *Journal of Materials Science*, *46*(10), 3387–3398. https://doi.org/10.1007/s10853-010-5227-4

Bulota, M., Tanpichai, S., Hughes, M., & Eichhorn, S. J. (2012). Micromechanics of TEMPO-oxidized fibrillated cellulose composites. *ACS Applied Materials and Interfaces*, *4*(1), 331–337. https://doi.org/dx.doi.org/10.1021/am201399q

Capadona, J., Shanmuganathan, K., Tyler, D., Rowan, S., & Weder, C. (2008). Stimuli-Responsive Polymer Nanocomposites Inspired by the Sea Cucumber Dermis. *Carbohydrate Polymers*, *319*(5868), 1370–1374.

Carlborn, K., & Matuana, L. M. (2006). Functionalization of wood particles through a reactive extrusion process. *Journal of Applied Polymer Science*, *101*(5), 3131–3142. https://doi.org/10.1002/app.22577

Chang, H., Luo, J., Liu, H. C., Bakhtiary Davijani, A. A., Wang, P. H., & Kumar, S. (2017). Orientation and interfacial stress transfer of cellulose nanocrystal nanocomposite fibers. *Polymer (United Kingdom)*, *110*, 228–234. https://doi.org/10.1016/j.polymer.2017.01.015

Chen, C., Li, D., Hu, Q., & Wang, R. (2014). Properties of polymethyl methacrylate-based nanocomposites: Reinforced with ultra-long chitin nanofiber extracted from crab shells. *Materials and Design*, *56*, 1049–1056. https://doi.org/10.1016/j.matdes.2013.11.057

Chen, L., Wang, Q., Hirth, K., Baez, C., Agarwal, U. P., & Zhu, J. Y. (2015). Tailoring the yield and characteristics of wood cellulose nanocrystals (CNC) using concentrated acid hydrolysis. *Cellulose*, *22*(3), 1753–1762. https://doi.org/10.1007/s10570-015-0615-1

Cherukupalli, S. S., & Ogale, A. a. (2004). Online measurements of crystallinity using Raman spectroscopy during blown film extrusion of a linear low-density polyethylene. *Polymer Engineering & Science*, *44*(8), 1484–1490. https://doi.org/10.1002/pen.20144

Christer Wretfors. (2006). *Bio fibre technology used for military applications an overview*.

Clift, M. J. D., Foster, E. J., Vanhecke, D., Studer, D., Wick, P., Gehr, P., … Weder, C. (2011). Investigating the interaction of cellulose nanofibers derived from cotton with a sophisticated 3D human lung cell coculture. *Biomacromolecules*, *12*(10), 3666–3673. https://doi.org/dx.doi.org/10.1021/bm200865j |

de Menezes, A. J., Siqueira, G., Curvelo, A. A. S., & Dufresne, A. (2009). Extrusion and characterization of functionalized cellulose whiskers reinforced polyethylene nanocomposites. *Polymer*, *50*(19), 4552–4563. http://dx.doi.org/10.1016/j.polymer.2009.07.038

De Souza Lima, M. M., & Borsali, R. (2004). Rodlike cellulose microcrystals: Structure, properties, and applications. *Macromolecular Rapid Communications*, *25*(7), 771–787. https://doi.org/10.1002/marc.200300268

Dhar, P., Bhardwaj, U., Kumar, A., & Katiyar, V. (2015). Poly (3-hydroxybutyrate)/cellulose nanocrystal films for food packaging applications: Barrier and migration studies. *Polymer Engineering & Science*, *55*(10), 2388-2395.

Dong, X. M., Revol, J.-F., & Gray, D. G. (1998). Effect of microcrystallite preparation conditions on the formation of colloid crystals of cellulose. *Cellulose*, *5*(1), 19–32. https://doi.org/10.1023/A:1009260511939

Dothée, D., Berjot, M., & Marx, J. (1988). Measurement of the degree of crystallinity of polyethylene wear debris by means of Raman spectroscopy. *Polymer Degradation and Stability*, *20*(2), 149–155. https://doi.org/10.1016/0141-3910(88)90083-3

Dufresne, A., & Belgacem, M. N. (2013). Cellulose-reinforced Composites : From Micro-to Nanoscale. *Polimeros*, *23*, 277–286.

Dumitriu, S. (1996). *Polysaccharides in medical application*.

Edgar, C. D., & Gray, D. G. (2003). Smooth model cellulose I surfaces from nanocrystal suspensions. *Cellulose*, *10*(4), 299–306. https://doi.org/10.1023/A:1027333928715

Edwards, H. G., Farwell, D. W., & Webster, D. (1997). FT Raman microscopy of untreated natural plant fibres. *Spectrochimica Acta. Part A, Molecular and Biomolecular Spectroscopy*, *53A*(13), 2383–2392.

Edwards, H. G. M., Farwell, D. W., & Webster, D. (1997). FT Raman microscopy of untreated natural plant fibres. *Spectrochimica Acta Part A*, *53A*(13), 2383–2392. https://doi.org/10.1016/S1386-1425(97)00178-9

Eichhorn, S. J. (2011). Cellulose nanowhiskers: promising materials for advanced applications. *Soft Matter*, *7*(2), 303. https://doi.org/10.1039/c0sm00142b

Eichhorn, S. J., Dufresne, A., Aranguren, M., Marcovich, N. E., Capadona, J. R., Rowan, S. J., … Peijs, T. (2010). *Review: Current international research into*

cellulose nanofibres and nanocomposites. *Journal of Materials Science* (Vol. 45). https://doi.org/10.1007/s10853-009-3874-0

Eichhorn, S. J., Sirichaisit, J., & Young, R. J. (2001). Deformation mechanisms in cellulose fibres, paper and wood. *Journal of Materials Science*, *36*(13), 3129–3135.

Eichhorn, S. J., & Young, R. J. (2001). The Young's modulus of a microcrystalline cellulose. *Cellulose*, *8*, 197–207.

Eichhorn, S. J., & Young, R. J. (2004). Composite micromechanics of hemp fibres and epoxy resin microdroplets. *Composites Science and Technology*, *64*(5), 767–772. https://doi.org/10.1016/j.compscitech.2003.08.002

Elazzouzi-Hafraoui, S., Nishiyama, Y., Putaux, J. L., Heux, L., Dubreuil, F., & Rochas, C. (2008). The shape and size distribution of crystalline nanoparticles prepared by acid hydrolysis of native cellulose. *Biomacromolecules*, *9*, 57–65. https://doi.org/10.1021/bm700769p

Espigulé, E., Puigvert, X., Vilaseca, F., Mendez, J. A., Mutjé, P., & Girones, J. (2013). Thermoplastic starch-based composites reinforced with rape fibers: Water uptake and thermomechanical properties. *BioResources*, *8*(2), 2620–2630. https://doi.org/10.15376/biores.8.2.2620-2630

Espino-Pérez, E., Bras, J., Ducruet, V., Guinault, A., Dufresne, A., & Domenek, S. (2013). Influence of chemical surface modification of cellulose nanowhiskers on thermal, mechanical, and barrier properties of poly(lactide) based bionanocomposites. *European Polymer Journal*, *49*(10), 3144–3154. https://doi.org/http://dx.doi.org/10.1016/j.eurpolymj.2013.07.017

Espinosa, S. C., Kuhnt, T., Foster, E. J., & Weder, C. (2013). Isolation of thermally stable cellulose nanocrystals by phosphoric acid hydrolysis. *Biomacromolecules*, *14*, 1223–1230. https://doi.org/dx.doi.org/10.1021/bm400219u

Eyley, S., & Thielemans, W. (2014). Surface modification of cellulose nanocrystals. *Nanoscale*, *6*, 7764–7779. https://doi.org/10.1039/c4nr01756k

Fareez, I. M., Ibrahim, N. A., Wan Yaacob, W. M. H., Mamat Razali, N. A., Jasni, A. H., & Abdul Aziz, F. (2018). Characteristics of cellulose extracted from Josapine pineapple leaf fibre after alkali treatment followed by extensive bleaching. *Cellulose*, *25*(8), 4407–4421. https://doi.org/10.1007/s10570-018-1878-0

Faruk, O., Bledzki, A. K., Fink, H. P., & Sain, M. (2012). Biocomposites reinforced with natural fibers: 2000-2010. *Progress in Polymer Science*, *37*(11), 1552–1596. https://doi.org/10.1016/j.progpolymsci.2012.04.003

Favier, V., Chanzy, H., & Cavaille, J. Y. (1995). Polymer nanocomposites reinforced by cellulose whiskers. *Macromolecules*, *28*, 6365–6367.

Ferraro, John R., Nakamato, Kazuo Brown, C. W. (2003). *Introductory Raman Spectroscopy*. Elsevier.

Fortea-Verdejo, M., Bumbaris, E., Burgstaller, C., Bismarck, A., & Lee, K. Y. (2017). Plant fibre-reinforced polymers: where do we stand in terms of tensile properties? *International Materials Reviews*, *62*(8), 441–464. https://doi.org/10.1080/09506608.2016.1271089

Fortunati, E., Peltzer, M., Armentano, I., Torre, L., Jiménez, a., & Kenny, J. M. (2012). Effects of modified cellulose nanocrystals on the barrier and migration properties of PLA nano-biocomposites. *Carbohydrate Polymers*, *90*(2), 948–956. https://doi.org/10.1016/j.carbpol.2012.06.025

French, A. D., & Santiago Cintrón, M. (2013). Cellulose polymorphy, crystallite size, and the Segal crystallinity index. *Cellulose*, *20*(1), 583–588. https://doi.org/10.1007/s10570-012-9833-y

Gassan, J., Chate, A., & Bledzki, A. K. (2001). Calculation of elastic properties of natural fibers. *Journal of Materials Science*, *36*(15), 3715–3720. https://doi.org/10.1023/A:1017969615925

Gay, D., V.;, H. S., & Tsai, S. W. (2002). *Composite Materials: Design and Applications. 1 ed. United States of America: CRC Press. 2002. 523 p*.

Gehman, S. D., & Osterhof, H. J. (1936). Raman spectrum of rubber and some related hydrocarbons. *Journal of the American Chemical Society*, *58*(2), 215–218. https://doi.org/10.1021/ja01293a009

Gherardi Hein, P. R., & Tarcísio Lima, J. (2012). Relationships between microfibril angle, modulus of elasticity and compressive strength in Eucalyptus wood. *Maderas. Ciencia y Tecnología*, *14*(3), 267–274. https://doi.org/10.4067/s0718-221x2012005000002

Gierlinger, N., Schwanninger, M., Reinecke, A., & Burgert, I. (2006). Molecular changes during tensile deformation of single wood fibers followed by Raman microscopy. *Biomacromolecules*, *7*(7), 2077–2081. https://doi.org/10.1021/bm060236g

Gindl, W., & Keckes, J. (2007). Drawing of self-reinforced cellulose films. *Journal OfApplied Polymer Science*, *103*, 2703–2708. https://doi.org/10.1002/app

Goffin, A. L., Raquez, J. M., Duquesne, E., Siqueira, G., Habibi, Y., Dufresne, A., & Dubois, P. (2011). Poly(e-caprolactone) based nanocomposites reinforced by surface-grafted cellulose nanowhiskers via extrusion processing: Morphology, rheology, and thermo-mechanical properties. *Polymer*, *52*(7), 1532–1538. https://doi.org/10.1016/j.polymer.2011.02.004

Gong, G., Pyo, J., Mathew, A. P., & Oksman, K. (2011). Tensile behavior, morphology and viscoelastic analysis of cellulose nanofiber-reinforced (CNF) polyvinyl acetate (PVAc). *Composites Part A: Applied Science and Manufacturing*,*42*(9),1275–1282. http://dx.doi.org/10.1016/j.compositesa.2011.05.009

Grunert, M., & Winter, W. T. (2002). Nanocomposites of cellulose acetate butyrate reinforced with cellulose nanocrystals. *Journal of Polymers and the Environment*, *10*(1–2), 27–30. https://doi.org/1566-2543/02/0400-0027/0

Guhados, G., Wan, W., & Hutter, J. L. (2005). Measurement of the elastic modulus of single bacterial cellulose fibers using atomic force microscopy. *Langmuir*, *21*(14), 6642–6646.

Habibi, Y., Lucia, L. A., & Rojas, O. J. (2010). Cellulose Nanocrystals : Chemistry , Self-Assembly , and Applications. *Chemical Reviews*, *110*, 3479–3500. https://doi.org/10.1021/cr900339w

Haddar, M., Elloumi, A., Koubaa, A., & Bradai, C. (2017). Effect of high content of deinking paper sludge (DPS) on the reinforcement of HDPE. *Journal of Polymers and the Environment*, *25*(3), 617–627. https://doi.org/10.1007/s10924-016-0837-9

Hajji, P., Cavaille, J. Y., Favier, V., Gauthier, C., & Vigier, G. (1996). Tensile behavior of nanocomposites from latex and cellulose whiskers. *Polymer Composites*, *17*(4), 161–164.

Hamad, W. ., & Eichhorn, S. . (1997). Deformation micromechanics of regenerated

cellulose fibers using Raman spectroscopy. *Journal of Engineering Materials and Technology*, 309–313. https://doi.org/10.1115/1.2812262.

Han, J., Zhou, C., Wu, Y., Liu, F., & Wu, Q. (2013). Self-assembling behavior of cellulose nanoparticles during freeze-drying: Effect of suspension concentration, particle size, crystal structure, and surface charge. *Biomacromolecules*, *14*(5), 1529–1540. https://doi.org/10.1021/bm4001734

Hanley, S. J., Giasson, J., Revol, J.-F., & Gray, D. G. (1992). Atomic force microscopy of cellulose microfibrils: comparison with transmission electron microscopy. *Polymer*, *33*(21), 4639–4642.

Heux, L., Chauve, G., & Bonini, C. (2000). Nonflocculating and chiral-nematic self-ordering of cellulose microcrystals suspensions in nonpolar solvents. *Langmuir*, *16*(21), 8210–8212. https://doi.org/10.1021/la9913957

Hoffmann, C. L., & Rabolt, J. F. (1996). Self-assembled thin-film blends by polymer codeposition: Poly(ethylene oxide) and poly(methyl methacrylate). *Macromolecules*, (29), 2543–2547. https://doi.org/10.1021/ma950076t

Hossain, K. M. Z., Ahmed, I., Parsons, A. J., Scotchford, C. a., Walker, G. S., Thielemans, W., & Rudd, C. D. (2012). Physico-chemical and mechanical properties of nanocomposites prepared using cellulose nanowhiskers and poly(lactic acid). *Journal of Materials Science*, *47*(6), 2675–2686. https://doi.org/10.1007/s10853-011-6093-4

Hsieh, Y. C., Yano, H., Nogi, M., & Eichhorn, S. J. (2008). An estimation of the Young's modulus of bacterial cellulose filaments. *Cellulose*, *15*(4), 507–513. https://doi.org/10.1007/s10570-008-9206-8

Hull, D., & Clyne, T. W. (1996). *An Introduction to Composite Materials*. Cambridge: Cambridge University Press. https://doi.org/10.1017/CBO9781139170130

Ifuku, S., Morooka, S., Morimoto, M., & Saimoto, H. (2010). Acetylation of chitin nanofibers and their transparent nanocomposite films. *Biomacromolecules*, *11*(5), 1326–1330. https://doi.org/10.1021/bm100109a

Ifuku, S., Nogi, M., Abe, K., Handa, K., & Nakatsubo, F. (2007). Surface modification of bacterial cellulose nanofibers for property enhancement of optically transparent composites : Dependence on acetyl-group DS. *Biomacromolecules*, (8), 1973–1978. https://doi.org/10.1021/bm070113b

Islam, M. T., Alam, M. M., & Zoccola, M. (2013). Review on modification of nanocellulose for application in composites. *International Journal of Innovative Research in Science, Engineering and Technology*, *2*(10), 5444–5451.

Iwamoto, S., Kai, W., Isogai, A., & Iwata, T. (2009). Elastic modulus of single cellulose microfibrils from tunicate measured by atomic force microscopy. *Biomacromolecules*, *10*(9), 2571–2576. https://doi.org/10.1021/bm900520n

Jonoobi, M., Harun, J., Mathew, A. P., & Oksman, K. (2010). Mechanical properties of cellulose nanofiber (CNF) reinforced polylactic acid (PLA) prepared by twin screw extrusion. *Composites Science and Technology*, *70*(12), 1742–1747. http://dx.doi.org/10.1016/j.compscitech.2010.07.005

Jorfi, M., Roberts, M. N., Foster, E. J., & Weder, C. (2013). Physiologically Responsive, Mechanically Adaptive Bio- Nanocomposites for Biomedical Applications. *ACS Applied Materials and Interfaces*, *5*, 1517–1526. https://doi.org/dx.doi.org/10.1021/am303160j

Ju, X., Bowden, M., Brown, E. E., & Zhang, X. (2015). An improved X-ray diffraction method for cellulose crystallinity measurement. *Carbohydrate Polymers*, *123*,

476–481. http://dx.doi.org/10.1016/j.carbpol.2014.12.071
Jun, D., Guomin, Z., Mingzhu, P., Leilei, Z., Dagang, L., & Rui, Z. (2017). Crystallization and mechanical properties of reinforced PHBV composites using melt compounding: Effect of CNCs and CNFs. *Carbohydrate Polymers*, *168*, 255–262. https://doi.org/10.1016/j.carbpol.2017.03.076
Kahar, A. W. M., Sarifuddin, N., & Ismail, H. (2017). Structural, thermal and physico-chemical properties of high density polyethylene/natural rubber/modified cassava starch blends. *Iranian Polymer Journal*, *26*(2), 149–159. https://doi.org/10.1007/s13726-017-0507-3
Kakade, M. V., Givens, S., Gardner, K., Lee, K. H., Chase, D. B., & Rabolt, J. F. (2007). Electric field induced orientation of polymer chains in macroscopically aligned electrospun polymer nanofibers. *Journal of the American Chemical Society*, *129*(10), 2777–2782. https://doi.org/10.1021/ja065043f
Kalia, S., Dufresne, A., Cherian, B. M., Kaith, B. S., Avérous, L., Njuguna, J., & Nassiopoulos, E. (2011). Cellulose-based bio- and nanocomposites: A review. *International Journal of Polymer Science*, *2011*, 1–35. https://doi.org/10.1155/2011/837875
Keshk, S. M. A. S., & Omar, M. S. (2014). Bacterial cellulose and its phosphonic dichloride for efficient removal of metal ions. *American Journal of Polymer Science*, *4*(2), 46–53. https://doi.org/10.5923/j.ajps.20140402.04
Khalil, H. P. S., Bhat, A. H., & Ireana Yusra, A. F. (2012). Green composites from sustainable cellulose nanofibrils: A review. *Carbohydrate Polymers*, *87*(2), 963–979. http://dx.doi.org/10.1016/j.carbpol.2011.08.078
Khandelwal, M., & Windle, A. H. (2013). Self-assembly of bacterial and tunicate cellulose nanowhiskers. *Polymer*, *54*(19), 5199–5206. http://dx.doi.org/10.1016/j.polymer.2013.07.033
Kida, T., Hiejima, Y., & Nitta, K. (2016). Raman spectroscopic study of high-density polyethylene during tensile deformation. *International Journal of Experimental Spectroscopic Techniques*, *1*(1), 1–6.
Kida, T., Oku, T., Hiejima, Y., & Nitta, K. H. (2015). Deformation mechanism of high-density polyethylene probed by in situ Raman spectroscopy. *Polymer (United Kingdom)*, *58*, 88–95. https://doi.org/10.1016/j.polymer.2014.12.030
Kim, H., Kim, S., Kim, H., & Yang, H. (2006). Thermal properties of bio-flour-filled polyolefin composites with different compatibilizing agent type and content, *451*, 181–188. https://doi.org/10.1016/j.tca.2006.09.013
Kimura, F., Kimura, T., Tamura, M., Hirai, A., Ikuno, M., & Horii, F. (2005). Magnetic alignment of the chiral nematic phase of a cellulose microfibril suspension. *Langmuir*, *21*(5), 2034–2037. https://doi.org/10.1021/la0475728
Klemm, D., Heublein, B., Fink, H. P., & Bohn, A. (2005). Cellulose: fascinating biopolymer and sustainable raw material. *Angewandte Chemie - International Edition*, *44*(22), 3358–3393. https://doi.org/10.1002/anie.200460587 Angew.
Klemm, D., Kramer, F., Moritz, S., Lindström, T., Ankerfors, M., Gray, D., & Dorris, A. (2011). Nanocelluloses: A new family of nature-based materials. *Angewandte Chemie - International Edition*, *50*(24), 5438–5466. https://doi.org/10.1002/anie.201001273
Klemm, D., Philipp, B., & Mischnick, P. (1998). *Comprehensive Cellulose Chemistry. Vols 1 & 2*. *Angewandte Chemie-International Edition*. Wiley-Vch.
Kodjie, S. L., Li, L., Li, B., Cai, W., Li, C. Y., & Keating, M. (2006). Morphology and

crystallization behavior of HDPE/CNT nanocomposite. *Journal of Macromolecular Science Part B-Physics*, *45*(2006), 231–245. https://doi.org/10.1080/00222340500522299

Koduru, H. K., Marino, L., Scarpelli, F., Petrov, A. G., Marinov, Y. G., Hadjichristov, G. B., … Scaramuzza, N. (2017). Structural and dielectric properties of NaIO4 - Complexed PEO/PVP blended solid polymer electrolytes. *Current Applied Physics*, *17*(11), 1518–1531. https://doi.org/10.1016/j.cap.2017.07.012

Kondo, T., & Sawatari, C. (1994). Intermolecular hydrogen bonding in cellulose/poly(ethylene oxide) blends: thermodynamic examination using 2,3-di-O- and 6-O-methylcelluloses as cellulose model compounds. *Polymer*, *35*(20), 4423–4428. https://doi.org/10.1016/0032-3861(94)90102-3

Kondo, T., Sawatari, C., Gray, D. G., June, R., Manuscript, R., & September, R. (1994). Characterization of hydrogen bonding in cellulose-synthetic polymer blend systems with regioselectively substituted, 210–215. https://doi.org/10.1021/ma00079a031

Kong, K., & Eichhorn, S. J. (2005). Crystalline and amorphous deformation of process-controlled cellulose-II fibres. *Polymer*, *46*(17), 6380–6390. https://doi.org/10.1016/j.polymer.2005.04.096

Kosaka, P. M., Kawano, Y., Petri, H. M., Fantini, M. C. A., Petri, D. F. S., & Sa, U. De. (2007). Structure and properties of composites of polyethylene or maleated polyethylene and cellulose or cellulose esters. *Journal of Appplied Polymer Science*, *103*, 402–411. https://doi.org/10.1002/app.24836

Kvien, I., & Oksman, K. (2007). Orientation of cellulose nanowhiskers in polyvinyl alcohol. *Applied Physics A: Materials Science and Processing*, *87*(4), 641–643. https://doi.org/10.1007/s00339-007-3882-3

Kvien, I., Tanem, B. S., & Oksman, K. (2005). Characterization of cellulose whiskers and their nanocomposites by atomic force and electron microscopy. *Biomacromolecules*, *6*, 3160–3165. https://doi.org/10.1021/bm050479t CCC:

Lee, J. H., Park, S. H., & Kim, S. H. (2014). Surface modification of cellulose nanowhiskers and their reinforcing effect in polylactide. *Macromolecular Research*, *22*(4), 424–430. https://doi.org/10.1007/s13233-014-2064-3

Lee, S. M., & Rowell, R. M. (1991). *International encyclopedia of composites*. New York: VCH-Publishers.

Lewandowska, A. E., & Eichhorn, S. J. (2016). Quantification of the degree of mixing of cellulose nanocrystals in thermoplastics using Raman spectroscopy. *Journal of Raman Spectroscopy*, *47*, 1337–1342. https://doi.org/10.1002/jrs.4966

Lewandowska, A. E., Inai, N. H., Ghita, O. R., & Eichhorn, S. J. (2018). Quantitative analysis of the distribution and mixing of cellulose nanocrystals in thermoplastic composites using Raman chemical imaging. *RSC Advances*, *8*(62), 35831–35839. https://doi.org/10.1039/C8RA06674D

Li, D., Liu, Z., Al-Haik, M., Tehrani, M., Murray, F., Tannenbaum, R., & Garmestani, H. (2010). Magnetic alignment of cellulose nanowhiskers in an all-cellulose composite. *Polymer Bulletin*, *65*(6), 635–642. https://doi.org/10.1007/s00289-010-0276-z

Lin, N., & Dufresne, A. (2013). Physical and/or chemical compatibilization of extruded cellulose nanocrystal reinforced polystyrene nanocomposites. *Macromolecules*, *46*(14), 5570–5583. https://doi.org/dx.doi.org/10.1021/ma4010154

Lin, N., & Dufresne, A. (2014). Nanocellulose in biomedicine: Current status and future prospect. *European Polymer Journal*, *59*, 302–325. https://doi.org/http://dx.doi.org/10.1016/j.eurpolymj.2014.07.025

Lin, N., Huang, J., Chang, P. R., Feng, J., & Yu, J. (2011). Surface acetylation of cellulose nanocrystal and its reinforcing function in poly(lactic acid). *Carbohydrate Polymers*, *83*(4), 1834–1842. http://dx.doi.org/10.1016/j.carbpol.2010.10.047

Lin, W., Cossar, M., Dang, V., & Teh, J. (2007). The application of Raman spectroscopy to three-phase characterization of polyethylene crystallinity. *Polymer Testing*, *26*(6), 814–821. https://doi.org/10.1016/j.polymertesting.2007.05.004

Littunen, K., Hippi, U., Saarinen, T., & Seppälä, J. (2013). Network formation of nanofibrillated cellulose in solution blended poly(methyl methacrylate) composites. *Carbohydrate Polymers*, *91*(1), 183–190. https://doi.org/10.1016/j.carbpol.2012.08.032

Liu, J.-C., Martin, D. J., Moon, R. J., & Youngblood, J. P. (2015). Enhanced thermal stability of biomedical thermoplastic polyurethane with the addition of cellulose nanocrystals. *Journal of Applied Polymer Science*, *132*(22). https://doi.org/10.1002/app.41970

Lu, J., Wang, T., & Drzal, L. T. (2008). Preparation and properties of microfibrillated cellulose polyvinyl alcohol composite materials. *Composites Part A: Applied Science and Manufacturing*, *39*(5), 738–746. https://doi.org/10.1016/j.compositesa.2008.02.003

Ma, L., Zhang, Y., Meng, Y., Anusonti-Inthra, P., & Wang, S. (2015). Preparing cellulose nanocrystal/acrylonitrile-butadiene-styrene nanocomposites using the master-batch method. *Carbohydrate Polymers*, *125*, 352–359. https://doi.org/10.1016/j.carbpol.2015.02.062

Manikandan Nair, K. C., Thomas, S., & Groeninckx, G. (2001). Thermal and dynamic mechanical analysis of polystyrene composites reinforced with short sisal fibres. *Composites Science and Technology*, *61*(16), 2519–2529. https://doi.org/S0266-3538(01)00170-1

Mariano, M., El Kissi, N., & Dufresne, A. (2014). Cellulose nanocrystals and related nanocomposites: Review of some properties and challenges. *Journal of Polymer Science Part B: Polymer Physics*, *52*(12), 791–806. http://doi.wiley.com/10.1002/polb.23490

Marques, M. F. V, Lunz, J. N., Aguiar, V. O., Grafova, I., Kemell, M., & Visentin, F. (2015). Thermal and mechanical properties of sustainable composites reinforced with natural fibers. *Journal of Polymers and the Environment*, *23*, 251–260. https://doi.org/10.1007/s10924-014-0687-2

Martinez-Romo, A., González-Mota, R., Soto-Bernal, J. J., & Rosales-Candelas, I. (2015). Investigating the degradability of HDPE, LDPE, PE-BIO, and PE-OXO films under UV-B radiation. *Journal of Spectroscopy*, *2015*, 1–6. https://doi.org/10.1155/2015/586514

Mathew, A. P., & Dufresne, A. (2002). Morphological investigation of nanocomposites from sorbitol plasticized starch and tunicin whiskers. *Biomacromolecules*, *3*, 609–617. https://doi.org/10.1021/bm0101769

Mathew, A. P., Gong, G., Bjorngrim, N., & Wixe, D. (2011). Moisture absorption behavior and its impact on the mechanical properties of cellulose whiskers-

based polyvinylacetate nanocomposites. *Polymer Engineering & Science*, *51*, 2136–2142. https://doi.org/10.1002/pen.22063

Maxfield, J., & Shepherd, I. W. (1975). Conformation of poly(ethylene oxide) in the solid state, melt and solution measured by Raman scattering. *Polymer*, *16*(7), 505–509. https://doi.org/10.1016/0032-3861(75)90008-7

Mendez, J., Annamalai, P. K., Eichhorn, S. J., Rusli, R., Rowan, S. J., Foster, E. J., & Weder, C. (2011). Bioinspired mechanically adaptive polymer nanocomposites with water-activated shape-memory effect. *Macromolecules*, *44*(17), 6827–6835. https://doi.org/dx.doi.org/10.1021/ma201502k

Migler, K. B., Kotula, A. P., & Hight Walker, A. R. (2015). Trans-Rich Structures in Early Stage Crystallization of Polyethylene. *Macromolecules*, *48*(13), 4555–4561. https://doi.org/10.1021/ma5025895

Missoum, K., Belgacem, M. N., & Bras, J. (2013). Nanofibrillated cellulose surface modification: A review. *Materials*, *6*(5), 1745–1766. https://doi.org/10.3390/ma6051745

Mohanty, S., Nayak, S. K., Verma, S. K., & Tripathy, S. S. (2004). Effect of MAPP as a coupling agent on the performance of Jute-PP composites. *Journal of Reinforced Plastics and Composites*, *23*(6), 625–637. https://doi.org/10.1177/0731684404032868

Mohanty, S., Verma, S. K., & Nayak, S. K. (2006). Dynamic mechanical and thermal properties of MAPE treated jute/HDPE composites. *Composites Science and Technology*, *66*(3–4), 538–547. https://doi.org/10.1016/j.compscitech.2005.06.014

Mohanty, S., Verma, S. K., Nayak, S. K., & Tripathy, S. S. (2004). Influence of fiber treatment on the performance of sisal-polypropylene composites. *Journal of Applied Polymer Science*, *94*(3), 1336–1345. https://doi.org/10.1002/app.21161

Mokhena, T. C., & Luyt, A. S. (2014). Investigation of polyethylene/sisal whiskers nanocomposites prepared under different conditions. *Polymer Composites*, *35*(11), 2221–2233. https://doi.org/10.1002/pc.22887

Moon, R. J., Martini, A., Nairn, J., Simonsen, J., & Youngblood, J. (2011). Cellulose nanomaterials review: structure, properties and nanocomposites. *Chemical Society Reviews*, *40*(7), 3941–3994. https://doi.org/10.1039/c0cs00108b

Morais, J. A. De, Gadioli, R., De Paoli, M.-A., & Paoli, M. De. (2016). Curaua fiber reinforced high-density polyethylene composites: Effect of impact modifier and fiber loading. *Polímeros*, *26*(2), 115–122. https://doi.org/10.1590/0104-1428.2124

Morán, J. I., Vázquez, A., & Cyras, V. P. (2013). Bio-nanocomposites based on derivatized potato starch and cellulose, preparation and characterization. *Journal of Materials Science*, *48*(20), 7196–7203. https://doi.org/10.1007/s10853-013-7536-x

Mueller, S., Sapkota, J., Nicharat, A., Zimmermann, T., Tingaut, P., Weder, C., & Foster, E. J. (2015). Influence of the nanofiber dimensions on the properties of nanocellulose/poly(vinyl alcohol) aerogels. *Journal of Applied Polymer Science*, *132*(13), n/a-n/a. https://doi.org/10.1002/app.41740

Mukherjee, T., Tobin, M. J., Puskar, L., Sani, M. A., Kao, N., Gupta, R. K., … Bhattacharya, S. (2017). Chemically imaging the interaction of acetylated nanocrystalline cellulose (NCC) with a polylactic acid (PLA) polymer matrix. *Cellulose*, *24*(4), 1717–1729. https://doi.org/10.1007/s10570-017-1217-x

Müller, K., Bugnicourt, E., Latorre, M., Jorda, M., Sanz, Y. E., Lagaron, J. M., … Lindner, M. (2017). Review on the processing and properties of polymer nanocomposites and nanocoatings and their applications in the packaging, automotive and solar energy fields. *Nanomaterials*, *7*(74), 1–47. https://doi.org/10.3390/nano7040074

Mwaikambo, L. Y., & Ansell, M. P. (2002). Chemical modification of hemp, sisal, jute, and kapok fibers by alkalization. *Journal of Applied Polymer Science*, *84*(12), 2222–2234. https://doi.org/10.1002/app.10460

Nagalakshmaiah, M., Pignon, F., El Kissi, N., & Dufresne, A. (2016). Surface adsorption of triblock copolymer (PEO- PPO-PEO) on cellulose nanocrystals and their melt extrusion with polyethylene. *RSC Advances*, *6*, 66224–66232. https://doi.org/10.1039/C6RA11139D

Nam, S., French, A. D., Condon, B. D., & Concha, M. (2016). Segal crystallinity index revisited by the simulation of X-ray diffraction patterns of cotton cellulose Iβ and cellulose II. *Carbohydrate Polymers*, *135*, 1–9. https://doi.org/10.1016/j.carbpol.2015.08.035

Newcomb, B. A., Chae, H. G., Gulgunje, P. V., Gupta, K., Liu, Y., Tsentalovich, D. E., … Kumar, S. (2014). Stress transfer in polyacrylonitrile/carbon nanotube composite fibers. *Polymer (United Kingdom)*, *55*(11), 2734–2743. https://doi.org/10.1016/j.polymer.2014.04.008

Ng, H. M., Sin, L. T., Bee, S. T., Tee, T. T., & Rahmat, A. R. (2017). Review of Nanocellulose Polymer Composite Characteristics and Challenges. *Polymer - Plastics Technology and Engineering*, *56*(7), 687–731. https://doi.org/10.1080/03602559.2016.1233277

Nicharat, A., Sapkota, J., Weder, C., & Johan Foster, E. (2015). Melt processing of polyamide 12 and cellulose nanocrystals nanocomposites. *Journal of Applied Polymer Science*, *132*(45), 1–10. https://doi.org/10.1002/app.42752

Nissan, A. H. (1956). The rheological behaviour of hydrogen-bonded solids. *Transactions of the Faraday Society*, (2), 700–709.

Oksman, K., Aitomäki, Y., Mathew, A. P., Siqueira, G., Zhou, Q., Butylina, S., … Hooshmand, S. (2016). Review of the recent developments in cellulose nanocomposite processing. *Composites: Part A*, *83*, 2–18. https://doi.org/10.1016/j.compositesa.2015.10.041

Oksman, K., Mathew, A. P., Bondeson, D., & Kvien, I. (2006). Manufacturing process of cellulose whiskers/polylactic acid nanocomposites. *Composites Science and Technology*, *66*(15), 2776–2784. https://doi.org/10.1016/j.compscitech.2006.03.002

Paradkar, R. P., Sakhalkar, S. S., He, X., & Ellison, M. S. (2003). Estimating crystallinity in high density polyethylene fibers using online Raman spectroscopy. *Journal of Applied Polymer Science*, *88*(2), 545–549. https://doi.org/10.1002/app.11719

Paralikar, S. a., Simonsen, J., & Lombardi, J. (2008). Poly(vinyl alcohol)/cellulose nanocrystal barrier membranes. *Journal of Membrane Science*, *320*(1–2), 248–258.

Park, W. Il, Kang, M., Kim, H. S., & Jin, H. J. (2007). Electrospinning of poly(ethylene oxide) with bacterial cellulose whiskers. *Macromolecular Symposia*, *249–250*, 289–294. https://doi.org/10.1002/masy.200750347

Paunikallio, T., Kasanen, J., Suvanto, M., & Pakkanen, T. T. (2003). Influence of

maleated polypropylene on mechanical properties of composite made of viscose fiber and polypropylene. *Journal of Applied Polymer Science*, *87*, 1895–1900.

Pereda, M., Kissi, N. El, & Dufresne, A. (2014). Extrusion of polysaccharide nanocrystal reinforced polymer nanocomposites through compatibilization with poly(ethylene oxide). *ACS Applied Materials and Interfaces*, *6*(12), 9365–9375. https://doi.org/dx.doi.org/10.1021/am501755p

Peresin, M. S., Vesterinen, A. H., Habibi, Y., Johansson, L. S., Pawlak, J. J., Nevzorov, A. a., & Rojas, O. J. (2014). Crosslinked PVA nanofibers reinforced with cellulose nanocrystals: Water interactions and thermomechanical properties. *Journal of Applied Polymer Science*, *131*(11), 1–12. https://doi.org/10.1002/app.40334

Piggott, M. R. (1980). *Load bearing fibre composites*. Oxford: Pergamon Press.

Prasad, K., & Grubb, D. T. (1989). Direct observation of taut tie molecules in high-strength polyethylene fibers by Raman spectroscopy. *Journal of Polymer Science Part B: Polymer Physics*, *27*(2), 381–403. https://doi.org/10.1002/polb.1989.090270212

Puglia, J. B. D., & Kenny, J. M. (2004). A Reviewon Natural Fibre Based Composites – Part I : Structure , Processing and Properties of Vegetable Fibres. *Journal of Natual Fibers*, *1*(January), 37–65. https://doi.org/10.1300/J395v01n02

Pullawan, T., Wilkinson, A. N., & Eichhorn, S. J. (2012). Influence of magnetic field alignment of cellulose whiskers on the mechanics of all-cellulose nanocomposites. *Biomacromolecules*, *13*(8), 2528–2536. https://doi.org/dx.doi.org/10.1021/bm300746r

Pullawan, T., Wilkinson, A. N., Zhang, L. N., & Eichhorn, S. J. (2014). Deformation micromechanics of all-cellulose nanocomposites: Comparing matrix and reinforcing components. *Carbohydrate Polymers*, *100*, 31–39. http://dx.doi.org/10.1016/j.carbpol.2012.12.066

Qiu, W., Zhang, F., Endo, T., & Hirotsu, T. (2004). Milling-induced esterification between cellulose and maleated polypropylene. *Journal of Applied Polymer Science*, *91*, 1703–1709. https://doi.org/10.1002/app.13368

Quazi, N., Mukherjee, T., Gupta, R. K., Kao, N., Sani, M., & Bhattacharya, S. (2013). Improved dispersion of cellulose microcrystals in polylactic acid (PLA) based composites applying surface acetylation. *Chemical Engineering Science*, *101*, 655–662. https://doi.org/10.1016/j.ces.2013.07.032

Quero, F., Nogi, M., Lee, K. Y., Poel, G. Vanden, Bismarck, A., Mantalaris, A., … Eichhorn, S. J. (2011). Cross-linked bacterial cellulose networks using glyoxalization. *ACS Applied Materials and Interfaces*, *3*(2), 490–499.

Raman, C. V. (1928). A change of wave-length in light scattering. *Nature*, 121, 619

Raman, C. V., & Krishnan, K. S. (1928). A New Type of Secondary Radiation. *Nature*, *121*, 501. https://doi.org/10.1038/121501c0

Reddy, N., & Yang, Y. (2005a). Biofibers from agricultural byproducts for industrial applications. *Trends in Biotechnology*, *23*(1), 22–27.

Reddy, N., & Yang, Y. (2005b). Biofibers from agricultural byproducts for industrial applications. *Trends in Biotechnology*, *23*(1), 22–27. https://doi.org/10.1016/j.tibtech.2004.11.002

Renishawservicemanual. (1997). In *Renishaw Raman Spectroscopy Manual User Guide M/8012/1798/02*.

Richard-lacroix, M., & Pellerin, C. (2017). Raman spectroscopy of individual poly(ethylene oxide) electrospun fibers: Effect of the collector on molecular orientation. *Vibrational Spectroscopy*, *91*, 92–98. https://doi.org/10.1016/j.vibspec.2016.09.002

Rocco, A. M., Pereira, R. P., & Felisberti, M. I. (2001). Miscibility, crystallinity and morphological behavior of binary blends of poly (ethylene oxide) and poly (methyl vinyl ether ± maleic acid). *Polymer*, *42*, 5199–5205. https://doi.org/10.1016/S0032-3861(00)00784-9

Rojas, O. J., Montero, G. A., & Forest, Y. H. (2009). Electrospun nanocomposites from polystyrene loaded with cellulose nanowhiskers. *Journal of Applied Polymer Science*, *11*, 927–935. https://doi.org/10.1002/app

Roman, M., & Winter, W. T. (2004). Effect of sulfate groups from sulfuric acid hydrolysis on the thermal degradation behavior of bacterial cellulose. *Biomacromolecules*, *5*(5), 1671–1677. https://doi.org/10.1021/bm034519+

Rusli, R., & Eichhorn, S. J. (2008). Determination of the stiffness of cellulose nanowhiskers and the fiber-matrix interface in a nanocomposite using Raman spectroscopy. *Applied Physics Letters*, *93*(3), 033111. https://doi.org/10.1063/1.2963491

Rusli, R., Shanmuganathan, K., Rowan, S. J., Weder, C., & Eichhorn, S. J. (2010). Stress-transfer in anisotropic and environmentally adaptive cellulose whisker nanocomposites. *Biomacromolecules*, *11*(3), 762–768. https://doi.org/10.1021/bm1001203

Rusli, R., Shanmuganathan, K., Rowan, S. J., Weder, C., & Eichhorn, S. J. (2011). Stress transfer in cellulose nanowhisker composites--influence of whisker aspect ratio and surface charge. *Biomacromolecules*, *12*(4), 1363–1369. https://doi.org/dx.doi.org/10.1021/bm200141x

Sacui, I. a., Nieuwendaal, R. C., Burnett, D. J., Stranick, S. J., Jorfi, M., Weder, C., … Gilman, J. W. (2014). Comparison of the properties of cellulose nanocrystals and cellulose nanofibrils isolated from bacteria, tunicate, and wood processed using acid, enzymatic, mechanical, and oxidative methods. *ACS Applied Materials and Interfaces*, *6*(9), 6127–6138. https://doi.org/dx.doi.org/10.1021/am500359f

Sapkota, J., Jorfi, M., Weder, C., & Foster, E. J. (2014). Reinforcing Poly(ethylene) with Cellulose Nanocrystals. *Macromolecular Rapid Communication*, *35*, 1747–1753. https://doi.org/DOI: 10.1002/marc.201400382

Sapkota, J., Kumar, S., Weder, C., & Foster, E. J. (2015). Influence of Processing Conditions on Properties of Poly (Vinyl acetate)/ Cellulose Nanocrystal Nanocomposites. *Macromolecular Materials and Engineering*, *300*, 562–571. https://doi.org/10.1002/mame.201400313

Sato, H., Shimoyama, M., Kamiya, T., Amari, T., Aic, S., Ninomiya, T., … Ozaki, Y. (2002). Raman spectra of high-density, low-density, and linear low-density polyethylene pellets and prediction of their physical properties by multivariate data analysis. *Journal of Applied Polymer Science*, *86*(2), 443–448.

Sato, H., Shimoyama, M., Kamiya, T., Amari, T., Sasic, S., Ninomiya, T., … Ozaki, Y. (2002). Raman spectra of high-density, low-density, and linear low-density polyethylene pellets and prediction of their physical properties by multivariate data analysis. *Journal of Applied Polymer Science*, *86*(2), 443–448. https://doi.org/10.1002/app.10999

Schwartz, M. M. (1997). *Composite Materials, Vol. II: Processing, Fabrication, and Applications*. Prentice Hall.

Sepet, H., Tarakcioglu, N., & Misra, R. D. K. (2016). Determination of the mechanical, thermal and physical properties of nano-CaCo3 filled high-density polyethylene nanocomposites produced in an industrial scale. *Journal of Composite Materials*, *50*(24), 3445–3456. https://doi.org/10.1177/0021998315621371

Shahzad, A. (2015). Mechanical Properties of Eco-friendly Polymer Nanocomposites. In *Eco-friendly Polymer Nanocomposites* (pp. 527-559). Springer, New Delhi.

Shanmuganathan, K., Capadona, J. R., Rowan, S. J., & Weder, C. (2010). Bio-inspired mechanically-adaptive nanocomposites derived from cotton cellulose whiskers. *Journal of Materials Chemistry*, *20*, 180–186. https://doi.org/10.1039/b916130a

Siqueira, G., Bras, J., & Dufresne, A. (2010). Cellulosic bionanocomposites: A review of preparation, properties and applications. *Polymers*, *2*(4), 728–765. https://doi.org/10.3390/polym2040728

Siró, I., & Plackett, D. (2010a). Microfibrillated cellulose and new nanocomposite materials: a review. *Cellulose*, *17*(3), 459–494. https://doi.org/10.1007/s10570-010-9405-y

Siró, I., & Plackett, D. (2010b). Microfibrillated cellulose and new nanocomposite materials: A review. *Cellulose*, *17*(3), 459–494. https://doi.org/10.1007/s10570-010-9405-y

Smeder, B., & Liljedahl, S. (1996). Market oriented identification of important properties in developing flax fibres for technical uses. *Industrial Crops and Products*, *5*(2), 149–162. https://doi.org/10.1016/0926-6690(96)00009-X

Smith, E., & Dent, G. (2005). *Modern Raman Spectroscopy*. *Wiley* (Vol. 1). https://doi.org/10.1016/S1072-7515(99)00299-9

Spinella, S., Lo, G., Liu, B., Dorgan, J., Habibi, Y., Lecl, P., … Gross, R. A. (2015). Polylactide/cellulose nanocrystal nanocomposites : Efficient routes for nano fiber modification and effects of nano fiber chemistry on PLA reinforcement. *Polymer*, *65*, 9–17. https://doi.org/10.1016/j.polymer.2015.02.048

Spoljaric, S., Genovese, A., & Shanks, R. A. (2009). Polypropylene-microcrystalline cellulose composites with enhanced compatibility and properties. *Composites Part A: Applied Science and Manufacturing*, *40*(6–7), 791–799. http://dx.doi.org/10.1016/j.compositesa.2009.03.011

Šturcová, A., Davies, G. R., & Eichhorn, S. J. (2005). Elastic modulus and stress-transfer properties of tunicate cellulose whiskers. *Biomacromolecules*, *6*(2), 1055–1061.

Suflet, D. M., Chitanu, G. C., & Popa, V. I. (2006). Phosphorylation of polysaccharides: New results on synthesis and characterisation of phosphorylated cellulose. *Reactive and Functional Polymers*, *66*(11), 1240–1249. https://doi.org/10.1016/j.reactfunctpolym.2006.03.006

Sunkyu Park, John O Baker, Michael E Himmel, Philip A Parilla, & David K Johnson. (2010). Cellulose crystallinity index: measurement techniques and their impact on interpreting cellulase performance. *Biotechnology for Biofuels*, *3*(10), 1–10. http://www.biotechnologyforbiofuels.com/content/3/1/10

Suryanegara, L., Nakagaito, A. N., & Yano, H. (2009). The effect of crystallization of

PLA on the thermal and mechanical properties of microfibrillated cellulose-reinforced PLA composites. *Composites Science and Technology*, *69*(7–8), 1187–1192. http://dx.doi.org/10.1016/j.compscitech.2009.02.022

Swatloski, R. P., Spear, S. K., Holbrey, J. D., & Rogers, R. D. (2002). Dissolution of cellulose with ionic liquids. *Journal of the American Chemical Society*, *124*(18), 4974–4975. https://doi.org/10.1021/ja025790m

Syverud, K., & Stenius, P. (2009). Strength and barrier properties of MFC films. *Cellulose*, *16*(1), 75–85. https://doi.org/10.1007/s10570-008-9244-2

Szymańska-Chargot, M., Cybulska, J., & Zdunek, A. (2011). Sensing the structural differences in cellulose from apple and bacterial cell wall materials by raman and FT-IR spectroscopy. *Sensors*, *11*(12), 5543–5560. https://doi.org/10.3390/s110605543

Taj, S., Khan, S., & Munawar, M. A. (2007). Natural fiber-reinforced polymer composites. *Proceedings of the Pakistan Academy of Sciences*, *44(2)*, 129–144.

Tanaka, F., & Iwata, T. (2006). Estimation of the elastic modulus of cellulose crystal by molecular mechanics simulation. *Cellulose*, *13*(5), 509–517. https://doi.org/10.1007/s10570-006-9068-x

Tanaka, M., & Young, R. J. (2006). Review Polarised Raman spectroscopy for the study of molecular orientation distributions in polymers. *Journal of Materials Science*, *41*(3), 963–991. https://doi.org/10.1007/s10853-006-6595-7

Tanpichai, S., Sampson, W. W., & Eichhorn, S. J. (2014). Stress transfer in microfibrillated cellulose reinforced poly(vinyl alcohol) composites. *Composites Part A: Applied Science and Manufacturing*, *65*, 186–191. https://doi.org/10.1016/j.compositesa.2014.06.014

TAPPI WI3021. *Proposed New TAPPI Standard:Standard Term and Definition for Cellulose Nanomaterial WI 3021*.

Tashiro, K. (1993). Molecular theory of mechanical properties of crystalline polymers. *Prog. Polym. Sci.*, *18*, 377–435. https://doi.org/10.1016/0079-6700(93)90013-3

Tashiro, K., Wu, G., & Kobayashi, M. (1988). Morphological effect on the Raman frequency shift induced by tensile stress applied to crystalline polyoxymethylene and polyethylene: spectroscopic support for the idea of an inhomogeneous stress distribution in polymer material. *Polymer*, *29*(10), 1768–1778. https://doi.org/10.1016/0032-3861(88)90389-8

Teja, M. S., Ramana, M. V., Sriramulu, D., & Rao, C. J. (2016). Experimental investigation of mechanical and thermal properties of sisal fibre reinforced composite and effect of sic filler material. *IOP Conference Series: Materials Science and Engineering*, *149*(1). https://doi.org/10.1088/1757-899X/149/1/012095

Thomas, S., Paul, S. A., Pothan, L. A., & Deepa, B. (2011). Natural fibres: Structure, properties and applications. In *Cellulose Fibers: Bio- and Nano-Polymer Composites Green Chemistry and Technology* (pp. 3–42). Berlin: Springer.

Thomsen, A. B., Thygesen, A., Bohn, V., Nielsen, K. V., Pallesen, B., & Jørgensen, M. S. (2006). Effects of chemical-physical pre-treatment processes on hemp fibres for reinforcement of composites and for textiles. *Industrial Crops and Products*, *24*(2), 113–118. https://doi.org/10.1016/j.indcrop.2005.10.003

Tingaut, P., Zimmermann, T., & Lopez-Suevos, F. (2010). Synthesis and

characterization of bionanocomposites with tunable properties from poly(lactic acid) and acetylated microfibrillated cellulose. *Biomacromolecules*, *11*(2), 454–464. https://doi.org/10.1021/bm901186u

Toozandehjani, M., Kamarudin, N., Dashtizadeh, Z., Lim, E. Y., Gomes, A., & Gomes, C. (2019). Conventional and advanced composites in aerospace industry: Technologies revisited. *American Journal of Aerospace Engineering*, *5*(1), 9. https://doi.org/10.11648/j.ajae.20180501.12

Tserki, V., Matzinos, P., Kokkou, S., & Panayiotou, C. (2005). Novel biodegradable composites based on treated lignocellulosic waste flour as filler. Part I. Surface chemical modification and characterization of waste flour. *Composites Part A: Applied Science and Manufacturing*, *36*(7), 965–974. https://doi.org/10.1016/j.compositesa.2004.11.010

Um, I. C., Ki, C. S., Kweon, H., Lee, K. G., Ihm, D. W., & Park, Y. H. (2004). Wet spinning of silk polymer: II. Effect of drawing on the structural characteristics and properties of filament. *International Journal of Biological Macromolecules*, *34*(1–2), 107–119. https://doi.org/10.1016/j.ijbiomac.2004.03.011

Wambua, P., Ivens, J., & Verpoest, I. (2003). Natural fibres: Can they replace glass in fibre reinforced plastics? *Composites Science and Technology*, *63*(9), 1259–1264. https://doi.org/10.1016/S0266-3538(03)00096-4

Wanasekara, N. D., & Eichhorn, S. J. (2017). Injectable highly loaded cellulose nanocrystal fibers and composites. *ACS Macro Letters*, *6*(10), 1066–1070. https://doi.org/10.1021/acsmacrolett.7b00609

Wang, W.-J., Wang, W.-W., & Shao, Z.-Q. (2014). Surface modification of cellulose nanowhiskers for application in thermosetting epoxy polymers. *Cellulose*, *21*(4), 2529–2538. http://link.springer.com/10.1007/s10570-014-0295-2

Wiley, J. H., & Atalla, R. H. (1987). Band assignments in the Raman spectra of celluloses. *Carbohydrate Research*, *160*, 113–129.

Wunderlich, B. (1990). *Thermal Analysis*. *Academic Press*.

Xu, X., Liu, F., Jiang, L., Zhu, J. Y., Haagenson, D., & Wiesenborn, D. P. (2013). Cellulose nanocrystals vs. cellulose nanofibrils: A comparative study on their microstructures and effects as polymer reinforcing agents. *ACS Applied Materials and Interfaces*, *5*(8), 2999–3009. https://doi.org/dx.doi.org/10.1021/am302624t

Yildirim, N., & Shaler, S. (2017). A study on thermal and nanomechanical performance of cellulose nanomaterials (CNs). *Materials*, *10*(7). https://doi.org/10.3390/ma10070718

Yoshiharu, N., Shigenori, K., Masahisa, W., & Takeshi, O. (1997). Cellulose microcrystal film of high uniaxial orientation. *Macromolecules*, *30*(20), 6395–6397. https://doi.org/10.1021/ma970503y

Young, R. J. (1995). Monitoring deformation processes in high-performance fibres using raman spectroscopy. *Journal of the Textile Institute*, *86*(2), 360–381. https://doi.org/10.1080/00405009508631340

Zarina, S., & Ahmad, I. (2015). Biodegradable composite films based on κ-carrageenan reinforced by cellulose nanocrystal from kenaf fibers. *BioResources*, *10*(1), 256-271.

Zhang, D., Zhang, Q., Gao, X., & Piao, G. (2013). A nanocellulose polypyrrole composite based on tunicate cellulose. *International Journal of Polymer Science*, *2013*, 1–6. https://doi.org/http://dx.doi.org/10.1155/2013/175609

Zhang, F., Qiu, W., Yang, L., Endo, T., & Hirotsu, T. (2002). Mechanochemical preparation and properties of a cellulose-polyethylene composite. *Journal of Materials Chemistry*, *12*(1), 24–26. https://doi.org/10.1039/b108255h

Zhang, P. P., Tong, D. S., Lin, C. X., Yang, H. M., Zhong, Z. K., Yu, H. Y., … Zhou, C. H. (2014). Effects of acid treatments on bamboo cellulose nanocrystals. *Asia-Pacific Journal of Chemical Engineering*, *9*, 686–695. https://doi.org/10.1002/apj.1812

Zhang, W., Yang, X., Li, C., Liang, M., Lu, C., & Deng, Y. (2011). Mechanochemical activation of cellulose and its thermoplastic polyvinyl alcohol ecocomposites with enhanced physicochemical properties. *Carbohydrate Polymers*, *83*(1), 257–263. https://doi.org/10.1016/j.carbpol.2010.07.062

Zhang, X., Ji, Z., Zhou, X., Ma, J. F., Hu, Y. H., & Xu, F. (2015). Method for automatically identifying spectra of different wood cell wall layers in Raman imaging data set. *Analytical Chemistry*, *87*(2), 1344–1350. https://doi.org/10.1021/ac504144s

Zia, Q., Androsch, R., Radusch, H.-J., & Ingoliç, E. (2008). Crystal morphology of rapidly cooled isotactic polypropylene: A comparative study by TEM and AFM. *Polymer Bulletin*, *60*, 791–798. https://doi.org/10.1007/s00289-008-0908-8

APPENDIX A

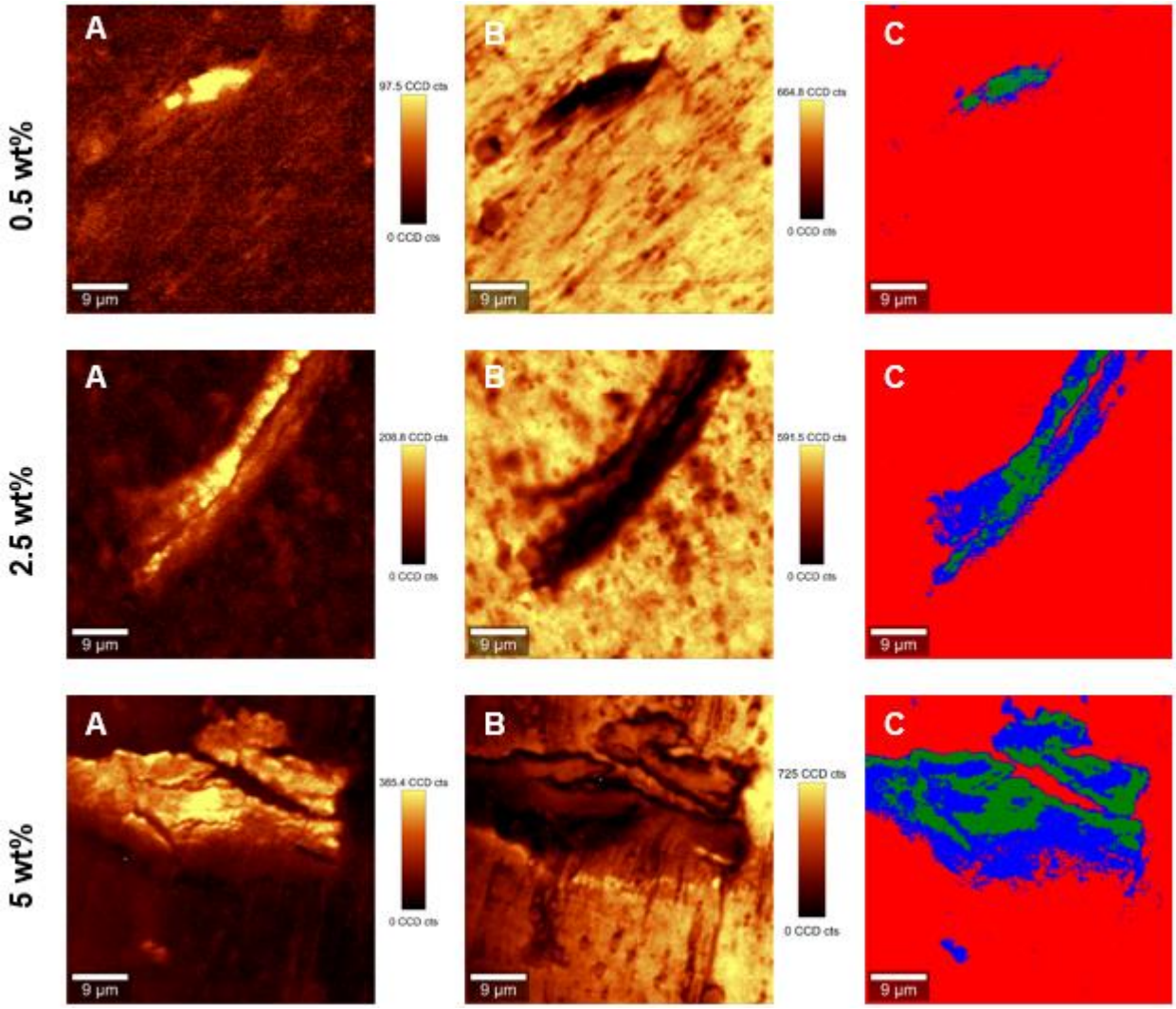

Figure A1. Raman images of 0.5% (top), 2.5% (middle) and 5% (bottom) of HDPE-cCNCs composites depicting the intensity of Raman bands located at ~1100 cm^{-1} (A) and ~1301 cm^{-1} (B). Chemical images of studied area (C) showing the chemical composition of a mapped cross-section.

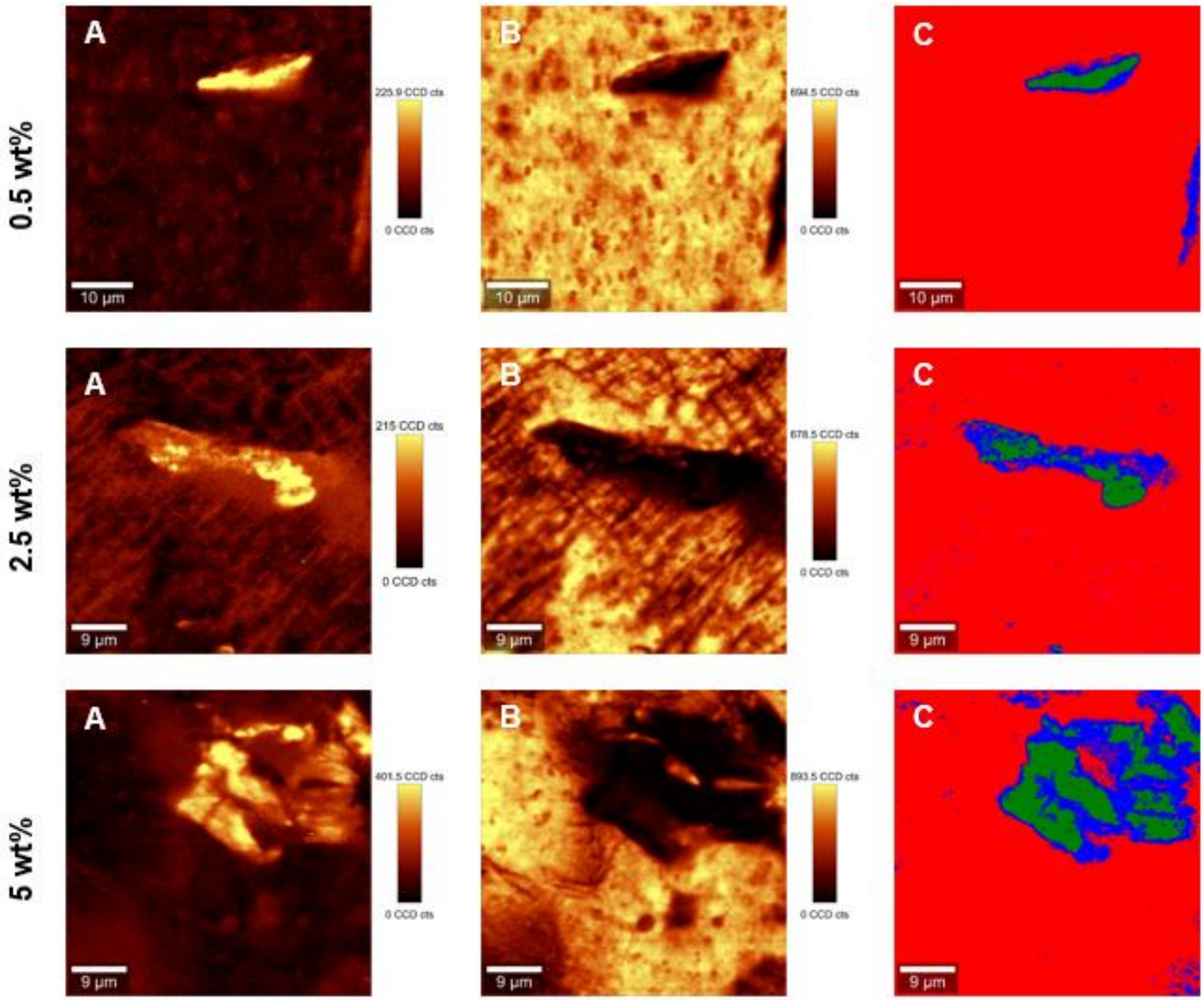

Figure A2. Raman images of 0.5% (top), 2.5% (middle) and 5% (bottom) of HDPE-MAPE/cCNCs composites depicting the intensity of Raman bands located at ~1100 cm^{-1} (A) and ~1301 cm^{-1} (B). Chemical images of studied area (C) showing the chemical composition of a mapped cross-section.

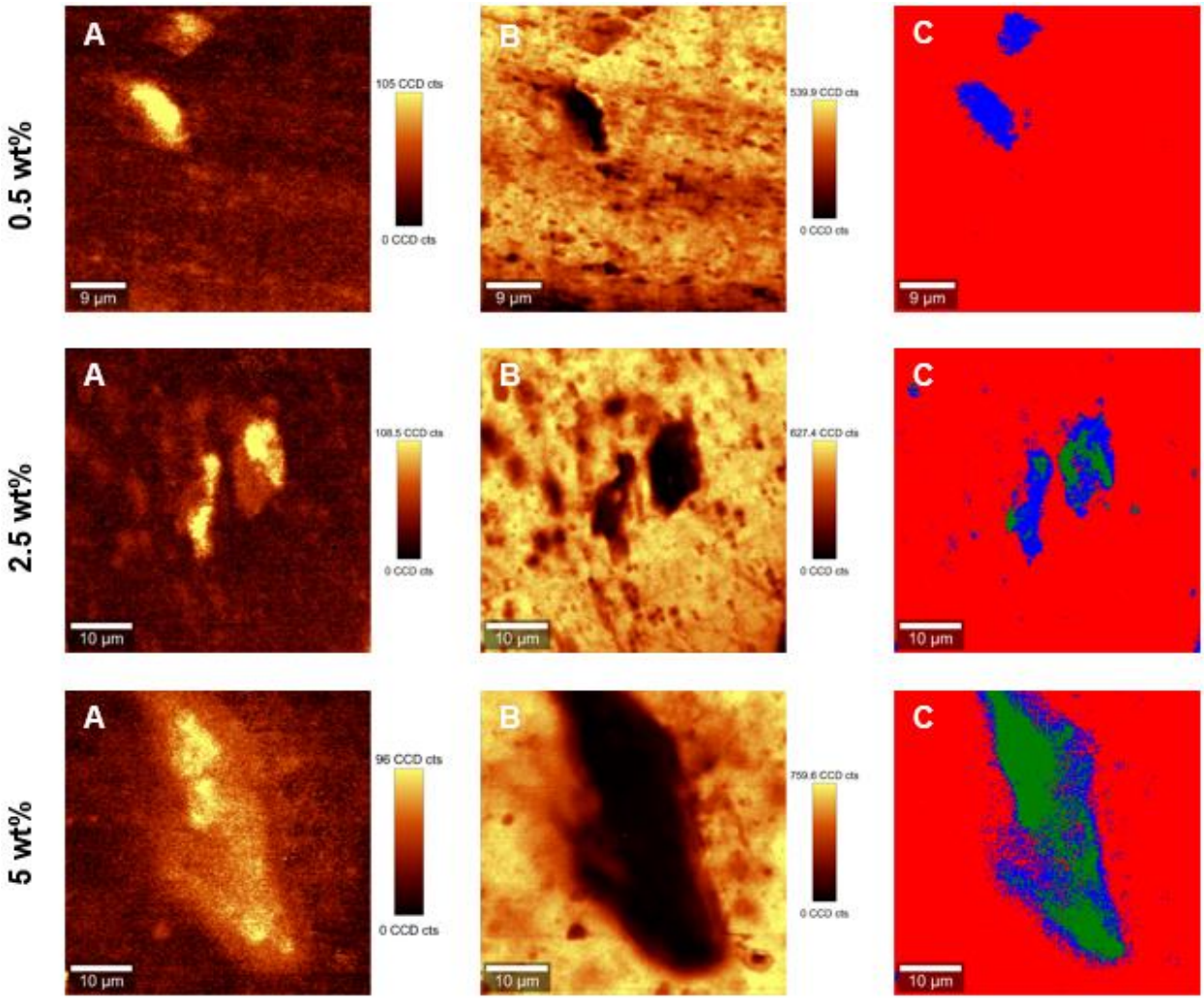

Figure A3. Raman images of 0.5% (top), 2.5% (middle) and 5% (bottom) of HDPE-PEO/cCNCs composites depicting the intensity of Raman bands located at ~1100 cm^{-1} (A) and ~1301 cm^{-1} (B). Chemical images of studied area (C) showing the chemical composition of a mapped cross-section.

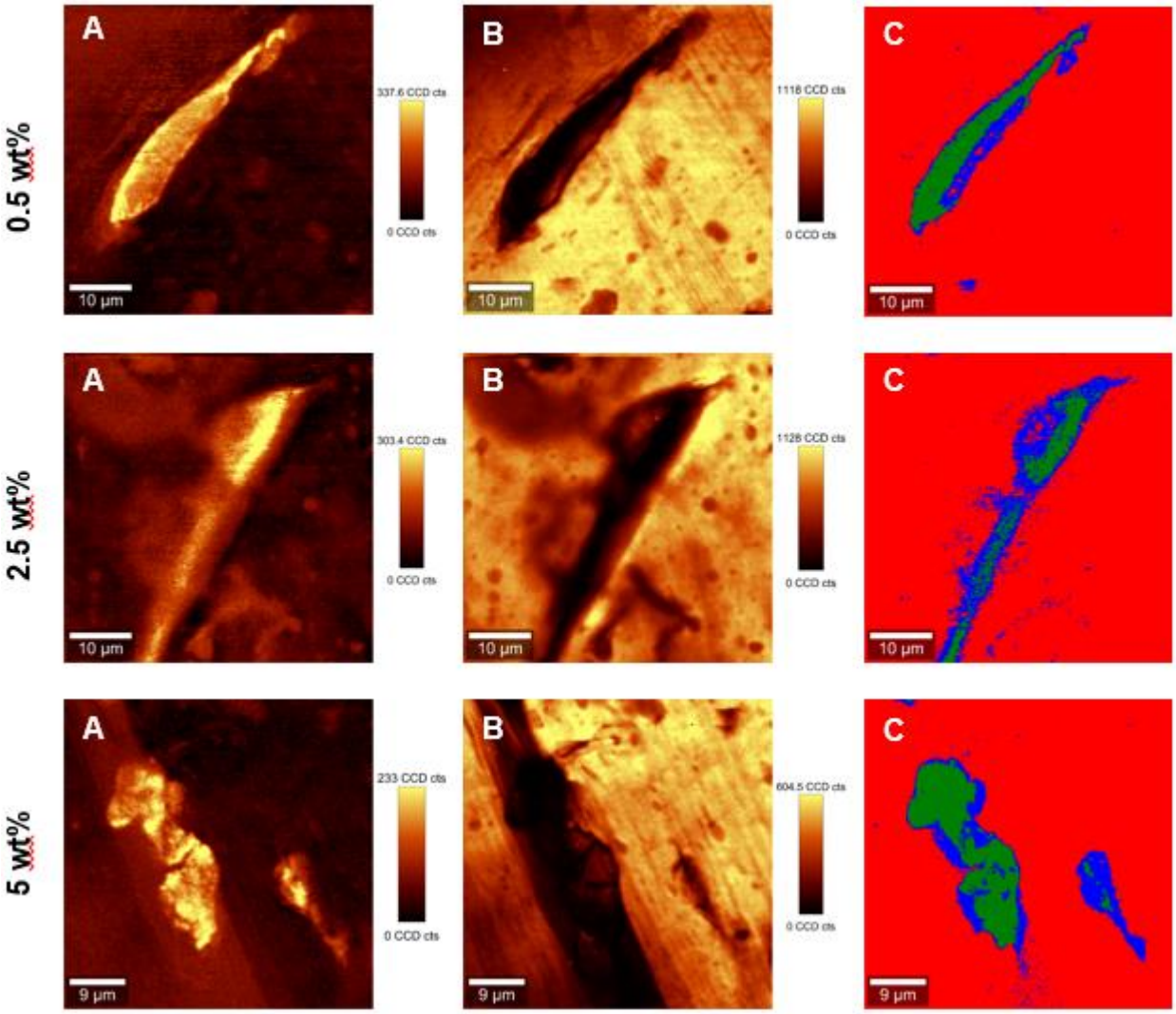

Figure A4. Raman images of 0.5% (top), 2.5% (middle) and 5% (bottom) of HDPE-tCNCs composites depicting the intensity of Raman bands located at ~1100 cm^{-1} (A) and ~1301 cm^{-1} (B). Chemical images of studied area (C) showing the chemical composition of a mapped cross-section.

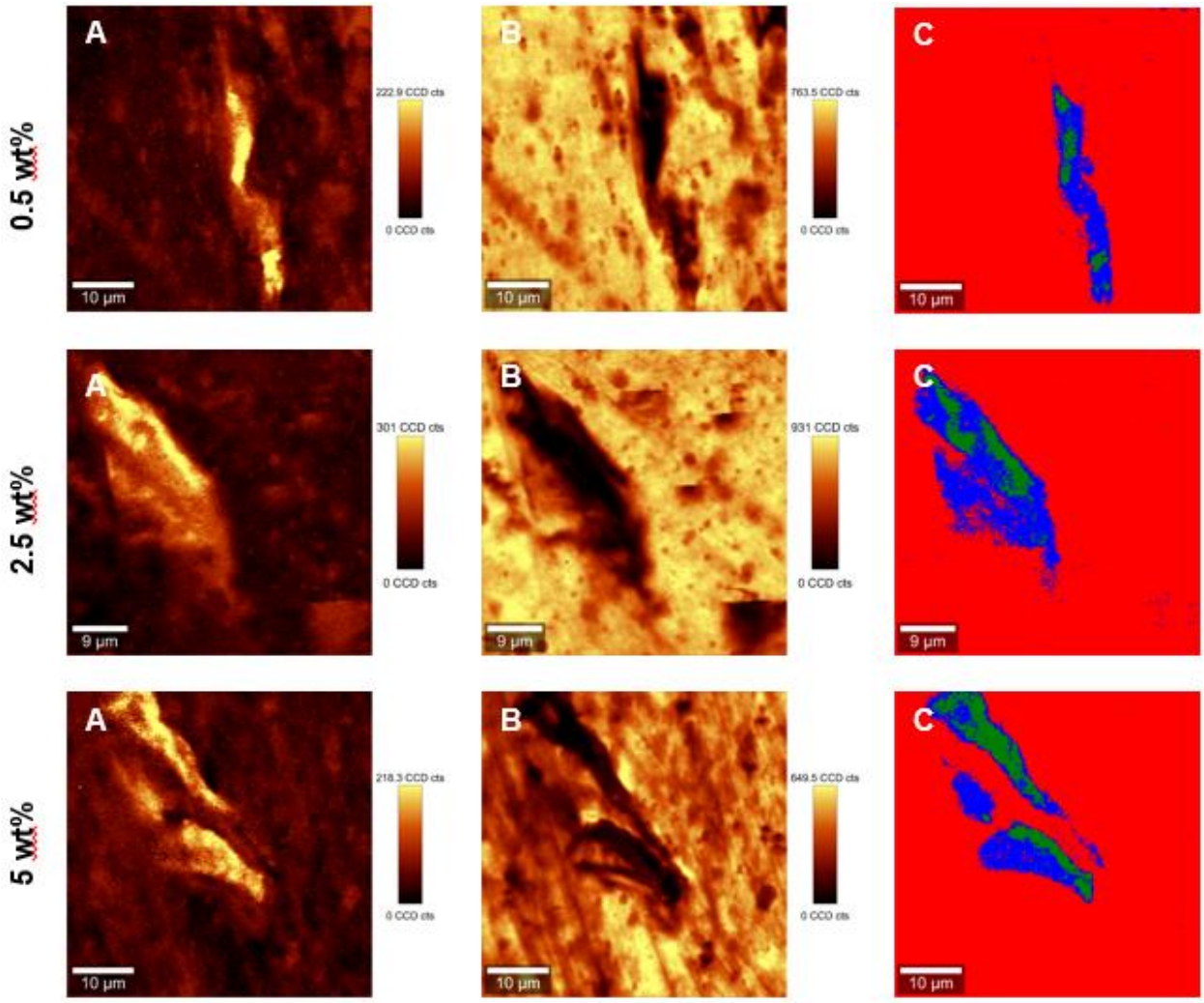

Figure A5. Raman images of 0.5% (top), 2.5% (middle) and 5% (bottom) of HDPE-MAPE/tCNCs composites depicting the intensity of Raman bands located at ~1100 cm^{-1} (A) and ~1301 cm^{-1} (B). Chemical images of studied area (C) showing the chemical composition of a mapped cross-section.

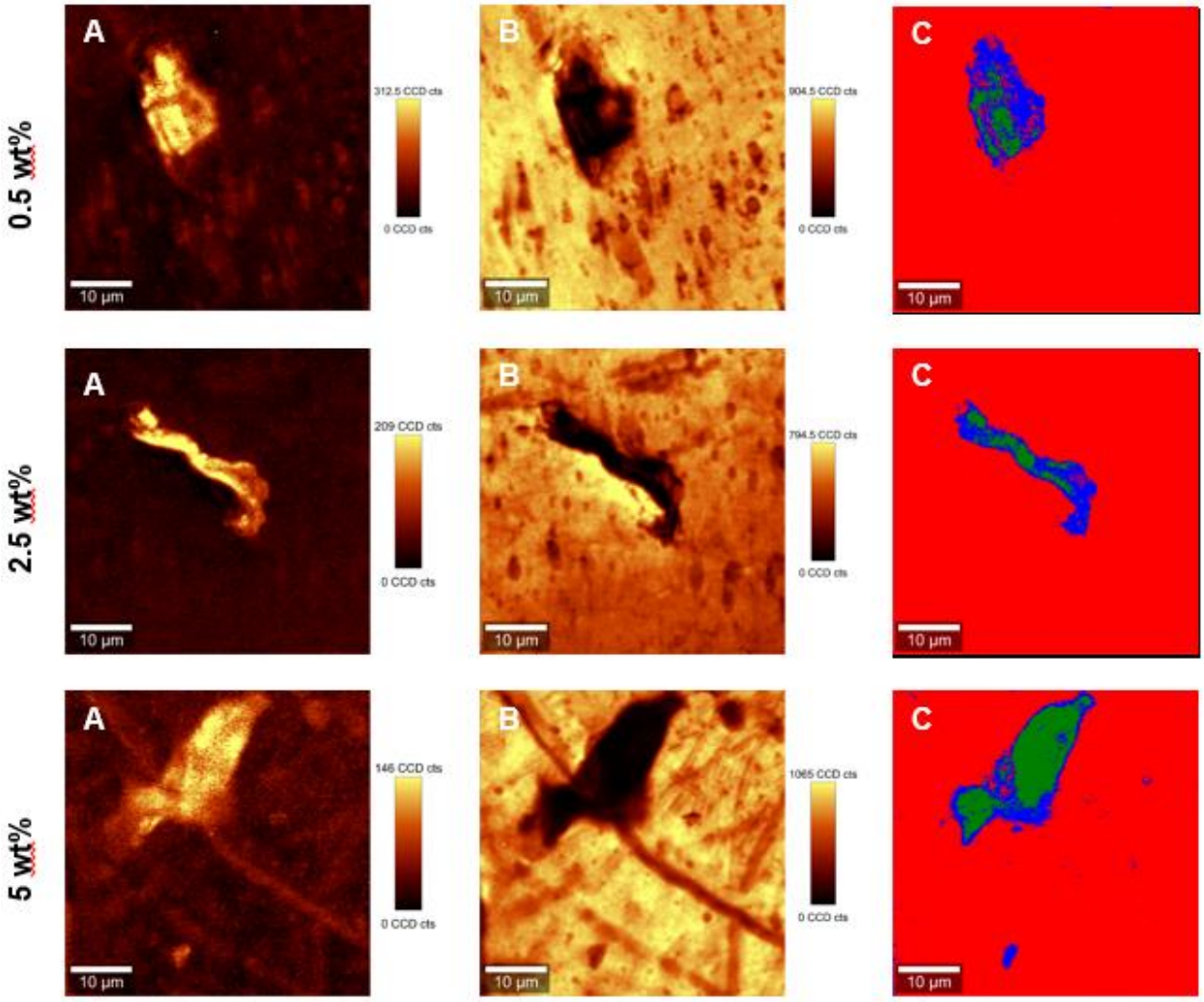

Figure A6. Raman images of 0.5% (top), 2.5% (middle) and 5% (bottom) of HDPE-PEO/tCNCs composites depicting the intensity of Raman bands located at ~1100 cm^{-1} (A) and ~1301 cm^{-1} (B). Chemical images of studied area (C) showing the chemical composition of a mapped cross-section.